THÈSE

En vue de l'obtention du

DOCTORAT DE L'UNIVERSITÉ DE TOULOUSE

Délivré par :

Institut National Polytechnique de Toulouse (Toulouse INP)

Discipline ou spécialité :

Energétique et Transferts

Présentée et soutenue par :

M. RÉGIS ANGHILANTE

le vendredi 2 octobre 2020

Titre :

Flexibilisation and integration of solid oxide electrolysis units in power to synthetic natural gas plants

---

Ecole doctorale :

Mécanique, Energétique, Génie civil, Procédés (MEGeP)

Unité de recherche :

Laboratoire de Génie Chimique (LGC)

Directeur(s) de Thèse :

M. PASCAL FLOQUET

MME ANNABELLE BRISSE

Rapporteurs :

M. CHAKIB BOUALLOU, MINESPARISTECH

M. JAN VAN HERLE, ECOLE POLYTECHNIQUE FEDERALE DE LAUSANNE

Membre(s) du jury :

Mme CATHERINE AZZARO-PANTEL, TOULOUSE INP, Président

M. FRANÇOIS MARECHAL, ECOLE POLYTECHNIQUE FEDERALE DE LAUSANNE, Membre

M. FRANK GRAF, , Membre

Mme ANNABELLE BRISSE, , Membre

Mme FLORENCE LEFEBVRE-JOUD, CEA GRENOBLE, Membre

M. PASCAL FLOQUET, TOULOUSE INP, Membre

“Vingt fois sur le métier remettez votre ouvrage,
Polissez-le sans cesse, et le repolissez,
Ajoutez quelquefois, et souvent effacez.“

Nicolas Boileau, L’Art Poétique

“We choose to go to the Moon in this decade and do the other things, not because they are easy, but because they are hard; because that goal will serve to organize and measure the best of our energies and skills, because that challenge is one that we are willing to accept, one we are unwilling to postpone, and one we intend to win, and the others, too.”

John F. Kennedy

"I've failed over and over and over again in my life. And that is why I succeed."

Michael Jordan

Acknowledgements

This PhD is the result of seven years of hard work, many long working days until late in the evening, many doubts and fears. But it was also about curiosity, perseverance, constant improvement, humility. I struggled a lot on my journey, but it was worth it and I think it made me a better person. This I owe to each and every one of the people mentioned hereafter. I humbly hope my journey can inspire others with all kind of projects they might have.

First, I would like to thank a lot Pascal Floquet for accepting me as his PhD student at the LGC and for supervising my work. I would like to thank a lot Annabelle Brisse for supervising my thesis and for all the work she has done at EIFER in the past 15 years, so that it was possible for me to undertake a PhD. Thanks a lot to both of them for their time, their valuable comments and advice during the PhD, as well as for their help improving the manuscript and preparing the PhD defense.

I would like to thank the reviewers Jan van Herle and Chakib Bouallou for their interest in my work, for their attentive reviewing, for all the positive comments they have made, but also their critical views, which are really important to me because this is what helps to get better.

I would like to thank all members of the jury for their interest in my work, for the interesting discussion, for the very positive feedbacks, as well as for the many relevant comments to improve the manuscript and suggestions for future work.

I would like to thank Frank Graf from the DVGW-EBI for supporting my application as a PhD student, but also for the many years of fruitful and pleasant collaboration between EIFER and the DVGW-EBI.

I would like to thank other important persons at EIFER: my group leader Mathieu Marrony for his support in this adventure, the directors Pascal Terrien and Nurten Avci, as well as the head of human resources Heike Stockmann. I would also like to thank David Colomar for our collaboration on the Res2CNG project and for showing me the path to be a good engineer.

Thanks also to the partner of the Res2CNG project, especially to Christian Müller from DVGW-EBI, Max Schmid from the IFK Stuttgart and Marlies Härdtlein from the IER Stuttgart. I really enjoyed our collaboration and your inputs were very helpful to obtain the results of this work.

I would like to thank the Region Baden-Württemberg for financing this work, but also for the ten very enriching years I have spent there since I started as a KIT student in mechanical engineering in 2010.

I would like to thank my family and my friends for their support, for the many discussions we had, for listening and motivating me when I was struggling. I am very happy that many of you were able to attend the PhD defense.

I would like to thank my muses, Michael Jordan, Kobe Bryant, Lebron James, and Louis Armstrong. Your achievements and passion for what you did or do is an infinite source of inspiration for me to get better every day in all things.

Last but not least, I would like to thank you Nicole for being who you are, for your support, your patience, your understanding. This PhD is also yours.

Table of contents

Introduction **15**
1. Fundamentals **19**
1.1. Power-to-SNG introduction 19
1.1.1. Presentation of power-to-SNG concept, interest, objectives and products 19
1.1.2. Economic, societal and environmental aspects of power-to-SNG 21
1.1.3. Power-to-SNG pathways 22
1.1.4. Power-to-SNG models with integrated SOE units 25
1.2. Water electrolysis 28
1.2.1. Thermodynamics 28
1.2.2. Operation of electrolysis cells 29
1.2.3. From the cell to the integrated electrolysis system 32
1.2.4. Operation modes of electrolysis units 33
1.2.5. Electrolysis technologies 33
1.2.6. Focus on existing SOE models 39
1.3. Methanation 43
1.3.1. Principle 43
1.3.2. Catalytic methanation technologies 46
1.3.3. Catalytic methanation processes 49
1.4. Feed gas production and gas treatment 51
1.4.1. Thermochemical biomass conversion to bio-syngas 51
1.4.2. Synthetic natural gas upgrading 55
1.5. Conclusions of Chapter 1 58
2. Energy assessment of power-to-SNG plants **61**
2.1. Plant performance indicators 61
2.2. Investigated plant concepts 62
2.2.1. Plant concept 1 – “Reference case” 63
2.2.2. Plant concept 2 – “CNG production” 63
2.2.3. Plant concept 3 – “LNG production” 63
2.3. Process modelling 64
2.3.1. Fluid property package development 64
2.3.2. Electrolysis 66
2.3.3. Catalytic methanation 71
2.3.4. Thermochemical biomass conversion in bio-syngas 73
2.3.5. Synthetic natural gas upgrading 76
2.3.6. Heat exchangers 77
2.4. Methodology for energy assessment of plant concepts 78
2.4.1. Preliminary energy assessment 78
2.4.2. Detailed energy assessment 80
2.5. Preliminary energy assessment 81
2.5.1. Pinch diagrams 81
2.5.2. Maximal theoretical efficiencies 86
2.6. Detailed energy assessment 87
2.6.1. Detailed plant layouts 87
2.6.2. Plant performance evaluation 96
2.6.3. Residual heat valorization 97
2.7. Model verification 99
2.8. Comparison of plant efficiencies with previous work 100
2.9. Conclusions of Chapter 2 103
3. Simulation of the transient behavior of SOE units **105**

3.1. Objectives and scope of the modelling work 105
3.2. Simulation hypotheses 106
3.2.1. Single repeat unit architecture 106
3.2.2. Modelling hypotheses 107
3.3. Methodology 108
3.3.1. Modelling pathway 108
3.3.2. Inlet gas flow rates and gas compositions 109
3.3.3. Flow characterization 110
3.3.4. Heat transfer characterization 112
3.3.5. Initial and boundary conditions 114
3.3.6. Description and implementation of the method of lines (MOL) 114
3.3.7. Exact solution in permanent regime 116
3.4. Transient behavior 119
3.4.1. Definition of the transients 119
3.4.2. SRU with integrated ESC (simplified model) 119
3.4.3. SRU with integrated CSC (simplified model) 122
3.4.4. SRU with integrated ESC (extended model) 125
3.4.5. SRU with integrated CSC (extended model) 126
3.4.6. Results discussion 128
3.5. Coupling with power profiles 132
3.5.1. SRU model with simplified power profile 132
3.5.2. H_2 production and storage unit with simplified power profile 133
3.5.3. H_2 production and storage unit with windpower profiles 138
3.6. Conclusions of Chapter 3 145
4. Economic evaluation of power-to-SNG plants 147
4.1. Methodology 147
4.1.1. Annualized costs calculation 147
4.1.2. Investment costs 148
4.1.3. Operation and maintenance costs 150
4.2. Scenarios description and main plant hypotheses 150
4.2.1. Scenarios description 150
4.2.2. Main techno-economic plant hypotheses 153
4.3. Investment costs of power-to-SNG plant components 153
4.3.1. Investment costs of the SOE unit 153
4.3.2. Investment costs of main plant components 163
4.4. Operation and maintenance costs 166
4.5. SNG production costs 168
4.5.1. Plant concept 1 168
4.5.2. Plant concept 2 169
4.5.3. Plant concept 3 171
4.5.4. Sensitivity analysis 173
4.6. Comparison with SNG, biomethane, and natural gas costs 175
4.7. Conclusions of Chapter 4 179
Conclusions 181
References 185
Appendix A – Additional results of Chapter 2 I
Fluid property package – validity domains of entropy and enthalpy functions I
Description of the secant method II
Overall heat transfer coefficients II
Extended SOE stack model III
Detailed description of pinch diagrams V
Plant concept 1 VI

Plant concept 2 VIII
Plant concept 3 X
Appendix B – Additional results of Chapter 3 XIII
List of parameters used for model comparison XIII
Main characteristics of the Repower 5M windmill XIII
Appendix C – Additional results of Chapter 4 XV
Chemical Engineering Plant Cost Index (CEPCI) annual values XV
SOE cell and stack manufacturing lines XV
SOE cell manufacturing line XV
SOE stack manufacturing line XVII
Determination of the different cost categories for SOE cells and stack production XVIII
Material costs XVIII
Equipment costs XVIII
Building costs XIX
Personnel costs XIX
Operation and maintenance costs XIX
Plant consumables and personnel costs of the power-to-SNG plants XX
Plant consumables XX
Personnel costs XX
Equipment repartition used for the cost evaluation XX
Résumé du manuscrit XXV
Contexte et enjeux XXV
Objectifs XXVII
Résultats XXVIII
Perspectives XXX

Nomenclature

Abbreviations

AC	alternative current
Ad	adsorption (column)
AER	absorption enhanced reforming
Bio-CH_4	biomethane
C	compressor
CCU	carbon capture utilization
CEPCI	chemical engineering plant cost index
CCS	carbon capture storage
CNG	compressed natural gas
CU	conditioning unit
D	drying column
DBT	dibenzyltoluene
DC	direct current
De	desorption (column)
DVGW	German Technical and Scientific Association for Gas and Water
EBI	Engler Bunte Institute at the Karlsruhe Institute of Technology
EIFER	European Institute for Energy Research
G	gasification unit
H	heater
HHV	higher heating value
HTE	high temperature electrolysis
HTEL	high temperature electrolyser
HX	heat exchanger
IER	Institute of Energy Economics and Rational Energy Use at the University of Stuttgart
IFK	Institute for Combustion and Power Plant Technology at the University of Stuttgart
KIT	Karlsruhe Institute of Technology
LHV	lower heating value
LNG	liquefied natural gas
M	mixer
P	pump
PEM	proton exchange membrane
PtSNG	power-to-synthetic natural gas
PtL	power-to-liquids
R	catalytic methanation reactor
RME	rapeseed methyl ester
SNG	synthetic natural gas
SOC	solid oxide cell
SOE	solid oxide electrolysis
SOEC	solid oxide electrolysis cell
T	tank (storage)
TRL	technology readiness level
WGSR	water-gas shift reaction

Chemical compounds

6Sc1CeSZ	6/1 mol% scandia/ceria-doped zirconia
C	carbon
C_2H_4	ethene
CH_4	methane
CO	carbon monoxide
CO_2	carbon dioxide
DME	dimethylether
GDC	gadolinium-doped ceria
H_2	dihydrogen
H_2O	water

O_2	dioxygen
LSCF	lanthanum strontium cobalt ferrite
N_2	nitrogen
NiO	nickel oxide
SSZ	scandia stabilized zirconia
ZnO	zinc oxide

Greek letters

α	interpolation constant ($A \cdot cm^{-2} \cdot K^{-1}$)
$\alpha_{F,CATH}$, $\alpha_{B,CATH}$	forward and backward transfer coefficients at the cathode (-)
β	interpolation constant ($A \cdot cm^{-2}$)
Υ	heat capacity ratio (-)
Υ_{CATH}	pre-exponential coefficient at the cathode (-)
ΔH_{ads}	reaction enthalpy of the adsorption reaction ($kJ \cdot mol^{-1}$)
$\Delta_R G$	Gibbs enthalpy of reaction ($kJ \cdot mol^{-1}$)
$\Delta_R G^0$	standard Gibbs enthalpy of reaction ($kJ \cdot mol^{-1}$)
$\Delta_R H$	enthalpy of reaction ($kJ \cdot mol^{-1}$)
$\Delta_R H^0$	standard enthalpy of reaction ($kJ \cdot mol^{-1}$)
$\Delta_f H_i^0$	standard formation enthalpy of compound i ($kJ \cdot mol^{-1}$)
$\Delta_R S$	entropy of reaction ($kJ \cdot mol^{-1} \cdot K^{-1}$)
ΔT_m	mean temperature difference or temperature driving force (K)
ΔT_{min}	approach temperature (K)
ϵ	porosity (-)
η_{PtSNG}	HHV or LHV efficiency of the power-to-SNG plant (%)
η_C	carbon efficiency (%)
η_{CELL}	cell efficiency (%)
η_{CATH} , η_{ANODE}	activation overpotential at the cathode or at the anode (V)
η_{INV}	AC/DC conversion efficiency (%)
η_{Ohm}	Ohmic losses in the cell (V)
η_{ISEN}	isentropic compression efficiency (%)
η_{MEC}	mechanical compression efficiency (%)
η_{SYS}	SOE system efficiency (%)
κ_i	concentration variation of compound i (-)
λ_i	thermal conductivity of compound i ($W \cdot m^{-1} \cdot K^{-1}$)
μ_i	dynamic viscosity of compound i (Pa·s)
ν_i	cinematic viscosity of compound i ($m^2 \cdot s^{-1}$)
ξ_i	stoichiometric coefficient of compound i (-)
ρ_i	density of compound i ($kg \cdot m^{-3}$)
σ_i	selectivity of compound i (%)
χ	conversion rate (%)
φ	dimensionless function for the calculation of the thermal conductivity of gas mixtures (-)

Index

$A, ANODE$	anode
AIR	air
AV	average
BIO	biomass
$COLD$	cold air for the biomass drying process
$C, CATH$	cathode
$S, CELL$	cell
CH	channel (cathode or anode)
$COMP$	compression work (SNG, synthesis gas, and blower of the biomass drying unit)
EXC	excess
g, GAS	gaseous state
GAS, IN	refers to thermal power of inlet gases injected in the SOE unit
GAS, OUT	refers to thermal power of the outlet gases injected in the SOE unit
HOT	hot air for the biomass drying process
IN	inlet

l	liquid state
$LOSSES$	thermal losses in the SOE unit
LIQ	liquefaction unit
OUT	outlet
$PtSNG$	power-to-synthetic natural gas
$REAC$	energy required for the steam electrolysis reaction
REQ	required
REM	water amount extracted from the biomass
SG	synthesis gas (syngas)
SNG	synthetic natural gas
SOL	solid
WW	wastewater

Symbols

A	annuity (€·year^{-1})
a	thermal diffusivity (m^2·s^{-1})
ASR	area specific resistance (Ω·cm^2)
b	exponent constant of H_2O concentration (-)
C	production costs for cell or stack production (€·kW^{-1})
c	exponent constant of H_2 concentration (-)
C_B	building costs for cell or stack production (€·kW^{-1})
C_{EQ}	equipment costs for cell or stack production (€·kW^{-1})
C_{MAT}	material costs for cell or stack production (€·kW^{-1})
C_{OP}	operation costs for cell or stack production (€·kW^{-1})
C_P	SNG production costs (€·MWh^{-1})
c_P	thermal capacity (J·kg^{-1}·K^{-1})
C_{PER}	personnal costs for cell or stack production (€·kW^{-1})
C_{REF}, C_{TAR}	target and reference costs of an equipment (€)
C_t	annual plant costs (€·year^{-1})
d_{CATH}	hydraulic diameter of the cathode channel (m)
d_r	discount rate (%)
E	operation voltage (V)
e_i	thickness of the element i (m)
E_N	open circuit voltage or Nernst potential (V)
E_t	annual plant energy output (MWh·year^{-1})
E_{th}	thermoneutral voltage (V)
E_a, $E_{a,CATH}$	activation energy, activation energy at the cathode (J·mol^{-1}·K^{-1})
F	Faraday constant (A·s·mol^{-1})
f	scaling factor (-)
F_t	temperature correction factor (-)
Gz	Graetz number (-)
H_i^0	higher or lower heating value of compound i (kJ·mol^{-1})
H_i	enthalpy of compound i (kJ·mol^{-1})
h	enthalpy (kJ·mol^{-1})
j	current density (A·cm^{-2})
$j_{0,CATH}$	exchange current density at the cathode (A·cm^{-2})
$j_{CATH,EY}$	current density at the interface between cathode and electrolyte (A·cm^{-2})
K	initial plant investment costs (€)
k	convective heat transfer coefficient (W·m^{-2}·K^{-1})
K_{ads}	adsorption constant (-)
K_{CH}, K_{OH}	adsorption constants of hydrocarbon and hydroxyl intermediates (-)
K_{H2}, K_{mix}	adsorption constants of the hydrogen and of the gas mixture respectively (-)
K_{eq}, K_p	equilibrium constant (-)
K_r	rate constant of a chemical reaction (-)
L	active cell length (m)
LC_P	SNG levelized production costs (€·MWh^{-1})
M	molar mass (g·mol^{-1})
m_i	mass of compound i (kg)

$\dot{m}_i$	mass flow rate of compound i (kg·s^{-1})
$\dot{n}_i$	molar flow rate of compound i (mol·s^{-1})
Nu	Nusselt number (-)
p	total pressure (Pa)
p_i	partial pressure of compound i (Pa)
P_i	thermal or electrical power corresponding to index i (kW)
p_0	standard pressure (Pa)
P_{AUX}	electrical power injected in the auxiliaries (kW)
P_{CELL}	electrical power injected in the cell (kW)
P_{EL}	electrical power injected in the SOE stacks (kW)
P_{HEAT}	electrical power injected in the heaters (kW)
Pr	Prandtl number (-)
P_{TH}	electrical power injected in the SOEC to reach thermoneutral operation (W)
Q,Q_{EXCH}	heat duty or total heat exchanged in a heat exchanger (kW)
Q_C, Q_H	cooling and heating duties extracted from pinch diagrams (kW)
Q_{CELL}	heat generation term in the cell (K·s^{-1})
Q_{DRY}	heat required for the biomass drying process (kW)
R	gas constant (J·mol^{-1}·K^{-1})
r	reaction rate (-)
Re	Reynolds number (-)
R_t	annual plant revenues (€·year^{-1})
S	active cell area (cm^2)
S_{REF}, S_{TAR}	target and reference capacity of an equipment (kW)
t	time (s)
T	temperature (K)
T_{AMB}	ambient temperature (K)
T_C, T_H	temperature at the cold side and at the hot side of heat exchangers (K)
u	gas velocity (m·s^{-1})
U_{CELL}	cell operating voltage (V)
V_{TANK}	storage capacity of the H_2 tank (m^3)
W	work (kW)
w	width (m)
X_i	humidity of compound i (%)
x_i	molar fraction of compound i (-)
y_i	yield of compound i (%)
Z	compressibility factor (-)

Introduction

In 2018, fossil fuels covered 85% of the energy consumption worldwide, oil in front [1]. The ongoing depletion of easily accessible, conventional oil resources could significantly reduce the amount of net energy available in the world economy and have serious consequences on our living standards [2]. Furthermore, there is an increasing awareness on climate change related issues in the public. Both aspects speak for a strong increase of renewable energies and their accelerated integration in the energy system. In Europe, the legislator has established the climate and energy package 2020, which aims by the end of 2020 at reducing the greenhouse gas emissions (GHG) by 20% compared to the level of 1990, increase the share of renewable energy consumption by 20% and increase energy efficiency by 20%. This has encouraged a strong and regular increase of renewable energy consumption in the EU.

However, renewable power sources are intermittent by nature and their integration in the energy system –most of all in the power grid– is challenging for the following reasons.

- The growing mismatch between power production and power consumption because of increasing photovoltaic (PV) and wind power shares in the power mix, which will probably make the power grid increasingly harder to balance in the future;
- The congestion of the power grid related to high concentration of renewable capacities in targeted areas, exceeding the transport capacities of the power network;
- The lack of available power storage capacities close to renewable power capacities, which often results in their curtailment from the power grid to ensure grid stability and the loss of the corresponding energy production;
- The limited potential in Europe for new dams and new pumped hydroelectric energy storage (PHES) capacities [3];
- The inexistence of mature, efficient solutions for the storage of electrical power as such and not as other forms of energy, e.g. chemical, potential, or kinetic energy;
- The limited possibility of balancing the power grid at European scale, amongst others for climatic reasons [4].

Moreover, the reduction of greenhouse gas (GHG) emissions still remains a delicate issue.

- Alternative solutions such as electric vehicles will require time to replace vehicles with internal combustion engines in the transportation sector;
- The substitution of fossil fuels with another energy source is sometimes impossible, for instance when used as a fuel in specific high temperature processes where the substitution with electrical power is not possible or as a feedstock in chemical processes. In these cases, only the substitution of fossil molecules with their renewable counterparts can have an impact on the carbon footprint of processes.
- Since 1990, most efforts for GHG reduction in France were obtained thanks to the reduction of manufacturing industry emissions, while the corresponding economic activity was probably relocated elsewhere (see Figure 0-1). Even though significant reductions can be observed in the energy industry, emissions e.g. in the transportation sector have known a significant increase over the same period.

A potential solution to these two issues could be so-called power-to-gas or power-to-fuels pathways, which enable the conversion of low carbon electricity (such as nuclear electricity) or renewable electricity into synthetic gaseous or liquid chemical energy carriers. This would enable to substitute fossil fuels or

chemical feedstocks with their alternative low carbon or renewable counterparts on the one hand, as well as be a way of storing and transporting renewable electricity as chemical energy in the other hand.

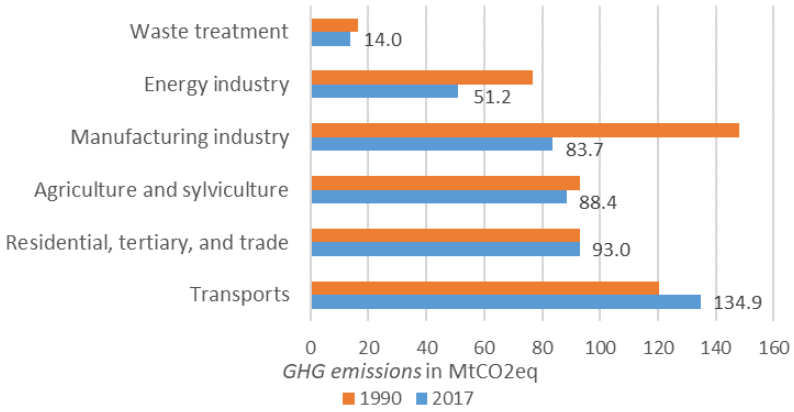


Figure 0-1: Evolution of the GHG emissions in France between 1990 and 2017 per sector [5]

Here, synthetic natural gas (SNG) seems to be a promising candidate. Indeed, in comparison to other chemical carriers, SNG presents the following advantages:

- An existing and fully developed gas infrastructure allowing the efficient transport of natural gas over long distances with a large energy storage capacity in comparison with other energy vectors (e.g. 265 TWh underground gas storage capacity in Germany [6], 152 TWh in France [7]);
- The widespread use of natural gas in many industrial sectors, potentially allowing an increased penetration of renewable energies in the economy.

The different pathways towards SNG are schematically represented in Figure 0-2, with the feedstocks on the left, the final product applications on the right, and the intermediate conversion steps in the center. SNG can be produced only with biogas (as biomethane) or bio-syngas, but a significant part of the biomass carbon content is lost and emitted as CO_2. The adjunction of H_2 produced by electrolysis enables to maximize the valorization of the biomass carbon content.

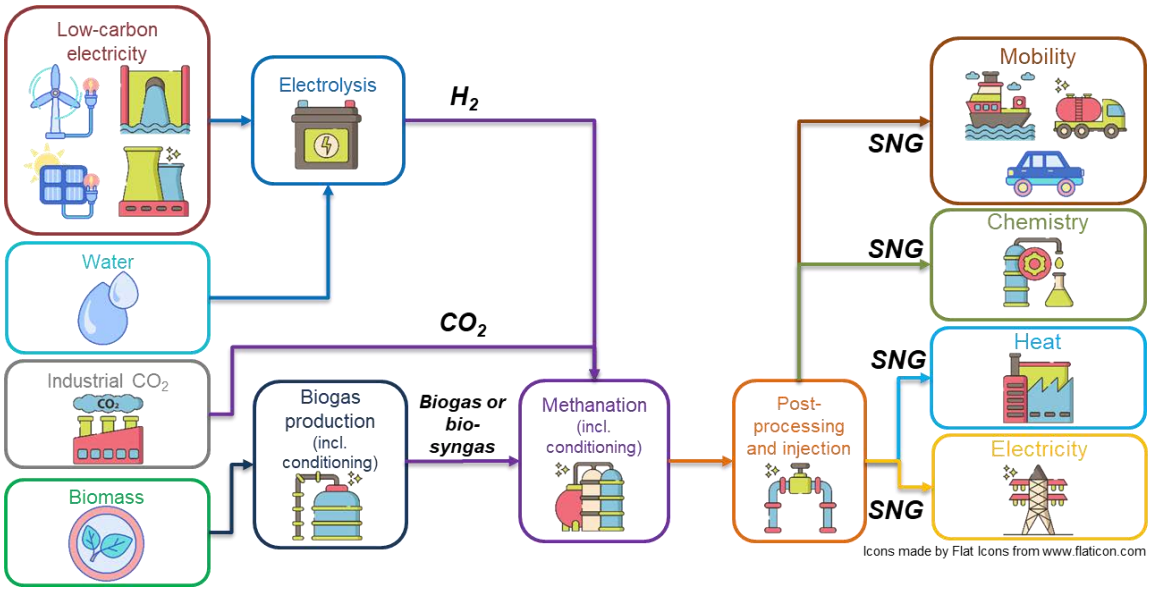


Figure 0-2: Schematic representation of power-to-SNG conversion routes

Past years have seen several semi-industrial scale power-to-SNG demonstration units being implemented in Europe. These units use low temperature (323 K to 353 K), liquid water electrolysis technologies such as alkaline and proton exchange membrane for the first conversion step from power to hydrogen, show rather low power-to-SNG efficiencies, and are expensive mostly because of the high

costs of electrolysis units. However, the solid oxide cell (SOC) technology based on ceramic materials and operating with steam at high temperatures (in the range of 973 K to 1173 K) could be a promising alternative. The cooling steam produced in the exothermic methanation process could be injected directly in the solid oxide electrolysis (SOE) unit, thus reducing the energy consumption of the electrolysis and increasing the power-to-SNG efficiency. Nonetheless, such a power-to-SNG concept was never demonstrated at industrial scale. The SOE technology remains expensive and the ultimate potential for cost reduction through mass production and large scale SOE units is not clear yet. Moreover, the SOE potential for flexible operation has been far less documented than that of other electrolysis technologies.

Hence, this dissertation will address the potential of the SOE technology in the context of power-to-SNG units, by investigating in which measure SOE units could improve the efficiency, the flexibility and the profitability of these installations. The approach applied to answer this research question will therefore be systemic, but also transversal, as it will rely on both technical and economical methods. Most results reported in this manuscript were obtained in the frame of the Baden-Württemberg project Res2CNG, which took place between 2015 and 2018. The acronym stands for “innovative production of SNG and compressed natural gas from biogenic residues and waste”. The results led to several scientific contributions often cited along this thesis [8-11], the structure of which is presented hereafter.

In a first chapter, the general concept of power-to-SNG will be introduced, followed by a literature review of the technologies involved in each conversion step from power and biomass to synthetic natural gas. Here, a strong focus will be made on the SOE technology, first on the description of its technical characteristics, second on previous technical and economic modelling work on the SOE as a stand-alone process, as well as in the particular context of power-to-SNG plants.

In a second chapter, energy assessments of selected power-to-SNG plant concepts will be implemented based on MATLAB® and Simulink® models. The plants will aim at upgrading gasification bio-syngas with electrolytic H_2 into SNG using different technological combinations and features. In this work, only the injection in the gas grid and mobility applications will be considered as final SNG applications. Each plant concept will be presented with its main modelling hypotheses, followed by the description of the methodology applied for the energy assessment. Performance indicators will be defined and applied to compare the different plant concepts.

The third chapter will investigate the operation of SOE systems under fluctuating power load in order to assess in which measure it can improve the flexibility of power-to-SNG installations. To do so, a dynamic model will be developed to investigate the thermal behavior of SOE units under fluctuating power load. In a second step, the model will be coupled with power profiles. H_2 production profiles will be generated and utilized to propose a first dimensioning of the H_2 storage unit and the catalytic methanation unit. Operation strategies and plant configurations to reduce or remove the storage unit will be discussed, along with the most suitable operation modes of SOE units depending on power load intermittency and thermal coupling configuration.

In a last chapter, a techno-economic evaluation of the plant concepts investigated in Chapter 2 will be implemented in order to determine the production cost of synthetic natural gas, with a particular focus on the investment costs of industrial SOE units. A sensitivity analysis of the SNG production costs will be made to identify the most influential cost parameters. Finally, the production cost will be compared to that of bio-methane and of conventional natural gas.

1. Fundamentals

In this chapter, the power-to-SNG concept will be first introduced and previous technical and economic works on power-to-SNG will be reviewed. Then, all processes and technologies for the conversion of power and biomass to SNG will be presented, which will include electrolysis water technologies, catalytic methanation technologies, feed gas production and gas treatment. The feed gas production part refers only to the production of bio-syngas for the methanation process and will focus on biomass drying, biomass gasification and bio-syngas purification. The reasons for the choice of bio-syngas upgrading can be seen at the end of Chapter 1.1.4.1. The gas treatment part refers to the upgrading of the SNG after the methanation process and encompasses SNG drying, SNG injection requirements, and further upgrading steps towards either compressed natural gas (CNG) or liquefied natural gas (LNG).

1.1. Power-to-SNG introduction

In this subchapter, the power-to-SNG concept will be introduced in the more general context of power-to-gas. First, the motivations, as well as the technical, economical, and environmental objectives of power-to-SNG will be discussed. In a second step, different power-to-SNG pathways and a selection of power-to-SNG demonstration projects will be presented, highlighting the interest of the SOE technology in comparison to liquid water electrolysis technologies. Finally, a review of technical and economic power-to-SNG models with integrated SOE units will be presented.

1.1.1. Presentation of power-to-SNG concept, interest, objectives and products

Power-to-SNG is with power-to-hydrogen one of the two main categories of power-to-gas conversion processes that can be applied to convert electrical power into a gaseous energy carrier.

- ***Power-to-hydrogen*** is based on an electrochemical converter called electrolyser or electrolysis unit which allows to split water molecules into hydrogen and oxygen when an electrical current is applied. The corresponding reaction can occur using water as a liquid or as a gas and requires in any case the use of a catalyst. The hydrogen produced can be compressed at different pressure levels and used for a wide range of applications such as mobility in fuel cell cars, industrial applications (steel industry, chemical industry e.g. for ammonia synthesis, refining industry for desulfurization of the oil or for fuel upgrading in reforming units, petrochemical industry or even energy industry e.g. in the alternators of nuclear power plants…), injection in the natural gas grid or even re-electrification. Possible storage solutions include injection in the natural gas grid, high pressure tanks, liquid organic carriers (LOHC) such as formic acid or metal hydride materials.
- ***Power-to-SNG*** refers to the conversion of electrical power into SNG. In the most common approach, the electrochemical synthesis of hydrogen by water electrolysis is followed by SNG synthesis in a hydrogenation unit (biological or catalytic methanation unit) where electrolytic hydrogen and oxidized carbon gas react together to form water rich SNG. A less common, more prospective approach is to directly react carbon dioxide and steam at high temperature in a high temperature electrolysis unit to synthesize syngas (a gaseous mixture mostly composed of hydrogen and carbon monoxide), the latter being then sent to the hydrogenation unit for SNG synthesis [12, 13]. In both cases, the idea is to synthesize a product that has a molecular composition and physico-chemical properties close enough to natural gas, so that it can be

injected in unlimited amounts in the natural gas grid and used as a substitute in all its current applications as a fuel (for industrial and domestic heating, for mobility in gas engines) or as a feedstock in the chemical and petrochemical industries.

The power-to-SNG and power-to-hydrogen conversion pathways are schematically represented in Figure 1-1 with their feedstocks on the left and end-product applications on the right.

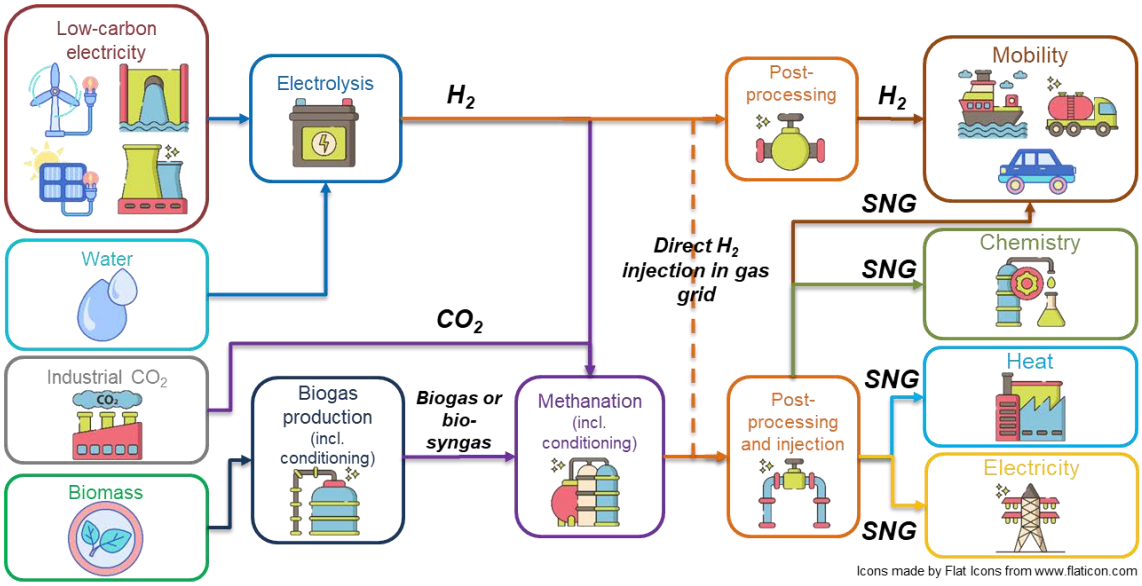


Figure 1-1: Schematic representation of the different power-to-gas pathways

As both conversion pathways allow for similar applications, it is relevant to compare the physico-chemical properties of hydrogen and methane. Several key properties of these two energy carriers are gathered in Table 1-1.

Table 1-1: Selected properties of hydrogen and methane at 0 °C and 1 atm (NTP after the norm DIN 1343)

	Density ($kg \cdot Nm^{-3}$)	**Higher heating value ($MJ \cdot Nm^{-3}$)**	**Lower heating value ($MJ \cdot Nm^{-3}$)**	**Flammability limits (%-vol in air)**	**Detonability limits (%-vol in air)**	**Minimum ignition energy (mJ)**
CH_4	0.7175	36.2	32.6	5.3-15	6.3-13.5	0.29
H_2	0.0899	11.9	10.1	4-75	11-18 to 59	0.02

Methane has a smaller range of inflammability and detonation limits than hydrogen. It is therefore safer to store. Nonetheless, the low density of hydrogen makes it much more difficult to accumulate than methane and consequently to land into these inflammability and detonation ranges, except in closed areas. Methane has an energy density 3.3 times higher than hydrogen, which means much more work is required for hydrogen to reach volumetric energy densities similar to methane. Even though this seems to favor methane over hydrogen, power-to-methane (and power-to-SNG) conversion efficiencies are lower than power-to-hydrogen efficiencies because of the additional hydrogenation step and the significantly higher efficiency of fuel cells compared to gas combustion engines.

The massive use of power-to-SNG to decarbonize the economy is less straightforward than power-to-hydrogen, for the following reasons.

- It is rather surprising to use a molecule containing carbon to decarbonize the economy;

- It raises the issue of ensuring the sustainability of the carbon source for SNG synthesis in addition to having a low carbon footprint of the power mix used for hydrogen production.

One key advantage of synthetic natural gas over hydrogen though is the existing and already developed gas infrastructure, allowing for the injection of synthetic natural gas in most locations and its transport on long distances. It also has been used for domestic and industrial heating for decades. On the contrary, hydrogen has been used in specific industrial areas equipped with local hydrogen networks for decades as well, but it is still not well known in the public. Furthermore, even though hydrogen could theoretically substitute methane for all its applications as a fuel, it will never be able to replace methane when used as a feedstock, e.g. in the chemical or the petrochemical industry.

The SNG produced after power-to-SNG conversion is a gaseous mixture with physicochemical properties and a composition similar to conventional natural gas. As a reminder, natural gas is mostly composed of methane (from 81 to 97%) and possibly of ethane, propane, butane, nitrogen and carbon dioxide. Nonetheless, it might contain other gases depending on the upstream processes and the biomass feedstock applied for its synthesis. It can be injected in the gas grid if the specifications for injection are fulfilled (more details can be found in Chapter 1.4.2.2). The SNG can be further processed in the following products.

- ***Liquefied natural gas (LNG)***: it is the product of the liquefaction of SNG or natural gas. It is produced and stored at 111 K (-162 °C) and at atmospheric pressure. Even though gas liquefaction comes at a high energy cost, it increases the energy density of the natural gas and enables an easier transportation. LNG market has experienced a considerable growth in the past decade. The number of LNG terminals has significantly increased as a result of the internationalization of the gas market. Nonetheless, the amount of LNG refueling stations is relatively small in Europe at present and is comparable to the amount of H_2 refueling stations;
- ***Compressed natural gas (CNG)***: it is the product of SNG or natural gas compression. It is stored at ambient temperature and at a pressure of 250 bar in a wide network of fuel stations. It is mainly used for light or heavy mobility applications, e.g. in passenger vehicles, trucks or boats.

1.1.2. Economic, societal and environmental aspects of power-to-SNG

Previous work results on the evaluation of SNG production costs from power-to-SNG pathways will be presented in this paragraph, along with the possible societal and environmental benefits of power-to-SNG installations. However, considerations on GHG reduction potential with power-to-SNG routes compared to fossil alternatives will not be discussed, as it is not at the chore of our work.

The production costs of SNG obtained from power-to-SNG conversion routes have been widely documented in the literature, amongst others in [14-21]. Reported costs fluctuate widely and range between 70 €·MWh^{-1} and 500 €·MWh^{-1} (based on the HHV of SNG), mostly because of the very different hypotheses made for economic evaluations, especially in terms of unit capacities, commodities prices (mostly electrical power), number of full load hours, technological choices (electrolysis technology), and by-product valorization (heat or pure oxygen). The electrolysis unit covers the largest share of investment costs (or so-called CAPEX, e.g. up to 80% in [22] and up to more than 60% in [16]). This equipment also represent the largest share of operation costs (more than 70% at present and expected to raise up to 90% by 2050 in [16]) mostly because of electrical power costs.

Furthermore, SNG production cost values mentioned above are in the best case almost two times higher than the conventional natural gas price for all sectors in France (average value 40.6 €·MWh^{-1} between 2011 and 2017, HHV based value without VAT) [23]. In other words, power-to-SNG installations cannot

produce SNG at a price competitive with conventional natural gas in the current economic conditions. Given the efficiency of power-to-SNG demonstration plants at present (roughly at 50% [24]), a natural gas price at least two times higher than the power price would be required for balancing the operational expenditures (OPEX) of power-to-SNG plants in first approximation. Actually, the opposite assertion is true: power prices for industrial consumers with volumes in the range of 70-150 GWh·year^{-1} were about 55 €·MWh^{-1} in France in 2017 (VAT excluded) [25].
Despite this unfavorable economic context, power-to-SNG installations could be beneficial for the society for the following reasons.

- The substitution of natural gas with its synthetic renewable or “low carbon” counterpart could reduce the carbon footprint of the industry. This could allow industrial activities to remain in the EU, thus maintaining employments and technical expertise.
- These installations allow a much higher valorization of the feedstock carbon content, in opposition to other processes for SNG or biomethane synthesis, such as biogas or landfill units, where methane only represents approx. half of the biogas content, the rest being CO_2 [26]. This increases the potential for substitution of fossil resources, provided that the electrical power used for conversion has a low carbon footprint.

The potential market for power-to-SNG was estimated in previous work, e.g. in [16, 27]. Based on the available raw CO_2 streams available, an accessible total of 104 Mt CO_2 was estimated in France for the heavy industry, the energy industry, biogas units, and gasification units [16]. This would correspond to a cumulated installed electrolysis power of 116 GW, and to a total methane output of 67.3 GW (HHV based value), assuming a power-to-methane conversion efficiency of 58%. The largest share of these power-to-SNG units would use fossil CO_2 from the industry. In that case, the SNG could also mitigate GHG emissions, depending on the carbon footprint of the electricity used for SNG production, on the power-to-SNG conversion efficiency, and on the storage duration of the SNG before use [28]. Considering only biogenic CO_2 streams would reduce the potential down to an electrolysis capacity of 5.2 GW and a total methane output of 3 GW (HHV based value). In Germany, the Fraunhofer ISE estimated that the cumulated capacity of electrolysis units for SNG production could reach approx. 50 GW by 2050, for a total installed electrolysis capacity including power-to-H_2 and power-to-liquids applications in the range of 137-275 GW [27].

As a preliminary conclusion, the competitiveness of power-to-SNG units is highly dependent on commodities costs (electrical power, natural gas and CO_2), as well as on the OPEX and the CAPEX of electrolysis units. It is therefore important to develop economic tools to evaluate the cost reduction potential of electrolysis units. The solid oxide electrolysis (SOE) technology is particularly interesting in comparison to alkaline and PEM technologies, especially in the context of power-to-SNG, because electrical power costs savings in the range of 40 to 60% could be achieved [29].

1.1.3. Power-to-SNG pathways

Different power-to-SNG pathways are represented in Figure 1-2. The feedstocks are represented on the left and the final products (SNG, LNG or CNG) and their applications on the right.

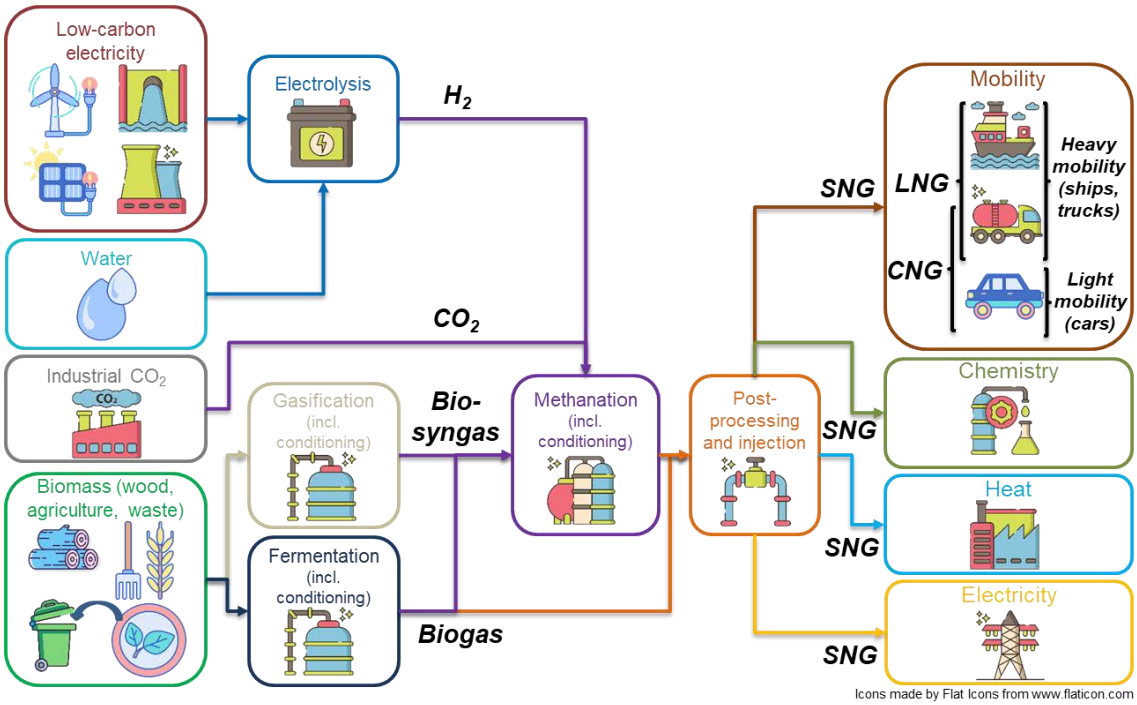


Figure 1-2: Overview of power-to-SNG pathways with their conversion efficiencies (LHV values)

The carbon required for the methanation process can be recovered from the following sources.

- Concentrated CO_2 emitted in industrial plants [22], such as cement plants, steel plants, lime plants, or thermal power plants. This last option requires electrolysis units with electrical power input higher than the electrical output of thermal power plants, which is not interesting from an energy standpoint;
- The capture of non-concentrated CO_2 in air is also possible. Numerous technologies exist, but they still have high energy requirements [30];
- Bio-syngas (a mixture mostly composed of H_2, CO, CO_2, and CH_4 similar to syngas) obtained by gasification of solid biomass or waste [22]. In that case, the adjunction of electrolytic hydrogen to bio-syngas is optional, since the ratio between hydrogen and carbon can be adjusted using a reverse water gas shift unit. However, a significant part of the biomass carbon content is emitted as CO_2 and not valorized;
- Biogas (a mixture of CH_4 and CO_2) [22], obtained by fermentation of organic waste or agricultural biomass, where fermentation occurs at low temperature (318-328 K) and at atmospheric pressure [26].

As for the electrolytic hydrogen, it is produced in low temperature electrolysis units using either alkaline or proton exchange membrane (PEM) technologies.

Past years have seen the commissioning of several power-to-SNG demonstration plants. Several key projects are presented afterwards with their main technical features.

The power-to-SNG plant of the project BioCat implemented in Avedore, Denmark [31, 32]. As a first step, H_2 is produced at 13 bar in a 1 MW alkaline electrolysis unit, while the biogas is conditioned by removing the hydrogen sulfide and compressed up to 10 bar. In a second step, H_2 and biogas are injected into a methanation unit operated at 333-338 K and at 5-10 bar, where the CO_2 contained in the biogas

and H_2 are converted by a biocatalyst (bacterias of the type “Archaea”) to SNG. After post-treatment, up to 58 $Nm^3 \cdot h^{-1}$ SNG (approx. 550 kW based on the HHV of CH_4) are injected in the distribution gas grid.
The power-to-SNG plant of the EU project STORE&GO implemented in Falkenhagen, Germany [33, 34]. H_2 is produced in an alkaline electrolysis unit of 1.8 MW composed of 6 modules of 300 kW each (360 $Nm^3 \cdot h^{-1}$ H_2 each, 2160 $Nm^3 \cdot h^{-1}$ in total). The CO_2 used as carbon feedstock is produced and liquefied in a bioethanol plant, transported to the site per truck, vaporized again and injected together with the H_2 in a single-stage catalytic methanation unit (please refer to Chapter 1.3.3.2 for more details on the methanation process). A SNG flow rate of 57 $Nm^3 \cdot h^{-1}$ (630 kW based on the HHV of CH_4) is injected in the transportation gas grid in order to reduce power grid congestion. No particular SNG applications are targeted. The entire H_2 production can also be used for direct injection in the transportation gas grid.

The power-to-SNG plant of the JUPITER 1000 project implemented in Fos-sur-Mer, France [35]. The required H_2 is produced in an alkaline unit and in a PEM unit with a capacity of 0.5 MW each, while the CO_2 is provided through a pipeline of a steel manufacturer located on the same industrial area. The two gases are then sent to a catalytic methanation unit based on the micro-channel technology with a SNG output capacity of 25 $Nm^3 \cdot h^{-1}$ (280 kW based on the HHV of CH_4). The product gas is planned to be injected in the transport gas grid with industrial clients as final users. The direct injection of H_2 in the transport gas grid is also targeted in the project.

The power-to-SNG plant of the AUDI e-gas project implemented in Werlte, Germany [24, 36]. Here, the hydrogen is produced in a 6 MW alkaline electrolysis unit qualified for the secondary reserve and composed of three modules of 2 MW each (total capacity 1200 $Nm^3 \cdot h^{-1}$). The H_2 is reacted with CO_2 captured from a biogas plant in a single-stage catalytic methanation unit (see Chapter 1.3.3.3 for more details on the methanation process). As a result, a maximal flow rate of 325 $Nm^3 \cdot h^{-1}$ SNG (3.5 MW based on the HHV of CH_4) can be injected in the distribution gas grid, where the AUDI e-gas concept specifically targets mobility applications. In addition, 30 $Nm^3 \cdot h^{-1}$ H_2 are dedicated to the investigation of direct injection. The plant reaches a power-to-SNG efficiency of 54% HHV. A schematic process flow diagram is provided in Figure 1-3.

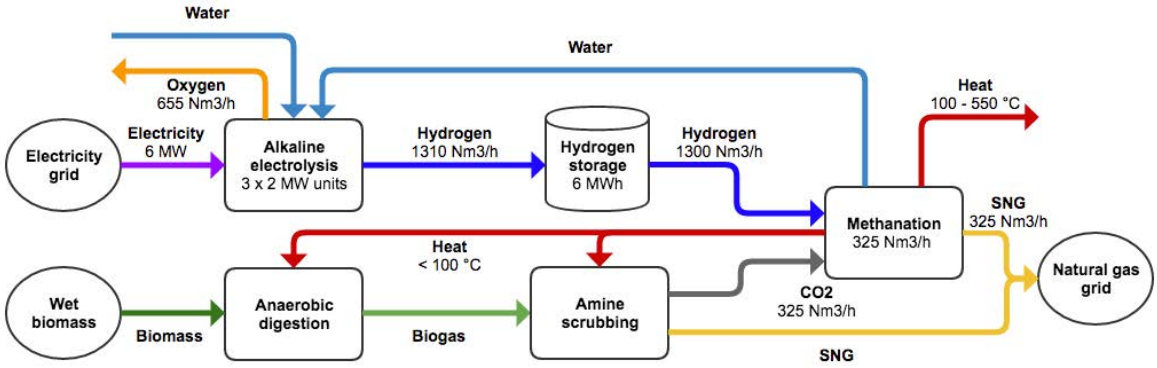


Figure 1-3: Process flow diagram of the power-to-SNG plant of the AUDI e-gas project in Werlte, Germany [37]

Based on this project list, it can be concluded that power-to-SNG plants have reached the size of semi-industrial units in past years, using mostly alkaline electrolysis and catalytic methanation technologies for the upgrading of biogas to SNG. These plants show rather low power-to-SNG efficiencies (in the range of 51-56% based on the HHV of SNG) in comparison for instance with power-to-H_2 (64-70% based on HHV of H_2) or power-to-power installations with pumped storage station (69-72%) [21, 38]. Power-to-

SNG efficiencies should not increase significantly when using other low temperature electrolysis technologies such as proton exchange membrane.
However, the solid oxide electrolysis (SOE) technology could help significantly improving the power-to-SNG efficiency of plants up to more than 70% (based on the HHV of SNG), because of an improved thermal integration between electrolysis and catalytic methanation units (please refer to Chapter 1.2.1 for more details). Even though the thermal coupling was not demonstrated at industrial scale so far, at least two prototypes were reported. A small scale biogas upgrading plant with a 40 kW SOE unit was implemented by the company Haldor Topsoe [37, 39], whereas another one was implemented in the frame of the EU project HELMETH [40, 41]. Furthermore, the steam recovery for a SOE unit was already implemented at significant scale in the frame of the EU project GrinHy [42], and the company Sunfire has already announced the construction of a 20 MW SOE unit for synthetic liquid fuels production in Norway [43], where heat from the fuel synthesis unit will probably be recovered for the SOE unit.
In the last case though, the SOE unit will not operate in steam electrolysis mode but in in co-electroylsis mode in order to produce syngas, a mixture of mostly hydrogen and carbon monoxide, starting from carbon dioxide and steam. In this work, it was decided not to investigate the co-electrolysis operation of SOE units for the following reasons. First, SOECs show high sensitivity to pollutants such as sulfur, which significantly decrease cell performance by deactivating the Ni catalyst at the cathode [44]. Therefore high purity levels of gases (especially CO_2) are required for SOECs, which are difficult to reach even after post treatment of biogas or bio-syngas streams. It seems therefore more straightforward to deal with the issue of pollutants in the catalytic methanation unit using well known solutions such as catalyst guard beds. Second, according to a Res2CNG project partner, the direct synthesis of syngas in SOECs increases the chances of soot formation in the catalytic methanation reactors. As a result, the partners decided to focus on steam electrolysis and to exclude co-electrolysis from the investigations.

Hence, as it seems to be the most promising technological option in terms of power-to-SNG efficiency, the plant concepts investigated in this work will consider several options coupling SOE units operated in steam electrolysis mode and catalytic methanation units. These options will furthermore be compared with a reference plant integrating a low temperature electrolysis technology. The plant size will be determined according to the carbon source chosen for SNG synthesis.

1.1.4. Power-to-SNG models with integrated SOE units

Technical and economic power-to-SNG models previously reported will be reviewed hereafter, but will only focus on those with integrated SOE units. Previous energy assessments and economic evaluations will be discussed and calculated power-to-SNG efficiencies and SNG costs will be commented.

1.1.4.1. Technical models

Past years have seen various research works on modelling the thermal coupling of SOE units with catalytic methanation units [45-57], where electrolytic H_2 or syngas were used as feedstock for catalytic hydrocarbon synthesis.
Biogas upgrading with a SOE unit (operated either in electrolysis or in co-electrolysis mode) and a catalytic methanation unit was investigated in the frame of the planSOEC project [45]. A full thermal integration of the plant was made and used as basis for an exergy and an economic analysis. The biogas was obtained by fermentation and injected without separation of the methane and the carbon dioxide in a catalytic methanation unit for an overall plant efficiency of 76.2 % (based on the LHV of SNG). Corresponding plant concepts were patented by the company Haldor Topsoe [58] which also implemented a small biogas upgrading prototype with an integrated 40 kW SOE unit [39].

De Saint Jean et al. investigated the theoretical coupling of a SOE unit and a catalytic methanation unit [46, 48], where the carbon source was pressurized CO_2 at 100 bar from a carbon capture storage unit. A full thermal integration and a pinch analysis of the power-to-SNG plant were implemented. The SOE system was operated under pressure and power-to-SNG plant efficiencies of 74.5% and 77% were calculated in [46] and in [48] respectively (based on the HHV of products).
Giglio et al. investigated the theoretical coupling of a SOE unit operated in either steam electrolysis or in co-electrolysis mode with the TREMP™ catalytic methanation process developed by Haldor Topsoe [49]. A full thermal integration of the plant was proposed and checked with a pinch-analysis. Power-to-SNG plant efficiencies of 81.4% and 76% were obtained in co-electrolysis and steam electrolysis mode respectively (LHV based value). Wang et al. investigated the optimal design of power-to-SNG plants with integrated SOE units operated either in steam or in co-electrolysis mode [51]. The influence of operating parameters, such as current density, operation mode of the SOE unit, steam utilization, and operating pressures of main plant processes, were investigated and resulted in plant efficiencies in the range of 73-85% on a HHV basis. Giglio et al. investigated the integrated design of a 10 MW SOE unit with a catalytic methanation unit in [50] in the frame of the HELMETH project [41], and reported power-to-SNG plant efficiencies of 77 % LHV (86 % HHV). A proof of concept was also implemented in the frame of the project with a power-to-SNG plant efficiency of 76% HHV [55]. The authors claim that values higher than 80% HHV could be reached assuming a steam utilization (or steam conversion rate) of 90%, reduced heat losses, and with the development of accurate steam flow control at the inlet of the SOE unit.
A power-to-SNG plant model with integrated steam electrolysis, gasification, and catalytic methanation units was implemented in [54]. Different wet biomass feedstocks were dried in a steam dryer and gasified in a two steps gasification process. The obtained syngas was then upgraded to SNG in a catalytic methanation unit and a power-to-SNG plant efficiency in the range of 69-70% LHV was reached. This work was extended in [56] in the frame of a techno-economic assessment of a multi-energy system with a reversible SOC unit, where the system showed a similar efficiency than in [54] when operated in power-to-SNG mode. Other research works reported power-to-SNG efficiencies of similar plant concepts as well, however they focused mostly on plant economics [59] or on environmental aspects [60] (such as CO_2 mitigation potential and availability of the biomass resource for different end products like DME, methanol and SNG) and did not provide any details on the thermal integration of plants [59].

Because limited work was reported on bio-syngas upgrading and much more on biogas upgrading, it was decided to focus on the first option in this work. Therefore, the perimeter of the technology review for feed gas production in Chapter 1.4 will be limited to bio-syngas production processes. This option seems also more interesting from a thermal integration standpoint, because the thermochemical process used for bio-syngas production operates at high temperatures (from 873 to 1273 K), whereas biogas production processes operate at low temperatures (from 318 to 328 K).
Furthermore, following missing or incomplete elements in the literature were identified for bio-syngas upgrading plants. They will be addressed in Chapter 2.

- Several plant features were not included, e.g. the last upgrading steps from SNG to CNG or LNG, other feedstocks than wood or several layouts of catalytic methanation unit;
- Similar bio-syngas upgrading plant concepts focused only on SOE and did not compare the energy performance of plants with integrated SOE and with low temperature electrolysis (LTE) units. In this context, the pinch technology was never applied.
- The energy performance of the full thermal integrated plants was never compared to the theoretical maximum the plant could possibly achieve, thus making it difficult to evaluate the performance of the implemented thermal integration;

- The detailed technical evaluation of several options for residual heat valorization was not considered, e.g. power production or coupling with a district heating network;
- The environmental impact of power-to-SNG plants e.g. in terms of water requirements, cooling water requirements and carbon valorization was not documented.

1.1.4.2. Economic models

Until several years ago, cost evaluations mostly considered SNG produced in power-to-SNG plants with low temperature electrolysis units, e.g. [18, 20, 21]. Nonetheless, with the development of the SOE technology observed in past years, the number of SNG cost evaluations based on power-to-SNG plants with integrated SOE units has significantly increased [14-17, 19, 61]. The hypotheses and SNG production cost values previously reported in the literature are summarized in Table 1-2.

Table 1-2: SNG production costs and main hypotheses of previous economic evaluations

Source and year	Plant capacity, SOE capacity	CO_2 source	Main plant hypotheses	SNG costs (HHV basis)
De Saint Jean, 2014 [14, 15]	67 $Nm^3 \cdot h^{-1}$ (SNG), 879 kW	CO_2 from carbon capture unit	4500 $h \cdot year^{-1}$, actualization rate 10% (reference case), plant lifetime 30 years.	304-597 €·MWh^{-1}
ADEME, GRTgaz and GrDF, 2014 [16]	780 $Nm^3 \cdot h^{-1}$ (7.8 MW based on the HHV of CH_4 produced by methanation), 10 MW	Biogas	By-product valorization (heat or O_2)	139-150 €·MWh^{-1} (by 2030) 102-113 €·MWh^{-1} (by 2050) (both on a HHV basis)
Giglio et al, 2015 [17]	940 $Nm^3 \cdot h^{-1}$ (8 MW LHV SNG), 10 MW	Captured CO_2, origin not specified	8000 $h \cdot year^{-1}$, power prices 0-58 €·MWh^{-1}, plant lifetime 30 years	[1] 7-80 €·MWh^{-1}
Wang et al. 2019 [19]	42 $Nm^3 \cdot h^{-1}$ (426 kW HHV CH_4), 510 kW in the reference case (up to 100 MW)	Captured CO_2, origin not specified	8000 $h \cdot year^{-1}$, power price 82 €·MWh^{-1} (EU average), interest rate 8%, plant lifetime 20 years, CO_2 price 40 €·ton^{-1}.	37-46 €·MWh^{-1} (levelized cost value)

The high SNG production cost values reported in De Saint Jean et al. can be related to the rather low system availability (4500 $h \cdot year^{-1}$) and the high CAPEX of the SOE unit, because of its relatively small capacity. A sensitivity analysis was performed and showed that the main parameters influencing the production cost are mostly the electrolysis CAPEX and the electricity price.

In their work, ADEME, GRTgaz and GRDF compared SNG production costs of power-to-SNG plants combining different electrolysis technologies (alkaline, PEM, SOE), methanation technologies (biological or catalytic), different CO_2 sources, and different product applications (transport or distribution) [16]. In

[1] Values originally in $ 2011 converted in € 2011 assuming an average exchange rate EUR/USD of 1.39 in 2011.

the case of the SOE technology, SNG cost estimates were only provided starting from 2030, because of the lower technology readiness level (TRL) of the SOE compared to PEM and alkaline technologies.
Giglio et al. implemented a comparative analysis of SNG production costs with SOE units operated in steam electrolysis and in co-electrolysis mode [17]. SNG production costs showed high sensibility to CO_2 feedstock costs, SOE stacks costs and to the SOE degradation rate.
As for Wang et al., their techno-economic analysis compared several plant concepts for the synthesis of various fuels, where SOE units were operated either in co-electrolysis or in steam electrolysis mode [19].

As a conclusion, the main hypotheses and results of previous SNG cost evaluations were presented. They will enable the choice of relevant working hypotheses in the economic evaluation of Chapter 4 and the comparison of this work results with previous literature values. Furthermore, cost evaluations of SNG produced by bio-syngas upgrading plants with integrated SOE units were scarcely reported so far. Therefore, this power-to-SNG plant concept should be considered in priority in this work.

1.2. Water electrolysis

1.2.1. Thermodynamics

The water electrolysis process is based on Equations (1.1) and (1.2), where the liquid or gaseous water molecule is dissociated in hydrogen and oxygen, and where $\Delta_R H^0$ refers to the standard enthalpy of reaction (in kJ·mol^{-1}).

$$H_2O(l) \rightarrow H_2(g) + \frac{1}{2}O_2(g) \qquad \Delta_R H^0 = 286\ kJ \cdot mol^{-1} \tag{1.1}$$

$$H_2O(g) \rightarrow H_2(g) + \frac{1}{2}O_2(g) \qquad \Delta_R H^0 = 242\ kJ \cdot mol^{-1} \tag{1.2}$$

The first principle of thermodynamics as written in Equation (1.3) allows to calculate the enthalpy of reaction $\Delta_R H$ as the sum of the free enthalpy of reaction or Gibbs free energy $\Delta_R G$ (in kJ·mol^{-1}) and the reaction heat, the latter being the product of the temperature *T* (in K) and the reaction entropy $\Delta_R S$ (in kJ·mol^{-1}·K^{-1}).

$$\Delta_R H = \Delta_R G + T \cdot \Delta_R S \tag{1.3}$$

The standard reaction enthalpies of Equation (1.1) and (1.2) can be determined with the formation enthalpies and entropies of each component using Equation (1.4), whereas Equation (1.5) allows for the determination of the reaction enthalpy at a given temperature and pressure. Since *S* and *G* also are state functions, they also can be calculated using Equation (1.5) by replacing all occurrences of *H*.

$$\Delta_R H^0 = \Delta_f H^0_{H2O} - \Delta_f H^0_{H2} - \frac{1}{2}\Delta_f H^0_{O2} \tag{1.4}$$

$$\Delta_R H_{T,P} = \left(H_{H2O,T,P} - H_{H2,T,P} - \frac{1}{2}H_{O2,T,P}\right) - \Delta_R H^0 \tag{1.5}$$

Finally, Equation (1.5) allows elaborating the thermodynamic diagram of the electrolysis reaction represented in Figure 1-4. The diagram can be divided in two parts delimited by the discontinuities related to the vaporization threshold of water: the left part corresponds to the theoretical domain for liquid water electrolysis and the right part to the theoretical domain for steam electrolysis. The following comments can be made on the graph.

- A pressure increase results in a higher vaporization temperature of water, which shifts the discontinuities of each curve towards the right;
- Increasing the temperature results in lowering the Gibbs energy, which allows to provide a higher share of the energy required for the electrolysis reaction as heat (e.g. from 237 kJ·mol^{-1} at 298 K down to 189 kJ·mol^{-1} at 1073 K, when the heat requirements of the reaction increase from 49 kJ·mol^{-1} up to 60 kJ·mol^{-1} at the same time). This is particularly interesting when a high temperature heat source is available (e.g. heat from a nuclear power plant).
- The reaction enthalpy is considerably lower in the steam electrolysis domain than in the liquid water electrolysis domain, because the vaporization enthalpy (44 kJ·mol^{-1} at 298 K) is no longer required. Still, water has to be vaporized prior to the electrolysis reaction, which makes the coupling with a steam source (such as a catalytic methanation unit or a Fischer Tropsch unit) particularly interesting to reduce the energy requirements of the electrolysis process.

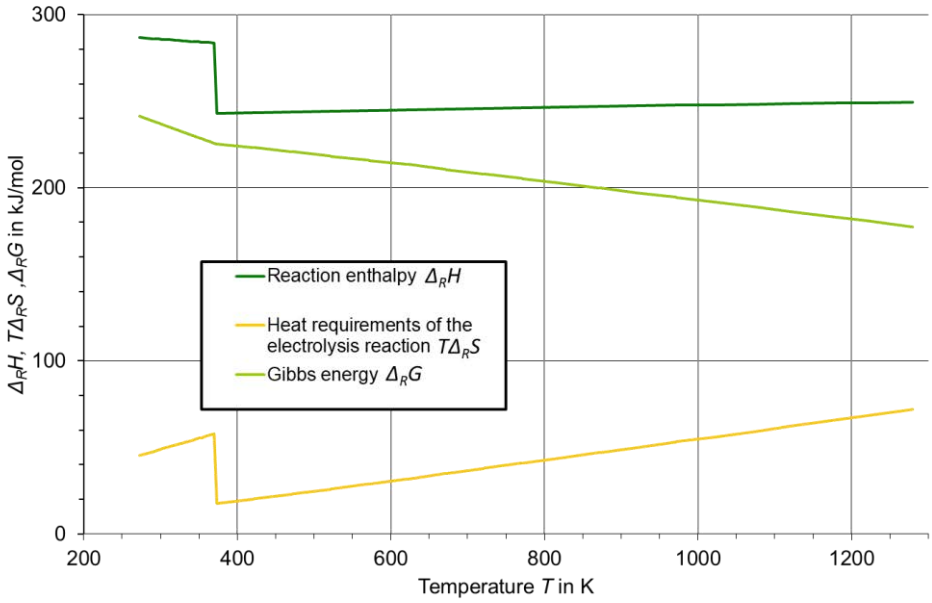


Figure 1-4: Thermodynamic diagram of the water electrolysis reaction at atmospheric pressure

1.2.2. Operation of electrolysis cells

In this subchapter, the main parameters and key notions for understanding the operation of electrolysis cells will be presented.

1.2.2.1. Reversible tension

The reversible tension can be written in electrolysis mode with Equation (1.6), where F is the Faraday constant (in A·s·mol^{-1}), R the gas constant (in J·mol^{-1}·K^{-1}), p_i the partial pressure of component i in Pa, $\Delta_R G^0$ the standard Gibbs free energy, and p_0 the standard pressure in Pa. It corresponds to the minimal required electrical energy input for the electrolysis reaction and is often referred as Nernst voltage or open-circuit voltage (OCV).

$$E_N = \frac{\Delta_R G^0}{2 \cdot F} + \frac{R \cdot T}{2 \cdot F} ln\left(\frac{p_{H2} \cdot p_{O2}^{0.5}}{p_{H2O} \cdot p_0^{0.5}}\right) \quad (1.6)$$

At 1073 K and 1 bar, the reversible voltage is only equal to 0.978 V, whereas it is about 1.230 V at 298 K and 1 bar.

1.2.2.2. Cell tension and composition

The cell tension U_{CELL} is the tension at which the cell is operated. It corresponds to the sum of the reversible tension, the Ohmic losses η_{Ohm}, the sum of the activation overvoltages at the cathode and the anode η_{ANODE}, and the sum of the concentration overvoltages at the anode and the cathode η_{CATH}, as shown in Equation (1.7).

$$U_{CELL} = E_N + \eta_{Ohm} + \eta_{ANODE} + \eta_{CATH} \tag{1.7}$$

The different contributions of the cell voltage are represented in Figure 1-6 (see Chapter 1.2.2.5). The concentration overvoltages result from the limitation of the gaseous mass transport in the cell [62], whereas the activation overvoltages result from the kinetic of the chemical reactions occurring in the cell. The latter ones can be depicted with different variations of the Butler-Volmer equation [62-64].The most general form of the equation is provided in Equation (1.8) at the cell cathode [65], with $j_{CATH,EY}$ the current density at the interface between cathode and electrolyte, $j_{0,CATH}$ the exchange current density at the cathode, and $\alpha_{F,CATH}$ and $\alpha_{B,CATH}$ the forward and backward transfer coefficients at the cathode.

$$j_{CATH,EY} = j_{0,CATH} \cdot \left[exp\left(\frac{\alpha_{F,CATH} \cdot F \cdot \eta_{CATH}}{R \cdot T}\right) - exp\left(\frac{\alpha_{B,CATH} \cdot F \cdot \eta_{CATH}}{R \cdot T}\right)\right] \tag{1.8}$$

The exchange current density $j_{0,CATH}$ at the interface between cathode and electrolyte can be determined with Equation (1.9), where $E_{a,CATH}$ corresponds to the activation energy at the cathode, γ_{CATH} to the pre-exponential coefficient, x_i to the molar fraction of species and b and c to constants expressing the concentration dependency. Similar Equations than (1.8) and (1.9) can be written at the anode.

$$j_{0,CATH} = \gamma_{CATH} \cdot x_{H2}^{c} \cdot x_{H2O}^{b} \cdot exp\left(-\frac{E_{a,CATH}}{R \cdot T}\right) \tag{1.9}$$

1.2.2.3. Faraday law of electrolysis

The Faraday law of electrolysis is presented in Equation (1.10). It enables to evaluate the amount of hydrogen produced in a cell $\dot{n}_{H2}$ (in mol·s^{-1}) based on the current density j injected in the cell (in A·m^{-2}) and on the active area of the cell S (in m^2). A good correlation between experimental hydrogen flow rates and theoretical flow rates calculated with this law can be observed.

$$\dot{n}_{H2} = j \cdot \frac{S}{2 \cdot F} \tag{1.10}$$

1.2.2.4. Area specific resistance

The area specific resistance (ASR) of a cell (in Ω.cm^2) characterizes the overvoltages as well as the Ohmic losses of a cell. It can be determined on a so-called I-V curve or polarization curve (e.g. Figure 1-5), where it corresponds to the slope of the curve.

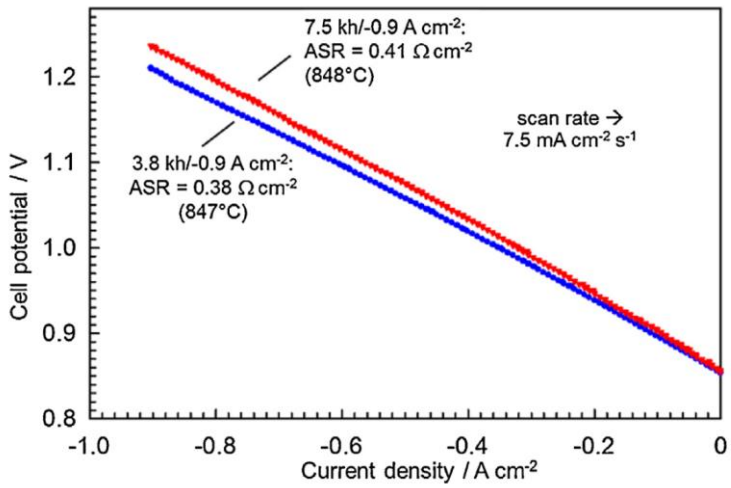


Figure 1-5: Polarization curve or I-V curve of an electrolysis cell [66], with permission of Elsevier.

In the literature, the relation between ASR, reversible voltage and operation voltage is often depicted with the linear approximation provided in Equation (1.11) [67-69]. Nonetheless, this approximation is only valid in the linear domain of the I-V curve. For instance, in case of high current density, the mass transport of the reacting species becomes limited and the activation overvoltages cannot be neglected anymore [68], so that the aspect of the I-V curve is not linear anymore but rather exponential, as schematically represented in Figure 1-6 (see Chapter 1.2.2.5).

$$U_{CELL} = E_N + j \cdot ASR \tag{1.11}$$

Furthermore, the ASR depends on the operating parameters and is usually expressed as a function of the temperature [12, 67] and sometimes of the pressure [49] or the current density [45].

1.2.2.5. Cell operating modes

The thermoneutral voltage E_{th} corresponds to the voltage at which the thermal requirements of the electrolysis reaction are equal to the thermal losses in the cell, the latter being equal to the sum of the Ohmic losses and the overvoltages. The thermoneutral voltage can be defined as the ratio of the reaction enthalpy and the Faraday constant as written in Equation (1.12).

$$E_{th} = \frac{\Delta_R H}{2 \cdot F} \tag{1.12}$$

At 1073 K and 1 bar, the thermoneutral voltage is only equal to 1.286 V, whereas it is about 1.481 V at 298 K and 1 bar.

The different operating modes of an electrolysis cell are represented in Figure 1-6. In case of thermoneutral operation, the inlet and outlet temperatures of the gases flowing on a cell are equal. When the thermal losses in the cell are lower than the heat requirements of the electrolysis reaction, the cell is operated in endothermic mode. In that case, the missing thermal energy of the electrolysis reaction is taken from the feed gases. Therefore, the outlet gas temperature is lower than the inlet gas temperature. When the thermal losses in the cell are higher than the thermal requirements of the electrolysis reaction, the cell is operated in exothermic mode and the excess heat is evacuated by the gases, so that the outlet gas temperature is higher than the inlet gas temperature.

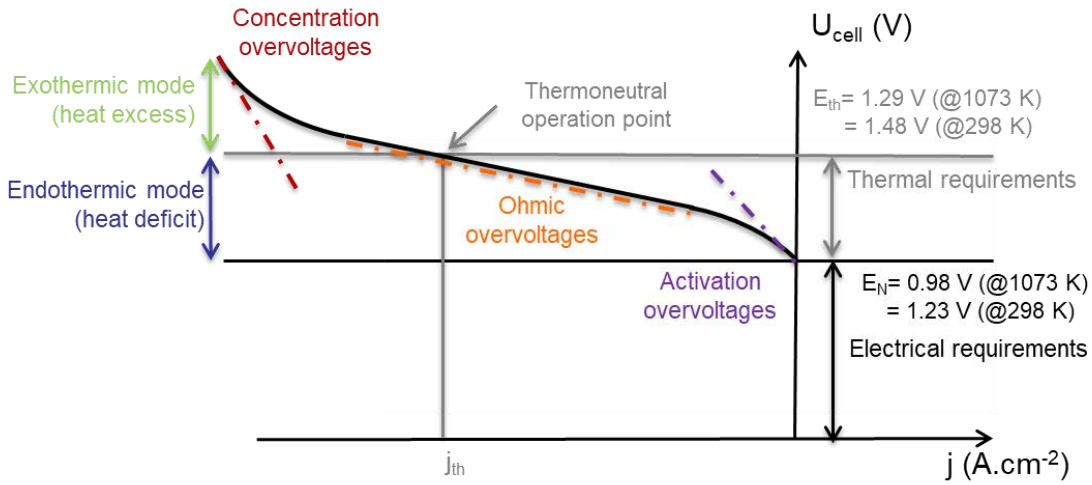


Figure 1-6: Schematic representation of the polarization curve of an electrolysis cell, adapted from [69] and [14]

1.2.2.6. Cell efficiency

The cell efficiency η_{CELL} can be defined as the ratio of the energy content of the hydrogen produced in a cell at 298 K and of the electrical power injected in a cell. Since the numerator is equivalent to the amount of hydrogen $\dot{n}_{H2}$ multiplied by the standard enthalpy of the electrolysis reaction $\Delta_R H^0$, the cell efficiency can be written as Equation (1.13) [38, 68, 70]. Here, $\Delta_R H^0$ corresponds either to Equation (1.1) and is also equal to the HHV of hydrogen or to Equation (1.2) and is then equal to the LHV of hydrogen.

$$\eta_{CELL} = \frac{\dot{n}_{H2} \cdot \Delta_R H^0}{P_{CELL}} \tag{1.13}$$

1.2.3. From the cell to the integrated electrolysis system

Once manufactured, electrolysis cells need to be assembled together to enable the injection of higher amounts of electrical power in order to reach industrial scale. In a first step, they are assembled together to form a stack. Even if the number of cells that are stacked can be significant, manufacturers need to put together several stacks to make so-called electrolysis modules. Even higher capacities can be obtained by the multiplication of modules. The same pattern for upscaling electrolysis units can be observed for all electrolysis technologies. Usually, each electrolysis module possesses its own auxiliary equipment, which includes the following components [38].

- Power conditioning units (e.g. transformation and rectification unit);
- Reactants conditioning units (for water and air or oxygen, e.g. water purification);
- Heat management units (e.g. heat exchangers, condensers, electrical heaters, electric fans or compressors);
- Products post-treatment units (e.g. drying, compression);
- System control units (electronic devices such as controllers, sensors controlling the different modules).

While the technologies further upscale, it is possible that some pieces of equipment will be shared between several modules, thus allowing significant reduction of investment costs. Hence, the efficiency of an electrolysis system η_{SYS} can be defined as written in Equation (1.14), where P_{EL} corresponds to the electrical power injected in the stacks and P_{AUX} to the electrical power injected in the auxiliaries.

$$\eta_{SYS} = \frac{\dot{n}_{H2} \cdot \Delta_R H^0}{P_{EL} + P_{AUX}} \quad (1.14)$$

1.2.4. Operation modes of electrolysis units

Different operation modes are possible for on-field electrolysis units. They are shortly depicted hereafter.

- In standby mode, the electrolysis unit does not produce any hydrogen, but it is maintained warm at a temperature close to or within the operating temperature range. The unit can be switched on very quickly (within seconds or minutes) to nominal load to produce hydrogen as soon as electrical power is provided. The transition from standby to operation with the first quantity of hydrogen produced is also referred to as hot startup [27].
- The cold startup corresponds to the transition from ambient temperature to operating temperature with the first amount of hydrogen produced by the unit [27].
- At nominal load, the unit is operated at an electrical power corresponding to 100% of its capacity. This usually corresponds to the operation point at which the system was initially designed to operate and at which the unit efficiency is usually the highest.
- At partial load, the electrical power injected in the electrolysis unit is lower than that at nominal load. Hence the amount of hydrogen produced is lower. Depending on the dimensioning of the BoPs, the unit efficiency might also be reduced compared to nominal load operation.

1.2.5. Electrolysis technologies

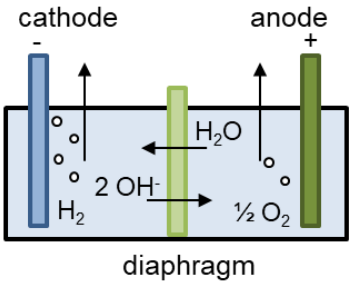
The aim of this chapter is to deliver the latest state of the art of the following electrolysis technologies: alkaline electrolysis, proton exchange membrane (PEM) electrolysis and solid-oxide electrolysis (SOE), because they are currently the most mature ones. The technical features of each technology will be presented. The review will not consider fuel cell applications and will focus on planar cell geometries, even though other geometries might also be mentioned. The power consumption of the electrolysis technologies reported afterwards mostly depends on the power load level and the degradation of the cells. As for the lifetime of the stacks, it is mostly determined by the operating conditions (e.g. operating point, base load or partial load, number of start and stop).

1.2.5.1. Alkaline electrolysis

The alkaline technology is the oldest one and was historically used for base load applications. It reached industrial maturity in the early 20th century. Several 100 MW units were commissioned in the 1920-30s, most of them using low-cost hydropower to produce the hydrogen required for the synthesis of ammonia fertilizers [71]. The largest unit ever implemented had a capacity of 37,000 $Nm^3 \cdot h^{-1}$ hydrogen (165 MW) and operated at atmospheric pressure [71]. All these large scale plants were eventually decommissioned in the 1970-80s, when cheap fossil fuels where increasingly applied for hydrogen production, e.g. through steam reforming [72]. The operating principle of alkaline electrolysis is summarized in Table 1-3.

Table 1-3: Operating principle of alkaline electrolysis

Charge carrier	Operating principle	Half equations

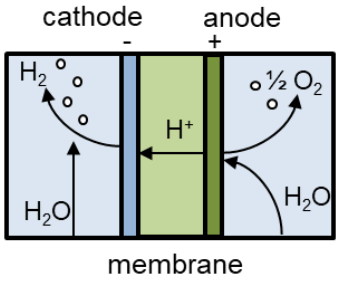
OH^-	 Figure 1-7: Schematic operation of alkaline electrolysis	Cathode $2H_2O + 2e^- \rightarrow H_2 + 2OH^-$ (1.15) Anode $2OH^- \rightarrow \frac{1}{2}O_2 + H_2O + 2e^-$ (1.16)

Alkaline electrolysis stacks are usually operated in the range of 333-353 K [73] and at pressures up to 30 bar [74]. The cells are operated with a voltage in the range of 1.8-2.4 V and at low current densities in the range of -0.2 to -0.4 A·cm^{-2} [73]. Most manufacturers favor pressurized operation to limit unit footprint and to reduce equipment costs and energy consumption, especially for hydrogen compression.
The power consumption of an alkaline electrolysis unit including auxiliaries ranges between 4.5-6.6 kWh·Nm^{-3}, which corresponds to a HHV efficiency of 54-79% or to a LHV efficiency of 45-67%. Stack lifetimes are usually comprised in the range of 60,000-90,000 hours [75].
Even tough alkaline electrolysis stacks show limited flexibility, their operating load range can be extended by increasing the number of stacks in a single module. For instance, the operating power load range of units commercialized by the company Hydrogenics can be extended from 40-100% to 5-100% by increasing the number of stacks in a module from one to six [74].
Among the latest and most representative alkaline electrolysis units integrated in power-to-SNG units at present, the 6 MW unit in Werlte and the 2 MW unit of the European project STORE&GO in Falkenhagen both located in Germany can be mentioned [33, 36]. A more detailed presentation of these projects can be found in Chapter 1.1.3.

1.2.5.2. Proton Exchange Membrane (PEM) electrolysis

The PEM technology was originally developed for fuel cells applications during the Gemini and the Apollo programs in the US in the 1960s and 1970s. The operating principle of PEM electrolysis is schematically represented in Table 1-4.

Table 1-4: Operating principle of proton exchange membrane (PEM) electrolysis

Charge carrier	Operating principle	Half equations
H^+	 Figure 1-8: Schematic operation of PEM electrolysis	Cathode $2H^+ + 2e^- \rightarrow H_2$ (1.17) Anode $H_2O \rightarrow \frac{1}{2}O_2 + 2H^+ + 2e^-$ (1.18)

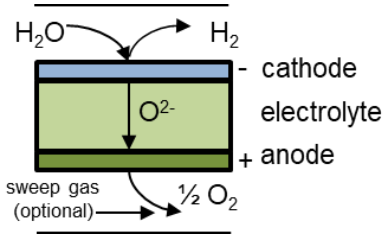
PEM electrolysis stacks are usually operated between 323 and 353 K [73], under pressures between 30 and 60 bar, while few systems can also be operated between 100 and 200 bar [76]. The cells are operated with a voltage in the range of 1.8-2.2 V similar to alkaline units, however with much higher current densities in the range of -0.6 to -2.0 $A \cdot cm^{-2}$ [73], usually around -1.2 $A \cdot cm^{-2}$. These high current densities allow for a much more compact unit design and a reduced footprint.
The power consumption of a PEM electrolysis unit with auxiliaries is comprised between 4.2 and 6.6 $kWh \cdot Nm^{-3}$, with a stack lifetime ranging from 60,000 to 90,000 hours [75]. This corresponds to a system efficiency in the range of 50-79% HHV or 45-71% LHV.
A significant advantage of the PEM technology is its high flexibility with a system response time in the order of the millisecond [76] as well as its wide operating power load range of 1% to 100% for each stack [74].
Past years have seen an increasing number of projects for the implementation of PEM electrolysis units, the largest ones being listed hereafter.

- A 10 MW unit operated by Shell and manufactured by ITM Power will be completed in the second half of 2020 on the refining site of Shell in Wesseling, Germany. The unit is implemented in the frame of the EU project REFHYNE and will produce the hydrogen required for the desulfurization of conventional fuels, thus replacing the hydrogen previously synthesized with steam methane reforming [77].
- A 20 MW unit ordered by Air Liquide to Hydrogenics will be commissioned by the end of 2020 on the Air Liquide site of Becancour, Canada. The unit will produce the hydrogen required on-site with hydroelectricity and increase the hydrogen capacity of the site by 50%, thus avoiding the corresponding CO_2 emissions related to hydrogen production with steam methane reforming [78].

1.2.5.3. Solid Oxide Electrolysis (SOE)

The first R&D works on the SOE technology were initiated in the 1960s in the US [79, 80]. They restarted in the 1970-80s, when companies like Lurgi, Dornier, and Westinghouse developed tubular cells [81, 82]. The operating principle of solid-oxide electrolysis is schematically represented in Table 1-5. In opposition to PEM and alkaline technologies, SOECs are fed with steam and not with liquid water. They can also be operated in fuel cell mode (SOFC), which makes their reversible operation possible [83]. Furthermore, they can also directly produce syngas (a mixture mostly composed of H_2 and CO) and O_2 with CO_2 and steam [84] when operated in so-called co-electrolysis mode.

Table 1-5: Operating principle of solid-oxide electrolysis

Charge carrier	Operating principle	Half equations
O^{2-}	 Figure 1-9: Schematic operation of solid-oxide electrolysis	Cathode (anode in SOFC mode) $H_2O + 2e^- \rightarrow H_2 + O^{2-}$ (1.19) Anode (cathode in SOE mode) $O^{2-} \rightarrow \frac{1}{2}O_2 + 2e^-$ (1.20)

The two main SOEC architectures are represented in Figure 1-10. The middle layer of the cell is called electrolyte, because it is where the transfer of anions O^{2-} takes place from the three phase boundary (TPB) layer at the cathode to the TPB layer at the anode. The reaction mechanism takes place at the TPB. This zone corresponds to the common boundary between the Ni catalyst, where the electrons are circulating, the Yttrium Stabilized Zirconia (YSZ), where the ions are conducted, and the pores, where the gases circulate [85]. YSZ is used as electrolyte because of its high O^{2-} anions conductivity, its low electric conductivity, and its gas tightness [86, 87], and because of the high density obtained after sintering. In addition, it presents a high crystallographic stability in operating conditions (at 1073 K, under reducing and oxidizing atmosphere), a low chemical reactivity with electrode materials [88], and a similar thermal expansion coefficient, thus limiting mechanical stress in the cells. At the TPB between the anode and the electrolyte, O^{2-} anions and electrons are combined into oxygen, whereas steam is decomposed into hydrogen, electrons and O^{2-} anions at the TPB between the cathode and the electrolyte. Either the cathode or the electrolyte can be chosen as support for the cell architecture. The other functional layers are then deposited on the support layer during the following steps of the cell manufacturing process. Since electrode materials have to be porous to allow gas transfer to the TPB, cathode supported cells are usually thicker than electrolyte supported cells for mechanical stability. The metallic interconnects, e.g. made of Crofer 22 APU, ensure the electrical contact between cells in the stack and a uniform gas distribution. It also includes the sealant to separate anode and cathode gas compartments.

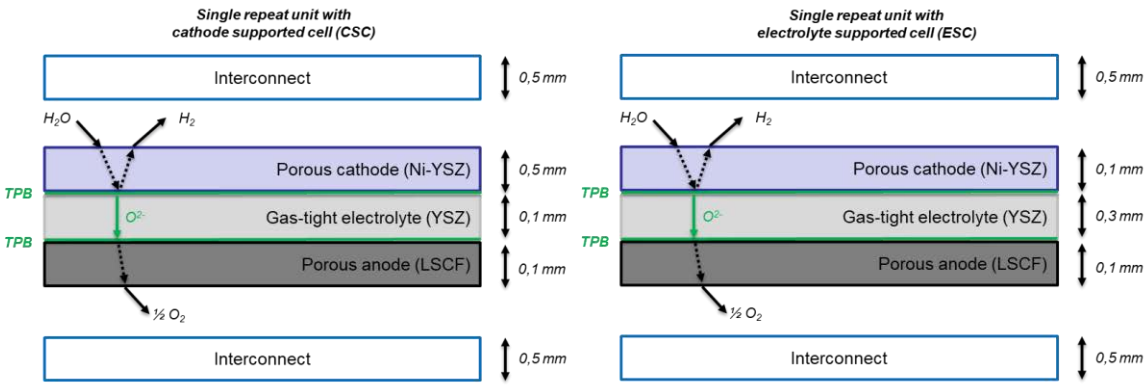


Figure 1-10: Schematic representation of single repeat unit (SRU) architectures with integrated cathode support (left) and electrolyte support (right) solid oxide electrolysis cells (SOECs), adapted from [38] and [89].

SOE stacks are usually inserted in so-called hot boxes (see Figure 1-11) made out of an insulating material to limit heat losses towards the environment and maintain stack temperature. The hot box presented here is also used to circulate the sweeping air at the anode of the SOECs.



Figure 1-11: Hot box configuration of the company Sunfire, adapted from [90]

Even though SOE stacks can be operated between 923 K and 1273 K [91], most systems operate in the range of 1023-1123 K. The high operating temperatures improve the electrolysis reaction kinetics, thus enabling a low cell voltage operation, at about 1.3 V [92].

According to SOECs manufacturers, the pressurized operation up to 20-30 bar should be possible [11]. Nonetheless, no pressurized SOE system operating at these pressure levels has been reported so far. A number of studies have been performed on the effect of pressurized operation on SOECs, amongst others [70, 93-95]. It has been verified that pressurized operation increases the open-circuit voltage of SOECs. However, it was also proven that the cell operating voltage can be reduced thanks to improved kinetics at high current densities. Even if pressurized cells were operated at low current densities with higher cell voltages than at atmospheric pressure, it could still remain interesting at system level, because it would enable the production of pressurized H_2. This would indeed considerably reduce H_2 compression work (which is the highest at low pressures) and this gain could outmatch the increased energy consumption of SOE system auxiliaries.

SOECs can be operated with current densities in the range of -0.3 to -2.0 $A \cdot cm^{-2}$ [91]. Nonetheless, stacks currently integrated in systems are usually operated at -0.6 $A \cdot cm^{-2}$ [96]. This combination of low voltage and intermediate current density allows for a compact design and a footprint similar to the one of PEM systems. For instance, commercial SOE units have a footprint of 6.7 $Nm^3 \cdot h^{-1}$ $H_2 \cdot m^{-2}$ (or 25 $kW \cdot m^{-2}$) [97], whereas it is in the range of 6.1-13.4 $Nm^3 \cdot h^{-1}$ $H_2 \cdot m^{-2}$ (33-67 $kW \cdot m^{-2}$) for commercial PEM electrolysis units [98]. The power consumption of SOE systems with auxiliaries is currently higher than 3.7 $kWh \cdot Nm^{-3}$, which corresponds to a system efficiency of max. 96% HHV.

At present, the best SOECs have reached a lifetime of more than 23,000 h in constant operation [99], with a reported degradation over the first 15,000 h during the SUNFIRE project of 0.6%·kh^{-1} at a current density of -0.9 $A \cdot cm^{-2}$ [66]. Assuming a 90% availability, this would correspond to three years system operation. A short stack lifetime of more than 20,000 h was reported by Frey et al. [100], with a current density of -0.5 $A \cdot cm^{-2}$, a steam conversion rate of 50% and at 1073 K. Even though on-field stacks operated in fuel cell mode (SOFC) have already reached 40,000 h and manufacturers aim at a mid-term lifetime above 60,000 h [101], it is more likely that SOE stack lifetime with reasonable degradation rate below 1%·kh^{-1} still lies below 10,000 h [102, 103]. On the longer run, SOE manufacturers are targeting a system lifetime of 80,000 h (approx. 10 years of operation) to reach similar levels than PEM and alkaline technologies [104].

At the cell level, an average area specific resistance as low as 0.165 $\Omega \cdot cm^2$ measured at 1073 K and -0.5 $A \cdot cm^{-2}$ was reported at the Forschungszentrum Jülich (FZJ) for SOECs integrated in a stack [105]. At the short stack level, a 5-cell stack with optimized sealing and protection design was tested in the frame of the EU project ADEL project, where similar ASR performances were observed at cell and stack level, in the range of 0.59-0.74 $\Omega \cdot cm^2$ [106]. An ASR value of 0.5 $\Omega \cdot cm^2$ was reported for a 10-cells stack of the company Haldor Topsoe, with a cell ASR of 0.4 $\Omega \cdot cm^2$ [107]. Research efforts by SOC manufacturers currently aim at reducing the cell ASR by 25% with new cell designs as well as reducing the ASR of interconnects with special coatings [101].

SOE units are currently operated with a steam utilization of 70%, which means that 70% of the steam provided to the cells is converted into hydrogen. Nonetheless, stacks were already successfully operated with steam utilization rates of 80% [96] and manufacturers are considering even higher values up to 90% [55]. Such high values enable the reduction of heat losses and limit the steam requirements of SOE units. In that case, no additional steam source would be required when coupled to a catalytic methanation unit, which would therefore simplify the thermal integration of processes [29]. Values higher than 90% are nonetheless not realistic, because of the subsequent steam starvation issues leading to local overvoltages, which accelerates cell degradation [108].

At present, SOE stacks integrate cells with an active area of 100-550 cm^2 [96, 109]. Nonetheless, the operation of cells with a wide active area under high current densities is challenging because of thermal management issues. Therefore, SOE manufacturers tend to limit the active cell area in order to allow higher current densities, which enables to reduce systems footprint.

According to manufacturers, SOE systems can be operated on a wide power load range from 0 to 125% [97]. As for the dynamic operation of the technology, one can distinguish between electrical and thermal cycling. The technical feasibility of electrical cycling on cells, short stacks, and stacks was already demonstrated in past work, e.g. in the frame of the EU project ADEL [106, 110]. More recently, Schefold et al. implemented 80,000 cycles of 2 min each at a current density of -0.7 $A \cdot cm^{-2}$ on an ESC where a degradation of 0.4%$\cdot kh^{-1}$ was reported [111]. The electrical cycling did not have any influence on cell degradation. At stack level, 16,000 cycles were also performed without increased impact on the degradation in the EU project GrInHy [112].
The thermal cycling of cells, short stacks and stacks was also investigated. Most results were obtained in laboratory conditions at cell, short stack, or stack level, where the SOE equipment is disposed in a furnace [96, 106, 110, 111]. In that case, it is difficult to extrapolate the thermal behavior of laboratory tested equipment to the performances of on-field devices. Nonetheless, the direct coupling of SOE systems with renewable power sources should be feasible from both electrical and thermal standpoint [110]. So far, experimental results of on-field SOE stacks or systems were scarcely reported. Here, the 15 kW SOE unit implemented at the refueling station of TOTAL in Karlsruhe, Germany [113] can be mentioned. However, the results provided were obtained in static regime and they did not enable to draw conclusions on the system thermal behavior in dynamic regime.

As it is also the case for the PEM technology, past years have seen an increasing number of projects for the implementation of SOE units, the largest ones being listed hereafter.

- A 150 kW SOE unit of the manufacturer Sunfire GmbH was implemented on the site of the steel manufacturer Salzgitter GmbH in Salzgitter, Germany, in the frame of the European project GrinHy. The unit produces hydrogen required for steel manufacturing process, thus substituting

hydrogen previously produced by steam reforming. The SOE unit is fed with steam coming from the steam network of Salzgitter [42].

- A 150 kW SOE unit of Sunfire GmbH will be implemented on the company's site in Dresden, Germany, in the frame of the German project SynLink (2019-2021). This unit will be the first step of upscaling the co-electrolysis process of the company. The syngas produced can be used for industrial applications or for e-fuels production through Fischer-Tropsch synthesis. The following step will be the implementation of a first commercial SOE unit of 20 MW on the industrial park of Heroya in Norway. The unit will be fed with low cost hydroelectricity and will produce the syngas required for the synthesis of 8,000 tons of synthetic crude oil [43].

1.2.6. Focus on existing SOE models

In this section, previous technical and economic SOE models will be reviewed. Since our work aims at understanding how SOE units can improve the flexibility and the efficiency of power-to-SNG plants, the technical review will be divided in two parts. The first part will review previous SOE system models when thermally coupled with other processes, with a focus on hydrogenation processes. The second part will be dedicated to previous dynamic models, their modeling features and results.
A review of economic SOE models will be implemented in a second step, based on the work reported in [8]. Since SOE units represents by far the largest contribution to CAPEX and OPEX costs of power-to-SNG plants, it is important to understand how SOE systems costs were evaluated in previous work.

1.2.6.1. Technical SOE models

There are less technical SOEC models available in the literature than SOFC models, even though their number has significantly increased over the last decade.
Past years have seen many research works being published on modelling the thermal coupling of SOE units with steam generating processes in static regime. Their thermal integration was investigated with nuclear power plants [108], geothermal plants [114], biomass boilers [115], and solar thermal units [116, 117]. Furthermore, other works reported the integration of SOE units with hydrogenation processes, such as Fischer-Tropsch units [12, 67, 118-123], methanol units [124-127], dimethylether (DME) units [128] and catalytic methanation units [45-57], where electrolytic H_2 or syngas were used as feedstock for catalytic hydrocarbon synthesis.
In the context of the thermal coupling, the behavior of SOE units was most of the time determined based on 0D models, where the stack ASR was expressed as a function of the temperature [12, 45, 49, 67, 118, 129] and sometimes of the pressure [45, 49, 118, 129], more rarely of the current density [45]. Several ASR functions used in previous work are presented hereafter.

- Equation (1.21) from Becker et al. [67] based on the work of Stoots et al. [130];
- Equation (1.22) from Giglio et al. [49] partly based on the work of Sun et al. [131];
- Equation (1.23) from [45] based on experimental results obtained in the Danish project planSOEC;
- Equation (1.24) from Fu et al. [12] based on experimental data obtained during the EU project ADEL, which was adapted in later works [9, 38, 68, 69, 117, 132];
- Equation (1.25) from De Saint Jean et al. [14, 46, 48], with the ASR as function of the thermoneutral voltage, the OCV, the inlet steam flow rate $\dot{n}_{H2O,IN}$ and the cathode flow rate $\dot{n}_{CATH}$ at 973 K or at 1073 K.
- Equation (1.26), based on the experimental work at stack level of O'Brien et al. [94] with $\alpha = -0.09$ and of Wendel and Braun [133] with $\alpha = -0.1$, which enables to extrapolate the behavior

of standard pressure P_0 to pressurized operation. This extrapolation was done e.g. in the work of [14, 46, 48].

$$ASR_{BECKER}(T) = ASR_{1100\,K} - 0.463 + 3.973 \cdot 10^{-5} \cdot exp\left(\frac{10{,}300}{T}\right) \quad (1.21)$$

$$ASR_{GIGLIO}(T,p) = 35.71 \cdot exp(-0.057 \cdot T) \cdot exp(-0.0217 \cdot p) \quad (1.22)$$

$$ASR_{planSOEC} = f(i,T,p_i) \quad (1.23)$$

$$ASR_{FU}(T) = exp\left(\frac{4{,}900}{T} - 5.95\right) \quad (1.24)$$

$$ASR_{DESAINTJEAN} = f\left(E_N, E_{th}, \dot{n}_{H2O,IN}, \dot{n}_{CATH}\right) \quad (1.25)$$

$$ASR(T,p) = ASR(T,p_0) \cdot \left(\frac{p}{p_0}\right)^{\alpha} \quad (1.26)$$

ASR functions are mostly based on cell results [12, 38, 67, 118, 129], more rarely on short stacks results [119, 134], under the assumption that cells and stack present the same ohmic resistance [12, 67] or adding an ohmic resistance to the cell in order to model stack behavior [38]. Occasionally, these functions were developed based on stack results directly [45, 94, 119, 133] or elaborated from the extrapolation of previous experimental work [67]. Most models assumed a linear cell behavior [12, 38, 49, 67], and few of them considered the non-linear cell behavior [45, 118, 129]. Experimental results at stack and system level are scarce, so that the validation of modeling results can be complicated. In few cases, models were either verified by comparison of the results with previous work [67, 118] or validated with experimental tests at stack level [45].

Previous works on the dynamic operation of SOC systems mostly focused on fuel cell mode (SOFC) [135-141]. The main modelling goal was the description of the voltage transients in SOFCs at channel [135], cell [138, 139], short stack [136, 140] and stack level [137] when changing reactant flow rate, current density, or temperature. Control strategies have been more rarely at the chore of investigations, e.g. by Kazempoor et al. in [141], where strategies either based on constant fuel utilization or on constant reactant flow rate were investigated. Most works only focused on the fluid and energy transport phenomena along the cells [135, 136, 138-141], but few of them considered the effects of gas diffusion phenomena in the porous electrodes [137].

In comparison to SOFC, the dynamic operation of SOE units was significantly less documented, even though the development of adequate models is important for the coupling with renewable power sources [38]. Cai et al. proposed a dynamic stack model [142], where the behavior of planar, electrode supported cells in the stack were assumed to be homogeneous and side effects were neglected. Furthermore, only theoretical power profiles were considered. Auxiliary equipment was composed of a sweep air compressor at the SOECs anode. Control strategies for optimal system operation were proposed using the anode air flow as single control variable. The optimal problems were solved using the software gPROMS Model Builder 3.4.

Botta et al. reported a 1D dynamic model for the reversible operation of a SOC stack in [143]. The model was obtained from merging two 1D models, one SOEC and one SOFC. The response of each model was verified by comparison with previous work. The stack transient behavior in terms of temperature gradient and fuel flow rate could be safely controlled with a PID controller. The SOEC model was implemented under Modelica and was simulated under Dymola. Only the convection was taken into account for the modelling of the heat transfer in the cells. Other phenomena such as conduction and radiation were not considered.

Past years have also seen an increase of dynamic models for the operation of SOECs in co-electrolysis mode. A 2D dynamic model of a planar reversible SOC in co-electrolysis mode was proposed by Yang et al. in [144]. Wang et al. investigated the behavior of a SOE stack operated in co-electrolysis mode with a 3D dynamic model. Control strategies were developed to limit thermal gradient in a stack when coupled to a wind power profile [145]. The dynamic behavior of tubular cells was investigated by Luo et al. in [146] and by Fogel et al. in [147], where 2D models of cells operated in co-electrolysis or steam electrolysis mode were proposed.

The dynamic models reported above are at least 1D models taking into account concentration and activation overpotentials and sometimes even mass diffusion transfer in the porous electrodes. This results in complex solving methods and long calculation times, which makes the development of real time control strategies difficult. Even though these models can be reduced to limit computation time, this requires a consequent time effort, which could be avoided using lighter models. Finally, for both static and dynamic models, the experimental validations of the modelling work still remain a challenge.

1.2.6.2. SOE models for economic evaluation

Even though first research works were published on electrolysis mode [81, 82, 148], solid oxide fuel cells (SOFC) systems have reached the market first and SOFC costs have been thoroughly investigated [149-160], whereas work on SOEC costs is more recent [45, 75, 102, 161-165].
An overview of previous work on SOC costs is presented in Table 1-6. Several studies on SOFC costs applied a bottom-up approach to determine stacks [154] and system costs [150-152, 156-158] in the past decade, expanding the work undertaken on SOFC costs in the early 2000's [149, 155, 159]. They investigated the potential for SOFC system cost reduction through upscaling of SOFC production capacities up to more than 10 GW [154, 156, 157] for different applications, cell geometries (planar [149-152, 154-158] or tubular [151, 153, 160]) and unit capacities up to 3.1 MW [151].
As for SOE, many cost values for stacks and systems can be found [45, 75, 102, 161-166] and several system cost breakdowns have been reported as well [45, 161, 163-165]. Reytier et al. performed a bottom-up cost analysis at cell and stack level, however the system level was not documented and no cell cost breakdown was provided [166].

Table 1-6: Overview of literature available on SOC costs, n.a.: not available, cost values between brackets () were converted using a specific SOE system consumption of 3.6 kWh·Nm^{-3} H_2 adapted from [8]

Source, year	SOEC or SOFC	Bottom-up cost analysis	Cost level detailed	SOE system costs	SOC unit capacity	Max. production capacity (MW·year^{-1})
Carlson et al. [155], 2004 extended from [149]	SOFC	Yes	Cell, stack	n.a.	5 kW	250
Thijssen et al. [151], 2007, extended from [159]	SOFC	Yes	Cell, stack, system	n.a.	up to 3.1 MW	1,000

Source, year	SOEC or SOFC	Bottom-up cost analysis	Cost level detailed	SOE system costs	SOC unit capacity	Max. production capacity ($MW \cdot year^{-1}$)
Otomo et al. [160], 2013	SOFC	Yes	Cell, stack, system	n.a.	1 kW	1
Weimar et al. [152], 2013	SOFC	Yes	Cell, stack, system	n.a.	270 kW	2,700
Battelle [150], 2014	SOFC	Yes	Cell, stack, system	n.a.	1-5 kW	250
James et al. [158], 2015	SOFC	Yes	Cell, stack, system	n.a.	1-100 kW	5,000
Scataglini et al. [157], 2015	SOFC	Yes	Cell, stack, system	n.a.	1-250 kW	12,500
Battelle [156], 2016	SOFC	Yes	Cell, stack, system	n.a.	100-250 kW	12,500
Otomo et al. [153], 2017	SOFC	Yes	Cell, stack, system	n.a.	220 kW	2,200
Scataglini et al. [154], 2017	SOFC	Yes	Cell, stack	n.a.	1-250 kW	12,500
planSOEC [45], 2011	SOEC	No	System	(194 €·kW^{-1}) 700 €·Nm^{-3}·h	(10.8 MW) >3,000 Nm^3 ·h^{-1}	500
Harvego et al. [163], 2012	SOEC	No	System	(174 €·kW^{-1}) 625 €·Nm^{-3}·h	(84 MW) 50 t·day^{-1}	n.a.
Reytier et al. [166], 2013	SOEC	Yes	Stack	Value in €·kW^{-1} and in €·Nm^{-3}·h n.a.	(840 MW) 500 t·day^{-1}	n.a.
Bertuccioli [75], 2014	SOEC	No	n.a.	300-2,000 €·kW^{-1}	n.a.	n.a.
FCH-JU [162], 2015	SOEC	No	n.a.	625 €·kW^{-1} (2,250 €·Nm^{-3}·h)	10 MW	n.a.
Reytier et al. [161], 2015	SOEC	No	System	(2,170 €·kW^{-1}) 7,800 €·Nm^{-3}·h	(0.17 MW) 100 kg·day^{-1}	(17)
US DoE [164, 165], 2016	SOEC	No	System	180-550 €·kW^{-1}	73 MW	n.a.

Source, year	SOEC or SOFC	Bottom-up cost analysis	Cost level detailed	SOE system costs	SOC unit capacity	Max. production capacity (MW·year^{-1})
Schmidt et al. [102], 2017	SOEC	No	n.a.	300-6,800 €·kW^{-1}	n.a.	n.a.

Hence, cost structures of SOE cells and stacks have been rarely documented. Furthermore, previous cost analysis at system level do not provide enough data to rebuild cost structures at cell and stack level. It is therefore difficult to have an exhaustive view on SOE costs at cell, stack and system level at the same time. In addition, adapting previous bottom-up SOFC cost analysis to SOEC should be avoided for the following reasons.

- Cell architectures considered in previous bottom-up cost analysis have considerably changed since;
- Costs analysis of SOFC systems do generally not provide data on cells or stacks when operated in electrolysis mode. Therefore, the behavior of cells or stacks in electrolysis mode would have to be extrapolated from the fuel cell mode, which would most likely result in important imprecisions;
- Assuming the same electrical power, SOFC systems require larger auxiliaries than SOEC systems because of larger amounts of heat involved in fuel cell mode. Hence, SOEC and SOFC system cost breakdowns can vary significantly.

1.3. Methanation

The synthesis of methane from hydrogen and carbon oxides using nickel catalysts was discovered in 1902 by Sabatier and Senderens [167]. It gained considerable interest during the oil crises in the 1970s: with the significant increase of oil and gas prices, SNG production from coal became profitable. Nowadays, the synthesis of renewable methane from biomass is considered by many stakeholders worldwide as an option to substitute conventional natural gas, thus reducing the carbon footprint of our societies. In this subchapter, the chemical and thermodynamic principles applied for the description of the catalytic methanation will be presented, followed by a review of the catalytic methanation technologies and processes. Past years have also seen the development of low temperature biocatalytic methanation processes, which produce low temperature heat. Since they present a rather limited interest on a thermal management perspective, they will not be reviewed.

1.3.1. Principle

1.3.1.1. Chemical reactions

Methanation is a strongly exothermic, heterogeneous, catalyst based process, which can occur either at low temperatures on a biocatalyst or at intermediate to high temperatures on a chemical catalyst. In this second option, the catalyst is usually a material based on the following metals: Ru, Fe, Ni, Co, Rh, Pd, Pt, Ir [168]. The material support for the metal is usually titanium oxide (TiO_2) or alumina (Al_2O_3). The catalytic methanation process can be depicted with the CO methanation reaction (Equations (1.27)), the Sabatier reaction (Equation (1.28)) and the water gas shift (WGS) reaction (Equation (1.29)).

$$3H_2 + CO \rightleftarrows CH_4 + H_2O \qquad \Delta_R H^0 = -206\ kJ \cdot mol^{-1} \qquad (1.27)$$

$$4H_2 + CO_2 \rightleftarrows CH_4 + 2H_2O \qquad \Delta_R H^0 = -165\ kJ \cdot mol^{-1} \qquad (1.28)$$

$$CO + H_2O \rightleftarrows CO_2 + H_2 \qquad \Delta_R H^0 = -41\ kJ \cdot mol^{-1} \qquad (1.29)$$

$$2CO \rightleftarrows C_{(s)} + CO_2 \qquad \Delta_R H^0 = -172\ kJ \cdot mol^{-1} \qquad (1.30)$$

$$CO_2 + 2H_2 \rightleftarrows C_{(s)} + 2H_2O \qquad \Delta_R H^0 = -90\ kJ \cdot mol^{-1} \qquad (1.31)$$

$$nCO + (2n+1)H_2 \rightleftarrows C_nH_{2n+2} + nH_2O \qquad \Delta_R H^0 = -158\ kJ \cdot mol^{-1} \qquad (1.32)$$

The Boudouard reaction (Equation (1.30)) and the carbon dioxide reduction reaction (Equations (1.31)) can also take place in the process and result in carbon deposition [169], which is known to deactivate the catalyst. However, this phenomenon can be avoided by adapting the thermodynamic conditions and the feed gas composition in the methanation reactor [169]. The CO methanation reaction and the Sabatier reaction are strongly exothermic, therefore an efficient thermal management of reactors is required to control the main reactions parameters (temperature and pressure) in order to maximize the process efficiency.

In case a gas mixture of CO and CO_2 is fed into a reactor, CO is firstly converted into methane following the CO methanation reaction. Because of the much higher interaction of CO for the active surface of the catalyst in comparison to CO_2, the Sabatier reaction can only initiate once almost all the CO has reacted, provided that the remaining H_2 amount is sufficient to feed the reaction. As for the WGS reaction, it takes place only at high temperatures, usually in a dedicated WGS reactor with a specific catalyst, in order to adjust the H_2/CO ratio before the methanation. Nonetheless, a WGS reactor is not required in the context of power-to-SNG, since the H_2/CO ratio can be adjusted with the electrolysis unit.

The formation of longer hydrocarbons (e.g. alkanes in Equation (1.32)) is also possible, but less likely to happen because of their much lower stability than methane.

The following parameters are important for the characterization of the reactions involved in the catalytic methanation process.

The conversion rate χ of the reaction can be written with Equation (1.33) as the sum of the molar flow rate of products divided by the sum of the molar flow rate of reactants in $mol \cdot s^{-1}$.

$$\chi = \frac{\dot{n}_{CH4,OUT} + \dot{n}_{CO,OUT} + \dot{n}_{CO2,OUT} + \dot{n}_{C,OUT}}{\dot{n}_{CH4,IN} + \dot{n}_{CO,IN} + \dot{n}_{CO2,IN}} \qquad (1.33)$$

The CH_4 selectivity σ_{CH4} is defined in Equation (1.34) as the ratio of the molar flow rate of CH_4 produced divided by the molar flow rate of all carbon species that might also be produced during the methanation reaction (CO, CO_2, CH_4, and C during carbon deposition).

$$\sigma_{CH4} = \frac{\dot{n}_{CH4,OUT}}{\dot{n}_{CH4,OUT} + \dot{n}_{CO,OUT} + \dot{n}_{CO2,OUT} + \dot{n}_{C,OUT}} \qquad (1.34)$$

The reaction yield can be expressed for any product and is written in Equation (1.35) for CH_4. The yield also corresponds to the product of the selectivity of CH_4 with the conversion rate of the reaction.

$$y_{CH4} = \frac{\dot{n}_{CH4,OUT}}{\dot{n}_{CH4,IN} + \dot{n}_{CO,IN} + \dot{n}_{CO2,IN}} = \sigma_{CH4} \cdot \chi \qquad (1.35)$$

1.3.1.2. Thermodynamics

During the methanation process, several reactions involving the same chemical compounds can occur simultaneously. Starting from an initial gaseous mixture composition injected in a methanation reactor, it is therefore important to determine in which direction the reactions are happening to be able to evaluate

the final composition of the gaseous mixture at the end of the process. This final composition can be evaluated by determining the thermodynamic equilibrium, which corresponds to the gas composition for which the Gibbs free energy of the chemical reactions is minimal. If the standard Gibbs free energy of reaction $\Delta_R G^0$ is known, the equilibrium constant K_{eq} of a reaction can be determined with Equation (1.36), where p_0 is the standard pressure and ξ_i the stoichiometric coefficient of compound i. Assuming that all gases are ideal, the equilibrium constant $K_p = K_{eq}$ can also be written with Equation (1.37) as a function of the partial pressures p_i. Another formulation using Dalton's law (see Equation (1.38)) with the molar fractions x_i and the total pressure p is also possible.

$$K_{eq} = exp^{-\frac{\Delta_R G^0}{RT}} \cdot \left(\frac{p}{p_0}\right)^{-\sum \xi_i} \tag{1.36}$$

$$K_p = \prod_i^n p_i^{\xi_i} = \prod_i^n x_i^{\xi_i} \cdot (p)^{\sum \xi_i} = K_i \cdot (p)^{\sum \xi_i} \tag{1.37}$$

$$p_i = x_i \cdot p \tag{1.38}$$

Using Equations (1.27) and (1.37), the equilibrium constant of the CO methanation reaction can be written as follows.

$$K_p = \frac{p_{CH4} \cdot p_{H2O} \cdot (p_0)^2}{p_{CO} \cdot p_{H2}^3} \tag{1.39}$$

The CO methanation reaction is characterized by a lower number of product moles than reactant moles. Hence, since K_p does not depend on the pressure p, a pressure increase results in an increase of K_i, which corresponds to a shift of the thermodynamic equilibrium towards reaction products. Similarly, increasing the product amount in the initial gas mixture results in a lower product yield. The same conclusions can be drawn from the equilibrium constant of the Sabatier reaction.

1.3.1.3. Reaction kinetics

The determination of reaction kinetics is a critical step for the design and dimensioning of reactors, as well as for the comparison of different catalysts [170]. The main parameter used for the description of reaction kinetics is the reaction rate r, which can be determined with Equation (1.40), κ_i being the concentration variation of compound i. The methanation reaction can be depicted with different reaction mechanisms combining several intermediate reactions or so-called steps that might occur on the surface of the catalyst. Reaction rates could be theoretically calculated for each step. In practice, they are usually only calculated for so-called rate determining steps, which are the reactions steps that are supposed to be the less rapid ones and which are therefore the most relevant ones for assessing the overall reaction rate.

$$r = K_r \cdot \prod_i p_i^{\kappa_i} \tag{1.40}$$

$$K_r = K_r^0 \cdot exp\left(-\frac{E_a}{R \cdot T}\right) \tag{1.41}$$

$$K_{ads} = K_{ads}^0 \cdot exp\left(-\frac{\Delta H_{ads}}{R \cdot T}\right) \tag{1.42}$$

The overall reaction rate can be determined as function of rate constants K_r (with Equation (1.41)) and of adsorption constants K_{ads} (with Equation (1.42)), where each constant corresponds to a reaction step.

Equation (1.41) is based on Arrhenius law, where E_a refers to the activation energy of the reaction. Equation (1.42) is based on van't Hoff equation [170], where ΔH_{ads} refers to the reaction enthalpy of the adsorption reaction.
As previously stated, assuming that the CO_2 methanation reaction mechanism initiates only after the CO methanation reaction is almost completed, the overall kinetics of the syngas methanation can be described with the reaction rates provided in Equation (1.43) and (1.44) determined by Kopyscinski et al. in [171] and by Koschany et al. in [170] respectively.

$$r_{CO\rightarrow CH4} = \frac{K_r \cdot K_{CH} \cdot p_{CO}^{0.5} \cdot p_{H2}}{(1 + K_{CH} \cdot p_{CO}^{0.5} \cdot p_{H2}^{0.5} + K_{OH} \cdot p_{H2O} \cdot p_{H2}^{-0.5})^2} \quad (1.43)$$

$$r_{CO2\rightarrow CH4} = \frac{k \cdot p_{H2}^{0.5} \cdot p_{CO2}^{0.5} \left(1 - \frac{p_{CH4} \cdot p_{H2O}^2}{p_{CO2} \cdot p_{H2}^4 \cdot K_{eq}}\right)}{\left(1 + K_{OH} \cdot \frac{p_{H2O}}{p_{H2}^{0.5}} + K_{H2} \cdot p_{H2}^{0.5} + K_{mix} \cdot p_{CO2}^{0.5}\right)^2} \quad (1.44)$$

Here, K_{CH}, K_{OH}, K_{H2}, K_{mix} refer to the adsorption constants of hydrocarbon intermediates, hydroxyl intermediates, hydrogen, and of the gas mixture respectively, whereas K_{eq}corresponds to the equilibium constant of the Sabatier reaction.

1.3.2. Catalytic methanation technologies

This subchapter will focus on the description of different methanation reactor technologies. Industrial catalytic methanation processes will be presented in Chapter 1.3.3. Catalytic methanation technologies can be classified in four main categories: fixed-bed reactors, fluidized-bed reactors, slurry bed reactors, and structured reactors [22]. For slurry-bed reactors, only the three-phase technology will be depicted, because it possesses the highest liquid proportion of this kind, thus allowing a very good temperature repartition [21]. As for structured reactors, only the honeycomb and micro-channel technologies will be presented. Methanation reactors can be operated in different modes. In adiabatic mode, there is no heat transfer from the reactor to the outside and all the heat generated in the reactor is evacuated by the feed gases. Hence, there is a significant temperature increase along the reactor, which affects the conversion rate of reactants so that several reactors in series with intermediate cooling are usually required. Reactors can also be operated in isothermal mode, where the temperature inside the reactor is kept at a constant value, so that inlet and outlet gas temperatures are identical. To do so, a coolant such as steam or oil is injected in cooling pipes inside the reactor. The reaction heat is evacuated by the coolant as sensible heat for the oil or as latent heat for the water. The reactor temperature is controlled by setting the steam pressure in a feed water boiler. The polytropic operation corresponds to a reactor design where only the second part of the reactor is cooled [172]. Hence, a strong temperature increase can be observed in the first part of the reactor, which results in a bell shape temperature profile along the reactor [173]. This enables the conversion of higher hydrocarbons into methane [172].

1.3.2.1. Fixed-bed technology

Fixed-bed reactors are the simplest technological solution and have been widely used in the industry. The catalyst is deposed on a fixed-bed, which can either be a succession of grids perpendicular to the feed gas flow or the space between water cooling tubes disposed in parallel in a reactor. The reacting gases are circulated on the catalyst. Different fixed-bed reactors concepts are schematically represented in Figure 1-12. Depending on the processes, the reactors can be operated at temperatures in the range of 533-923 K and at pressures up to 25 bar, whereas cooling steam up to 100 bar can be produced for

power production [174]. A so-called catalyst guard bed disposed at the feed gas inlet absorbs the gas contaminants and protects the rest of the catalyst bed.

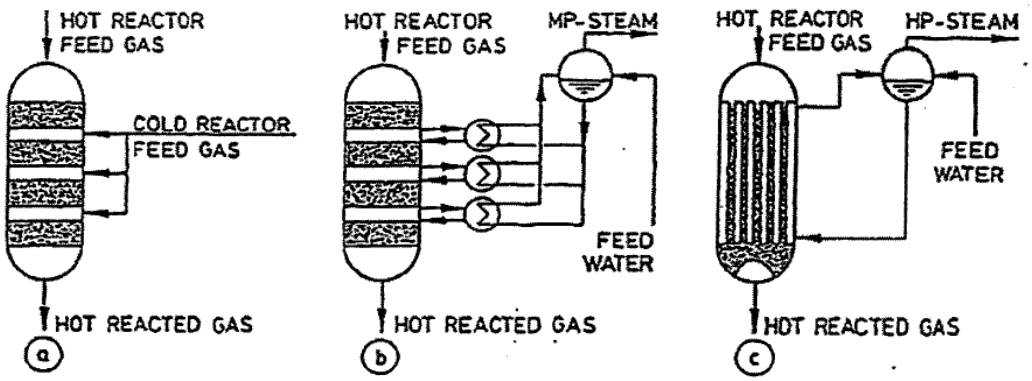


Figure 1-12: Schematic representation of different fixed-bed methanation reactor concepts, grid based a) or b), and multi-tubular c) [21]

Grid fixed-bed reactors allow for a high product gas purity and a quick start-up because of the limited thermal inertia of the reactor. Their adiabatic operation results in very high temperature gradients and the formation of so-called hot spots that can deactivate or damage the catalyst. This can be limited or avoided by intermediate cooling of the beds either with the injection of cold feed gas or with cooling water (see concept a) and b) in Figure 1-12). Because of the low thermal inertia, the temperature changes rapidly in case of load fluctuation or interruption, which is not compatible with extended load range or intermittent operation.

Multi-tubular fixed-bed reactors (see concept c) in Figure 1-12) are filled with catalyst and pressurized water is circulated in cooling tubes. The water evaporates, which enables to evacuate the reaction heat. The reactor temperature is easily controlled by adjusting the steam pressure in a feed water boiler. Nonetheless, hot spots can appear in the middle of space between tubes and a long warming-up time is required to heat up the cooling water. This technology is also commonly applied in Fischer-Tropsch reactors [175].

1.3.2.2. Fluidized-bed technology

In the fluidized-bed technology, the catalyst powder is circulated in turbulent regime using the feed gases. The forced convection movement in the reactor results in an isothermal temperature profile, which allows an easy control of the reactor temperature. Nonetheless, the repartition of feed gas injectors has to be studied carefully to enable an equal fluid repartition and avoid that the catalyst exits the reactor. Moreover, a minimum flow rate is required to maintain the turbulent movement, which limits the possibilities of partial load operation. The turbulent dynamics also result in the abrasion of the catalyst and of the reactor inner walls [21]. The reactors reported in the literature are operated at temperatures in the range of 473-803 K and at pressures from a few atmospheres up to 87 bar [176, 177].

1.3.2.3. Slurry-bed technology

This technology is also referred to as three-phase, because of the three phases (liquid, solid and gas) present in the reactor. A solid catalyst powder with an average grain size of 50-100 µm is mixed into a liquid medium with high vaporization temperature and the inlet gases are fed at the bottom of the reactor. The liquid medium is usually an oil with good gas solubility, low vapor pressure (e.g. 30 mbar), high boiling point and not reacting with the catalyst. It allows an efficient removal of the reaction heat from the reactor

and thus an isothermal operation. It is also used as a buffer for the gases to travel to and react with the catalyst. A coolant (usually water) is injected in cooling pipes at a temperature slightly lower than the vaporization temperature. The water vaporizes in the cooling pipes, thus driving the reaction heat out of the reactor. The reactor can be operated at 548-598 K and at 5-20 bar [178]. It is schematically represented in Figure 1-13.

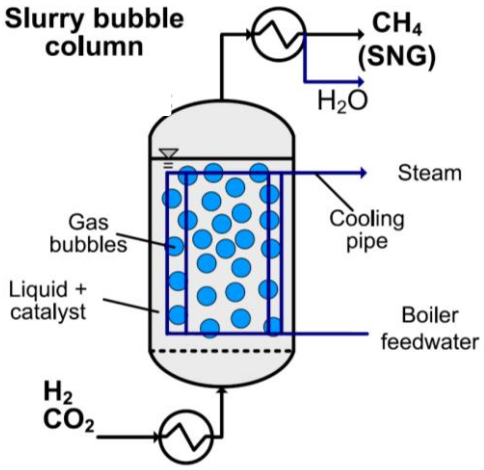


Figure 1-13: Schematic representation of a three-phase methanation reactor [178]

The liquid phase enables to homogenize the temperature in the reactor, thus removing the risk of hot spots. It also stores consequent amounts of thermal energy, which enables the operation at reduced load and even interruptions. However, a long warming-up phase of the reactor is required.
This technology was already investigated for different operating conditions (pressure, temperature, gas velocity, or catalyst concentration) and operating modes (steady state and transient operation) [178, 179]. Promising results were obtained for dynamic operation. Furthermore, the technology is expected to have lower operating and maintenance costs, e.g. because the catalyst can be recycled during operation [21]. Future research area include the improvement of the cooling system design and the understanding of the complex 3D hydrodynamic phenomena. A demonstration unit of 100 kW was commissioned early 2019 at the Campus North of the Karlsruhe Institute of Technology in Germany, in the frame of the so-called Energy Lab 2.0 platform [180, 181].

1.3.2.4. Structured reactors

Structured reactors are the most recent reactor technologies. They were invented to tackle the main drawbacks of adiabatic fixed-bed reactors: hot spots and pressure drops [22]. This subchapter will focus on the description of the honeycomb and the micro-channel technologies.
The honeycomb technology is named after the shape of its inner structure, on which the catalyst is deposited. The honeycomb design enables a high radial heat capacity and an improved radial heat transfer, as well as a lower abrasion of the catalyst and a lower pressure drop. Nonetheless, the cooling design still needs to be improved. The deposition of the catalyst as well as the manufacturing and the design of the reactor are complex [21]. This technology is currently investigated in the power-to-gas unit of Falkenhagen, Germany, which is one of the three demonstration sites of the EU project STORE&GO [33, 182]. More information on the project can be found in Chapter 1.1.3. Honeycomb reactors are operated in polytropic mode with a temperature usually in the range of 523-773 K and under pressure, up to 20 bar [182].

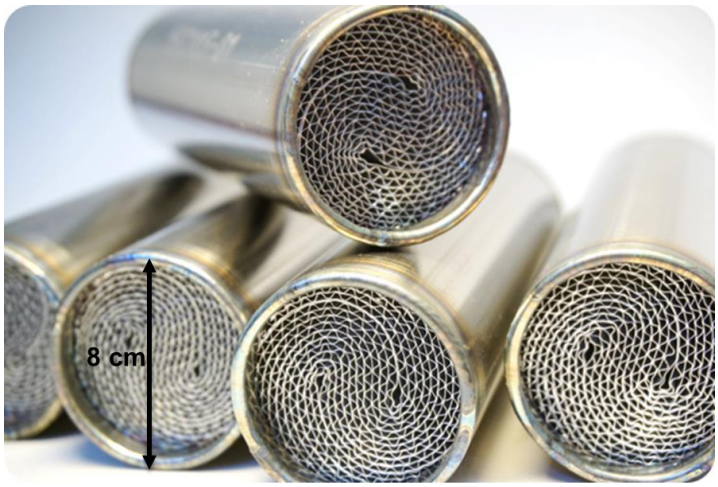


Figure 1-14: Honeycomb cylinders used in the catalytic methanation reactor of the Falkenhagen plant, adapted from [183]

The first micro-channel reactor prototypes were developed in the 1970s. The feed gas circulates along process channels in the range of 0.1-10 mm, which are coated with a catalyst [184]. These channels are interleaved with water-filled coolant channels for the evacuation of the reaction heat released during hydrocarbon synthesis (see Figure 1-15).

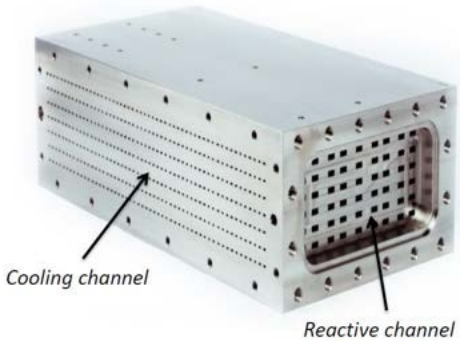


Figure 1-15: Micro-channel reactor developed by the company Atmostat [185]

This technology enables a very compact reactor design, a high catalyst activity, high conversion rates, low residence times. The efficient heat removal results in a homogeneous temperature profile, an isothermal operation and an easy temperature control [184]. Nonetheless, the reactors have high manufacturing costs and the potential of cost savings through mass production seems rather limited. Once the catalyst is deactivated, the entire reactor has to be replaced. Micro-channel reactors can be operated at temperatures in the range of 523-823 K and at pressure up to 50 bar [185-187]. The capacity of a single unit can be increased by adding more reactors in parallel. This technology is also applied at commercial scale for Fischer-Tropsch synthesis [184].

1.3.3. Catalytic methanation processes

The development of processes for the production of SNG from coal was initiated in the 1960s in the US, because of the raising demand of natural gas and the fear of natural gas shortage. As a result, several catalytic methanation processes based on fixed and fluidized-bed reactors were developed in the 1970-80s worldwide. Since then, numerous processes were not implemented at industrial scale and operating industrial plants were also decommissioned. Recent works include the development of catalytic

methanation processes starting from coal in the US in the 2000s after the increase of gas prices and the development of SNG production processes using biomass feedstocks [177].
Hence, the process review will focus on industrial catalytic methanation processes using coal as a feedstock and still implemented at present. Recent developments in the US will not be included, since they were probably undermined by the significant decrease of gas prices after the massive production of schist gas in past years. Recent demonstration units for the synthesis of SNG based on biomass feedstocks and using electrolytic H_2 will also be included.

1.3.3.1. TREMP™ process

The TREMP™ process was developed in the 1970-80s for the synthesis of SNG from coal and is commercialized by the Danish company Haldor Topsoe. It is schematically represented in Figure 1-16. A syngas feed with a H_2/CO ratio of 3:1 is fed to three adiabatic fixed-bed reactors in series with heat exchangers for intermediate cooling. The number of methanation reactors and process configuration can be adjusted depending on product application [174]. The temperature increases from 563 K up to 873 K in the first reactor, from 623 K up to 723 K in the second reactor, and from 523 K to 583 K in the third reactor [177].

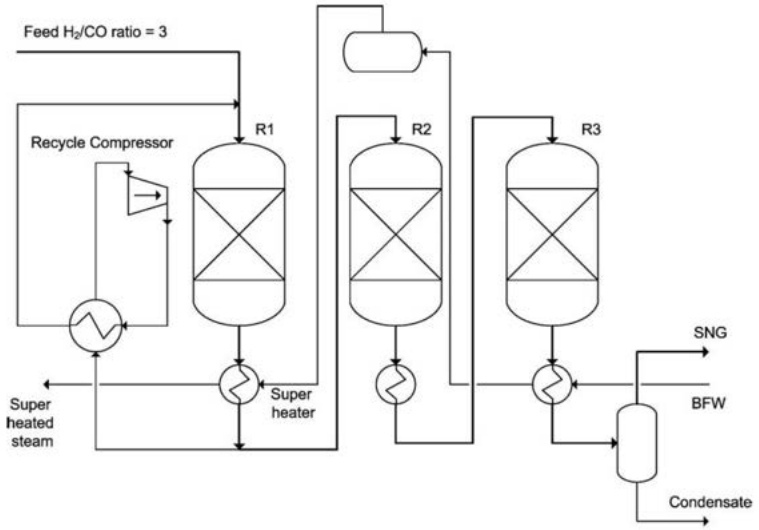


Figure 1-16: Process flow diagram of the TREMP process [177]

A significant part of the outlet gases of the first reactor is recycled to limit the temperature increase in the first reactor. The high temperature in the first reactor enables to produce high pressure superheated steam at 813 K and 100 bar. The process has been implemented on the largest single-train SNG plant worldwide in Qinghua, China, with a capacity[3] of approx. 0.18 million $Nm^3 \cdot h^{-1}$ SNG [174].

1.3.3.2. STORE&GO unit (Falkenhagen)

The CO_2 methanation unit of Falkenhagen is implemented on one of the three demonstration sites of the European project STORE&GO. The unit has a SNG capacity of 57 $Nm^3 \cdot h^{-1}$ with the following composition (>96% CH_4, >2% CO_2, <2% H_2) [34]. It is composed of two honeycomb reactors in series, which are operated in polytropic mode with a H_2/CO_2 ratio of 4:1 at temperatures in the range of 623-673 K and at 16 bar. A nickel based catalyst developed by the KIT is applied. The first reactor is composed of

[3] Assuming a unit operating 8000 $h \cdot year^{-1}$.

186 honeycomb tubes of 40 cm length and 8 cm diameter each, for a total reactor diameter of approx. 2 m, whereas the second reactor is composed only of 80 tubes. After the first reactor, the CO_2 conversion rate is about 70%, whereas it reaches 99.7% after the second reactor. Both reactors are cooled with oil, which is then cooled in turn by pressurized liquid water at 433 K and 16 bar provided by a saw mill not far from the site. The liquid water heated up to 453 K is then returned to the saw mill. The reactor preheating phase takes 24 hours and uses heat from the saw mill. The remaining heat required to reach operating temperature is provided by electrical heating of the reactor and of the reactor inlet and outlet pipes. The CO_2 is provided by a bioethanol plant and delivered per truck on-site[4].

1.3.3.3. AUDI e-gas unit (Werlte)

The CO_2 methanation unit of Werlte has been implemented in the frame of the Audi e-gas project [36]. The unit has a nominal CH_4 capacity of 310 $Nm^3 \cdot h^{-1}$, with a typical CH_4 content in the SNG of 93%. It is composed of a single multi-tubular reactor [188] operated at temperatures in the range of 473-523 K and at a pressure of 7.5 bar. The gases are fed at the top of the reactor and travel through tubes filled with a nickel-based catalyst down to the bottom of the reactor. The average temperature decreases from the top of the reactor at 523 K down to the bottom at 473 K. The reactor temperature is controlled using the sensible heat of molten salts [188], which are driven out of the reactor at 423-453 K. The cooling down of molten salts allows in turn to generate 600 kW of steam at 443-453 K, which is used afterwards for solvent regeneration in the amine unit of the biogas plant nearby. The CO_2 separated in the amine unit is used for the methanation process[5].

1.4. Feed gas production and gas treatment

A review of the process steps for feed gas production and gas treatment will be implemented in this subchapter. The feed gas production part will only consider the thermochemical conversion of solid biomass and waste to bio-syngas (a gas mixture of mostly H_2, CO and CO_2 comparable to syngas) through gasification. The reasons of this technological choice are detailed at the end of Chapter 1.1.4.1. Biomass conditioning and purification processes of the raw bio-syngas will be included. Furthermore, the biomass conditioning will be limited to the biomass drying process. The SNG upgrading will focus on the following steps: drying, compression, and liquefaction. It will also present the specifications required for the injection of SNG in the gas grid.

1.4.1. Thermochemical biomass conversion to bio-syngas

The thermochemical conversion of biomass to bio-syngas involves different steps. First, the biomass has to be conditioned, which means giving the biomass a shape adapted for the conversion (e.g. pellets) and drying it to reduce its water content. Only afterwards can the biomass be thermochemically converted into bio-syngas. The raw bio-syngas has then to be cleaned before the catalytic methanation process.

1.4.1.1. Biomass drying

Raw biomass feedstocks usually have a high moisture content up to more than 60%, which reduces the energy output obtained during their thermochemical conversion, since a part of their energy content is used for water vaporization. Not only can biomass drying increase the recovery of the biomass energy

[4] Source: Thyssen Krupp principal engineer in charge of the operation of the Falkenhagen methanation unit, 2019.

[5] Source: AUDI engineers and technicians in charge of the operation of the Werlte methanation unit, 2014.

content, but it also can help reducing the emissions of unburned solids, the size of the thermochemical equipment, and the process control issues related to biomass moisture fluctuations. It is nonetheless an energy intensive process. There are several types of dryers: rotary dryers, belt dryers, fluidized-bed dryers, and flash dryers. Several criteria have to be considered when choosing a dryer, mainly the size of the feedstock particles, the possibility for heat recovery, the risk of fire, the possibility of using steam, and the amount of air emitted. Design parameters and performance indicators for dryers include the evaporation rate, the drying temperature, the dryer capacity, the pressure drop, the inlet and outlet moisture, the particle size and the thermal requirements [189]. The heat required for the biomass drying process Q_{DRY} (in kW) can be evaluated using Equation (1.45), based on the considerations of [190], where $\dot{m}_{H2O,REM}$ refers to the water amount extracted from the biomass, c_{AIR} to the heat capacity of the air, $T_{AIR,HOT}$ and $T_{AIR,COLD}$ to the temperature of the hot air and the air supply respectively. The humidity of inlet and outlet air $X_{AIR,IN}$ and $X_{AIR,OUT}$ (in g·kg^{-1}) can be determined from a Mollier diagram.

$$Q_{DRY} = \frac{\dot{m}_{H2O,REM} \cdot c_{AIR} \cdot \left(T_{AIR,HOT} - T_{AIR,COLD}\right)}{\left(X_{AIR,IN} - X_{AIR,OUT}\right)} \quad (1.45)$$

1.4.1.2. Gasification

The first gasification technologies were developed in the 1930s in Germany as a key process step to produce the syngas required for coal liquefaction [175]. The gasification process takes place in a reactor at high temperatures in the range of 873-1273 K under the presence of an oxidizing agent, such as steam, oxygen, air, nitrogen, carbon dioxide or a mixture of these [191]. A catalyst can be used in addition. For biomass feedstocks, reactors usually operate at atmospheric pressure, nonetheless pressurized operation up to more than 30 bar have been reported [192]. During the process, the feedstock is converted into synthesis gas (a mixture of e.g. H_2, CO, CO_2, H_2O, CH_4), tar, char and ashes. It can be divided in the following steps [193].

- Drying: the water remaining in the feedstock evaporates using the heat released during the oxidation of gases, which takes place at 373-523 K;
- Pyrolysis: in the absence of oxygen, the volatiles decompose into gas, chars and tars from 473 K up to more than 673 K;
- Oxidation: heat is released during the oxidation of gases, volatiles and chars at 873-1173 K
- Reduction: the chars and tars release gases at 873-1223 K.

The chemical reactions generally involved in the gasification process include the steam reforming reaction (Equation (1.27)), the water gas shift reaction (Equation (1.29)), and the Boudouard reaction (Equation (1.30)) already mentioned in Chapter 1.3.1.1, as well as Equations (1.46) to (1.50) [191]. The pyrolysis reaction is depicted by Equation (1.46), the partial and complete oxidation reactions by Equations (1.47) and (1.48), the water gas reaction by Equation (1.49), and the hydrogasification reaction by Equation (1.50).

$$C_xH_yO_z \rightleftarrows aCO_2 + bH_2O + cCH_4 + dCO + cH_2 + fC_{2+} + char + tar \quad (1.46)$$

$$C_{(s)} + \frac{1}{2}O_2 \rightleftarrows CO \qquad \Delta_R H^0 = -111\ kJ \cdot mol^{-1} \quad (1.47)$$

$$C_{(s)} + O_2 \rightleftarrows CO_2 \qquad \Delta_R H^0 = -393\ kJ \cdot mol^{-1} \quad (1.48)$$

$$C_{(s)} + H_2O \rightleftarrows CO + H_2 \qquad \Delta_R H^0 = 131\ kJ \cdot mol^{-1} \quad (1.49)$$

$$C_{(s)} + 2H_2 \rightleftarrows CH_4 \qquad \Delta_R H^0 = -75\ kJ \cdot mol^{-1} \qquad (1.50)$$

Gasifier technologies can be divided into fixed-bed and fluidized-bed reactors. Fixed bed reactors can be of updraft or downdraft types (see Figure 1-17).

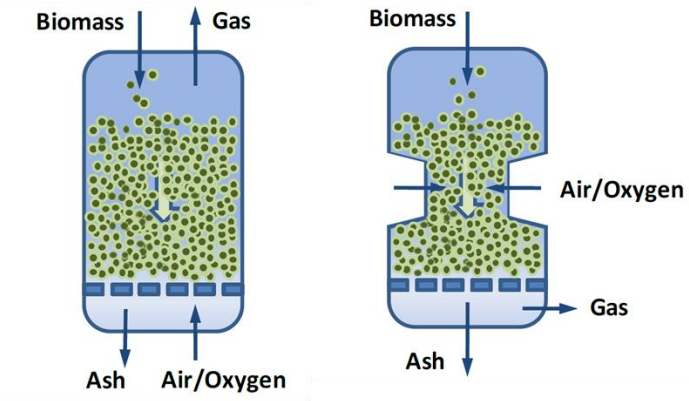


Figure 1-17: Schematic representation of updraft (a) and downdraft (b) fixed-bed gasification reactors [192]

In updraft or countercurrent gasifiers, the feedstock is fed at the top of the reactor, whereas the oxidizing agents are fed at the bottom of the reactor, so that both are moving in opposite directions. The product gases exit at the top of the reactor with a rather low temperature (773 K) leading to a consequent tar and methane formation. In the downdraft or concurrent gasifier, both feedstock and oxidizing agents are injected at the top of the reactor, so that the product gases exit at the bottom of the reactor at a much higher temperature (1073 K) which limits the formation of tars [191, 192].

Among the fluidized-bed reactors, the bubbling and circulating types can be mentioned (see Figure 1-18). In these gasifiers, the feedstock is injected at the bottom of the chamber and fluidized with the oxidizing agent, while the product gas is evacuated at the top. This ensures a good heat transfer quality to the feedstock particles and thus higher conversion rates and efficiencies. These reactors can operate with a wide range of fuel types and characteristics. However, the product gas contains more particulates [191]. In bubbling fluidized bed reactors, fluidizing medium such as alumina or silica materials are used, since they can operate at high temperatures and have a high specific heat capacity. Circulating fluidized-bed reactors have higher flow rates of fluidizing agents which bring the solid and unconverted particulates to a cyclone separator, where they can be separated and reinjected at the base of the gasifier [191, 192].

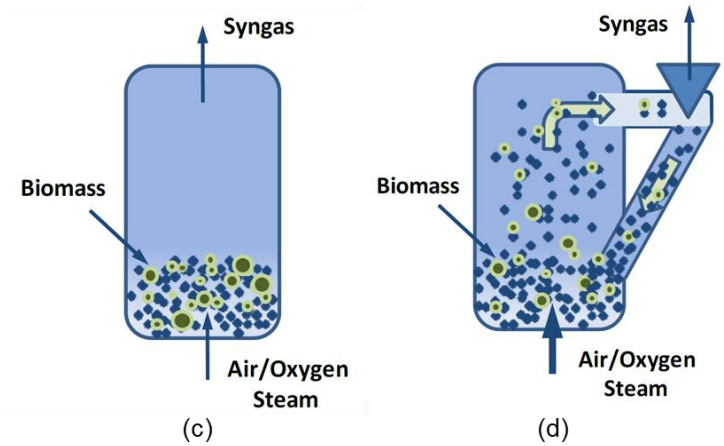


Figure 1-18: Schematic representation of bubbling (c) and circulating (d) fluidized-bed gasification reactors [192]

Other reactor technologies include entrained flow, dual-bed or plasma gasifiers [192]. Reactors can alternatively be sorted between directly and indirectly heated, depending if the heat required for the gasification process is generated in the gasification chamber or in a separated combustion chamber [191].

1.4.1.3. Bio-syngas purification

The purification of bio-syngas produced during the gasification process is required for further product use e.g. for power production, for the valorization of H_2 or CO as industrial feedstocks, or for further transformation steps into hydrocarbons [194]. In order to obtain a bio-syngas which will not damage the downstream equipment (e.g. the hydrogenation catalyst), so-called syngas contaminants have to be removed. They include tars, nitrogen based compounds (e.g. NH_3 or HCN), sulfur based compounds (e.g. H_2S or COS), hydrogen halides (e.g. HCl or HF) and metal traces (e.g. Na or K) [195]. Given the number of contaminants, a combination of processes rather than a single process is required for the treatment.

Biogas cleanup technologies can be divided into cold gas and hot gas technologies [195]. Cold gas technologies are usually implemented at room temperature and are based on the following processes.

- Wet processes, which remove contaminants by adsorption, absorption, filtration or a combination thereof and use for instance spray and wash towers, impingement and venturi scrubbers and wet electrostatic precipitators or cyclones. These are commonly applied because they allow the removal of multiple contaminants soluble in water. Oil based liquid scrubbing solvents belong to this category;
- Dry processes, which use mechanical, physical and electrostatic separation such as cyclones, adsorbing beds or other filters, or electrostatic precipitators.

As for hot gas technologies, they operate at temperatures above 573 K and apply catalysts or sorbents based for instance on alkaline earth metals, transition metals (such as iron, nickel, zinc, and copper), and zeolites.

Cold gas cleanup technologies are conventional and highly efficient solutions, however they require to cool down the bio-syngas, which reduces the efficiency of the overall bio-syngas synthesis process and generates additional costs for waste streams treatment. On the contrary, hot gas cleanup technologies are associated with a higher efficiency and a significant reduction of waste streams [195].

Several innovative processes for bio-syngas purification have been investigated in the past 15 years.

The OLGA process stands for oil-based gas washing and was developed by ECN in the Netherlands. It aims at removing tars from the bio-syngas using three columns in series: a collector where the heavy tars

are condensed, collected and reinjected in the gasifier, an absorber where light tars are absorbed by the oil, and a stripper, where the oil charged in light tars is regenerated with hot air [196].
The gasification plan of Güssing, Austria was implemented in the frame of the EU project Bio-SNG. The bio-syngas was cooled down and the tars separated with a rapeseed methyl ester (RME, a type of biodiesel) scrubber were recycled to the gasifier. Active carbon columns followed by zinc oxide columns were used to remove the sulfur contaminants [197].
In the frame of the GoBiGas (Gothenburg Biomass Gasification) project, the bio-syngas produced in the 20 MW gasifier is cooled down to 433-493 K. The particles are then removed in a textile bag filter and the tars are collected in a RME scrubber. The bio-syngas could be used for combustion purposes at this stage, however further treatments are required before methanation. First, the remaining tars are adsorbed in active carbon beds. Second, olefins are hydrogenated in a reactor. Third, sulfur and chloride based contaminants are removed in an amine unit. As a last step, the last contaminant traces are removed in a guard bed [198].
During the bioliq® process implemented at the KIT in Germany, the bio-syngas is treated at high pressure and temperature. After cooling down to 873 K, particulates and ashes are removed in a ceramic filter. Sulfur and chlorine based contaminants are then removed in sorption units, whereas other contaminants mostly the remaining tars and NH_3 are treated in a catalyst bed afterwards. A safeguard bed ensures that the required gas quality for downstream processes is respected [199].
At present, bio-syngas purification is one of the main drawbacks for the economic profitability of gasification projects [200]. To tackle this issue, the development of solutions adaptable to the wide variability of biomass compositions and contaminants concentration is crucial, as is the development of hot gas cleanup catalysts and sorbents with limited deactivation [201].

1.4.2. Synthetic natural gas upgrading

After the catalytic methanation process, the raw SNG has to be upgraded before use. Once upgraded, it is usually injected in the gas grid before valorization. In order to do so, the SNG has to respect the grid specifications for injection. Therefore, the main upgrading steps from catalytic methanation to SNG injection in the gas grid (e.g. drying and compression) will be presented, along with the requirements for SNG injection in France and Germany. In addition, two alternative additional steps for conditioning will be discussed: compression to obtain compressed natural gas (CNG) and liquefaction to obtain liquefied natural gas (LNG). Even though the odorization step will be shortly mentioned, it will not be considered in the following Chapters of this work because of its negligible energy consumption.

1.4.2.1. Drying

After methanation, the raw SNG has a high water content because considerable amounts of steam are formed during CO methanation and Sabatier reactions (one mole steam for each mole CO converted and two moles steam for each mole CO_2). However, catalytic methanation processes are run under pressure, so that a considerable amount of steam can be separated by cooling down the SNG and condensing the steam. Nonetheless, the steam partial pressure in the SNG is not low enough afterwards to make sure that the temperature will not go below the water dew point, which would result in water condensation on pipe walls and the formation of carbon or methane hydrates that can plug the equipments. Therefore, conventional drying processes must be applied, which have been depicted e.g. in [202].

- The most common one is tri-ethylene-glycol (TEG) drying, an absorption technique. The water-rich, high pressure gas enters a collector where water is absorbed by the TEG. The TEG is then regenerated in a second column with a reboiler.

- Another option is the adsorption of water by a solid desiccant, which can be a mole sieve, a silica gel or alumina. The process is based on two columns: when one column adsorbs the water, the solid desiccant is regenerated in the other one. Two process options are possible: temperature swing adsorption (TSA) and pressure swing adsorption (PSA). The idea is to modify the gas pressure or temperature to enable water adsorption or desorption from the solid desiccant, knowing that the number of adsorbed water molecules increases with the gas pressure and decreases with the gas temperature.

The process flow diagram of the TEG process and of the TSA process are represented in Figure 1-19. Other techniques not depicted here include condensation and supersonic separation.

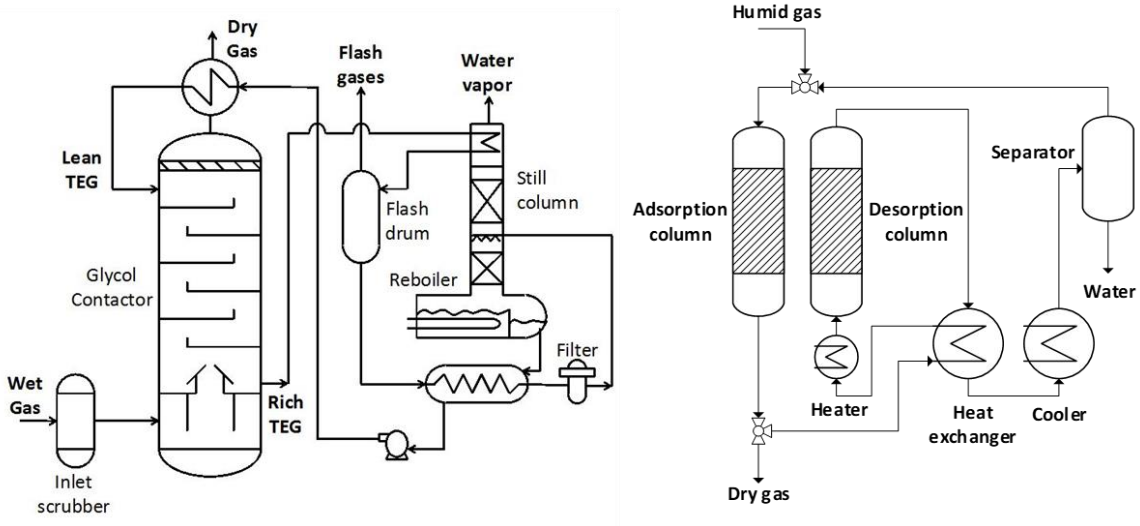


Figure 1-19: Process flow diagrams of the TEG (left) and the TSA (right) drying processes [202]

1.4.2.2. Grid requirements for SNG injection

The natural gas transported and distributed in the French or in the German networks has to comply with the specifications gathered in Table 1-7.

Table 1-7: Specifications of the natural gas in the German and the French networks [203-206], with MOP: maximal operating pressure, "-" not defined.

	Gas H or L (Germany)	Gas H (France)	Gas B (France)
Higher heating value ($kWh \cdot Nm^{-3}$)	8.4 – 13.1	10.7 – 12.8	9.5 – 10.5
Wobbe-Index ($kWh \cdot Nm^{-3}$)	11.0 – 15.7	13.6 – 15.7	12.0 – 13.1
Density ($kg \cdot Nm^{-3}$)	0.55 – 0.75	0.555 – 0.70	
CH_4 content (%-vol)	> 90 / 95 (L gas / H gas)	-	
H_2 content (%-vol)	< 2 (in CNG)	< 6	
CO_2 content (%-vol)	< 5 / 10 (H gas / L gas)	< 2.5 < 3.5 or < 11.5 (gas H or B, when allowed by the distributor)	
CO content (%-vol)	-	< 2	
H_2O dew point	< 200 $mg \cdot Nm^{-3}$ (MOP ≤ 10 bar) < 50 $mg \cdot Nm^{-3}$ (MOP > 10 bar)	< 268 K at the MOP of the network downstream	

The maximum H_2 content allowed in the SNG is significantly higher in France than in Germany, whereas the maximal CO_2 content is lower. More generally, specifications for injection in the gas grid are considerably different amongst EU countries. Hence, harmonization would be required. Before injection, gases other than natural gas have to be odorized. In France, a tetrahydrothiophene (THT) content of 15-40 mg·Nm^{-3} is added to the gas before injection [206], whereas a combination of different odorants for a cumulated minimum content of 27 mg·Nm^{-3} is required in Germany, as defined in the DVGW standard G 280 [207]. According to the operation pressure of the catalytic methanation and the pressure level of the gas network, a SNG compression step might be required before odorization to enable grid injection.

1.4.2.3. Compression (CNG production)

Once injected in the gas grid, the SNG has to be compressed in a CNG station to reach 250 bar. The usual pressure of the CNG used in vehicles is 200 bar, both in Germany and in France [208, 209]. Mechanical compressors are usually applied and the number of compression stages depends on the pressure level of the gas network the CNG station is connected to. Mechanical compressors can be operated with a maximum compression ratio of about six, where this ratio is the quotient between output and input pressure. The gas distribution network is usually operated at rather low pressures (e.g. 18 bar in Germany) and two mechanical stages are therefore required to reach 250 bar. The gas transportation network is operated at higher pressures (e.g. 80 bar), therefore one compression stage is usually sufficient. The SNG compression work W_{COMP} (in kW) can be calculated using Equation (1.51), which can also be applied for the determination of the compression work of other gases or gas mixtures.

$$W_{COMP} = \frac{\Upsilon}{(\Upsilon - 1)} \cdot \frac{\dot{n}_{GAS} \cdot Z \cdot R \cdot T_{IN}}{\eta_{ISEN} \cdot \eta_{MEC}} \cdot \left(\frac{p_{OUT}^{\frac{\Upsilon-1}{\Upsilon}}}{p_{IN}} - 1 \right) \quad (1.51)$$

Previous work estimated that CNG compression work reduced the power-to-SNG conversion efficiency by 0.8-1% [21, 38].

1.4.2.4. Liquefaction (LNG production)

After drying, the SNG can be also liquefied in a LNG unit. LNG is a product mostly composed of methane and stored at 111 K (-162 °C) and at atmospheric pressure. Typical unit sizes range from a few 1,000 t·year^{-1} up to several 100,000 t·year^{-1}. Several processes were developed. For instance, the Finish company Wärsilä proposes different units applicable for natural or biogas liquefaction depending on the required capacity [210]. Units in the range of 2,000-20,000 t·year^{-1} are based on a single stage process using a proprietary mix of hydrocarbons as cooling media with an energy consumption of minimum 0.7 kWh·kg^{-1} LNG. Larger units in the range of 20,000-300,000 t·year^{-1} are based on a Brayton cycle with nitrogen as cooling media. The company already has many references of small-scale liquefaction units. The feed gas requirements are high for conventional LNG processes, e.g. below 50 ppmv CO_2 and below 0.1 ppmv H_2O for LNG units in the range of 0.5-10+ Mt·year^{-1} based on the OSMR® process of the company LNG limited [211]. Nonetheless, smaller scale units have been developed, in which a CO_2 content in the feed gas of up to 5%-vol can be tolerated [212].

1.5. Conclusions of Chapter 1

In this first Chapter, the concept of power-to-SNG was introduced and the potential of power-to-SNG plants to contribute to the integration of renewable power sources, to the defossilization of the industry, to the decongestion of power grid, as well as to the full valorization of CO_2 content of biogenic feedstocks was presented. Nonetheless, power-to-SNG units are currently very expensive. First, because the CAPEX and OPEX of water electrolysis units are too high and represent the largest share of the power-to-SNG plant costs. Second, because electrical power prices are too high and gas prices too low. Third, because the power-to-SNG efficiency of units is currently too low.

In this context, SOE units seem like a promising alternative to alkaline and proton exchange membrane units integrated in installations at present. Indeed, they could significantly improve the efficiency of power-to-SNG plants and reduce electrical power costs, because of the improved thermal integration of processes, where the cooling steam of the catalytic methanation unit can be recovered for the SOE unit. Nonetheless, the potential for flexible SOE operation is less documented than the one of other electrolysis technologies. Consequently, a strong focus was made on previous technical and economic modelling work on the SOE technology. The main hypotheses and features of models were identified. In particular, static models for the thermal integration of the SOE unit in power-to-SNG plants and dynamic models for the coupling with renewable power sources were presented.

Among the different possibilities of carbon sources, it was decided to investigate in priority bio-syngas upgrading. This option shows more potential for process thermal integration and it was scarcely investigated in previous technical and economic works.

A technical review of the main technologies and processes that can be applied for the conversion of power and biomass into SNG was implemented. This included electrolysis technologies, catalytic methanation technologies, gasification technologies, biomass drying processes, bio-syngas treatment processes, and SNG upgrading processes. Here, the main physicochemical principles applied for the description of each process were depicted. The technologies were presented with their operating parameters, along with their integration in industrial process layouts. Based on previous considerations, only bio-syngas production processes were considered for feed gas synthesis.

In order to tackle the low efficiency of power-to-SNG plants at present, several innovative compressed natural gas (CNG) and liquefied natural gas (LNG) plant concepts for bio-syngas upgrading through steam electrolysis and catalytic methanation will be depicted and thoroughly investigated in Chapter 2. They will present the following main improvements compared to previous works. The plant concepts will consider a high number of features in terms of feedstock, technologies and products. They will enable the performance comparison of plants with integrated SOE units and plants with integrated low temperature electrolysis units. Their energy performance will be assessed based on process layouts with full thermal integration and compared to their maximum theoretical efficiency evaluated with pinch technology. Not only will the plants be evaluated on an energetic performance basis, but also on their environmental impact in terms of water requirements, cooling water requirements and carbon valorization. The detailed technical evaluation of several options for residual heat valorization will be provided, e.g. power production or coupling with a district heating network.

The intermittency of renewable power sources is expected to be absorbed by the electrolysis unit in power-to-SNG plants. Indeed, the SNG composition out of catalytic methanation units operated in

dynamic mode fluctuates significantly and the specifications for injection in the gas grid are difficult to meet. Therefore, it is crucial to understand in which measure SOE units can cope with the intermittency of renewable power sources and their behavior under fluctuating power loads has to be understood. Several dynamic models of SOE units were already reported. However, most of them are characterized by a high level of complexity and long calculation times, which makes the development of real time control strategies difficult. Hence, Chapter 3 will focus on the development of a 1D dynamic model of a SOE unit with fast calculation times, allowing the development of real time control strategies. The model will enable to investigate the thermal response of SOE units under fluctuating power load and to generate hydrogen production profiles, based upon which the downstream H_2 storage and catalytic methanation units will be dimensioned.

Cost evaluations of SNG produced in bio-syngas upgrading plants with integrated SOE units were scarcely reported so far. Hence, Chapter 4 will evaluate the SNG production cost of plant concepts modelled in Chapter 2. SOE costs represent the largest contribution to SNG production costs. It is therefore important to evaluate SOE costs and in which measure they can be reduced though mass production and large unit capacities. Previous cost evaluation models of SOE units did not report any analysis covering the entire production chain from powder to installed system and provide cost breakdowns simultaneously at cell, stack, and system level. Moreover, a limited amount of estimates for the CAPEX of large industrial SOE units in the range of 10-100 MW was reported. The SNG production costs evaluated in this work will consider power-to-SNG installations with integrated SOE units in this particular power range and will include a CAPEX evaluation of installed SOE systems starting from the oxide powders. The CAPEX of SOE units thermally coupled to catalytic methanation units will also be compared to the one of stand-alone SOE units to determine if significant cost savings can be achieved.

2. Energy assessment of power-to-SNG plants

Several innovative compressed natural gas (CNG) and liquefied natural gas (LNG) plant concepts for bio-syngas upgrading through steam electrolysis and catalytic methanation will be investigated in this chapter. First, the main indicators considered for the evaluation of plant performance will be defined. Then, the plant concepts will be detailed and their main technical features justified. The process models will be presented afterwards, along with the main assumptions made for process operation. The methodology applied for evaluation of plant performance will be detailed and applied to each plant concept. The plant concepts will be compared based on their conversion efficiencies and environmental impact. The calculated efficiency values will be verified and their coherence with previous literature work will be extensively discussed.

The results presented in this chapter are extended from preliminary work undertaken in [52] and in [9]. The corresponding plant concepts were investigated in the frame of the German public funded project Res2CNG [213]. A similar concept is currently investigated in the frame of the Danish project SYNFUEL [214], with the aim of implementing a proof-of-principle. However, no modelling work on power-to-LNG or power-to-CNG plants was reported in the frame of this project so far.

2.1. Plant performance indicators

Several indicators were used for the evaluation of plant performance. In this work, not only conversion efficiencies of plants from power to SNG products were considered, but also water requirements, cooling water requirements and valorization of biomass carbon content. These last three indicators were rarely considered in previous works.

Plant efficiencies η_{PtSNG} were determined using Equation (2.1), which corresponds to the energy content of methane (product of the flow rate $\dot{n}_{CH4}$ and of the heating value H^0_{CH4} of methane) and hydrogen (product of the flow rate $\dot{n}_{H2}$ and of the heating value H^0_{H2} of hydrogen, when the latter one is present in the end-products) divided by the sum of the energy content of biomass (product of the flow rate $\dot{n}_{BIO}$ and of the heating value H^0_{BIO} of biomass) and of all electrical power requirements of the plant. The latter includes the SOE power P_{EL} (in kW) taking into account the inverter efficiency η_{INV}, the power required for compression P_{COMP} (in kW), for electrical heating P_H (in kW), and for methane liquefaction P_{LIQ} (in kW), when relevant. In order to facilitate comparison with previous literature values, efficiencies were calculated both on a LHV and a HHV basis.

$$\eta_{PtSNG} = \frac{\dot{n}_{CH4} \cdot H^0_{CH4} + \dot{n}_{H2} \cdot H^0_{H2}}{\frac{P_{EL}}{\eta_{INV}} + P_{COMP} + P_{HEAT} + P_{LIQ} + \dot{n}_{BIO}\, H^0_{BIO}} \quad (2.1)$$

The valorization of the biomass carbon content was also considered and determined with Equation (2.2). It was thereby assumed that biomass is entirely converted into bio-syngas, which is why the carbon efficiency η_C is calculated as the ratio between the molar flow rate of valorized carbon (equal to the methane flow rate in the SNG) divided by the molar flow rate of carbon in the biomass feedstock (considered equal to the molar flow rate of carbon gases (CH_4, CO, CO_2 and C_2H_4) in the syngas (SG)).

Therefore, the value of this indicator corresponds to the reactant utilization of the carbon reactants during the catalytic methanation process, which is determined by considerations on the thermodynamic equilibrium in the catalytic methanation reactors.

$$\eta_C = \frac{\dot{n}_{CH4,SNG}}{\dot{n}_{CH4,SG} + \dot{n}_{CO,SG} + \dot{n}_{CO2,SG} + 2\,\dot{n}_{C2H4,SG}} \quad (2.2)$$

The cooling water requirements correspond to the water amount (in $kg \cdot s^{-1}$) required for thermal management of plant processes, amongst others for the removal of residual heat out of the power-to-SNG plant assuming identical CH_4 production capacities in all investigated plant concepts

The net water requirements correspond to the water amount (in $kg \cdot s^{-1}$) required by the power-to-SNG plant for all plant uses, assuming identical CH_4 production capacities in all investigated plant concepts. It comprises process water (e.g. for the gasification or the electrolysis unit) and cooling water for process thermal management (e.g. for heat exchangers, condensers, or the cooling system of catalytic methanation reactors).

2.2. Investigated plant concepts

All the plant concepts investigated in this work can be summarized in Figure 2-1. H_2 produced in the electrolysis unit is fed to the catalytic methanation unit, whereas O_2 produced in the electrolysis unit is fed to the gasification unit. Steam recovered from the exothermic catalytic methanation process is fed to the gasification unit and to the SOE unit.

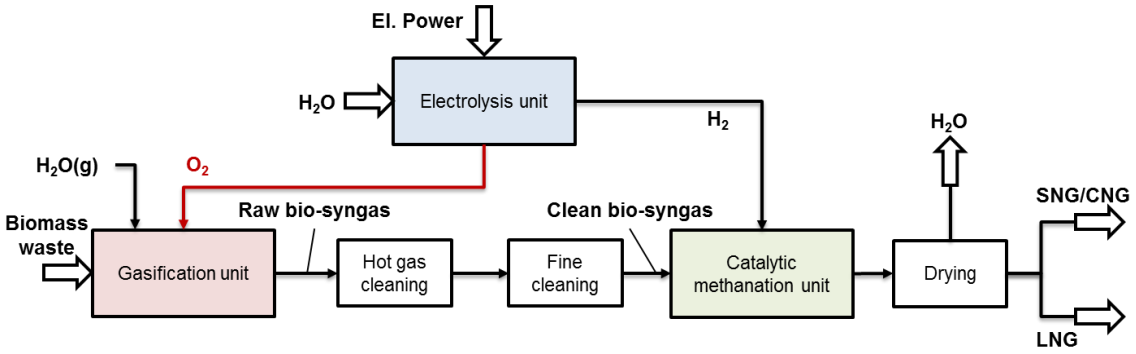


Figure 2-1: Schematic representation of investigated LNG or CNG plant concepts for bio-syngas upgrading [9]

The main plant features implemented in the three different power-to-SNG plant concepts investigated in this work are summarized in Figure 2-2. The proposed concepts aim at investigating various plant configurations with different biomass feedstocks, operating conditions, and technologies for the synthesis of different SNG products. A more detailed description of each plant concept is provided afterwards (see Chapters 2.2.1 to 2.2.3).

In plant concept 2 and 3, the catalytic methanation unit is composed by two reactors in series. Similar post-treatment processes and SNG compositions were obtained in plant concepts 1 and 2 to enable their comparison. All plant concepts were assumed to have the same capacity of 20 MW CH_4 (HHV based value).

2.2.1. Plant concept 1 – "Reference case"

This plant corresponds to the reference case configuration assumed for CNG production. All processes chosen correspond to state of the art ones, at the exception of the electrolysis technology, for which a PEM unit was preferred to an alkaline unit. The gasification process is operated at atmospheric pressure with wood as biomass feedstock. After cleaning, the bio-syngas is compressed in a two stage mechanical compressor up to 20 bar. The electrolytic H_2 and the bio-syngas are then injected in a methanation unit with four reactors in series based on the TREMP™ process [174], whose detailed description is provided in Chapter 1.3.3.1. The SNG produced at 20 bar is then dried and compressed up to 250 bar in a two stage mechanical compressor. It fulfills the standards required for injection in the German gas grid defined in the DVGW-Arbeitsblatt G 262 (specifications available in Chapter 1.4.2.2).

Plant concept	Biomass feedstock	Gasifier operating pressure	Syngas conditioning	Electrolysis unit	Catalytic methanation unit	SNG conditioning	End product
1) Reference case	Wood	1 bar	-Hot gas & fine cleaning -2 stage comp.	PEM 20 bar	Fixed bed 4 reactors (TREMP™ process)	2 stage comp.	CNG 250 bar
2) CNG chain	Wood	20 bar	-Hot gas & fine cleaning	SOE 20 bar	Three phase 1 reactor Honeycomb 1 reactor	2 stage comp.	CNG 250 bar
3) LNG chain	Mix Wood, straw, sewage sludge	20 bar	-Hot gas & fine cleaning	SOE 20 bar	Three phase 1 reactor Honeycomb 1 reactor	CH_4 liq. unit	LNG

Figure 2-2: Main plants features of the three power-to-SNG plant concepts investigated in this work, adapted from [9]

2.2.2. Plant concept 2 – "CNG production"

This concept corresponds to a prospective plant configuration for CNG production. The gasification unit operates at 20 bar and uses wood as feedstock. The raw, pressurized bio-syngas is cleaned at high temperature. The corresponding power requirements were neglected in the energy assessments. Electrolytic H_2 is produced in a SOE unit operated at 20 bar and is then reacted with bio-syngas in a two stage catalytic methanation unit, where the first reactor is a three-phase reactor and the second reactor a honeycomb reactor. More information on these methanation technologies can be found in Chapter 1.3.2. The SNG is dried and compressed up to 250 bar as in plant concept 1 and presents a similar final composition. Hence it also respects the standards required for injection in the German gas grid of the DVGW-Arbeitsblatt G 262 (specifications available in Chapter 1.4.2.2).

2.2.3. Plant concept 3 – "LNG production"

Plant concept 3 corresponds to a prospective plant for LNG production. A feedstock mix composed of wood, sewage sludge and straw in equal mass proportions is gasified at 20 bar. A hot gas cleaning process is applied for bio-syngas cleaning. As was done in the other plant concepts, the corresponding

energy requirements are neglected in the energy assessment. Here again, the electrolytic H_2 is produced in a SOE unit operated at 20 bar and the same catalytic methanation unit as in plant concept 2 is applied. The SNG is then dried and sent to a liquefaction unit for LNG production. The technical features of the liquefaction unit can be seen in Table 2-8.

2.3. Process modelling

In a first part, the fluid property package developed to calculate energy streams of plant processes will be depicted. Then, the sub-models used to simulate the behavior of each process involved in the power-to-SNG plant concepts will be presented. For each process, main modelling hypotheses and their operating conditions will be detailed. The sub-models were either integrated in a single MATLAB® script in the preliminary energy assessment (see Chapter 2.4.1) or implemented as block functions in Simulink® and connected with each other to simulate power-to-SNG plant behavior in the detailed energy assessment (see Chapter 2.4.2).

2.3.1. Fluid property package development

The following paragraph presents the fluid property package applied in this work. It was developed to determine enthalpy and entropy values of fluids or fluid mixtures in order to calculate energy streams and to implement the energy assessments of the plant concepts presented earlier. Even though several softwares or databases are available, such as the commercial software REFPROP of the National Institute for Standards and Technology (NIST) or as the free software CoolProp, the development of an in-house property package was preferred in this work.
In a first part, the methodology implemented for the determination of state functions will be detailed. In a second part, a secant method based solver developed to determine the temperature of a fluid for a given couple of enthalpy and pressure values (h, p) will be presented.

2.3.1.1. State functions

The first step identified for fluid property package development was the determination of mathematical functions of both temperature and pressure returning either enthalpy or entropy values for each fluid, as mentioned in Equation (2.3) for the enthalpy h. The determination of the enthalpy function will be presented hereafter, but the same method was followed for the entropy function s.

$$h = f(T, p) \tag{2.3}$$

The enthalpy functions were determined by interpolating enthalpy values publicly available in the Chemistry Webbook from the National Institute of Standards and Technology (NIST) [215]. A temperature delta of 5 K was chosen between two temperature values at a given pressure. For pressures higher than 1 bar, a pressure delta of 1 bar was chosen between two sets of temperature values, whereas a pressure delta of 0.1 bar was considered for pressures lower than 1 bar.
A first polynomial interpolation was done for each pressure value on the whole temperature domain. As a result, polynomial coefficients $a_{i,j}$ were obtained interpolating h as function of the temperature for each pressure value, as shown in Equation (2.4).

$$\begin{aligned} h_{0.1bar}(T) &= a_{0.1bar,m} \cdot T^m + a_{0.1bar,m-1} \cdot T^{m-1} + \cdots + a_{0.1bar,0} \\ h_{0.2bar}(T) &= a_{0.2bar,m} \cdot T^m + a_{0.2bar,m-1} \cdot T^{m-1} + \cdots + a_{0.2bar,0} \end{aligned} \tag{2.4}$$

$$\dots$$
$$h_{1bar}(T) = a_{1bar,m} \cdot T^m + a_{1bar,m-1} \cdot T^{m-1} + \dots + a_{1bar,0}$$
$$h_{2bar}(T) = a_{2bar,m} \cdot T^m + a_{2bar,m-1} \cdot T^{m-1} + \dots + a_{2bar,0}$$
$$\dots$$
$$h_{p_{max}}(T) = a_{p_{max},m} \cdot T^m + a_{p_{max},m-1} \cdot T^{m-1} + \dots + a_{p_{max},0}$$

A second interpolation of the $a_{i,j}$ coefficients on each pressure range was implemented to determine $b_{i,j}$ coefficients, allowing us to write the enthalpy as presented in Equation (2.5).

$$h(T,p) = {}^{T}\left(\begin{pmatrix} b_{m,n} & b_{m,n-1} & \dots & b_{m,0} \\ b_{m-1,n} & b_{m-1,n-1} & & \dots \\ \dots & \dots & & \dots \\ b_{0,n} & \dots & & b_{0,0} \end{pmatrix} \otimes \begin{pmatrix} p^n \\ p^{n-1} \\ \dots \\ \dots \\ 1 \end{pmatrix}\right) \otimes \begin{pmatrix} T^m \\ T^{m-1} \\ \dots \\ \dots \\ 1 \end{pmatrix} \quad (2.5)$$

The degree of interpolation was increased until reaching a sufficient precision for all fluids (maximal error of 0.3% for the interpolated points). As a result, a matrix with polynomial coefficients was obtained for each fluid. The validity domains and maximal errors between interpolating functions and NIST values obtained at the interpolated points for the different fluids are summarized in Appendix A.

2.3.1.2. Phase change

Dealing with the issue of phase change was critical to provide a satisfying precision of water enthalpy values. A first evaluation showed that the obtained precision was not sufficient when enthalpy of both liquid and gaseous phases were interpolated with one single function.

Hence, to reach a better precision, the enthalpy tables of water were split in two parts according to the different water states considered (liquid or gaseous). The interpolation of the temperature on each domain was then implemented using Shomate polynomials [215], which can be written as follows.

$$h(T) = A \cdot T^4 + B \cdot T^3 + C \cdot T^2 + D \cdot T + E + \frac{F}{T} \quad (2.6)$$

Instead of interpolating the enthalpy directly, the product of enthalpy and temperature was interpolated according to Equation (2.7).

$$g(T) = T \cdot h(T) = A \cdot T^5 + B \cdot T^4 + C \cdot T^3 + D \cdot T^2 + E \cdot T + F \quad (2.7)$$

The same steps presented earlier in Chapter 2.3.1.1 were followed to determine $g(T,p)$.
A last interpolation was then implemented to get the vaporization temperature T_{vap} as function of the pressure. According to the literature, the best results are given by the equation of Antoine [215] which is written in Equation (2.8), where A, B, and C are constants in Pa, Pa·K, and in K respectively.

$$log_{10}(p) = A - \frac{B}{T_{vap} + C} \quad (2.8)$$

With $T' = T_{vap} + C$, Equation (2.8) can be reformulated in Equation (2.9).

$$T' \cdot log_{10}(p) = A \cdot T' - B \quad (2.9)$$

The term $T' \cdot log_{10}(p)$ was then interpolated according to Equation (2.9) for pressure values between 0.05 bar and 22 bar, which enabled to determine the values of A and B. However, the maximal error obtained at the interpolated points was considered not acceptable (0.73%). In order to reduce it, the error was then interpolated using Equation (2.10). Here, a third degree polynomial was chosen for the interpolation after several attempts, because it proved to be the most suitable choice to fit to the error curve.

$$\epsilon(p) = b_3 \cdot log^3(p) + b_2 \cdot log^2(p) + b_1 \cdot log(p) + b_0 \quad (2.10)$$

Hence, the vaporization temperature T_{vap} could be written as Equation (2.11).

$$T_{vap}(p) = f(p) + \epsilon(p) \quad (2.11)$$

As a result, a maximal error of 0.0094% was obtained for the interpolated points.

2.3.1.3. Solver choice and description

The implementation of a solver was required to enable the determination of the temperature of a fluid or a fluid mixture starting from a couple of state function value (either entropy or enthalpy) and pressure value. Indeed, the degree of the polynomials used for the interpolation of NIST data was too high to use conventional resolution methods usually applied to find polynomials roots. Hence, numerical methods were required. In this work, a solver based on the secant method was chosen. Even though other methods exist, e.g. the Newton method, the secant method was selected because it is particularly adapted to situations where two initial values are at opposite sides of the root [216]. This was a perfect match with our working case, because it was easy to identify a temperature interval in which the solution would be located. A description of the secant method is provided in Appendix A.

2.3.2. Electrolysis

The operating parameters and the models implemented for the description of the electrolysis technologies used in this dissertation will be presented afterwards. A first part will focus on the description of the SOE unit model used in plant concepts 2 and 3, whereas a second part will present the PEM unit model applied in plant concept 1.

2.3.2.1. SOE unit model

The model chosen to depict the SOE unit behavior in this Chapter is a static 0D model. This type of model was already used many times in previous work (see Chapter 1.2.6.1). It presents the advantage of limited computational time and is perfectly adapted to system modelling in permanent regime, where the accurate description of the internal behavior of SOE stacks is not crucial.

Here, the SOE unit is assumed to operate in steam electrolysis mode, where the steam electrolysis reaction can be found in Equation (1.2) in Chapter 1.2.1. As a consequence, the OCV can be calculated with the partial pressure of the gases and the temperature with Equation (1.6) (see Chapter 1.2.2.1). Assuming that SOECs are operated in the linear domain of the I-V curve, Equation (1.11) introduced in Chapter 1.2.2.4 is valid and Equation (2.12) can be derived.

$$j = \frac{E_N}{2 \cdot ASR} + \sqrt{\frac{P_{CELL}}{S \cdot ASR} + \left(\frac{E_N}{2 \cdot ASR}\right)^2} \quad (2.12)$$

The stack ASR is expressed as a function of the temperature following Equation (2.13), based on previous experimental work on cathode supported cells (CSCs) by Fu et al. [12] and Petipas et al. [38]. The stack behavior is extrapolated from the cell behavior assuming that the integration of SOECs in a stack induce a constant additional ASR contribution of 0.1, and that all cells in the stack present the same behavior [38].

$$ASR(T) = exp^{\frac{4900}{T} - 5.95} + 0.1 \quad (2.13)$$

Previous experimental work on SOE cells and stacks have confirmed the OCV increase related to pressurized operation vs. atmospheric operation. However, the impact of pressurized operation on cell voltage depends on the operating conditions, mostly on the current density [70, 93-95, 217].

According to thermodynamics, pressurized operation results in an increase of operating cell voltage, since the reaction enthalpy of the electrolysis reaction increases. Indeed, at 1073 K, the reaction enthalpy of the electrolysis reaction increases from 248.3 to 248.5 kJ·mol^{-1} when the pressure raises from 1 bar to 20 bar and the thermoneutral voltage subsequently increases from 1.286 to 1.288 V.

However, experimental works on CSCs at cell [95, 218] and stack level [94] show that this effect can be partially or completely compensated by improved reaction kinetics (e.g. for current densities above approx. -0.3 A·cm^{-2} in [94, 218] and in the range of approx. -0.6 to -1.2 A·cm^{-2} in [95]). The main reasons for this are the increased probability of reactant collision with a three phase boundary and the lower diffusion resistance [217]. Higher current densities above -1.2 A·cm^{-2} can even result in a lower operation voltage than at atmospheric pressure [95]. As the CSCs modelled in this work show intermediate current densities at thermoneutral voltage (see Table 2-1), it was assumed that pressurized operation at 20 bar would have no influence on their thermoneutral voltage.

As for ESCs, less results are available. Riedel et al. implemented pressurized tests with short stacks from 1.4 to 8.8 bar, where current densities up to -0.5 or -0.6 A.cm^{-2} resulted in operation voltages slightly higher than at atmospheric pressure [219, 220]. However, these were done at relatively low current densities and no results on the impact of higher current densities on pressurized ESCs were reported so far. It is nonetheless likely that an increase of performance should be observed, as was observed for CSCs, but for very high current densities, because of the thicker electrolyte. Since the ESCs modelled in Chapter 4 operate at current densities significantly higher than in [219, 220], it was considered that the benefits of improved kinetics would offset the penalty related to thermodynamics. Hence, the pressurized operation at 20 bar was assumed to have no influence on the thermoneutral voltage of ESCs.

The cell power P_{CELL} (in kW) can be determined with Equation (2.14), which corresponds to the energy balance of one cell integrated in a SOE stack (assuming all cells in the stack exhibit the same behavior). This energy balance is verified at the operating point where the stack ohmic losses per cell match the heat requirements of the steam electrolysis reaction, e.g. for which the inlet and outlet gas temperatures of the stack are identical.

$$P_{CELL} + P_{GAS,IN} - P_{REAC} - P_{LOSSES} - P_{GAS,OUT} = 0 \quad (2.14)$$

The energy balance can be closed by determining the inlet and outlet gas flow rates (H_2, O_2 and steam) in a cell using the Faraday law of electrolysis already presented in Equation (1.10) in Chapter 1.2.2.3 and assuming a 100% Faraday efficiency. The stacks are assumed to be integrated in hot boxes, as was depicted in Chapter 1.2.5.3. The stack thermal losses P_{LOSSES} per cell to the environment were determined

with Equation (2.15) derived from Fourier's law, where the thermal conductivity λ (in $W \cdot m^{-1} \cdot K^{-1}$) correspond to the average value in the insulant layer, assuming a linear temperature profile in the insulant, with T_{Stack} the stack temperature, and T_{AMB} the ambient temperature equal to 298 K. Here, a thickness $e = 5\ cm$ of the insulation material Microtherm® was assumed. Based on the work of Apfel et al. in [221], its thermal conductivity can be expressed as function of the temperature with Equation (2.16).

$$P_{LOSSES} = \frac{\lambda \cdot S \cdot (T_{Stack} - T_{AMB})}{e} \quad (2.15)$$

$$\lambda(T) = 2.09 \cdot 10^{-2} - 4.07 \cdot 10^{-6} \cdot T + 1.30 \cdot 10^{-8} \cdot T^2 \quad (2.16)$$

The electrical power per cell was determined by successive iterations of the routine depicted in Figure 2-3. This routine solves a nonlinear equation to calculate the electrical power per cell that has to be injected in the stack in order to have the same gas temperature at the inlet and the outlet of the stack.

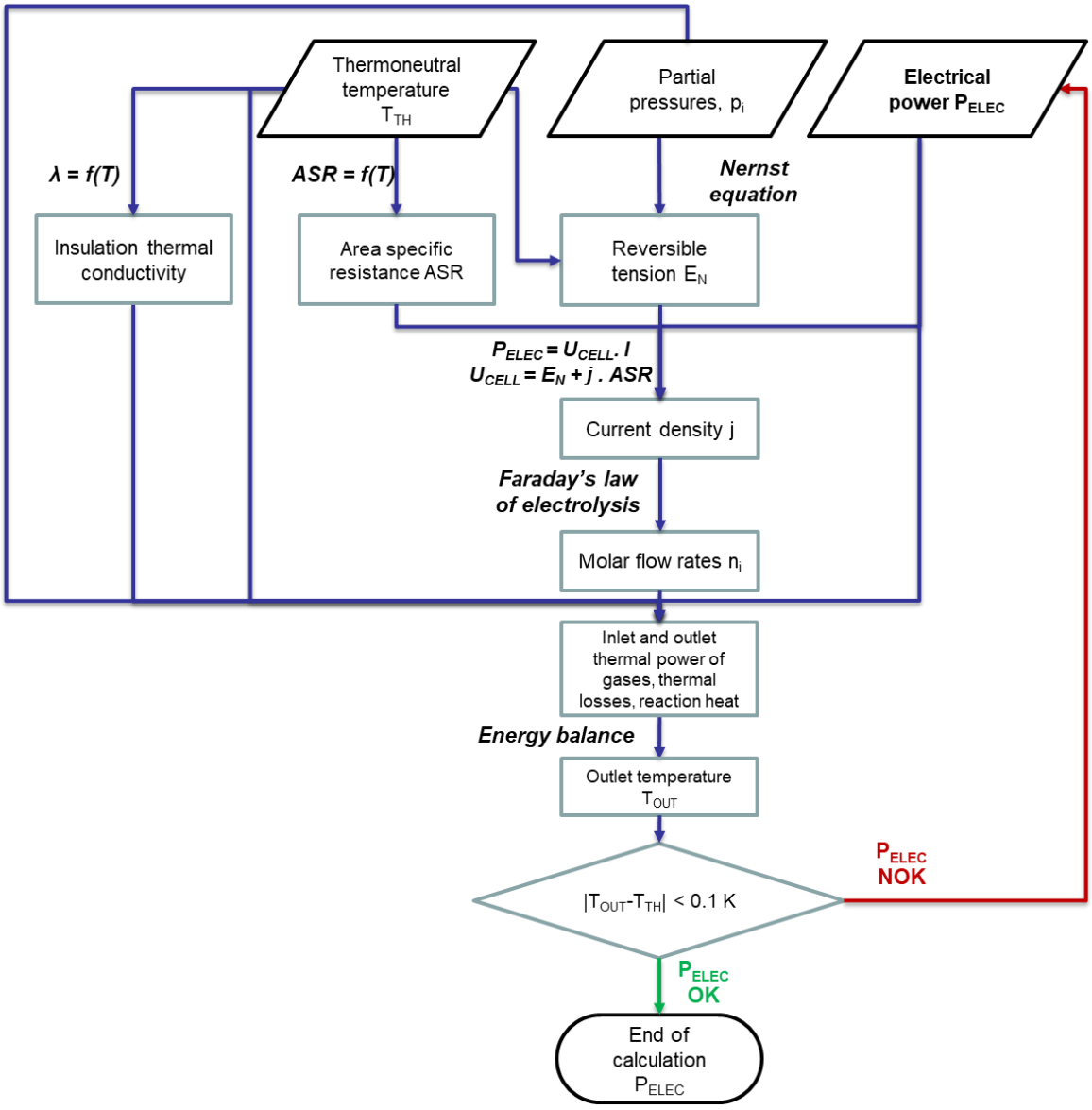


Figure 2-3: Flowchart describing the determination of the electrical power injected in the SOE stack

This MATLAB model was improved in an iterative algorithm to enable SOE operation in endothermic or in exothermic mode, as well as in partial load [222]. The algorithm presented a similar architecture to the work of Petipas et al. [38] and was also based on the cell experimental work of Fu et al. [12]. However, it additionally enables the modelling of pressurized SOE units, whereas the model of Petipas et al. only focused on the operation at atmospheric pressure. In addition, SOE energy balances were calculated based on the enthalpy of fluids and not on their thermal capacity and took into account the partial pressure of fluids, which resulted in a higher precision. A detailed flowchart of the improved model can be found in Figure A-2 in Appendix A.

The main operating parameters of the SOE unit are gathered in Table 2-1. The unit is operated at 20 bar and at 1073 K in steam electrolysis mode. Pure O_2 is produced at the anode and fed to the gasification unit. A reactant utilization of 80% was assumed, which is coherent with assumptions made in previous modelling work [38, 45, 108] and with current stack manufacturer's values [96]. The operation voltage, current density, and cell power were determined using the iterative approach detailed in Figure 2-3, assuming an active cell area of 128 cm^2. The high current density values considered are coherent with values reported for electrode supported cells in previous experimental work [223, 224]. The cells are operated in slightly exothermic mode (1.32 V against 1.29 V in thermoneutral mode at 1073 K and 20 bar), as is the case for cells implemented in SOE units at present [55].

Table 2-1: Main operating parameters of the SOE unit [9]

Parameter	Unit	Value
Cell power	W	142
Operating temperature	K	1073
Operating pressure	bar	20
Reactant (steam) utilization	%	80
Cell operating voltage	V	1.32
Current density	$A \cdot cm^{-2}$	-0.84
Electrical consumption (stack+inverter only)	$kWh \cdot Nm^{-3}$ H_2	3.3 (3.2+0.1)

The SOE electric consumption is 3.3 $kWh \cdot Nm^{-3}$ H_2, which corresponds to an efficiency of about 91% LHV and 108% HHV. The low electrical consumption can mostly be explained by the recovery of the cooling steam in the catalytic methanation unit, which enables to spare the electric work normally required for steam vaporization in case of a stand-alone SOE unit. Similar values of electrical consumption were already reported for SOE units thermally coupled with catalytic methanation units, e.g. in [45]. Furthermore, this value only includes the electrical consumption of the SOE stack and the inverter (the latter supposed to have an efficiency of 96%, value based on manufacturer data from demonstration projects). The electrical work of the heaters was not included in this value to avoid double counting, as it is already included in the pinch analysis of the plant concepts or calculated separately in the detailed process layouts of investigated plant concepts (see Chapter 2.5 and Chapter 2.6 respectively). The electrical consumption of the water pump was neglected, as it is small compared to other electrical contributions. Pure oxygen is produced at the anode, hence no air sweep system is required and the corresponding compression work is not required. Moreover, no H_2 drying step was assumed before injection in the catalytic methanation unit, since the methanation process is dimensioned to enable the presence of steam in the bio-syngas injected in the reactors (up to 10 wt%).

2.3.2.2. PEM electrolysis unit model

The PEM electrolysis technology operates with liquid water according to the water electrolysis reaction in Equation (1.1). The behavior of the PEM stacks was simulated with a 0D model based on the algorithm depicted in Figure 2-4. This algorithm solves a nonlinear equation to determine the water to H_2 conversion rate per pass r in the PEM unit for which the targeted temperature increase in the PEM stack ΔT_{MAX} is satisfied. Once r is determined, all inlet and outlet mass flow rates and thermal power of the PEM unit are calculated.

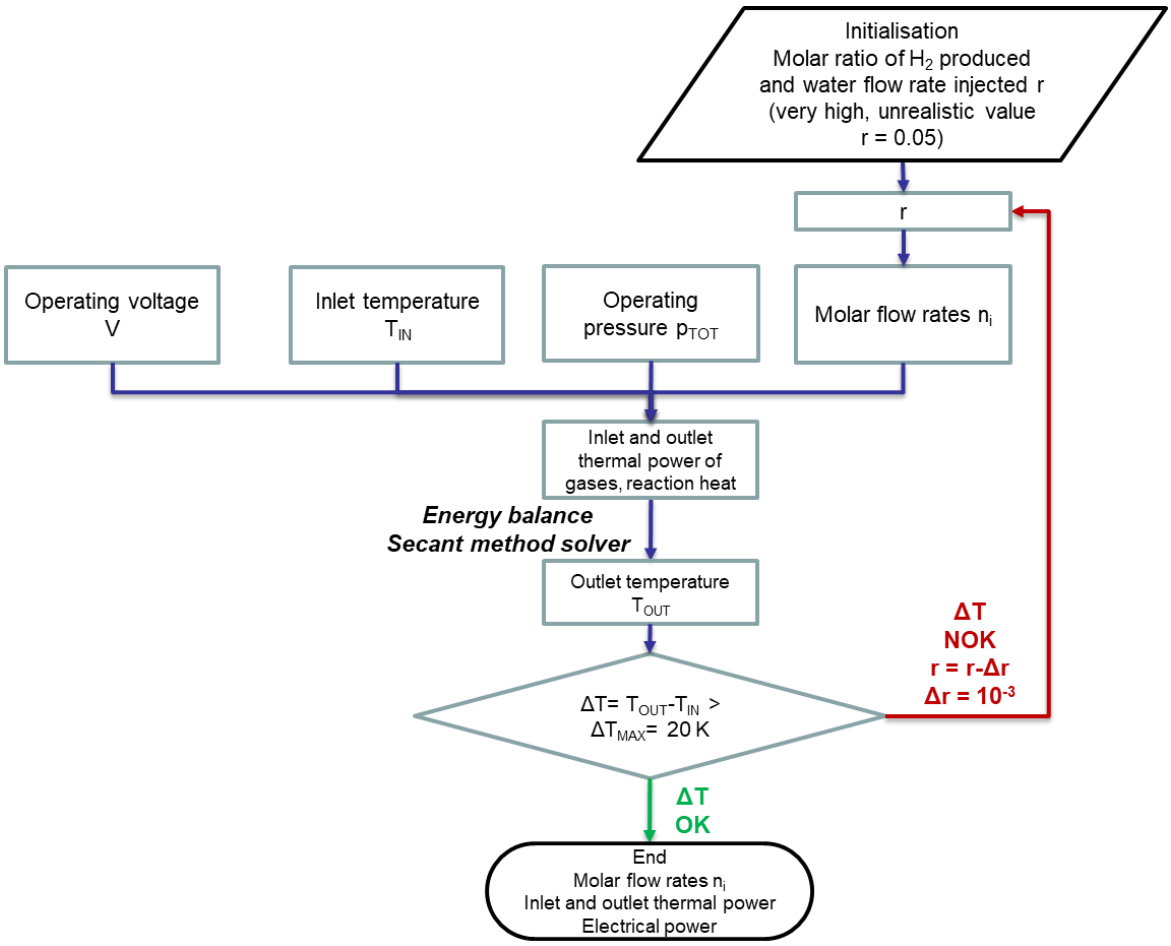


Figure 2-4: Flowchart of the algorithm applied for the determination of the mass and energy streams of the PEM unit

The operating parameters of the PEM electrolysis unit are summarized in Table 2-2.

Table 2-2: Main operating parameters of the PEM electrolysis unit [9]

Parameter	Unit	Value
Operating voltage	V	1.8
Current density	$A \cdot cm^{-2}$	-1.2
Inlet temperature	K	323
Outlet temperature	K	343
Operating pressure	bar	20
Electrical consumption (stack+inverter)	$kWh \cdot Nm^{-3}$ H_2	4.5 (4.3+0.2)

The PEM electrical consumption is 4.5 kWh·Nm^{-3} H_2, which corresponds to an efficiency of about 67% LHV and 79% HHV. It is in the range of present catalog values of PEM unit manufacturers, e.g. from 4.4 to 4.8 kWh·Nm^{-3} in [225]. This electrical consumption value is in the lower range of the interval, because it only includes the consumption of the stack and the inverter but not other BoP components such as the pumps and the H_2 purification step, as is done in [225]. The purification step enables to reach a high H_2 purity (slightly lower than 5.0) usually required for mobility or industrial applications, e.g. in fuel cells. However, the H_2 used in a catalytic methanation reactor does not require such a high purity level and the purity level reached before purification is usually sufficient, which was confirmed by PEM manufacturers. Hence, no H_2 drying step was assumed in this work. Furthermore, the same assumptions than for the SOE unit were made regarding the electrical consumption of the inverter, the heaters, the pumps and the air sweep system (see Chapter 2.3.2.1).

2.3.3. Catalytic methanation

The catalytic methanation units considered in this work will be presented afterwards. In a first part, the principles applied for reactor modelling will be detailed, along with the main operation parameters selected for each reactor technology. The second and third parts will focus on process layouts of the catalytic methanation units implemented in each plant concept. The unit layouts and the reactor outlet gas compositions were determined by the DVGW-EBI and used in this work to determine and verify mass and energy balances for each reactor. More details on the elaboration of unit layouts can be found in [11].

2.3.3.1. Reactor modelling

Reactor simulations were run assuming thermodynamic equilibrium, where the equilibrium was determined based on the CO methanation, the Sabatier, and the water gas shift reactions (Equations (1.27), (1.28), and (1.29) introduced in Chapter 1.3.1.1). Mass and energy balances were then exported and integrated to the full thermal integrated Simulink® model. Three different types of catalytic methanation reactors were modelled and the parameters selected for operation are summarized in Table 2-3. It was assumed for all technologies that the considerable amounts of heat produced during the methanation reaction would be recovered using steam as a cooling medium. The reactant utilization of the catalytic methanation units were tuned to obtain similar SNG product compositions in all plant concepts.

Table 2-3: Main technical features of the catalytic methanation technologies modelled in this work [9]

Parameter	Unit	Three-Phase	Honeycomb	Fixed-bed
Inlet temperature	K	593	538	533-573
Outlet temperature	K	593	563	618-923
Operating mode	-	isothermal	polytropic	adiabatic
Operating pressure	bar	20	20	20
Cooling steam	bar	20	20	20

2.3.3.2. Plant concept 1

In plant concept 1, the fixed-bed technology was applied for the catalytic methanation unit, as this technology corresponds to the state of the art. Based on thermodynamic equilibrium considerations, a total of four reactors operated adiabatically had to be disposed in series to respect the specifications for grid injection (see Chapter 1.4.2.2). A process unit similar to the one of the TREMP™ process from the company Haldor Topsoe was selected [29, 174]. It is represented in Figure 2-5. Temperature and

pressure levels, as well as conversion rates of carbon monoxide and carbon dioxide are provided for each reactor. A rather low steam pressure of 20 bar was chosen for the intermediate cooling of the methanation reactors. As was suggested in [29], higher steam pressures such as 60 bar should be favored in order to produce steam at higher temperature given the high outlet temperatures of the outlet gases (up to 923 K) in reactor 1. Nonetheless, a lower cooling steam pressure was chosen here in order to limit costs related to expensive high pressure equipment. The consequences of this choice on plant efficiency will be discussed in Chapter 2.5.1. As was done in the TREMP™ process, a recycling loop was implemented on the first reactor in order to increase the conversion rate of reactants. In this work, a recycle ratio of 1.86 was chosen. Using the process layout of Figure 2-5 and the bio-syngas compositions provided in Chapter 2.3.4.2, the heat generated during the catalytic methanation reaction amounts to 0.19 $kWh \cdot kWh^{-1}$ CH_4 (based on the HHV of CH_4).

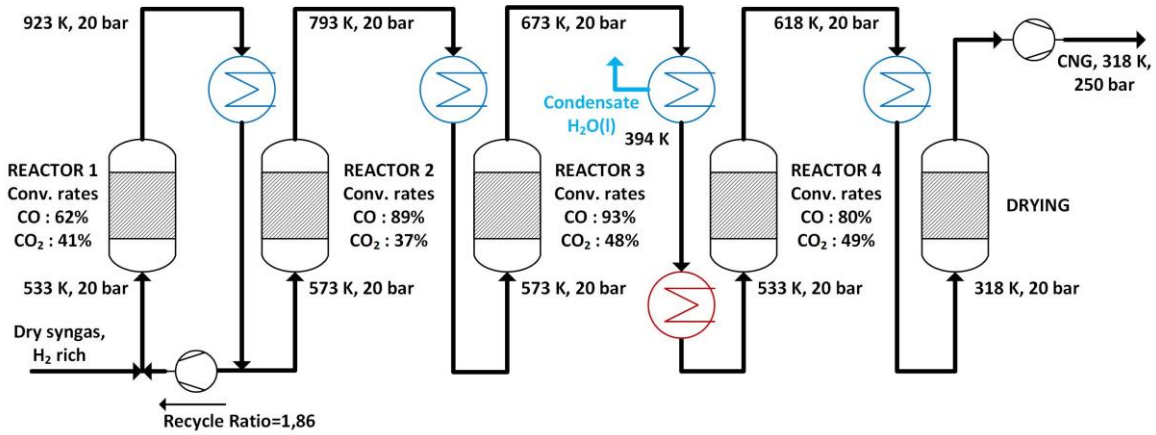


Figure 2-5: Process layout of the four stage catalytic methanation unit of plant concept 1, adapted from [11]

2.3.3.3. Plant concepts 2 and 3

In concepts 2 and 3, a two stage methanation process was implemented. A first reactor based on the three-phase technology and a second reactor based on the honeycomb technology were disposed in series. The first reactor was assumed to be operated isothermally, whereas the second one was assumed to operate in polytropic mode. The catalytic methanation unit is shown in Figure 2-6, in which the oil and steam cooling system are also represented. The energy consumption related to the recirculation of the condensed oil in reactor 1 and to the cooling oil in reactor 2 are low compared to the electrical consumption or the heat duties of other plant components. Hence, they were neglected in the energy assessment. Furthermore, only a small amount of oil is vaporized in the SNG in reactor 1. Therefore, the heat exchanged for its condensation and recycling to the reactor 1 is low. As a result, the corresponding heat exchanger was not represented in the detailed plant layouts in Chapter 2.6.1, the heat duty of the heat exchanger was neglected in the energy assessment and so were the corresponding costs in the SNG cost evaluation of Chapter 4. Moreover, the thermal losses during steam generation with the cooling oil in reactor 2 were neglected. Hence, this heat transfer did not have any impact on the energy assessment and the corresponding heat exchanger was also not represented in the detailed plant layouts.

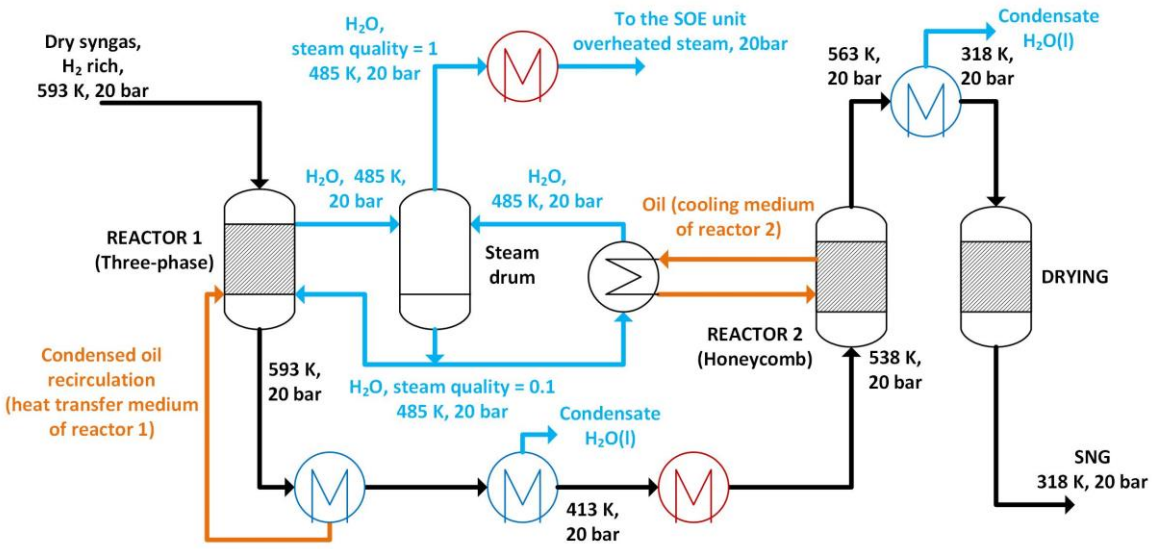


Figure 2-6: Process layout of the two stage catalytic methanation unit of plant concept 2 and 3, adapted from [11]

Using the parameters of Figure 2-6 and the bio-syngas compositions provided in Chapter 2.3.4.2, the heat produced during the methanation reaction amounts to 0.16 kWh·kWh^{-1} CH_4 (based on the HHV of CH_4) in both plant concept 2 and 3. This value is slightly lower than in plant concept 1, because of the lower operation temperatures in the reactors and the lower CO and CO_2 concentrations in the bio-syngas in plant concepts 2 and 3. Indeed, the pressurized operation of the gasification unit favors CH_4 formation and lowers the concentration of CO_2 and CO in the bio-syngas.

2.3.4. Thermochemical biomass conversion in bio-syngas

2.3.4.1. Biomass drying

The heat duty required for the biomass drying process was evaluated using Equation (1.45), based on the considerations of [190]. The parameters chosen for modelling the biomass drying process are gathered in Table 2-4.

Table 2-4: Main parameters of the biomass drying process [9]

Parameter	Unit	Value	Source
Admission air temperature	K	298	Authors hypothesis
Inlet air temperature	K	423	Authors hypothesis
Outlet air and biomass temperature	K	338	Authors hypothesis
Extracted water amount	kg·s^{-1}	0.23-0.24	Authors hypothesis
Inlet humidity	g·kg^{-1} (H_2O)	10	Authors hypothesis
Outlet humidity (incl. losses)	g·kg^{-1} (H_2O)	37.5	Mollier diagram
Biomass heating losses	kW	10% of the vaporization heat	[190]
Dryer heat losses	kW	10% of the vaporization heat	[190]

2.3.4.2. Gasification

An autothermal steam and O_2 single bed gasification process was considered in all plant concepts (see Chapter 1.4.1.2 for technology description). The gasification of the different feedstocks was modelled in Aspen Plus®. In the model, the biomass is decomposed into its elements C, H, O, N, S, Cl according to the respective elemental analyses of the fuels [226], which are then converted into syngas in two model stages. In a non-equilibrium stage, the syngas components CH_4, C_2H_4 and impurities (tar=$C_{10}H_8$, NH_3, HCl, H_2S) are produced with fixed yields (RYield block in Aspen Plus®) according to technical scale experiments [226]. In a second stage, the remaining elements are converted into syngas following the thermodynamic equilibrium (Rgibbs block in Aspen Plus®). The CO methanation reaction and the water gas shift reaction (Equations (1.27) and (1.29) respectively) were considered for the determination of the thermodynamic equilibrium. The oxygen requirements for the autothermal gasifier operation are determined with an energy balance. The mass balances of each plant concept were determined by the IFK and are gathered in Table 2-5. They were determined starting from compositions of different biomass substrates reported in [226], in the frame of gasification experiments on biological waste valorization at lab and pilot scale [226-228]. It was thereby assumed that char is fully converted to syngas.

Table 2-5: Mass balances of the gasification process with biomass compositions for all plant concepts, with "<<" negligible flow rate [9].

		Plant concept 1		**Plant concept 2**		**Plant concept 3**	
Mass flow rate		**Inlet ($kg \cdot s^{-1}$)**	**Outlet ($kg \cdot s^{-1}$)**	**Inlet ($kg \cdot s^{-1}$)**	**Outlet ($kg \cdot s^{-1}$)**	**Inlet ($kg \cdot s^{-1}$)**	**Outlet ($kg \cdot s^{-1}$)**
Biomass (dry, no ashes)	C	0.2791	-	0.2783	-	0.2797	-
	H	0.0320	-	0.0319	-	0.0348	-
	O	0.2314	-	0.2308	-	0.2231	-
	N	-	-	-	-	0.0108	-
	S	-	-	-	-	0.0032	-
	Cl	-	-	-	-	0.0012	-
	Total	0.5425	-	0.5410		0.5527	-
Ashes		<<	<<	<<	<<	0.1217	0.1217
H_2O		0.4183	0.3325	0.4171	0.3290	0.4353	0.3691
O_2		0.1736	-	0.1315	-	0.1658	-
H_2		-	0.0294	-	0.0183	-	0.0184
CO		-	0.2535	-	0.1650	-	0.1547
CO_2		-	0.4623	-	0.4758	-	0.4943
CH_4		-	0.0400	-	0.0848	-	0.0850
C_2H_4		-	0.0138	-	0.0138	-	0.0132
N_2		-	-	-	-	-	0.0095
Impurities		-	0.0023	-	0.0023	-	0.0037
Sum		1.1344	1.1338	1.0896	1.0891	1.2755	1.2696

Obtained mass and energy balances were then exported to the full thermal integrated Simulink® model for the simulation of the power-to-SNG plants. The operating parameters selected for the gasification process are gathered in Table 2-6. The gasification unit is operated at atmospheric pressure in plant concept 1, which corresponds to the state of the art of biomass gasification processes, whereas pressurized operation at 20 bar was assumed in plant concept 2 and 3.

Table 2-6: Main process parameters of the steam and oxygen assisted single bed gasification process [9]

Parameter	Unit	Value
Biomass feed temperature	K	298
Steam inlet temperature	K	973
Oxygen inlet temperature	K	1073
Gasification temperature	K	1123
Bio-syngas temperature	K	1123
Operating pressure	bar	1 (concept 1) 20 (concept 2 & 3)

2.3.4.3. Bio-syngas purification

Two process chains were selected for the bio-syngas cleaning unit. In plant concept 1, the bio-syngas was first injected into a dibenzyltoluene (DBT) cleaning unit for ashes removal at high temperatures. The fine particles remaining in the bio-syngas were then removed in a rapeseed methyl ester (RME) cleaning unit or biodiesel unit. As a last step, pollutants such as hydrogen sulfide (H_2S) were then removed in a zinc oxide (ZnO) column. As for plant concept 2 and 3, the bio-syngas cleaning was assumed to take place first in a DBT cleaning unit, second in an active carbon unit and third in a ZnO column. More details on the elaboration of the technologies and the process chains can be found in [11].

Each gas cleaning process was implemented in the power-to-SNG model as a black-box model. The operating parameters for each technology are summarized in Table 2-7. As they are significantly lower than the electrical consumption of other plant components, the electrical consumption of these processes were neglected in the energy assessment of power-to-SNG plants.

Table 2-7: Operating parameters of the bio-syngas purification processes, adapted from [11]

Parameter	Unit	Plant concept 1 (reference case, CNG)	Plant concept 2 and 3 (CNG resp. LNG)
		DBT-unit	
Syngas inlet temperature	K	653	
Syngas outlet temperature	K	393	453
DBT inlet temperature	K	413	
DBT outlet temperature	K	613	
Syngas and DBT pressures	bar	1	20
		Active carbon unit	
Inlet temperature	K	-	318
Outlet temperature	K	-	318
Operating pressure	bar	-	20
		RME-unit	
Syngas inlet temperature	K	393	-
Syngas outlet temperature	K	338	-
RME inlet temperature	K	333	-
RME outlet temperature	K	348	-
Operating pressure	bar	1	-
Regenerating steam temperature	K	436	-
Regenerating steam pressure	bar	1	-

Parameter	Unit	Plant concept 1 (reference case, CNG)	Plant concept 2 and 3 (CNG resp. LNG)
		ZnO column	
Inlet and outlet temperature	K	593	593
Operating pressure	bar	20	20

2.3.5. Synthetic natural gas upgrading

2.3.5.1. Drying

A drying step is required after cooling down the SNG to further reduce its water content to meet the specifications for gas grid injection. In this work, it was supposed that SNG would be dried up using a zeolite based molecular sieve, because of their efficiency and the absence of other resources required in the process. The selected process layout chosen by DVGW-EBI is based on two adsorbing columns [202] and can be seen on the right inside in Figure 2-14, Figure 2-15, or Figure 2-16. A part of the SNG dried in the active column is recycled, warmed up, and circulated in the second column for zeolite regeneration. In order to respect the German specifications for injection in the gas grid, the water content in the SNG has to be lower than 50 $mg \cdot Nm^{-3}$, which corresponds to a dew point of 255 K at a pressure of 20 bar. The residual and maximal load of the zeolite can both be determined with the dew point and the regeneration temperature [11]. Based on the operation window, the cycle duration and the bulk density of the zeolite, it is possible to dimension the adsorbing columns. The recirculated gas corresponds to 10% of the SNG product flow rate.

Since the energy consumption of the drying process is significantly lower than that of other plant processes, they were neglected in the energy assessment. The effects of SNG recirculation on mass and energy balances in the plant were also neglected.

2.3.5.2. Compression unit

The compression unit was assumed to be composed of two compression stages, each of them equipped with a mechanical compressor. The same compression ratio was assumed in each stage. The compression work in each stage was calculated using Equation (1.51) presented earlier in Chapter 1.4.2.3).

2.3.5.3. Liquefaction unit

The liquefaction unit was implemented as a black box model with the technical features provided in Table 2-8. The value of electrical consumption corresponds to the one reported for industrial units with production capacities similar to the plant capacity considered in this work [210]. The waste heat corresponds to the heat available after compression of the cooling medium used for SNG liquefaction. It was assumed that this heat would be recovered as steam at 373 K and 1 bar. It is represented on the detailed layout of plant concept 3 by the water cooled heat exchanger HX 10 (see Figure 2-16).

Table 2-8: Main technical features of the SNG liquefaction unit

Parameter	Unit	Value
Electrical consumption	$kWh \cdot kg^{-1}$ CH_4	0.35
Heat production	$kWh \cdot kg^{-1}$ CH_4	0.60
Waste heat temperature	K	373

2.3.6. Heat exchangers

A particular attention was given to the modelling of heat exchangers. These components are critical to evaluate the heat that can be recovered within plants to assess the relevance of their thermal integration as well as their overall energy performance. The heat exchanger model implemented here is based on a pinch analysis depicted in the following paragraph, and does not include the choice of particular heat exchanger technologies and the dimensioning of these components.

The iterative approach followed for heat exchangers modelling is depicted in Figure 2-7. The main objective is to determine the outlet temperature T_{OUT}, the partial pressures p_i and the flow rates n_i of the fluids at both sides of the heat exchanger as well as the total heat exchanged Q_{EXCH}. To do so, a pinch analysis was implemented. The temperature on both sides of heat exchangers were plotted as functions of the heat exchanged (so-called hot and cold composite curves) and positioned using a pinch condition corresponding to a minimal temperature difference between hot and cold composite curves. More details on the elaboration on composite curves and on pinch analysis can be found in Chapter 2.4.1.
The model capabilities were also extended to enable the modelling of condensers with diphasic mixtures in order to evaluate the recoverable heat in particular heat transfer cases, such as the condensation of steam during SNG cooling.

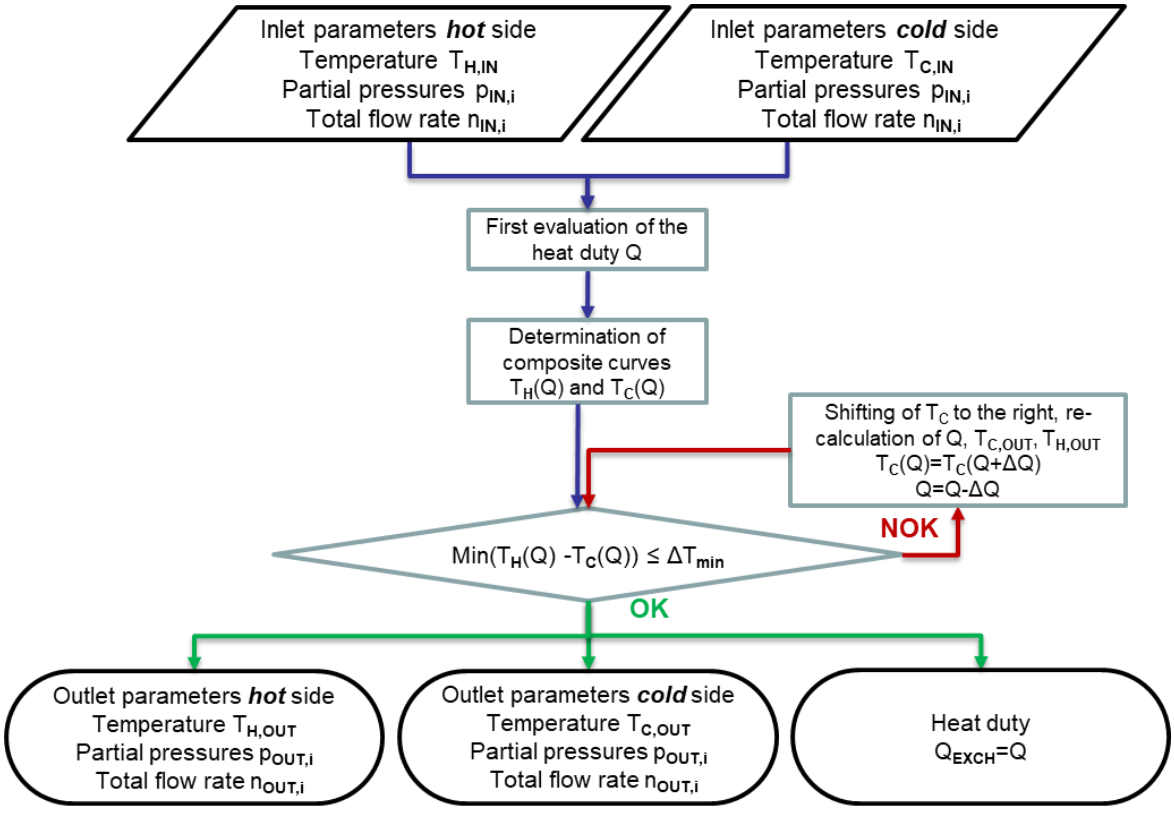


Figure 2-7: Flowchart of the heat exchanger sub-model

Furthermore, the following assumptions were made.

- A conservative minimal temperature difference ΔT_{min} (often referred to as approach temperature, e.g. in [229]) of 20 K was assumed for all heat exchangers. This encompasses both gas-gas and gas-liquid heat exchange configurations;

- A minimum partial pressure of steam allowed after condensation was set at 0.1 bar in all condensers;
- All thermal losses during the heat exchange were neglected.

For each heat exchanger, a first evaluation of the heat transfer area S_{EXCH} (in m^2) was made using well established Equation (2.17) [230, 231], with k the overall heat transfer coefficient (in $W \cdot m^{-2} \cdot K^{-1}$) and ΔT_m the mean temperature difference or temperature driving force (in K). The heat transfer coefficients values used in this work are summarized in Table A-3 in Appendix A.

$$S_{EXCH} = \frac{Q}{k \cdot \Delta T_m} \tag{2.17}$$

The temperature driving force can be determined with Equation (2.18) for a counter-current flow heat transfer configuration, with the temperature correction factor F_t supposed to be equal to 1 as a first approximation.

$$\Delta T_m = F_t \cdot \frac{\left(T_{H,IN} - T_{C,OUT}\right) - \left(T_{H,OUT} - T_{C,IN}\right)}{ln\frac{\left(T_{H,IN} - T_{C,OUT}\right)}{\left(T_{H,OUT} - T_{C,IN}\right)}} \tag{2.18}$$

2.4. Methodology for energy assessment of plant concepts

The methodological steps followed for the energy assessment of the plant concepts will be detailed hereafter. In a first step, a preliminary thermal assessment of each plant concept was made, in order to determine the maximal theoretical power-to-SNG plant efficiency. In a second step, a full thermal integration was implemented to calculate more accurately the power-to-SNG plant efficiency. The latter is compared to the maximal theoretical efficiency in Chapter 2.6.2 to assess the performance of each plant concept from an energy standpoint.

2.4.1. Preliminary energy assessment

Each plant concept was thermally assessed based on the pinch theory developed by Linnhoff et al. in the 1990s [232, 233]. Since then, it has been widely applied in the industry [234, 235]. Many contributions extending the original work have been reported for heat integration at process or at plant scale, for the retrofitting of heat exchanger networks, or even in different areas such as water, power or hydrogen integration [236]. The pinch theory is based on a so-called pinch diagram, where the temperature is represented as function of the thermal power or the enthalpy. This diagram is determined following the steps depicted hereafter.

- First, cooling and heating requirements in a plant or a process are listed with their associated temperature levels or temperature intervals;
- Second, the so-called cold stream composite curve is obtained by adding the thermal contributions of all heating requirements on each temperature level or interval. The hot stream composite curve is obtained doing the same for the cooling requirements;
- Third, both composite curves are positioned assuming a pinch condition, which corresponds to a minimum temperature delta ΔT_{min} between them (so-called approach temperature);
- Fourth, heating or cooling duties (respectively Q_H and Q_C) at high temperature and at low temperature can be determined on basis of the difference between the two composite curves in respect to the thermal power (i.e. x-axis), as schematically shown in Figure 2-8;

Alternatively, the grand composite curve can be used. It corresponds to the difference between thermal power of hot stream and cold stream composite curves.
Once this first diagram is done, the goal of the pinch theory is to dimension and optimize the heat recovery system by maximizing heat recuperation in the plant and reducing the cost of the heat exchanger network, assuming a constant and known minimal approach temperature for all heat exchangers. To reach the best compromise between these two objectives, adjustments of process operating parameters can also be proposed and implemented.

In this work though, pinch theory was not applied for dimensioning or optimization purposes, but for the calculation of maximal theoretical efficiencies of power-to-SNG plants. To do so, the steps listed above were followed and the following additional steps were added to determine the maximum theoretical plant efficiency.

- The heating duties at high and low temperatures are extracted from the composite curves and correspond to the thermal power which has to be provided by external heat sources such as electrical heaters. They are accounted for as P_H in the calculation of the plant efficiency in Equation (2.1);
- The maximum theoretical plant efficiency can now be calculated using Equation (2.1), based on the utilities' consumption (electrical consumption of the SOE unit, inverter, compression units, heaters, blowers) and the energy content of plant products and feedstock.

This methodology was implemented using an algorithm written in a MATLAB® script file, starting from a list of hot and cold streams obtained from a process flow diagram not thermally integrated (e.g. in Figure 2-9 or in Figure 2-10). The algorithm uses the gasifier mass balance, the operating parameters of each plant process, and the targeted plant output (expressed in MW HHV CH_4) as inputs and returns pinch diagrams (hot and cold streams composite curves) as well as the theoretical work of the electrical heaters and the maximal theoretical plant efficiency for each plant concept. The calculation sequence of the algorithm is presented hereafter.

- Scaling of mass and energy balances of all plant processes to the desired plant output. For each process mass and energy balances were verified ;
- Formulation of each heat stream as a vector with the corresponding operating parameters and additional stream properties such as presence of steam or reaction heat;
- Concatenation of all vectors in two distinct arrays, for hot and cold streams respectively;
- Decomposition of each vector in several vectors to identify other relevant temperature values for the elaboration of pinch diagrams, for instance in case of steam condensation;
- Concatenation of the two expanded arrays with the vectors obtained after decomposition;
- Determination of the temperature intervals where the aggregated thermal contributions will be calculated;
- Calculation of the thermal contribution for each temperature interval (elaboration of composite curve arrays);
- Verification that the cumulated thermal power contribution of all temperature intervals is equal to the total thermal power of all heat streams before decomposition;
- Adaptation of the two composite curves to the same thermal power scale (required for pinch calculation at each value of the x-axis);
- Rearrangement of the two composite curves assuming a pinch condition of 20 K;
- Determination of the heating duties at high and low temperatures, of the theoretical work of the heaters, and of the maximum theoretical plant efficiency.

Furthermore, the following hypotheses were made. The heat requirements of the hot gas cleaning process were neglected. The pressure drops and heat losses were neglected in all plant processes, at the exception of thermal losses in the SOE unit. All these assumptions were taken into account in the elaboration of the composite curves.
Also, hot and cold streams composite curves were preferred to the grand composite curve (corresponding to the difference of hot and cold streams). Even though the grand composite curve is a more synthetic representation, the information on absolute values of hot and cold streams is lost. Hence, composite curves were preferred.

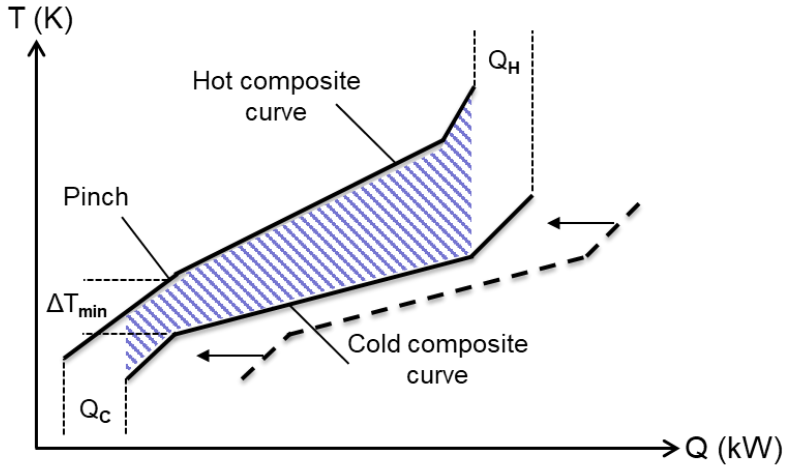


Figure 2-8: Schematic representation of a pinch diagram with pinch condition, thermal requirements, and the heat transfer area (blue dashed area), after [229]

2.4.2. Detailed energy assessment

Previous work mostly reported energy assessment of power-to-SNG plants based on full implicit thermal integrations, e.g. in [19] and in [14], where the performance of the heat exchanger network was estimated with so-called heat cascade calculations, in which the heat exchange configuration in each heat exchanger does not need to be defined.
As for full explicit thermal integration of power-to-SNG plants, they were rarely reported in previous work, e.g. in [54, 237]. They correspond to a thermal integration taking into account all heat streams in the power-to-SNG plant, and where the heat transfer configuration is explicitly defined for each heat integration equipment (heat exchangers, condensers, heaters). Different levels of detail are possible and can be depicted as follows. A first step is to define each component with an enthalpy balance and a pinch condition, which enables to determine hot and cold heat streams with their input and output characteristics (flow rate, temperature, partial pressures etc.) as well as the heat duty. A second step focuses on the choice of the adapted technology and the dimensioning of the equipment. A third step aims at optimizing the plant architecture based on engineering, process and/or costs considerations.
In this work, the detailed energy assessment of three power-to-SNG concepts was implemented based on a full explicit thermal integration including a first dimensioning of the heat exchanger network, with a variety of technological features and configurations which was not reported so far (see Chapter 1.1.4.1). The heat integrations were implemented by manual iterations following the principles listed hereafter. These principles were applied in order to maximize process heat recovery to ensure high plant efficiency, while limiting the number of heat integration components to obtain a realistic plant layout and maintain plant costs at a reasonable level.

- Heat sources and sinks were matched starting from high temperature levels and progressively going down to low temperature levels to maximize high temperature heat recovery and limit the amount of residual heat;
- A limited number of heat exchangers was implemented. Indeed, for heat amounts lower than 50 kW (0.25% of the CH_4 plant output of 20 MW HHV), no heat exchanger was implemented and the heat was not recovered for plant processes.

Furthermore, the thermal integrations were verified with different mass and energy balances at component, unit and plant level (see Chapter 2.7 for more details).

2.5. Preliminary energy assessment

2.5.1. Pinch diagrams

Pinch diagrams were elaborated following the methodology developed in Chapter 2.4.1, based on mass and energy balances of plant processes, assuming the same methane output of 20 MW (HHV based value) for each plant concept. The heat sources and sinks considered for the elaboration of pinch diagrams are represented in the process flow diagrams in Figure 2-9 for plant concept 1 and in Figure 2-10 for plant concepts 2 and 3. Several components were not mentioned in these diagrams in order to improve readability and simplify representation. These diagrams do not correspond to the full explicit thermal integration of investigated plant concepts, which can be seen in Figure 2-14, Figure 2-15, and Figure 2-16 in Chapter 2.6.1.

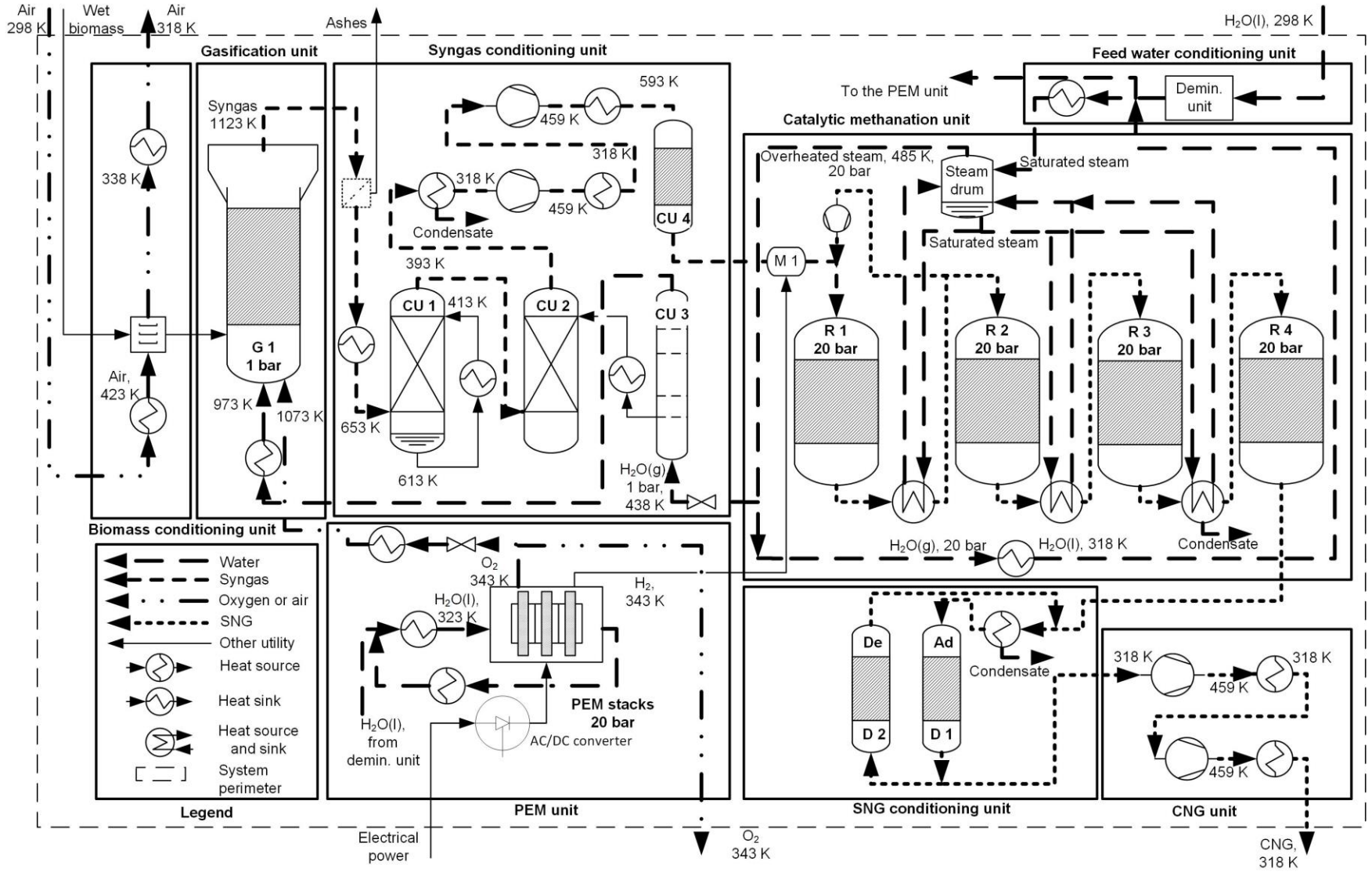


Figure 2-9: Heat sources and sinks considered for the elaboration of the pinch diagram of plant concept 1, adapted from [9]

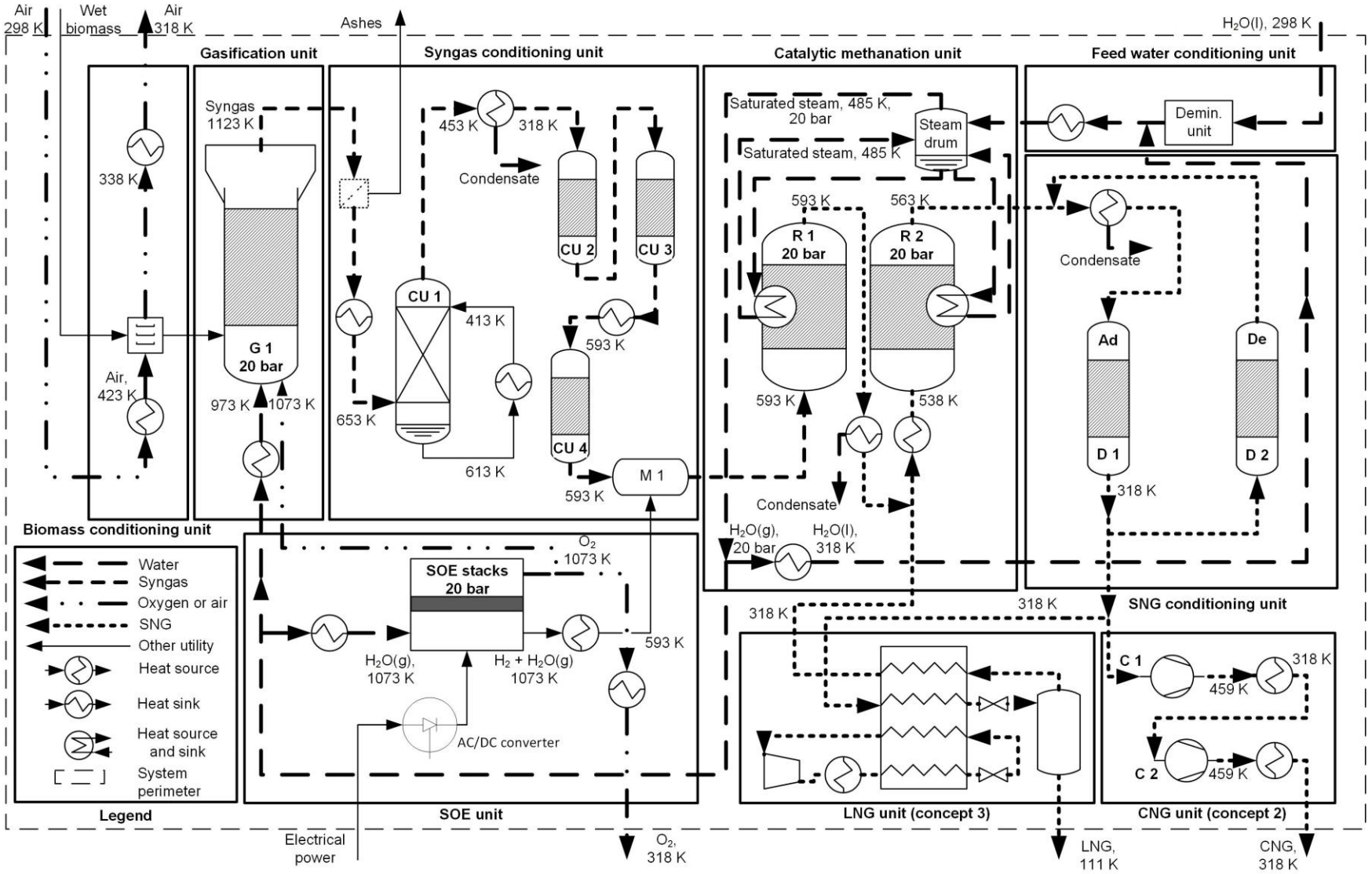


Figure 2-10: Heat sources and sinks considered for the elaboration of the pinch diagram of plant concept 2 and 3, adapted from [9]

A pinch diagram was elaborated for each plant concept. As explained in Chapter 2.4.1, it is composed of two composite curves: one corresponding to the cold streams, the other to the hot streams. They are represented in Figure 2-11, Figure 2-12, and Figure 2-13. A detailed description of each pinch diagram can also be found in Appendix A. It must be noted that in all diagrams, the hot and cold stream curves do not touch one another and are always distanciated by at least 20 K (approach temperature ΔT_{min}).

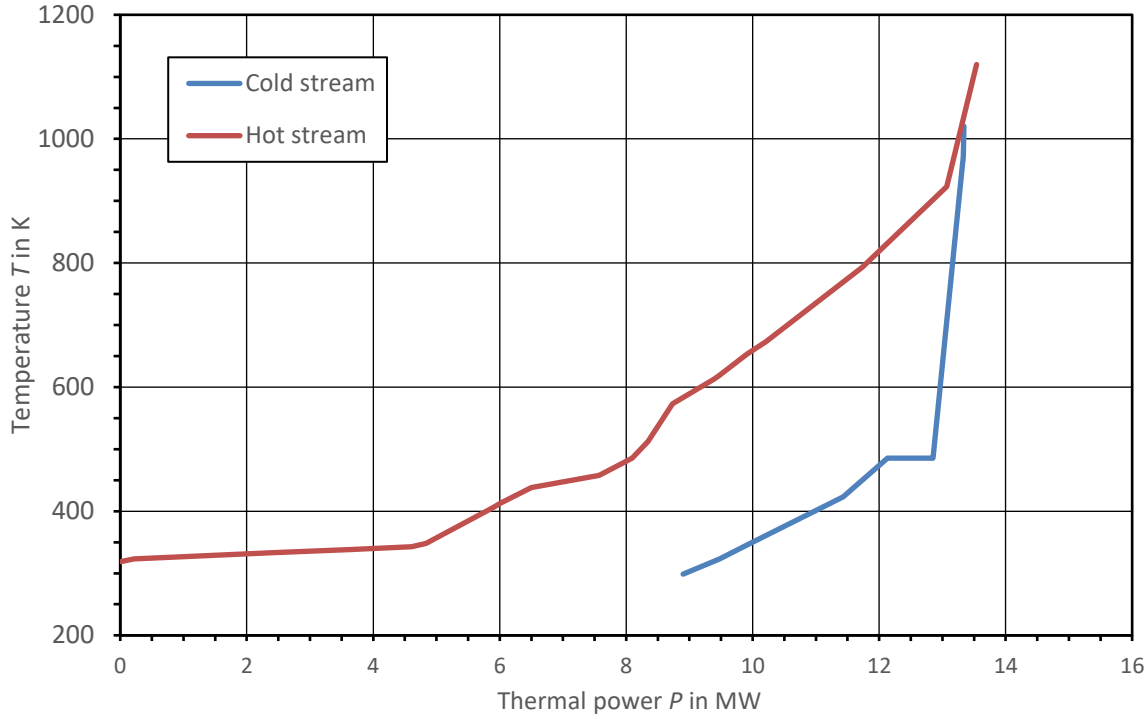


Figure 2-11: Composite curves of hot and cold streams in plant concept 1 [9]

The composite curves show that the heat available from the plant processes is theoretically sufficient (in terms of both temperature level and thermal power) to cover the heat requirements of all plant processes. Therefore, no external heat source is theoretically required.

There is a significant difference between temperature levels of hot and cold streams in plant concept 1, which means that the high temperature heat recovered from the adiabatic methanation reactors is not valorized in an optimal way. Replacing the low temperature electrolysis unit by a high temperature SOE unit would allow the use of overheated steam in the SOE unit and potentially result in a significant improvement of the plant efficiency, as was reported in [29].

In Figure 2-12 and Figure 2-13, the threshold at 593 K (red curve, hot stream) corresponds to the reaction heat removed from the three phase reactor (isothermal), whereas the threshold at 485 K (blue curve, cold stream) corresponds to the vaporization heat of water required in the SOE unit and in the gasification unit. The hot and cold composite curves could be brought closer to one another by setting up a steam pressure higher than 20 bar in the cooling system of the catalytic methanation unit, as was done in [29]. This was however not done here to limit investment costs related to high pressure components. The threshold at 373 K in Figure 2-13 corresponds to the residual heat available from the CH_4 liquefaction unit in plant concept 3.

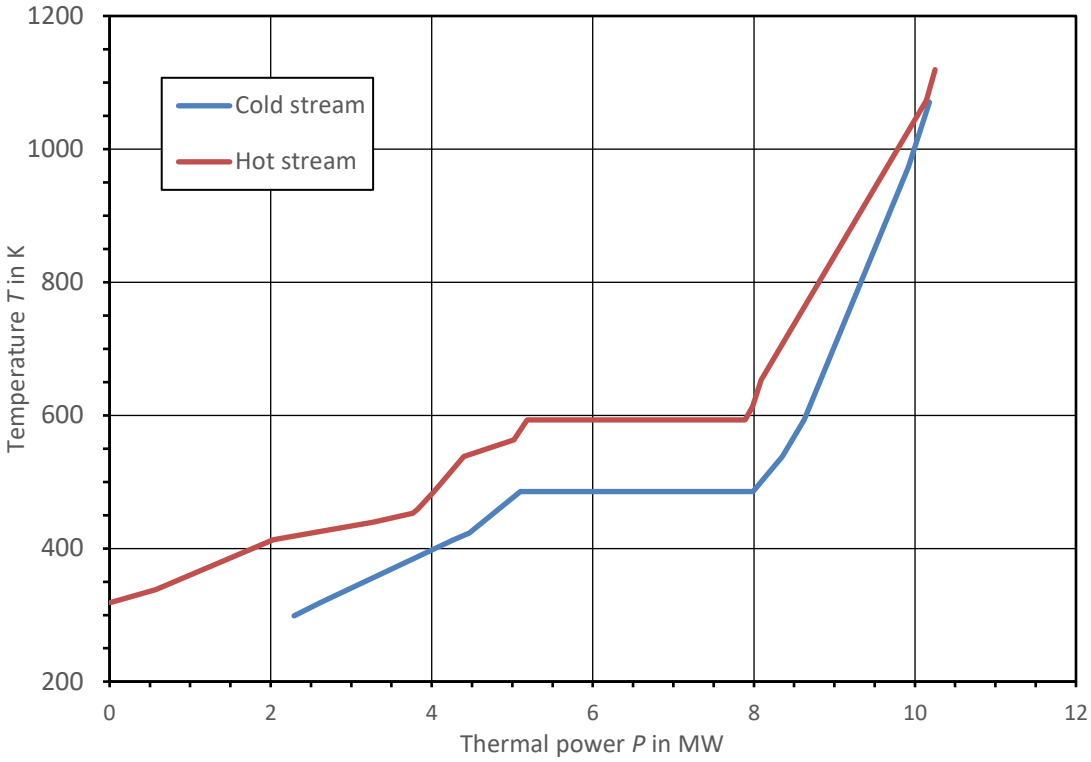


Figure 2-12: Composite curves of hot and cold streams in plant concept 2 [9]

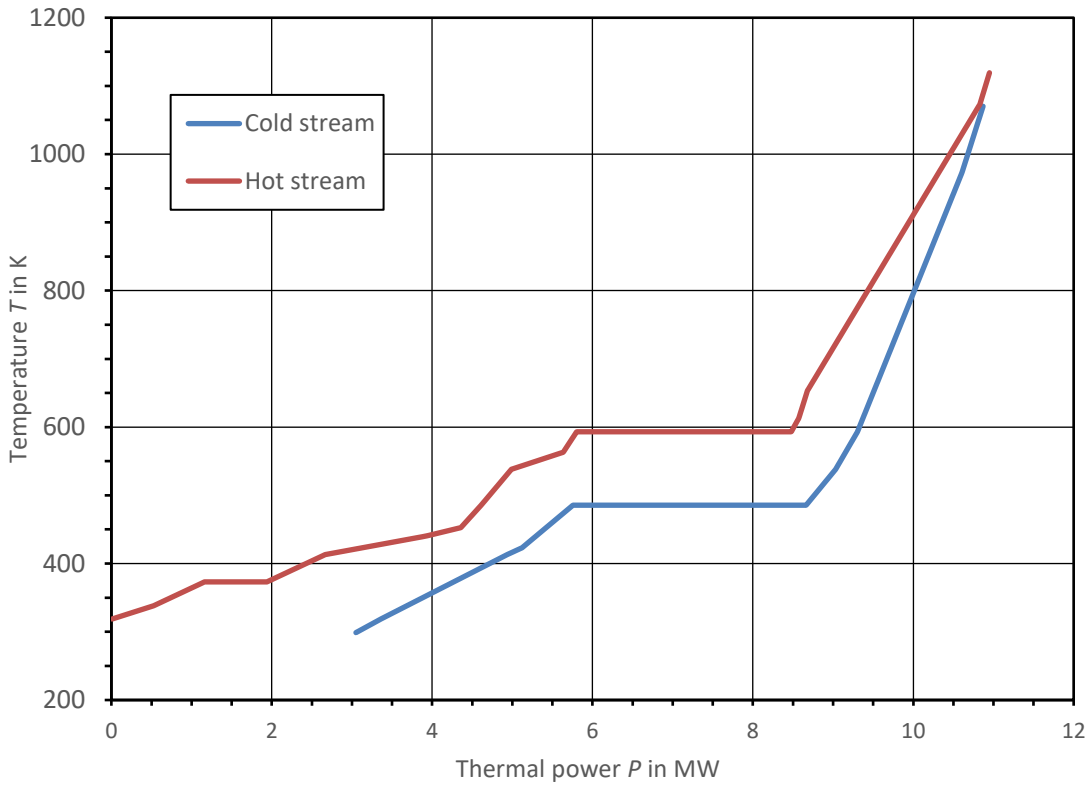


Figure 2-13: Composite curves of hot and cold streams in plant concept 3 [9]

2.5.2. Maximal theoretical efficiencies

The maximal theoretical efficiencies were calculated with the inputs provided in Table 2-9, which were determined based on mass and energy balances of plant processes, assuming a methane output of each plant concept of 20 MW (HHV based value). The values of theoretical heater consumptions are equal to zero and were derived from the pinch diagrams. They imply that for each plant concept, the heat requirements can be theoretically covered with the heat sources available.

Table 2-9: Main parameters used for the calculation of the theoretical plant efficiencies [9]

Parameter End-product	Plant concept 1 CNG	Plant concept 2 CNG	Plant concept 3 LNG
Elec. power electrolysis without inverter	18 560 kW (PEM)	13 015 kW (SOE)	13 140 kW (SOE)
Inverter efficiency	96%	96%	96%
Energy content biomass (HHV)	10 760 kW	10 720 kW	11 090 kW
Air blower (biomass drying)	210 kW	220 kW	200 kW
Compression – SNG Compression – syngas	257 kW 591 kW	257 kW 0 kW	0 kW 0 kW
CH_4 liquefaction	0 kW	0 kW	454 kW
Theoretical heater consumption	0 kW	0 kW	0 kW
Energy content H_2 (HHV)	59 kW	59 kW	0 kW
Energy content CH_4 (HHV)	20 000 kW	20 000 kW	20 000 kW

The maximal theoretical efficiencies were then calculated with Equation (2.1) introduced in Chapter 2.1. They are summarized in Table 2-10. They correspond to the maximal efficiency each plant concept can reach in case all heating requirements can be satisfied with available heat sources in the plant. Therefore, they will be used as comparison basis to evaluate the performance of the full explicit thermal integrations proposed in Chapter 2.6.2. The power-to-SNG efficiencies correspond to the efficiencies after SNG drying and before the last conversion step (compression or liquefaction) to the end-product (CNG or LNG). Hence, power-to-SNG efficiencies are always higher than power-to-CNG or power-to-LNG efficiencies.

Table 2-10: Maximal theoretical plant efficiencies of investigated plant concepts for different end-products [9]

Parameter	Plant concept 1	Plant concept 2	Plant concept 3
Maximal theoretical efficiency (pinch) HHV (%)	64.4 (CNG) 64.9 (SNG)	81.0 (CNG) 81.9 (SNG)	78.6 (LNG) 80.4 (SNG)
Maximal theoretical efficiency (pinch) LHV (%)	59.4 (CNG) 59.9 (SNG)	75.1 (CNG) 75.9 (SNG)	73.1 (LNG) 74.7 (SNG)

2.6. Detailed energy assessment

2.6.1. Detailed plant layouts

As a second step of the energy assessment, a full thermal integration of each plant concept was implemented in Simulink® with all required balance of plant components (heaters, heat exchangers, condensers, compressors, pumps), following the principles depicted in Chapter 2.4.2. The abbreviated names of components can be found in the Nomenclature. For each plant concept, a detailed process flow diagram of the full explicit thermal integration is provided hereafter, along with a table summarizing operating parameters and fluid compositions at selected plant locations or nodes. In the latter, the values in bold correspond to the final characteristics and composition of the plant product (CNG in concept 1 and 2, LNG in concept 3). The main characteristics of the heat exchanger networks of all plant concepts are summarized in Table 2-14. For each heat exchanger, the heat duty, the mean temperature difference and a first evaluation of the heat exchange area are provided.
Several comments on the tables and the figures content are provided below. Plant concept 1 will be thoroughly depicted, whereas the description of plant concept 2 and 3 will focus on the main differences with plant concept 1.

Plant concept 1 is presented in Figure 2-14 and in Table 2-11. The raw biomass is fed to a belt dryer operated at atmospheric pressure and directly injected to the gasifier. After filtration and compression in a blower (B 1), the drying air is heated up to 423 K in HX 11 with the hot air out of the dryer and in C 4 with the cooling steam of the methanation unit. The syngas is cooled down in HX 1, HX 2, and HX 4 before being its first cleaning step in the DBT unit (CU 1). It is then sent to the RME unit (CU 2), where the water in the syngas is condensed in C 1 and sent for treatment to the waste water treatment unit before being rejected to the environment. The syngas is compressed in CP 3 and CP 4, heated up to 593 K, and injected into the ZnO column (CU 4) for removal of sulfur compounds. It is then mixed with the electrolytic H_2 produced in the PEM unit and injected into the first adiabatic methanation reactor (R 1). The ashes rich DBT is cooled down in HX 6 and in HX 5 and sent to a tank, where the ashes are separated by decantation. The impurities rich RME is sent to the stripping column CU 3, where it is regenerated with steam at 1 bar from the cooling system of the methanation unit. The steam loaded with impurities is then heated up in HX 2 and fed to the gasifier. The pure oxygen produced in the PEM unit is expanded in DET 2, heated up in HX 1 and fed to the gasifier. The liquid water required for the intermediate cooling of the methanation reactors and for syngas cooling is vaporized in C 2 and fed to the steam drum, where it is dispatched to each intermediate cooler (HX 7, HX 8, and HX 9) and to the syngas cooler (HX 4) as saturated steam, and returned to the steam drum as overheated steam. The overheated steam is then sent to the RME stripping column and to the gasifier, as well as to the biomass dryer. The steam excess is cooled down in C 5. After the last methanation step, the SNG is cooled down in HX 10, sent to C 3 for the first drying step, and then dried up in the adsorption unit (zeolite columns D 1 and D 2). The dried SNG is then compressed up to 250 bar in a two stage mechanical compressor (CP 1 and CP 2) with intermediate cooling (HX 13 and HX 14).
The high flow rate values in the first methanation reactor (see nodes 6 and 7 in Table 2-11) are related to the recycling loop where an important amount of the outlet stream is recycled to the reactor, assuming a recycling ratio of 1.86. This value means that the recycled stream is 1.86 times higher than the feed stream sent to R 2. The total water flow rate required for the cooling of the catalytic methanation unit is equal to the sum of the cooling water flow rates provided to each of the intermediate cooling stages located after the three first methanation reactors (HX 7, HX 8, and HX 9) and to the syngas cooler (HX 4). Hence, the sum of the flow rates of nodes 21, 22, 23, and 24 is equal to the flow rate of node 20.

Furthermore, the sum of the water flow rates in the demineralization unit and of the cooling water out of HX 7 matches the water flow rates required in the PEM unit, the intermediate stage coolers, and the syngas cooler. In other words, the sum of the flow rates of nodes 18 and 19 is equal to the sum of the flow rates of nodes 20 and 25.

Plant concept 2 is presented in Figure 2-15 and in Table 2-12. After a first cooling step and after treatment in the DBT unit, the syngas is further treated in active carbon columns (CU 2 and CU 3). The electrolytic H_2 produced in the SOE unit is cooled down in HX 2 and mixed with the treated syngas in order to be fed to the first methanation reactor. A part of the O_2 produced in the SOE unit is directly injected in the gasifier, whereas the oxygen excess is cooled down and rejected in the air. The cooling steam is directly injected in the cooling system of the methanation reactors to enable a better temperature control (isothermal or polytropic operation) and thus a higher conversion rate of the carbon oxide gases. The total water flow rate required for the cooling of the catalytic methanation unit corresponds to the sum of the cooling water flow rates provided to each methanation reactor and to the syngas cooler (HX 4). Hence, the sum of the flow rates of nodes 13, 14, and 15 is equal to the flow rate of node 12. Similarly to plant concept 1, the dried SNG is then compressed up to 250 bar in a two stage mechanical compressor (CP 1 and CP 2) with intermediate cooling (HX 10 and HX 11).

Plant concept 3 is presented in Figure 2-16 and in Table 2-13. The plant architecture is the same than plant concept 2, except for the final transformation step into the end product, for which the SNG is sent to the liquefaction unit (at the bottom right of Figure 2-16).

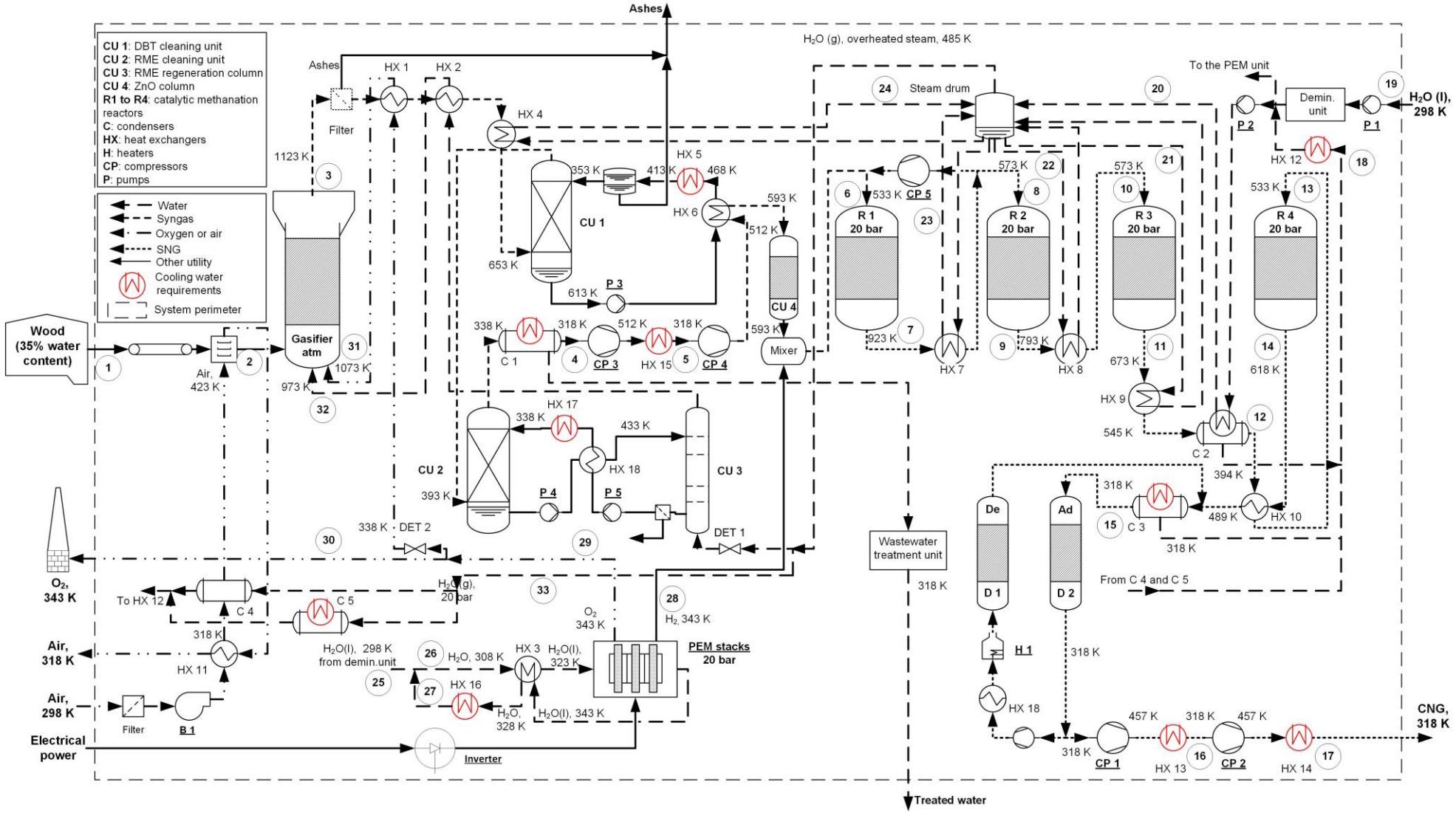


Figure 2-14: Full explicit thermal integration of plant concept 1, adapted from [11]

Table 2-11: Main parameters for the nodes of plant concept 1 in Figure 2-14, with "<<" negligible flow rate

Node	Flow rate ($kg \cdot s^{-1}$)	T (K)	P (bar)	H_2O ($kg \cdot s^{-1}$)	H_2 ($kg \cdot s^{-1}$)	O_2 ($kg \cdot s^{-1}$)	CH_4 ($kg \cdot s^{-1}$)	CO_2 ($kg \cdot s^{-1}$)	CO ($kg \cdot s^{-1}$)	C_2H_4 ($kg \cdot s^{-1}$)	N_2 ($kg \cdot s^{-1}$)	Tars ($kg \cdot s^{-1}$)	Ashes ($kg \cdot s^{-1}$)	Biomass (dry, no ashes, $kg \cdot s^{-1}$)
1	0.835	298	1	0.292	0	0	0	0	0	0	0	0	0	0.542
2	0.580	298	1	0.038	0	0	0	0	0	0	0	0	0	0.542
3	1.134	1123	1	0.333	0.029	0	0.040	0.462	0.254	0.014	0	0.003	0	0
4	0.873	318	1	0.072	0.029	0	0.040	0.462	0.254	0.014	0	0.003	0	0
5	0.873	318	4.5	0.072	0.029	0	0.040	0.462	0.254	0.014	0	0.003	0	0
6	2.806	533	20	0.934	0.200	0	0.576	0.747	0.337	0.014	0	<<	0	0
7	2.806	923	20	1.321	0.096	0	0.824	0.438	0.128	<<	0	<<	0	0
8	0.981	573	20	0.462	0.033	0	0.288	0.153	0.045	<<	0	<<	0	0
9	0.981	793	20	0.534	0.015	0	0.331	0.097	0.005	<<	0	<<	0	0
10	0.981	573	20	0.534	0.015	0	0.331	0.097	0.005	<<	0	<<	0	0
11	0.981	673	20	0.575	0.005	0	0.351	0.050	$7.2.10^{-5}$	<<	0	<<	0	0
12	0.458	394	20	0.051	0.005	0	0.351	0.050	$7.2.10^{-5}$	<<	0	<<	0	0
13	0.458	533	20	0.051	0.005	0	0.351	0.050	$7.2.10^{-5}$	<<	0	<<	0	0
14	0.458	618	20	0.071	$4.2.10^{-4}$	0	0.360	0.025	$7.2.10^{-5}$	<<	0	<<	0	0
15	0.388	318	20	0.002	$4.2.10^{-4}$	0	0.360	0.025	$7.2.10^{-5}$	<<	0	<<	0	0
16	0.386	318	70.7	<<	$4.2.10^{-4}$	0	0.360	0.025	$7.2.10^{-5}$	<<	0	<<	0	0
17	**0.386**	**318**	**250**	**<<**	**$4.2.10^{-4}$**	**0**	**0.360**	**0.025**	**$7.2.10^{-5}$**	**<<**	**0**	**<<**	**0**	**0**
18	2.319	318	20	2.319	0	0	0	0	0	0	0	0	0	0
19	0.751	298	1	0.751	0	0	0	0	0	0	0	0	0	0
20	2.106	485	20	2.106	0	0	0	0	0	0	0	0	0	0
21	1.455	485	20	1.455	0	0	0	0	0	0	0	0	0	0
22	0.306	485	20	0.306	0	0	0	0	0	0	0	0	0	0
23	0.079	485	20	0.079	0	0	0	0	0	0	0	0	0	0
24	0.266	485	20	0.266	0	0	0	0	0	0	0	0	0	0
25	0.963	298	20	0.963	0	0	0	0	0	0	0	0	0	0
26	41.987	308	20	41.987	0	0	0	0	0	0	0	0	0	0
27	40.934	308	20	40.934	0	0	0	0	0	0	0	0	0	0
28	0.108	343	20	0	0.108	0	0	0	0	0	0	0	0	0
29	0.856	343	20	0	0	0.856	0	0	0	0	0	0	0	0
30	0.682	343	20	0	0	0.682	0	0	0	0	0	0	0	0
31	0.174	1073	1	0	0	0.174	0	0	0	0	0	0	0	0
32	0.381	973	1	0.381	0	0	0	0	0	0	0	0	0	0
33	1.726	485	20	1.726	0	0	0	0	0	0	0	0	0	0

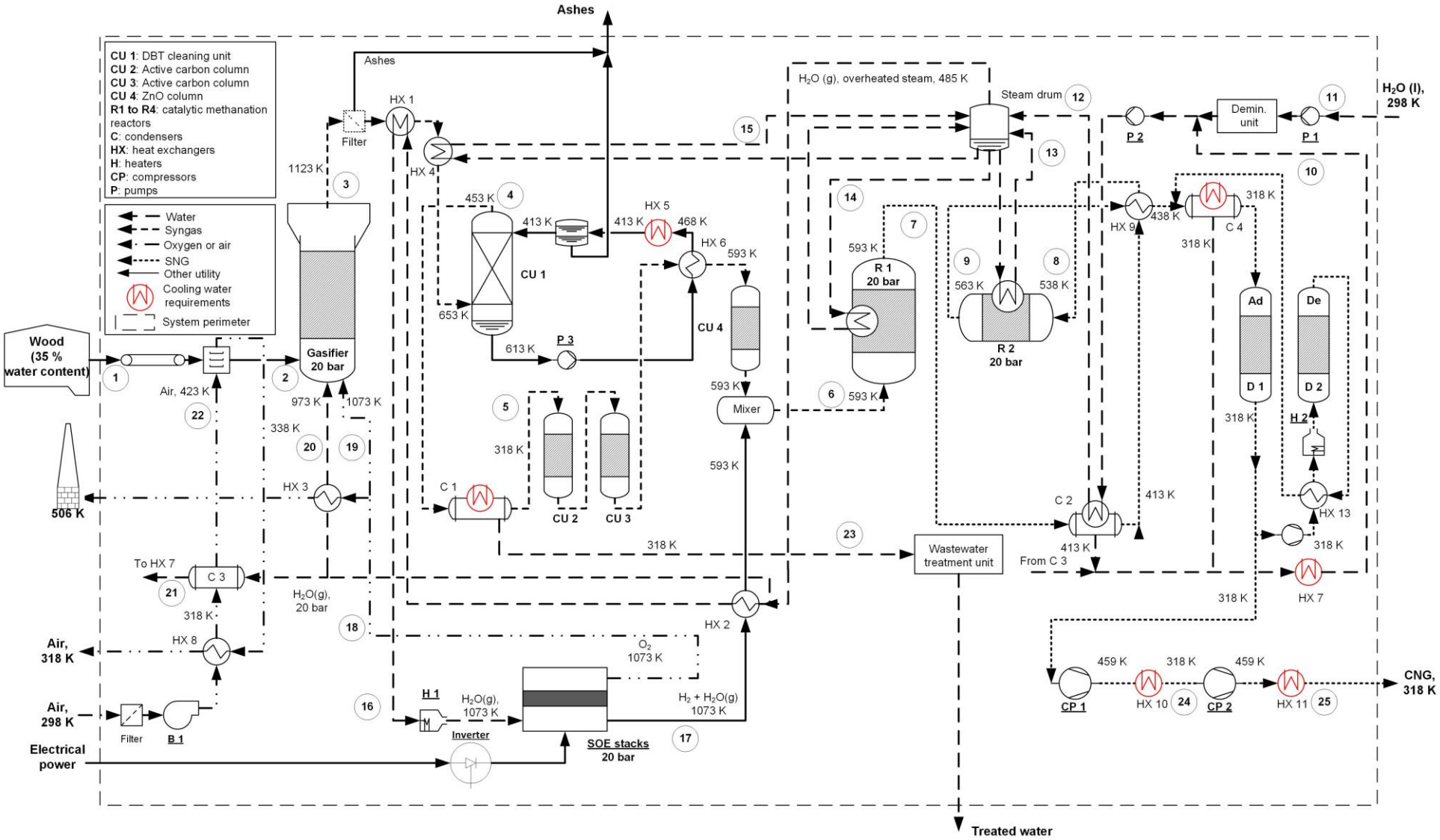


Figure 2-15: Full explicit thermal integration of plant concept 2, adapted from [11]

Table 2-12: Main parameters for the nodes of plant concept 2 in Figure 2-15, with "<<" negligible flow rate

Node	Flow rate ($kg \cdot s^{-1}$)	T (K)	P (bar)	H_2O ($kg \cdot s^{-1}$)	H_2 ($kg \cdot s^{-1}$)	O_2 ($kg \cdot s^{-1}$)	CH_4 ($kg \cdot s^{-1}$)	CO_2 ($kg \cdot s^{-1}$)	CO ($kg \cdot s^{-1}$)	C_2H_4 ($kg \cdot s^{-1}$)	N_2 ($kg \cdot s^{-1}$)	Tars ($kg \cdot s^{-1}$)	Ashes ($kg \cdot s^{-1}$)	Biomass (dry, no ashes) ($kg \cdot s^{-1}$)
1	0.832	298	1	0.291	0	0	0	0	0	0	0	0	0	0.541
2	0.578	298	1	0.037	0	0	0	0	0	0	0	0	0	0.541
3	1.090	1123	20	0.329	0.018	0	0.085	0.476	0.165	0.014	0	0.002	0	0
4	1.090	453	20	0.329	0.018	0	0.085	0.476	0.165	0.014	0	0.002	0	0
5	0.763	318	20	0.003	0.018	0	0.085	0.476	0.165	0.014	0	0.002	0	0
6	1.093	593	20	0.232	0.121	0	0.085	0.476	0.165	0.014	0	<<	0	0
7	1.093	593	20	0.611	0.022	0	0.316	0.143	<<	<<	0	<<	0	0
8	0.619	538	20	0.134	0.022	0	0.316	0.143	<<	<<	0	<<	0	0
9	0.619	563	20	0.236	$4.2.10^{-4}$	0	0.360	0.023	<<	<<	0	<<	0	0
10	1.088	318	20	1.088	0	0	0	0	0	0	0	0	0	0
11	0.820	298	1	0.820	0	0	0	0	0	0	0	0	0	0
12	1.908	485	20	1.908	0	0	0	0	0	0	0	0	0	0
13	0.235	485	20	0.235	0	0	0	0	0	0	0	0	0	0
14	1.431	485	20	1.431	0	0	0	0	0	0	0	0	0	0
15	0.242	485	20	0.242	0	0	0	0	0	0	0	0	0	0
16	1.148	1073	20	1.148	0	0	0	0	0	0	0	0	0	0
17	0.332	1073	20	0.230	0.103	0	0	0	0	0	0	0	0	0
18	0.815	1073	20	0	0	0.815	0	0	0	0	0	0	0	0
19	0.131	1073	20	0	0	0.131	0	0	0	0	0	0	0	0
20	0.417	973	20	0.417	0	0	0	0	0	0	0	0	0	0
21	0.381	338	20	0.381	0	0	0	0	0	0	0	0	0	0
22	9.233	423	1.2	0	0	2.151	0	0	0	0	7.082	0	0	0
23	0.326	318	20	0.326	0	0	0	0	0	0	0	0	0	0
24	0.383	318	70.7	<<	$4.2.10^{-4}$	0	0.360	0.023	<<	<<	0	<<	0	0
25	**0.383**	**318**	**250**	**<<**	**$4.2.10^{-4}$**	**0**	**0.360**	**0.023**	**<<**	**<<**	**0**	**<<**	**0**	**0**

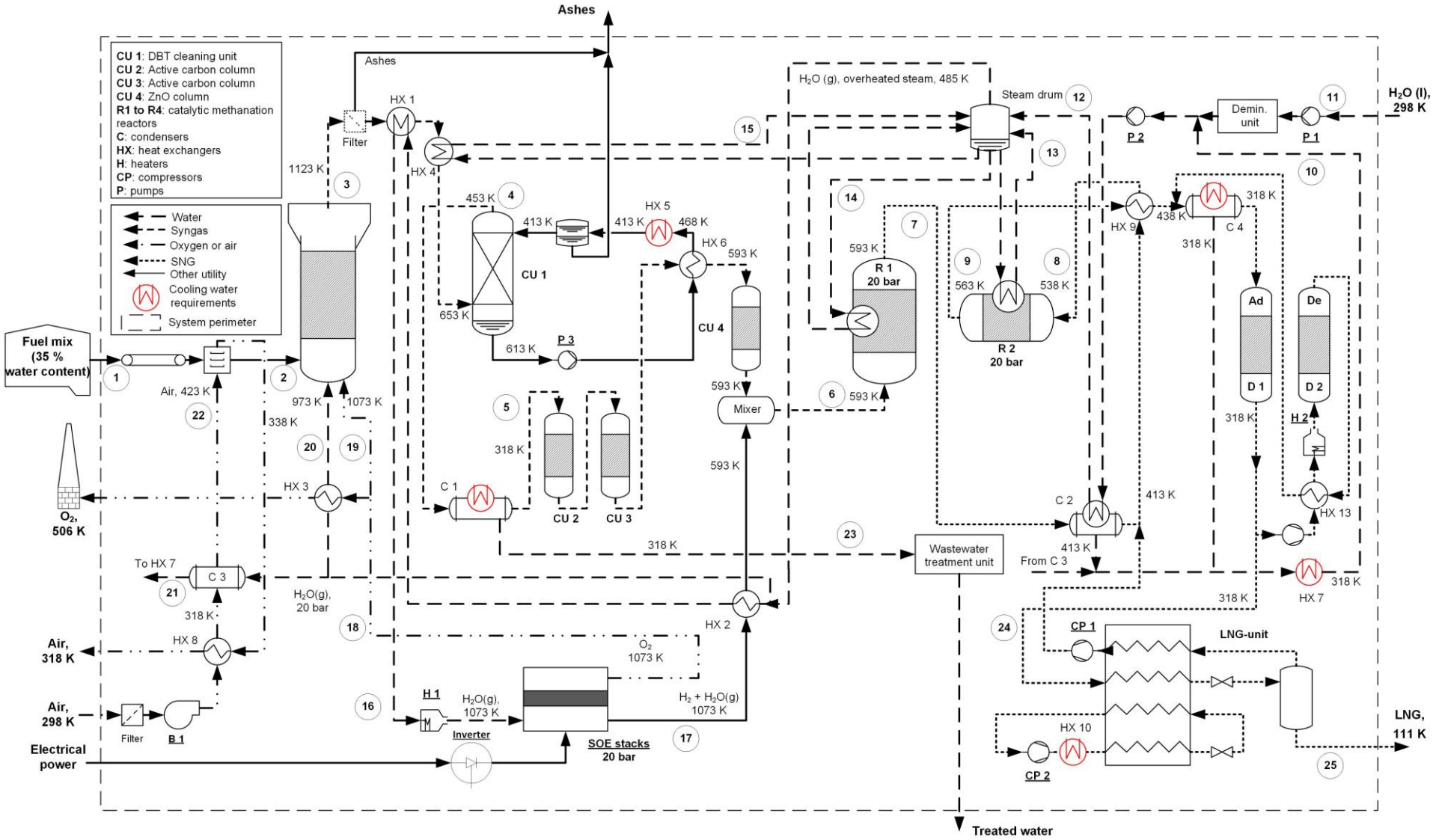


Figure 2-16: Full explicit thermal integration of plant concept 3, adapted from [11]

Table 2-13: Main parameters for the nodes of plant concept 3 in Figure 2-16, with "<<" negligible flow rate

Node	Flow rate ($kg \cdot s^{-1}$)	T (K)	P (bar)	H_2O ($kg \cdot s^{-1}$)	H_2 ($kg \cdot s^{-1}$)	O_2 ($kg \cdot s^{-1}$)	CH_4 ($kg \cdot s^{-1}$)	CO_2 ($kg \cdot s^{-1}$)	CO ($kg \cdot s^{-1}$)	C_2H_4 ($kg \cdot s^{-1}$)	N_2 ($kg \cdot s^{-1}$)	Tars ($kg \cdot s^{-1}$)	Ashes ($kg \cdot s^{-1}$)	Biomass (dry, no ashes) ($kg \cdot s^{-1}$)
1	0.972	298	1	0.291	0	0	0	0	0	0	0	0	0.122	0.552
2	0.731	298	1	0.057	0	0	0	0	0	0	0	0	0.122	0.552
3	1.270	1123	20	0.369	0.018	0	0.085	0.494	0.155	0.013	0.010	0.004	0.122	0
4	1.148	453	20	0.369	0.018	0	0.085	0.494	0.155	0.013	0.010	0.004	0	0
5	0.782	318	20	0.003	0.018	0	0.085	0.494	0.155	0.013	0.010	0.004	0	0
6	1.113	593	20	0.234	0.122	0	0.085	0.494	0.155	0.013	0.010	<<	0	0
7	1.113	593	20	0.617	0.023	0	0.315	0.148	<<	<<	0.010	<<	0	0
8	0.634	538	20	0.138	0.023	0	0.315	0.148	<<	<<	0.010	<<	0	0
9	0.634	563	20	0.240	$5.4.10^{-4}$	0	0.360	0.024	<<	<<	0.010	<<	0	0
10	1.095	318	20	1.095	0	0	0	0	0	0	0	0	0	0
11	0.820	298	1	0.820	0	0	0	0	0	0	0	0	0	0
12	1.915	485	20	1.915	0	0	0	0	0	0	0	0	0	0
13	0.246	485	20	0.246	0	0	0	0	0	0	0	0	0	0
14	1.415	485	20	1.415	0	0	0	0	0	0	0	0	0	0
15	0.254	485	20	0.254	0	0	0	0	0	0	0	0	0	0
16	1.159	1073	20	1.159	0	0	0	0	0	0	0	0	0	0
17	0.335	1073	20	0.232	0.104	0	0	0	0	0	0	0	0	0
18	0.823	1073	20	0	0	0.823	0	0	0	0	0	0	0	0
19	0.166	1073	20	0	0	0.166	0	0	0	0	0	0	0	0
20	0.378	973	20	0.378	0	0	0	0	0	0	0	0	0	0
21	0.378	338	20	0.378	0	0	0	0	0	0	0	0	0	0
22	8.418	423	1.2	0	0	1.961	0	0	0	0	6.457	0	0	0
23	0.366	318	20	0.366	0	0	0	0	0	0	0	0	0	0
24	0.384	318	20	<<	<<	0	0.360	0.024	<<	<<	<<	<<	0	0
25	**0.360**	**111**	**1**	**<<**	**<<**	**0**	**0.360**	**<<**	**<<**	**<<**	**<<**	**<<**	**0**	**0**

Table 2-14: Main characteristics of the heat exchanger network for each plant concept, with “HX”: heat exchanger and “C”: condenser.

	Plant concept 1				Plant concept 2				Plant concept 3			
	Heat duty (kW)	**Mean T difference (K)**	**Heat transfer type**	**Heat transfer area (m^2)**	**Heat duty (kW)**	**Mean T difference (K)**	**Heat transfer type**	**Heat transfer area (m^2)**	**Heat duty (kW)**	**Mean T difference (K)**	**Heat transfer type**	**Heat transfer area (m^2)**
HX 1	1131	254.9	Gas-Gas	147.9	553	36.1	Gas-Gas	511.3	581	33.1	Gas-Gas	584.8
HX 2	429	233.0	Gas-Gas	61.4	977	157.0	Gas-Gas	207.4	980	157.0	Gas-Gas	208.0
HX 3	2564	20.0	Liq-Liq	111.5	407	55.8	Gas-Gas	243.1	391	55.8	Gas-Gas	233.5
HX 4	503	268.2	Gas-Vap	28.9	457	263.2	Gas-Vap	26.7	481	263.2	Gas-Vap	28.1
HX 5	402	123.6	Liq-Liq	2.8	66	121.9	Liq-Liq	0.5	83	124.7	Liq-Liq	0.6
HX 6	123	152.9	Gas-Liq	5.0	329	157.0	Gas-Liq	13.1	335	60.2	Gas-Liq	34.8
HX 7	2753	218.1	Gas-Vap	194.2	226	19.5	Liq-Liq	10.1	227	19.5	Liq-Liq	10.1
HX 8	579	175.6	Gas-Vap	50.7	187	20.0	Gas-Gas	311.7	170	20.0	Gas-Gas	283.3
HX 9	150	156.7	Gas-Vap	14.7	208	25.5	Gas-Gas	271.9	212	25.5	Gas-Gas	277.2
HX 10	168	89.9	Gas-Gas	62.3	142	62.0	Gas-Liq	14.3	778	38.0	Gas-Liq	127.8
HX 11	175	20.0	Gas-Gas	291.7	178	62.0	Gas-Liq	18.0	-	-	-	-
HX 12	741	41.9	Liq-Liq	15.4	-	-	-	-	-	-	-	-
HX 13	142	62.0	Gas-Liq	14.3	-	-	-	-	-	-	-	-
HX 14	178	62.0	Gas-Liq	18.0	-	-	-	-	-	-	-	-
HX 15	275	76.6	Gas-Liq	22.4	-	-	-	-	-	-	-	-
HX 16	3354	10.0	Liq-Liq	291.7	-	-	-	-	-	-	-	-
HX 17	578	31.9	Liq-Liq	15.7	-	-	-	-	-	-	-	-
HX 18	1296	13.0	Liq-Liq	86.7	-	-	-	-	-	-	-	-
C 1	392	20.0	Liq-Vap	15.7	1002	60.2	Liq-Vap	13.3	1107	60.2	Liq-Vap	14.7
C 2	1651	114.4	Liq-Vap	11.5	1485	114.5	Gas-Liq	81.1	1494	114.5	Gas-Liq	81.6
C 3	358	70.4	Gas-Liq	31.8	962	37.1	Gas-Vap	398.7	955	37.1	Gas-Vap	395.8
C 4	925	37.1	Gas-Vap	383.4	704	56.1	Gas-Liq	78.4	728	56.1	Gas-Liq	81.1
C 5	3381	43.9	Liq-Vap	61.6	-	-	-	-	-	-	-	-

2.6.2. Plant performance evaluation

The main performance indicators of each plant concept are presented in Table 2-15. The maximal theoretical efficiencies are reported as a reminder to allow the comparison with plant efficiencies calculated from the full thermal integrations, also calculated with Equation (2.1). The values of biomass carbon content utilization are identical in preliminary and detailed assessments. The cooling water and net water requirements were determined based on the detailed plant layouts and the corresponding tables provided in Chapter 2.6.1.

Table 2-15: Main performance indicators of the investigated plant concepts for different end-products [9]

Parameter	Plant concept 1	Plant concept 2	Plant concept 3
Maximal theoretical efficiency (pinch) HHV (%)	64.4 (CNG) 64.9 (SNG)	81.0 (CNG) 81.9 (SNG)	78.6 (LNG) 80.4 (SNG)
Full thermal integration efficiency HHV (%)	64.4 (CNG) 64.9 (SNG)	81.0 (CNG) 81.8 (SNG)	78.5 (LNG) 80.3 (SNG)
Maximal theoretical efficiency (pinch) LHV (%)	59.4 (CNG) 59.9 (SNG)	75.1 (CNG) 75.9 (SNG)	73.1 (LNG) 74.7 (SNG)
Full thermal integration efficiency LHV (%)	59.3 (CNG) 59.9 (SNG)	75.1 (CNG) 75.9 (SNG)	73.0 (LNG) 74.6 (SNG)
Carbon utilization (%)	97.5 (CNG, SNG)	97.8 (CNG, SNG)	97.8 (SNG) 100 (LNG)
Residual heat (MW)	9.2	2.4	3.1
Cooling water requirements	110.4 $kg \cdot s^{-1}$	29.2 $kg \cdot s^{-1}$	37.6 $kg \cdot s^{-1}$
Amount of heat exchangers required	23	15	14
Net water requirements	0.75 $kg \cdot s^{-1}$	0.82 $kg \cdot s^{-1}$	0.82 $kg \cdot s^{-1}$

For each plant concept, full thermal integration efficiencies close to the maximal theoretical efficiencies were reached. The slight efficiency difference observed in some cases is related to the electrical work of heaters, which could not be avoided. Therefore, proposed plant integrations are close to the theoretical maximum.
All plants present the same carbon efficiencies, the slight difference observed in plant concepts 1, 2, and 3 (0.3% maximum) being related to the differences in syngas compositions.

The lower plant efficiency in plant concept 1 can be explained by:

- The impossibility of recovering the reaction heat of the catalytic methanation process for the electrolysis process, as is the case in plant concepts 2 and 3 with the SOE unit;
- The lower CH_4 yield of the gasification in plant concept 1 compared to plant concepts 2 and 3, because the gasification process is operated at atmospheric pressure, which is less favorable to CH_4 formation than the pressurized gasification process. Therefore, approx. 5.6% more H_2 is required in plant concept 1 than in plant concept 2 for the methanation of the bio-syngas, which is in addition produced by a PEM electrolysis unit with a lower power-to-H_2 efficiency than a SOE

unit. Would the H_2 be produced in a SOE unit instead of a PEM unit in plant concept 1, then the electrical power required for the electrolysis including the inverter would be 14.3 MW and the power-to-CNG efficiency would increase up to 76.8% HHV (to be compared to the 81% HHV power-to-CNG efficiency in plant concept 2). Hence, the use of a pressurized gasification unit instead of an atmospheric one would increase the power-to-CNG efficiency by approx. 4.2%.

The residual heat amount is much larger in plant concept 1 (9.2 MW) because the cooling steam produced in the catalytic methanation unit cannot be valorized in the electrolysis unit and because of the considerable amount of low temperature heat produced in the PEM unit. The residual heat available in plant concept 3 (3.1 MW) is higher than in plant concept 2 (2.4 MW) because of the residual heat from the SNG liquefaction unit.
A significantly higher amount of heat exchangers is required for the thermal integration in plant concept 1, which is mostly related to technological choices.

- The TREMP™ process is based on fixed-bed adiabatic methanation reactors, where the reaction heat is evacuated in dedicated heat exchangers for intermediate stage cooling and not directly in the reactor as it is the case in the isothermal and polytropic reactors in plant concept 2 and 3. Hence, six heat exchangers are required against three in plant concept 2 and 3 (only five though when counting the methanation reactors as heat exchangers).
- The RME purification at low temperature requires two heat exchangers compared to the first step high temperature syngas purification treatment in plant concept 2 and 3 where none is required.
- The low temperature electrolysis process, in which the cooling steam of the methanation cannot be valorized and must be cooled down in a condenser.
- The atmospheric operation of the gasification unit, which requires a two stage compression unit for the bio-syngas with a heat exchanger for intermediate stage cooling. This component is not required in the other plant concepts with a pressurized gasification unit.

2.6.3. Residual heat valorization

The valorization of residual heat sources for each plant concept will be discussed hereafter. Two valorization pathways will be considered: the coupling with a district heating network or the production of electrical power in a steam turbine.

2.6.3.1. Steam turbine

A first option to valorize the residual heat would be to utilize it for power generation in a steam turbine. In plant concept 1, superheated steam could be produced at much higher temperature (903 K) and used in a steam turbine (without condensation). According to the IEA, coal fueled steam turbines for conventional power plants usually show net LHV fuel-to-power efficiencies in the range of 30-45% [238]. Assuming a fuel-to-power efficiency of 30% (conservative assumption, however still an optimistic one since the electrical power of the turbine in plant concept 1 would be much lower than the electrical power of steam turbines in coal power plants) and a boiler thermal efficiency of 90%, this is equivalent to a steam-to-power efficiency of approx. 33%. In our case, it corresponds to a power output of 400 kW and a power-to-SNG efficiency increase of 1.3% up to 65.7% HHV in plant concept 1. This option would however not be feasible in plant concepts 2 and 3 because the generation of significant superheated steam amounts is not possible due to the much lower operating temperatures of the catalytic methanation reactors. Furthermore, even in case of excess steam in plant concept 2 and 3, it would be much more efficient to

use it to produce additional H_2 in an overdimensioned SOE unit rather than in a turbine, since the power-to-H_2 efficiency of a SOE unit is much higher than the electrical efficiency of a turbine.

2.6.3.2. District heating network

A second option for the valorization of the residual heat would be the coupling with a district heating network.

The residual heat sources in plant concept 1 and plant concept 2 are represented in Figure 2-17 and in Figure 2-18 respectively. The amount of total residual heat theoretically recoverable in plant concept 1 is approx. 9.2 MW at 318 K and approx. 2.4 MW in plant concept 2 (assuming a 20 K approach temperature and a cooling water temperature at 298 K). This approach temperature was chosen in order to enable the comparison with the cooling requirements on the pinch diagrams in Figure 2-11 and in Figure 2-12 respectively. It can be observed on the pinch diagrams that these quantities match indeed. Hence, the pie charts can be considered exhaustive (no residual heat source was forgotten) and verified.

However, the dispersion of the heat sources would make the entire heat recovery difficult and costly because of the additional number of heat exchangers required. Hence, to simplify the heat utilization concept, only the most relevant heat sources (that is the sources with both the highest temperature levels and the largest heat quantities) should be considered.

In plant concept 1, the heat recovery of excess superheated steam is the most relevant. Assuming a coupling with the district heating network of Karlsruhe, which is operated with a forward temperature of 403 K and a backward temperature of 328 K [239], a thermal power of approx. 3.4 MW at 328 K could be recovered.

As for plant concept 2, the most interesting heat sources would be the SNG after the second methanation step and the syngas after processing in the cleaning unit. These two heat sources would enable to inject a total thermal power of 1.3 MW at 328 K in the district heating network of Karlsruhe.

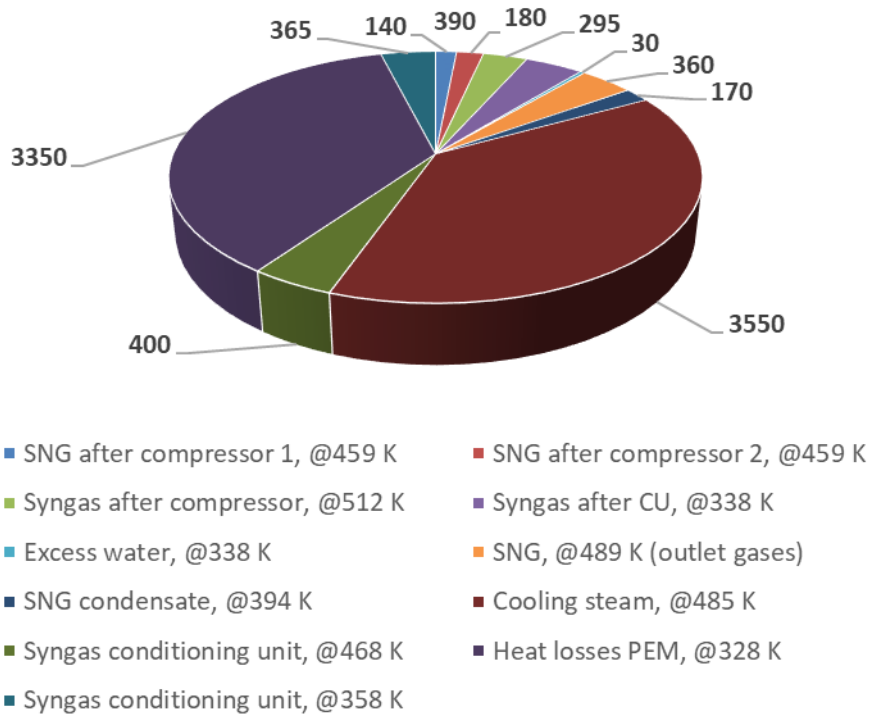


Figure 2-17: Residual heat sources available @318 K for plant concept 1 (in kW, total approx. 9.2 MW) [9]

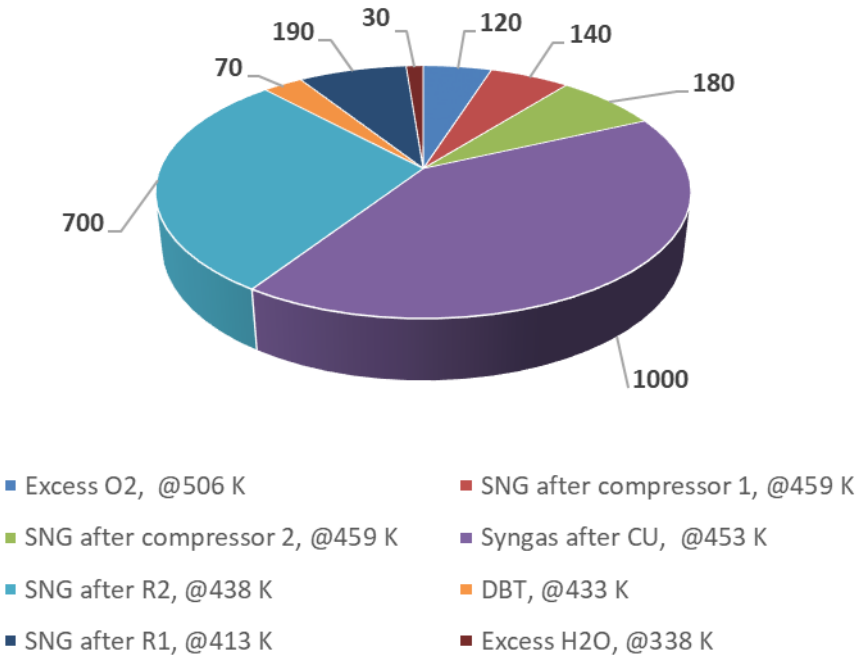


Figure 2-18: Residual heat sources available @318 K for plant concept 2 (in kW, total approx. 2.4 MW) [9]

2.7. Model verification

Several steps were implemented for the verification of the models used in this work. Mass and energy balances were used for the verification of all process streams considered for the elaboration of composite curves in Chapter 2.5.1, as well as for the full thermal integrations. In all cases, mass balances were

verified. As for energy balances, the corresponding error values are summarized in Table 2-16. They can be considered as acceptable, since their maximal value was 0.28%.

Table 2-16: Absolute and percentage error of energy balances on main plant processes based on the total input process energy, adapted from [11]

	Plant concept 1		**Plant concept 2**		**Plant concept 3**	
	Absolute error (kW)	Error (%)	Absolute error (kW)	Error (%)	Absolute error (kW)	Error (%)
Catalytic methanation reactor 1	15	0.022	45	0.18	43	0.17
Catalytic methanation reactor 2	23	0.10	1.2	0.006	3.8	0.018
Catalytic methanation reactor 3	5	0.022	-	-	-	-
Catalytic methanation reactor 4	0.068	$3.3\ 10^{-4}$	-	-	-	-
Steam and oxygen gasifier (HHV)	34	0.28	17	$1.4\ 10^{-4}$	15	0.12
Steam and oxygen gasifier (formation enthalpies)	22	0.27	0.78	$9.7\ 10^{-3}$	0.97	0.011
Electrolysis unit (SOE or PEM)	51	0.13	1.6	$9.2\ 10^{-3}$	1.7	$9.7\ 10^{-3}$

Overall mass balances of full integrated plants were verified as well using Equation (2.19).

$$\dot{n}_{BIO} + \dot{n}_{H2O,REQ} - \dot{n}_{SNG} - \dot{n}_{O2,EXC} - \dot{n}_{H2O,WW} = 0 \qquad (2.19)$$

Furthermore, cooling water requirements were also verified. Since cooling water with identical inlet and outlet temperatures were assumed in all plant concepts, similar ratios between cooling water flow rates and cooling requirements (thermal power) should be observed. On the composite curve diagrams, thermal cooling requirements at 318 K of approx. 9.1 MW can be observed in plant concept 1, whereas they are of about 2.4 MW in plant concept 2 and of about 3.1 MW in plant concept 3. Using the cooling water flow rates provided in Table 2-15, a ratio of 12.1 was calculated in each plant concept, thus verifying the calculated values of cooling water requirements.

2.8. Comparison of plant efficiencies with previous work

In this paragraph, power-to-SNG efficiencies calculated in this work are quantitatively compared to previous literature values.

Several energy assessments of PEM or alkaline electrolysis units integrated with catalytic methanation units were already reported in the literature, e.g. [21, 22, 240-242], and at least one MW scale unit is already operating [36]. Corresponding power-to-SNG efficiencies are usually in the range of 50-60% (based on the LHV of products). The power-to-SNG efficiency obtained in plant concept 1 corresponds to the highest values of this interval (59.3% LHV for CNG and 59.9% LHV for SNG). Power-to-SNG plants comparable to plant concept 1 with integrated low temperature electrolysis and gasification units were

reported in [240, 241, 243]. A power-to-SNG efficiency up to 69.6% LHV was obtained in [241] considering a maximized SNG production. This value is much higher than the ones obtained for plant concept 1, mostly because of the high LHV power-to-H_2 efficiency of 85% assumed for the electrolysis process compared to approx. 70% LHV in plant concept 1. A power-to-SNG efficiency in the range of 60.3-60.5% LHV was reported in [240]. In comparison to plant concept 1, no inverter was assumed. However, the corresponding electrical power losses were equivalent to the additional syngas compression work required in [240]. This additional compression work can be explained by the higher H_2 concentration in the syngas compared to the one obtained in plant concept 1, due to the absorption enhanced reforming (AER) gasification process applied in [240], and because of the higher outlet pressure of the syngas after compression (35 bar in [240] against 20 bar in this work, with the same inlet pressure at approx. 1 bar in both cases). This explains why rather close overall plant efficiencies were obtained in [240] and in plant concept 1. Power-to-SNG plant efficiencies in the range of 55.2-57.7% LHV were reported in [243]. A plant concept with steam and oxygen assisted gasification similar to plant concept 1 was investigated. The corresponding power-to-SNG efficiency of 57.7% LHV was lower than the one of plant concept 1 mostly because of the higher power consumption of the PEM electrolysis unit (4.69 kWh Nm^{-3} H_2 against 4.5 kWh Nm^{-3} H_2 in this work).

Energy efficiencies of plant concepts with integrated SOE units for upgrading gasification bio-syngas into methane based products have been scarcely documented so far. A power-to-SNG efficiency of 69-70% LHV was reported in [54], where the investigated plant was similar to plant concept 2. The efficiency is lower than the 75.9% power-to-SNG efficiency obtained in plant concept 2. First, electrical work is required for the compression of syngas from 1 to 7 bar in [54], whereas no compression is required in plant concept 2 because the gasification unit is pressurized. Second, the energy content of the biomass feedstock is higher in [54] than in plant concept 2. Third, a higher electrical work is required for the steam drying process in [54] than for the air drying process in plant concept 2. Assuming the same CH_4 output in [54] and in plant concept 2, the same energy content of biomass than in plant concept 2 and no syngas compression work, the power-to-SNG efficiency in [54] would increase up to 75-76% LHV, which is coherent with the 75.9% LHV power-to-SNG efficiency in plant concept 2.

Other energy assessments investigated SOE units integrated with catalytic methanation units for the upgrading of CO_2 obtained from different sources such as biogas, industrial CO_2 or captured CO_2 [45, 46, 48-51]. In most cases, the conversion process into a rich oxidized carbon gas was usually not integrated in the energy analysis. Giglio et al. reported a LHV efficiency of 76% in [49], which is higher than the 75.1% LHV obtained in this work for plant concept 2. The main reasons are the higher inverter efficiency (98% compared to the 96% in this work) and the need for external heat at high temperatures, the latter resulting from the temperature match between cooling steam and operating temperatures of the catalytic methanation units. The work required for external heating has to be removed from plant efficiency calculation to enable a fair comparison with plant concept 2, since negligible external heating is required there. Hence, the inverter efficiency would reduce the plant efficiency in [49] down to 74.5% LHV, whereas the absence of electrical heating would increase it again up to 75.7% LHV. This value is coherent with the 75.4 % LHV efficiency in plant concept 2 after the first SNG compression stage at 72 bar (in comparison to [49], where SNG is produced at 80 bar). In [46, 48], a HHV efficiency of 74.5% was calculated in the reference case. This value is lower than the plant efficiency calculated in plant concept 2 mostly because of the lower inverter efficiency (92% against 96% in this work). Since the value of steam utilization in the SOE unit is not high enough to use only the cooling steam produced in the catalytic methanation unit, additional electrical work is required to produce the steam complement, which decreases the plant efficiency by an additional 1%. The advantage of seeking high steam reactant utilization in the range of 74-80% in the context of SOE units integrated with catalytic methanation units

was already identified in [38, 45, 51, 55]. These two factors would increase the plant efficiency up to 79.5% HHV, to be compared with the 81.0% HHV efficiency in plant concept 2. Giglio et al. reported a power-to-SNG efficiency of 77.4% LHV in [50]. The inverter consumption was not included in the calculation and the external heat requirements were 185 kW (for a 10 MW SOE unit). If an inverter efficiency of 96% was assumed, plant efficiency would decrease down to 74.7% (LHV). Furthermore, if no external heat was required, the plant efficiency would increase up to 76.0% (LHV), which is very close to the 75.9% (LHV) obtained in plant concept 2 for SNG synthesis. Wang et al. reported HHV efficiencies of power-to-methane plants in the range of 73-85% HHV in [51]. From the many plant configurations simulated, one was reported to have an efficiency of approx. 82.6% (HHV) in steam electrolysis mode with a reactant utilization of 75%. The methane flow rate obtained was $6.9 \cdot 10^{-5}$ kg.s^{-1}, which corresponds to a methane energy content of 3.8 kW and to an electrical power consumption of approx. 4.5 kW, including the 0.15 kW required for the electrical heaters. Assuming an inverter efficiency of 96% and no electrical heating, the power-to-methane efficiency would drop down to 81.9% (HHV), which is comparable to the power-to-SNG efficiency of 81.8% (HHV) obtained for plant concept 2. As for plant concept 3, a power-to-LNG efficiency of 73% (LHV) was calculated, which is much higher than the 46.3% (LHV) reported in [242], mostly because the SOE unit enables a higher power-to-SNG efficiency compared to the alkaline unit assumed in [242], and also because of the lower electrical work for SNG liquefaction assumed in this work (0.35 kWh kg^{-1} CH_4 against 0.6 kWh·kg^{-1} CH_4 in [242]).
Interestingly, plant concepts 2 and 3 require theoretically no electrical heating as can be seen in Figures 5 b) and 5 c), which was confirmed later on for the full thermal integration of these plant concepts, where limited electrical heating was required (up to 0.2% of the SOE power without inverter, to be compared e.g. to the 2% reported in [50]). This can be explained by the integration of the gasification unit in the power-to-SNG plant, since the gasifier produces high temperature heat at 1123 K that can be recovered for preheating the inlet gases of the SOE unit up to 1073 K. On the contrary, external heating cannot be avoided when integrating processes for rich oxidized carbon gas synthesis at lower temperatures such as biogas units or when upgrading captured CO_2, as was shown in [46, 48-51]. An exothermic operation of the SOE unit is still possible, but it is most likely to reduce the power-to-H_2 efficiency [244] and in turn the overall plant efficiency. Therefore, these considerations tend to prove the benefits of gasification processes compared to anaerobic digestion processes from an energetic standpoint when integrated with SOE units and catalytic methanation units in power-to-methane plants.

2.9. Conclusions of Chapter 2

Several innovative power-to-SNG plant concepts for gasification bio-syngas upgrading to LNG or CNG through steam electrolysis and catalytic methanation processes were reported in this work. The investigated plant concepts show high efficiency values up to 81.8% for SNG, up to 81.0% for CNG and up to 78.5% for LNG (based on the HHV of end-products), which are significantly higher than the reference case values with integrated PEM electrolysis unit (64.9% or 64.4% with SNG resp. with CNG as end-products). This efficiency increase can be explained by the steam recovered from the catalytic methanation unit, which can be fed into the SOE unit. These values highlight the potential for efficiency improvement and operating cost reduction of the SOEC technology compared to the PEM technology (and to the alkaline technology in a larger extent) when coupled to steam sources. The power-to-SNG efficiencies of full thermal integrated plants are very close to the maximal theoretical plant efficiencies, thus validating the relevance of the implemented thermal integrations from an energy standpoint.

The power-to-SNG efficiency values of this work are coherent with previous literature values reported for power-to-SNG plants using different CO_2 sources, such as captured CO_2, biogas, and bio-syngas. The differences can be mostly explained by the hypotheses on inverter efficiency, reactant utilization, and electrical heating requirements of plant processes. Furthermore, much lower electrical heating is required when the gasification process is integrated to a power-to-methane plant with a SOE unit and a catalytic methanation unit. This seems to prove that it would be beneficial from an energy standpoint for such power-to-SNG plants to integrate high temperature processes producing rich oxidized carbon gases such as gasification rather than low temperature processes producing rich oxidized carbon gases such as anaerobic digestion. Hence, these two options should be compared with an energy and an economic analysis.

Options for the valorization of residual heat were also discussed. The valorization of the excess steam in a steam turbine could result in a plant efficiency increase of 1.3% up to 65.7% HHV in plant concept 1. However, this option is not suited for plant concepts 2 and 3, where the residual heat should preferably be injected in a district heating network like the one of Karlsruhe.

3. Simulation of the transient behavior of SOE units

In this Chapter, the transient behavior of SOE units will be investigated based on a single repeat unit (SRU) model implemented in this work. First, the model objectives and hypotheses will be presented, as well as the methodology followed for its implementation. Second, the thermal response of SRUs with different SOEC architectures to power transients will be investigated and compared. Third, the behavior of a SOE unit composed of two modules and coupled with different electrical power profiles will be investigated. Finally, operation strategies and power-to-SNG plant configurations aiming at reducing the size of the H_2 storage will be discussed, as well as the operation mode of SOECs in the context of power-to-SNG plants.

3.1. Objectives and scope of the modelling work

The widespread use of power-to-SNG conversion pathways in all economical sectors could be facilitated not only with efficient but also with flexible conversion processes, which would enable to tackle the issue of intermittent renewable power sources. From all processes integrated in the plant concepts discussed in Chapter 2, water electrolysis, as it is an electrochemical conversion process, has a key role to play in addressing this issue and will therefore be at the chore of the work presented in this Chapter. The operation of the catalytic methanation unit with a fluctuating electrolytic H_2 supply should be avoided, because it can generate significant fluctuations of the SNG composition, which are likely to hinder the SNG injection in the gasgrid. Moreover, the intermittent operation of the gasification unit would likely result in an instable syngas composition. Therefore, the catalytic methanation and gasification units will be operated at constant load or at partial load when needed in this work.

As a consequence, this Chapter will focus on the ability of SOE units to cope with intermittent power sources in order to improve the flexibility of power-to-SNG plants. The modelling work implemented hereafter will address the following research questions.

- What are the thermal gradients admissible along single repeat units (SRU) composed of an interconnect and a SOEC and what is the corresponding electrical power range? Should the power range be adapted to limit local overvoltages?
- What would be the behavior of a SOE unit composed of several modules, where each module is operated on the power range previously defined?
- What are the thermal gradients for different SOEC architectures and which architecture would be the most suitable for intermittent operation?
- Starting from the H_2 production profiles of a SOE unit coupled with a fluctuating power source, how to dimension and operate the main components of a power-to-SNG plant, e.g. the electrolysis unit, the catalytic methanation unit and the H_2 storage unit?
- What would be the most suitable operation mode of SOE units when thermally coupled with a catalytic methanation unit?

To address these questions, the following tasks will be implemented.

First, a dynamic model will be developed to investigate the thermal behavior of a SRU integrated in a SOE stack. The SOE thermal management is crucial under fluctuating power loads, because it can result in significant temperature fluctuations and in local overvoltages along SOECs, which can lead to cell and

stack failure. The description of these phenomena involves the calculation of thermal gradients and local voltages, which should preferably be evaluated using at least 1D models. In this work, a 1D model will be preferred to a 2D or 3D model following the considerations of Chapter 1.2.6.1 to enable short calculation times, suitable for the development of real time control strategies in future work. The model will be adapted from the work of Cai et al. [142] and will evaluate the following parameters.

- The temperature profiles of all SRU components (cell, interconnect) and streams along the cathode and anode channels;
- The main outlet parameter values of the cathode and anode streams (temperature and composition).

Furthermore, the model should be easily adaptable to different SOEC architectures, in order to compare the thermal response of SRUs with electrolyte supported cells (ESC) or cathode supported cells (CSCs). The modelling of the cell behavior will be based on the empirical evaluation of the area specific resistance (ASR), which is a common parameter in the industry to evaluate cell performance.

Second, the thermal behavior of SRUs with ESCs or CSCs during power transients will be investigated and compared with the model, in order to determine maximal thermal gradients along the SRUs and the corresponding electrical power range in which they can be operated.

Third, the behavior of a SOE unit composed of several modules and coupled with different electrical power profiles will be investigated. H_2 production profiles will be generated based on a windmill power profile and used as a basis for a first dimensioning of a H_2 storage tank and a downstream catalytic methanation unit. Operating strategies and power-to-SNG unit configurations to reduce the size of the H_2 storage will be discussed, as well as the operation mode of SOECs in the context of power-to-SNG plants.

3.2. Simulation hypotheses

3.2.1. Single repeat unit architecture

The main parameters of the two different single repeat unit (SRU) architectures considered for the development of the model are summarized in Table 3-1.

Table 3-1: SRU properties and operating parameters selected for model development

Parameter/property	Source	Unit	Value/hypothesis with ESC	Value/hypothesis with CSC
Cell operation parameters and properties				
Steam conversion rate	[112]	(%)	70	
Air ratio	[112, 113]	(-)	2	
Cathode inlet composition	[112]	(%-mol H_2O /H_2)	90/10	
Cell architecture & global geometry	[112, 245]	(-)	Flat square cell	
Cell thickness	[66, 99, 245]	(µm)	190	450
Cell active area	[112, 245]	(cm^2)	128	
Channel width (anode and cathode)	[112, 245]	(m)	0.113	
Channel height (anode and cathode)	[137]	(m)	$1.0\ 10^{-3}$	
Average porosity		(-)	0.12	0.24

Parameter/property	Source	Unit	Value/hypothesis with ESC	Value/hypothesis with CSC
Cell operation parameters and properties				
Cell thermal conductivity	[137]	(W m^{-1} K^{-1})	1.86	
Cell density	[137]	(kg m^{-3})	5.94 10^3	
Cell heat capacity	[137]	(J kg^{-1} K^{-1})	4.4 10^2	
Inlet temperature (cathode)	[112]	(K)	1103	1073
Inlet temperature (anode)	[112]	(K)	1103	1073
Interconnect geometrical and physico-chemical properties				
Thermal conductivity	[246]	(W m^{-1} K^{-1})	24	
Density	[246]	(kg m^{-3})	7.7 10^3	
Heat capacity	[246]	(J kg^{-1} K^{-1})	6.6 10^2	
Thickness	[27]	(m)	2.5 10^{-4}	
Inlet temperature	[112, 142]	(K)	1103	1073

3.2.2. Modelling hypotheses

SOCs are electrochemical converters, in which several physicochemical phenomena occur at the same time (listed hereafter from [247]).

- Mass diffusion in the cell porous layers;
- Ion and electron transport based on electrochemical reactions;
- Convective, conductive and radiative heat transfer, including heat losses.

Based on the objectives presented in Chapter 3.1, the detailed modelling of all these phenomena is not required. The model implemented hereafter will focus on the heat transfer phenomena in the SRU. The mass diffusion and the ion and electron transport phenomena will not be depicted.

In addition, the following working hypotheses were made.

- The single dimension considered corresponds to the direction of the gas flow along the cell;
- A so-called co-flow configuration was chosen for the gas streams in the channels;
- Temperature and concentration gradients are neglected in the directions perpendicular to the gas flow;
- Edge effects are neglected in all directions;
- All heat losses from the cell to the environment are neglected;
- All contact resistances were not considered, e.g. between interconnect and cell;
- The time constant of the electrochemical reactions is supposed to be very small in comparison to the thermal response of the system. Therefore, all phenomena besides the heat transfer are supposed to be in static regime (this hypothesis was also made, e.g. in [137]). As a result, knowing the power injected in the cell, one can easily determine the amount of H_2 produced in the cell and in turn the outlet composition of the cathode gas. Similarly, the amount of O_2 produced can be easily evaluated and thus the composition and the flow rate of air or pure O_2 at the anode;
- The gas density $\rho_{CATH,GAS}$, the gas thermal capacity $c_{P,CATH,GAS}$, and the gas thermal conductivity $\lambda_{CATH,GAS}$ in the cathode channel are taken as the average between inlet and outlet values. The same hypothesis was made for the anode channel. This hypothesis was made in previous modelling work by Udagawa et al. in [248] based on the original work of Iora et al. in [249]. The

local temperature output assuming constant gas flow properties taken as inlet conditions was compared to the local temperature output with gas flow properties varying along the cell and resulted in a difference lower than 7 K;

- The ASR is assumed to be linear on the entire operation domain of the SOECs.

The single repeat unit configuration retained for model development is schematically represented in Figure 3-1.

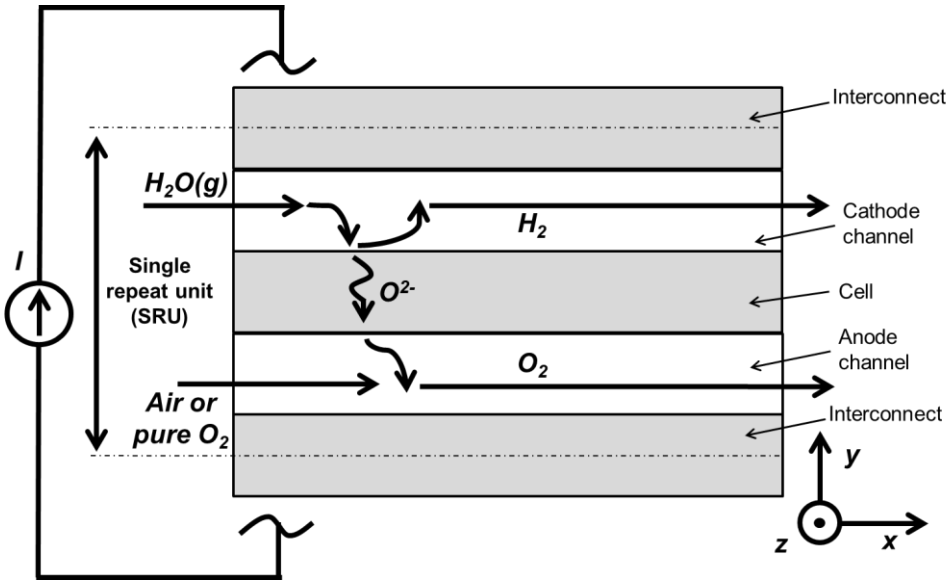


Figure 3-1: Schematic representation and perimeter of the SRU considered for model development

The following hypotheses were also made regarding the upscaling from the SRU to the SOE module.

- The stack behavior will be extrapolated from a single SRU, assuming the behavior of all SRUs in a stack is identical;
- All stacks in a SOE module are also assumed to exhibit the same behavior.

3.3. Methodology

3.3.1. Modelling pathway

The modelling approach followed for the determination of the SRU transient behavior is summarized in Figure 3-2. First, the inlet gas flow rates are set based on the electrical power injected in the SRU, on the inlet composition, and on the steam utilization target. The outlet gas compositions are estimated with the steam utilization and the inlet gas composition. Using the estimated average gas composition, it is possible to determine the properties of the gas mixtures, e.g. their thermal conductivity and viscosity. These gas mixture properties, combined with the SRU geometrical and material properties, enable to calculate characteristic numbers (Reynolds, Prandtl, and Nusselt) of the gas flow in the SRU and to obtain the convective transfer coefficients along the cathode and the anode channels. The discretized heat transfer equations are therefore fully defined at each node and can be solved at each timestep with the provided initial and boundary conditions. A detailed description of the main steps presented in Figure 3-2 can be found in Chapters 3.3.2 to 3.3.6.

In its current version, the model does not aim at developing control strategies. Nonetheless, it could be easily adapted for such applications in future work, for instance for galvanostatic operation (at constant current density) or potentiostatic operation (at constant cell voltage), the latter being the most frequently

used for the operation of SOE systems at present. The inlet flow rates and the electrical power can be assimilated to control variables, which remain constant during each calculation interval.

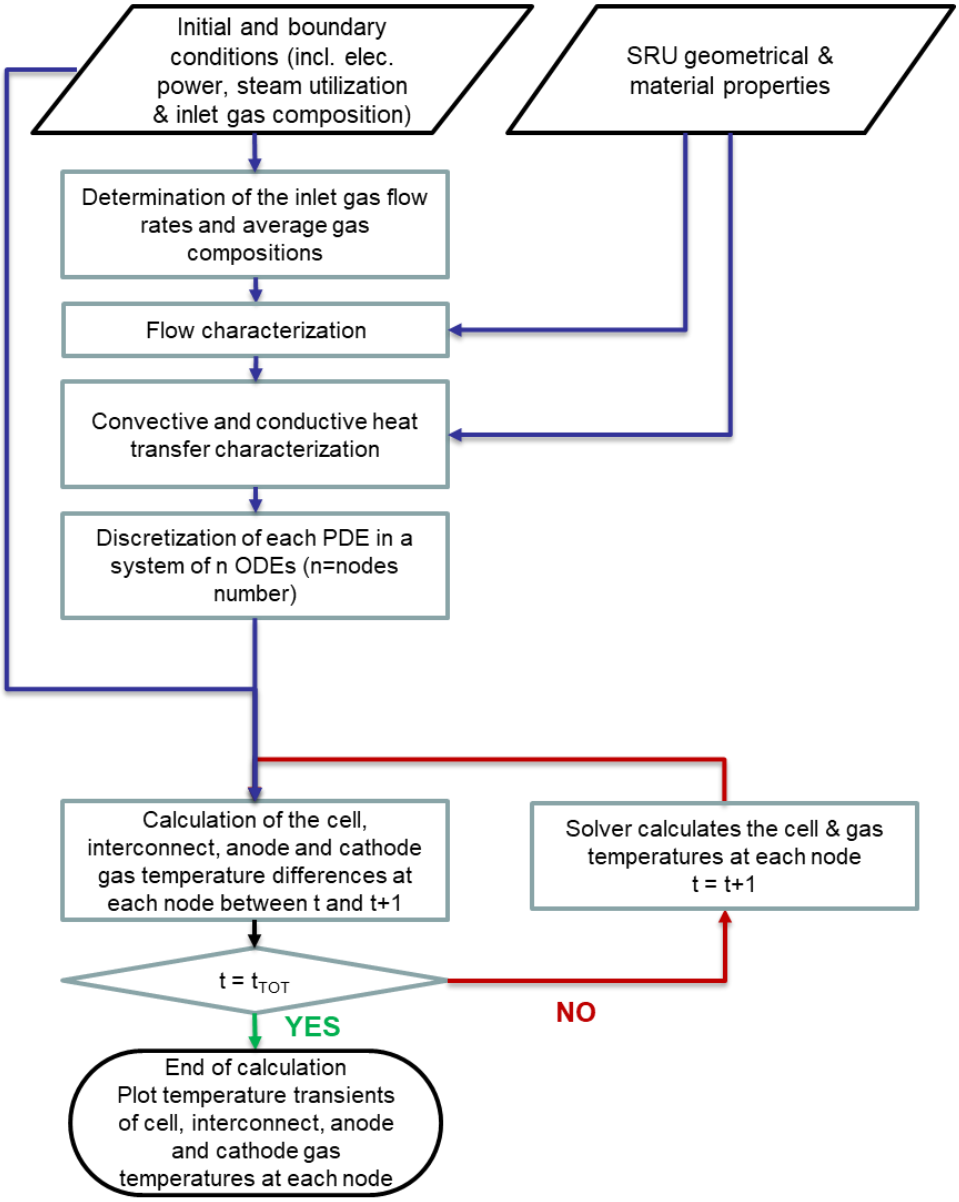


Figure 3-2: Modelling pathway followed to determine the temperature profiles along the cell, the interconnect, and the anode and cathode channels in transient regime

3.3.2. Inlet gas flow rates and gas compositions

The electrical power changes from one calculation interval to the next. Hence, the inlet flow rates should also be adjusted at each calculation interval rather than being kept constant in order to ensure sufficient steam utilization. Therefore, the following method was applied.

The H_2 flow rate produced in the SOEC can be determined with Equation (3.1), which derives from an energy balance at cell level at the thermoneutral operation point, assuming all heat losses are neglected.

$$\dot{n}_{H2} = \frac{P_{CELL}}{\Delta_R H} \tag{3.1}$$

The value of inlet gas flow rate at the cathode can be set with Equation (3.1), with the inlet gas composition, and the assumption on steam utilization provided in Table 3-1. The inlet flow rate at the anode is set with the value of air ratio also provided in Table 3-1 and the O_2 flow rate produced in the cell. This method was also applied to set the inlet gas flow rates for power loads above and below thermoneutral operation point.
The outlet gas composition was also estimated with the inlet gas composition and the assumption on steam utilization. The average gas compositions along the cathode and the anode were assumed to be constant and equal to the average between inlet and outlet gas compositions.
This results in a significant approximation of the gas composition along the channels. However, as mentioned earlier, this hypothesis was made in previous modelling work by Udagawa et al. in [248] based on the original work of Iora et al. in [249] and resulted in very low temperature error compared to simulations with gas flow properties varying along the cell. As this work does not aim at determining the evolution of gas compositions along the channels, this hypothesis was considered to be acceptable.

The actual outlet gas composition can be determined by combining Equation (3.2) and the Faraday law of electrolysis (Equation (1.10)), which enables to obtain the actual H_2 amount $\dot{n}_{H2}$ produced in the cell. Depending if the ASR is function or not of the cell temperature (see Chapters 3.3.4.3 and 3.3.4.4), the outlet gas composition can be determined at the same time than the inlet flow rates or just after the calculation of the cell temperature at each node by the solver (see Figure 3-2).

$$j = \frac{E_N}{2 \cdot ASR} \cdot \left(-1 + \sqrt{1 + \frac{4 \cdot P_{CELL} \cdot ASR}{S \cdot {E_N}^2}} \right) \tag{3.2}$$

It should be noted that Equation (3.2) is valid in the operation domain where the ASR is linear only. Furthermore, an assumption on the average gas composition is still required for the calculation of the OCV (see Equation (1.6)). Nonetheless, the error on the OCV remains below 1% in the conditions presented in Table 3-1 in case of a 10% deviation from the steam utilization target of 70%, which is acceptable.

3.3.3. Flow characterization

The pathway applied for the characterization of the flow in the cathode channel is presented hereafter. The same methodology was applied for the anode channel. Hence, the same Equations can be applied at the anode by replacing the indexes referring to the cathode with their equivalents at the anode.
The gas velocity at the cathode channel u_{CATH} (in $m \cdot s^{-1}$) is given by the ratio of the mass flow rate and the fluidic section, which can be written with Equation (3.3), where $\rho_{CATH,GAS}$, $w_{CATH,CH}$, and $e_{CATH,CH}$ correspond to the average gas density (in $kg \cdot m^{-3}$), to the width (in m), and to the height in the cathode channel (in m) respectively.

$$u_{CATH} = \frac{\dot{n}_{H2O} + \dot{n}_{H2}}{\rho_{CATH,GAS} \cdot w_{CATH,CH} \cdot e_{CATH,CH}} \tag{3.3}$$

The Reynolds number Re can be calculated with Equation (3.4), where the characteristic length L (in m) corresponds to the active cell length or the square root of the active cell area and ν_{CATH} to the cinematic

viscosity (in $m^2 \cdot s^{-1}$). Another variation is possible, where the cinematic viscosity is substituted by the ratio of the dynamic viscosity μ_{CATH} (in Pa·s) and the average gas density [250].

$$Re = \frac{u_{CATH} \cdot L}{\nu_{CATH}} = \frac{u_{CATH} \cdot L \cdot \rho_{CATH,GAS}}{\mu_{CATH}} \tag{3.4}$$

Values of Reynolds number in the range of approx. 200-1200 were obtained at the cathode and the anode channels, which is significantly lower than the commonly accepted transition domain between laminar and turbulent flow in the range of $2 \cdot 10^3$-$3 \cdot 10^3$. Hence, the flow at the cathode and the anode is laminar. The Prandtl number can be determined with Equation (3.5), a being the thermal diffusivity (in $m^2 \cdot s^{-1}$) [250].

$$Pr = \frac{\nu_{CATH} \cdot \rho_{CATH,GAS} \cdot c_{P,CATH,GAS}}{\lambda_{CATH,GAS}} = \frac{\nu_{CATH}}{a} \tag{3.5}$$

The thermal conductivity of the gas mixture $\lambda_{CATH,GAS}$ was obtained from the Wilke formula written in Equation (3.6), where x_i corresponds to the molar fraction of compound i.

$$\lambda_{CATH,GAS} = \sum_{i=1}^{n} \frac{x_i \cdot \lambda_i}{\sum_{j=1}^{n} x_j \cdot \varphi_{ij}} \tag{3.6}$$

The expression of the dimensionless function φ_{ij} for the calculation of the thermal conductivity of gas mixtures is shown in Equation (3.7), with λ_i and M_i the thermal conductivity and the molar mass (in $g \cdot mol^{-1}$) of the gaseous compound i respectively.

$$\varphi_{ij} = \frac{\left(1 + \left(\frac{\lambda_i}{\lambda_j}\right)^{\frac{1}{2}} \cdot \left(\frac{M_j}{M_i}\right)^{\frac{1}{4}}\right)^2}{\left(8 + 8 \cdot \frac{M_i}{M_j}\right)^{\frac{1}{2}}} \tag{3.7}$$

Based on the recommendations of [251], Equations (3.6) and (3.7) were also applied to determine the dynamic viscosity μ (in Pa·s) by replacing all λ_i by μ_i.

The Graetz number Gz can be evaluated with Equation (3.8) and is a function of the axial position, with d_{CATH} the hydraulic diameter of the cathode channel (in m) [137]. As simplifying hypothesis, only the average value of the axial position x_{AV} along the cell was considered in this work. The hydraulic diameter is provided in Equation (3.9).

$$Gz = \frac{d_{CATH} \cdot Re \cdot Pr}{x_{AV}} \tag{3.8}$$

$$d_{CATH} = \frac{2 \cdot w_{CATH,CH} \cdot e_{CATH,CH}}{w_{CATH,CH} + e_{CATH,CH}} \tag{3.9}$$

The Nusselt number can be calculated empirically with Equation (3.10) as was done in [137], which allows to determine the value of the convective heat transfer coefficient k_{CATH} (in $W \cdot m^{-2} \cdot K^{-1}$) with Equation (3.11) [250].

$$Nu = 3.095 + 8.933 \cdot \left(\frac{1000}{Gz}\right)^{-0.5386} \cdot exp^{\frac{-6.7275}{Gz}} \tag{3.10}$$

$$k_{CATH} = \frac{Nu \cdot \lambda_{CATH,GAS}}{d_{CATH}} \tag{3.11}$$

Moreover, the thermal conductivity and the heat capacity of the porous cell material are calculated with Equations (3.12) based on the considerations of [65] and with Equation (3.13), where ε refers to the porosity of the cell material.

$$\lambda_{CELL} = \varepsilon \cdot \lambda_{CATH,GAS} + (1-\varepsilon) \cdot \lambda_{CATH,SOL} \tag{3.12}$$

$$c_{P,CELL} = \varepsilon \cdot c_{P,CATH,GAS} + (1-\varepsilon) \cdot c_{P,CATH,SOL} \tag{3.13}$$

3.3.4. Heat transfer characterization

3.3.4.1. Cathode and anode channels

The evolution of the gas temperature T_C along the cathode channel can be depicted with the convection equation (Equation (3.14)), as was done in [142]. The first derivative term in x is the convective term. The evolution of the cathode gas temperature also depends on the difference between the cell temperature T_S and the cathode gases temperature on one hand and on the difference between the interconnect temperature T_I and the cathode gases temperature on the other hand, as can be seen in the second term of the equation. The same convection equation can also be written for the anode gases temperature T_A, by replacing all cathode parameters by their anode equivalents (Equation (3.15)).

$$\frac{\partial T_C(x,t)}{\partial t} = -u_{CATH} \cdot \frac{\partial T_C(x,t)}{\partial x} + \frac{k_{CATH}}{\rho_{CATH,GAS} \cdot c_{P,CATH,GAS} \cdot e_{CATH,CH}} \cdot \left(T_S(x,t) + T_I(x,t) - 2 \cdot T_C(x,t)\right) \tag{3.14}$$

$$\frac{\partial T_A(x,t)}{\partial t} = -u_{ANODE} \cdot \frac{\partial T_A(x,t)}{\partial x} + \frac{k_{ANODE}}{\rho_{ANODE,GAS} \cdot c_{P,ANODE,GAS} \cdot e_{ANODE,CH}} \cdot \left(T_S(x,t) + T_I(x,t) - 2 \cdot T_A(x,t)\right) \tag{3.15}$$

3.3.4.2. Interconnect

The heat transfer phenomena in the interconnect can be depicted with Equation (3.16), as was reported in [142]. The second order derivative term in T_I corresponds to the conduction term in the solid. The terms in T_I correspond to convective terms, the first one referring to the convection between interconnect and cathode channel gases and the second one to the convection between interconnect and anode channel gases.

$$\frac{\partial T_I(x,t)}{\partial t} = \frac{\lambda_{INTER,AV}}{\rho_{INTER} \cdot c_{P,INTER}} \cdot \frac{\partial^2 T_I(x,t)}{\partial x^2} - \frac{k_{CATH}}{\rho_{INTER} \cdot c_{P,INTER} \cdot e_{INTER}} \cdot \left(T_I(x,t) - T_C(x,t)\right) - \frac{k_{ANODE}}{\rho_{INTER} \cdot c_{P,INTER} \cdot e_{INTER}} \cdot \left(T_I(x,t) - T_A(x,t)\right) \tag{3.16}$$

3.3.4.3. Cell – simplified heat transfer model

The heat transfer phenomena in the cell can be depicted with Equation (3.17), also reported in [142] and is similar to Equation (3.16) depicted in Chapter 3.3.4.2. The additional term Q_{CELL} corresponds to the heat produced or consumed in the cell because of the electrolysis reaction.

$$\frac{\partial T_S(x,t)}{\partial t} = \frac{\lambda_{CELL}}{\rho_{CELL} \cdot c_{P,CELL}} \cdot \frac{\partial^2 T_S(x,t)}{\partial x^2} - \frac{k_{CATH}}{\rho_{CELL} \cdot c_{P,CELL} \cdot e_{CELL}} \cdot \left(T_S(x,t) - T_C(x,t)\right) - \frac{k_{ANODE}}{\rho_{CELL} \cdot c_{P,CELL} \cdot e_{CELL}} \cdot \left(T_S(x,t) - T_A(x,t)\right) + Q_{CELL} \quad (3.17)$$

The expression of Q_{CELL} applied in [142] is provided in Equation (3.18), with ΔH the reaction enthalpy of steam electrolysis (in J·mol^{-1}), j the current density in the SOEC (in A·cm^{-2}), F the Faraday constant (in A·s·mol^{-1}), P_{EL} the electrical power injected in the cell (in W), and S the active cell area (in m^2).

$$Q_{CELL} = \frac{1}{\rho_{CELL} \cdot c_{P,CELL} \cdot e_{CELL}} \cdot \left[-\Delta H \cdot \frac{j}{2 \cdot F} + \frac{P_{EL}}{S}\right] \quad (3.18)$$

In this work, two different approaches were used to model the heat generation phenomena in the cell. In a first approach, a simplified model where the ASR was assumed to be constant was implemented. The selected ASR values were about 0.25 Ω·cm^2 for CSCs and about 0.55 Ω·cm^2 for ESCs. They were obtained from Equation (3.19) and (3.20) with a cell temperature of 1073 K for CSCs and of 1103 K for ESCs.
The main interest of this simplified model is that it can be verified and then easily improved into an extended, more accurate version where the ASR depends on the cell temperature at each point along the cell. This extended model is depicted in the following paragraph.

3.3.4.4. Cell – extended heat transfer model

The so called extended model is also based on Equations (3.17) and (3.18). This time however, the ASR varies with the temperature. In the case of CSCs, the relationship between ASR and cell temperature considered in this work is provided in Equation (3.19) and is based on the experimental work of Fu et al. in [12]. In the case of ESCs, Equation (3.20) is based on the experimental work of Schefold et al. at cell level in the frame of the EU project GrinHy.

$$ASR(T_S) = exp^{\frac{4900}{T_S} - 5.95} \quad (3.19)$$

$$ASR(T_S) = 0.462 - (T_S - 1123) \cdot 0.462 \cdot 0.01 \quad (3.20)$$

Equations (3.18) and (2.12) can be combined with either Equation (3.19) or (3.20) depending on cell type to write down the current density as a linear function of the cell temperature, where α and β correspond to the constant parameters used for linearization. As a result, Equation (3.18) can be reformulated as Equation (3.21).

$$Q_{CELL} = \frac{1}{\rho_{CELL} \cdot c_{P,CELL} \cdot e_{CELL}} \cdot \left[-\Delta H \cdot \frac{\alpha}{2 \cdot F} \cdot T_S - \Delta H \cdot \frac{\beta}{2 \cdot F} + \frac{P_{EL}}{S}\right] \quad (3.21)$$

In conclusion, the heat source term in the cell Q_{CELL} will be approximated in a first approach with Equation (3.18) assuming a constant ASR. Only this expression of the heat source term will be considered in Chapter 3.3. The corresponding model will be referred to as simplified model. The more accurate expression of the heat source term provided in Equation (3.21) will be used in the so-called extended model. The corresponding results will be presented in Chapter 3.4.

3.3.5. Initial and boundary conditions

The following boundary conditions were assumed for the investigated system. On the left side (inlet) of the SRU, the cell, the interconnect, the anode and the cathode gas temperatures were supposed to be constant at T_{IN}, where T_{IN} depends on the cell architecture (see Table 3-1). Furthermore, an adiabatic Neumann condition was assumed at the right side (outlet) of the system for the cell and the interconnect temperatures. These conditions are written in Equations (3.22) to (3.27), where L corresponds to the active length of the cell. The system is defined with four partial differential equations (PDE), two of the second order and two of the first order. Hence, the system is fully defined with the six conditions listed hereafter.

$$T_S(0,t) = T_{IN} \tag{3.22}$$

$$T_I(0,t) = T_{IN} \tag{3.23}$$

$$T_C(0,t) = T_{IN} \tag{3.24}$$

$$T_A(0,t) = T_{IN} \tag{3.25}$$

$$\frac{\partial T_I(L,t)}{\partial x} = 0 \tag{3.26}$$

$$\frac{\partial T_S(L,t)}{\partial x} = 0 \tag{3.27}$$

In the initial conditions, all temperatures are assumed to be equal to T_{IN} along the cell and the spatial derivatives of T_I and T_S are equal to zero.

$$T_S(x,0) = T_I(x,0) = T_C(x,0) = T_A(x,0) = T_{IN} \tag{3.28}$$

$$\frac{\partial T_I(x,0)}{\partial x} = \frac{\partial T_I(x,0)}{\partial x} = 0 \tag{3.29}$$

3.3.6. Description and implementation of the method of lines (MOL)

The method of lines (MOL) has been frequently used in the literature for solving heat transfer problems [252-255]. This method allows the conversion of a partial differential equation (PDE) in a system of ordinary differential equations (ODE), much easier to solve. Hence, this method was applied here.
As a first step, Equations (3.14) to (3.17) were discretized with the explicit method using Equations (3.30) and (3.31), n being the number of the node considered (see schematic representation of discretized system in Figure 3-3) and t the time (in s). They can be derived from an energy balance at a single node [250]. The derivative of x was expressed as its backward version in Equation (3.31).

$$\frac{\partial^2 T_S(x,t)}{\partial x^2} \approx \frac{T_S^{n+1} + T_S^{n-1} - 2 \cdot T_S^n}{\Delta x^2} \tag{3.30}$$

$$\frac{\partial T_C(x,t)}{\partial x} \approx \frac{T_C^n - T_C^{n-1}}{\Delta x} \tag{3.31}$$

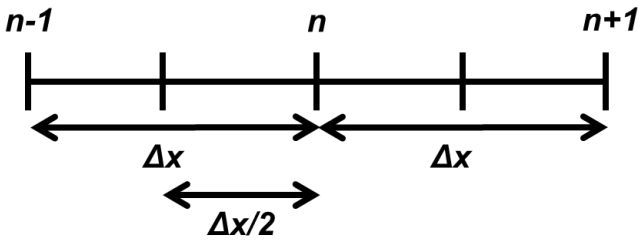


Figure 3-3: Schematic representation of the nodal network

In order to improve the model readability, the following constants were introduced (Equations (3.32) to (3.40)).

$$E_{CATH} = \frac{k_{CATH}}{\rho_{CATH,GAS} \cdot c_{P,CATH,GAS} \cdot e_{CATH,CH}} \tag{3.32}$$

$$E_{ANODE} = \frac{k_{ANODE}}{\rho_{ANODE,GAS} \cdot c_{P,ANODE,GAS} \cdot e_{ANODE,CH}} \tag{3.33}$$

$$A_{CELL} = \frac{\lambda_{CELL}}{\rho_{CELL} \cdot c_{P,CELL}} \tag{3.34}$$

$$B_{CELL} = \frac{k_{CATH}}{\rho_{CELL} \cdot c_{P,CELL} \cdot e_{CELL}} \tag{3.35}$$

$$G_{CELL} = \frac{k_{ANODE}}{\rho_{CELL} \cdot c_{P,CELL} \cdot e_{CELL}} \tag{3.36}$$

$$A_{INTER} = \frac{\lambda_{INTER}}{\rho_{INTER} \cdot c_{P,INTER}} \tag{3.37}$$

$$B_{INTER} = \frac{k_{CATH}}{\rho_{INTER} \cdot c_{P,INTER} \cdot e_{INTER}} \tag{3.38}$$

$$G_{INTER} = \frac{k_{ANODE}}{\rho_{INTER} \cdot c_{P,INTER} \cdot e_{INTER}} \tag{3.39}$$

$$Q_{CELL} = \frac{1}{\rho_{CELL} \cdot c_{P,CELL} \cdot e_{CELL}} \cdot \left[-\Delta H \cdot \frac{j}{2 \cdot F} + \frac{P_{EL}}{S}\right] \tag{3.40}$$

Using the constants defined above and the discretization of derivatives, the following discretized system of ODEs can be obtained at each node.

$$\frac{dT_C^n}{dt} = -u_{CATH} \cdot \frac{T_C^n - T_C^{n-1}}{\Delta x} + E_{CATH} \cdot \left(T_{S,t}^n + T_{I,t}^n - 2 \cdot T_{C,t}^n\right) \tag{3.41}$$

$$\frac{dT_A^n}{dt} = -u_{ANODE} \cdot \frac{T_A^n - T_A^{n-1}}{\Delta x} + E_{ANODE} \cdot \left(T_{S,t}^n + T_{I,t}^n - 2 \cdot T_{A,t}^n\right) \tag{3.42}$$

$$\frac{dT_I^n}{dt} = A_{INTER} \cdot \frac{T_I^{n+1} + T_I^{n-1} - 2 \cdot T_I^n}{\Delta x^2} - B_{INTER} \cdot \left(T_{I,t}^n - T_{C,t}^n\right) - G_{INTER} \cdot \left(T_{I,t}^n - T_{A,t}^n\right) \tag{3.43}$$

$$\frac{dT_S^n}{dt} = A_{CELL} \cdot \frac{T_S^{n+1} + T_S^{n-1} - 2 \cdot T_S^n}{\Delta x^2} - B_{CELL} \cdot \left(T_{S,t}^n - T_{C,t}^n\right) - G_{CELL} \cdot \left(T_{S,t}^n - T_{A,t}^n\right) + Q_{CELL} \tag{3.44}$$

The system of ODE was solved with the solver “ode15s” in MATLAB, which is best suited for stiff problems with short time constants.

3.3.7. Exact solution in permanent regime

The pathway towards exact solution in permanent regime will be presented hereafter. The exact solution in permanent regime will be used to verify the output of the simplified model in Chapter 3.4.2.3.

3.3.7.1. Conversion in array form

As explained earlier, the system is depicted with Equations (3.14) to (3.17). The following notations were applied hereafter for all the different temperatures considered in the model.

$$T_i(x,t) = T_i \tag{3.45}$$

$$\frac{\partial T_i(x,t)}{\partial x} = T_i' \tag{3.46}$$

$$Z_S = T_S' \tag{3.47}$$

$$Z_I = T_I' \tag{3.48}$$

As a result, the 2nd order Equations (3.16) and (3.17) can be converted in two 1st order equations, which enables to write down the following system.

$$\begin{aligned} T_S' &= Z_S \\ T_I' &= Z_I \\ T_C' &= \frac{E_{CATH}}{u_{CATH}} \cdot (T_S + T_I - 2 \cdot T_C) \\ T_A' &= \frac{E_{ANODE}}{u_{ANODE}} \cdot (T_S + T_I - 2 \cdot T_A) \\ Z_I' &= +\frac{B_{INTER}}{A_{INTER}} \cdot (T_I - T_C) + \frac{G_{INTER}}{A_{INTER}} \cdot (T_I - T_A) \\ Z_S' &= +\frac{B_{CELL}}{A_{CELL}} \cdot (T_S - T_C) + \frac{G_{CELL}}{A_{CELL}} \cdot (T_S - T_A) - \frac{Q_{CELL}}{A_{CELL}} \end{aligned} \tag{S1}$$

Which can be written as follows in matrix form:

$$\begin{pmatrix} T_S' \\ T_I' \\ T_C' \\ T_A' \\ Z_I' \\ Z_S' \end{pmatrix} = M \cdot \begin{pmatrix} T_S \\ T_I \\ T_C \\ T_A \\ Z_I \\ Z_S \end{pmatrix} + T$$

$$= \begin{pmatrix} 0 & 0 & 0 & 0 & 0 & 1 \\ 0 & 0 & 0 & 0 & 1 & 0 \\ \frac{E_{CATH}}{u_{CATH}} & \frac{E_{CATH}}{u_{CATH}} & \frac{-2 \cdot E_{CATH}}{u_{CATH}} & 0 & 0 & 0 \\ \frac{E_{ANODE}}{u_{ANODE}} & \frac{E_{ANODE}}{u_{ANODE}} & 0 & \frac{-2 \cdot E_{ANODE}}{u_{ANODE}} & 0 & 0 \\ 0 & \frac{B_{INTER} + G_{INTER}}{A_{INTER}} & \frac{-B_{INTER}}{A_{INTER}} & \frac{-G_{INTER}}{A_{INTER}} & 0 & 0 \\ \frac{B_{CELL} + G_{CELL}}{A_{CELL}} & 0 & \frac{-B_{CELL}}{A_{CELL}} & \frac{-G_{CELL}}{A_{CELL}} & 0 & 0 \end{pmatrix} \cdot \begin{pmatrix} T_S \\ T_I \\ T_C \\ T_A \\ Z_I \\ Z_S \end{pmatrix} + \begin{pmatrix} 0 \\ 0 \\ 0 \\ 0 \\ 0 \\ -\frac{Q_{CELL}}{A_{CELL}} \end{pmatrix} \tag{3.49}$$

3.3.7.2. Determination of the solution

The solution of the problem $U(x)$ can be decomposed in a general solution $U_{SG}(x)$ and a particular solution $U_{SP}(x)$ as presented hereafter, where the expression of $U(x)$ is provided in Equation (3.51).

$$U(x) = U_{SG}(x) + U_{SP}(x) \tag{3.50}$$

$$U(x) = \begin{pmatrix} T_S \\ T_I \\ T_C \\ T_A \\ Z_I \\ Z_S \end{pmatrix} \tag{3.51}$$

$U_{SG}(x)$ can be determined by reducing the matrix M (see Equation (3.49)) which can be done by determining its eigenvalues r_i and eigenvectors U_i. The usual approach to determine eigenvalues consists in factorizing the characteristic polynomial $P(\lambda)$ associated to the matrix, which is by definition:

$$P(\lambda) = det(M - \lambda \cdot I) = (-1)^n \cdot \prod_1^n (\lambda - r_i) \tag{3.52}$$

Since M is a 6 by 6 matrix, $P(\lambda)$ is a degree 6 polynomial and n is equal to 6. As for the eigenvectors U_i, they can be determined by the resolution of the systems of equations for each eigenvalue given by:

$$M \cdot \begin{pmatrix} u_1 \\ u_2 \\ u_3 \\ u_4 \\ u_5 \\ u_6 \end{pmatrix} = r_i \cdot \begin{pmatrix} u_1 \\ u_2 \\ u_3 \\ u_4 \\ u_5 \\ u_6 \end{pmatrix} \tag{3.53}$$

Several unsuccessful attempts were made to manually factorize the polynomial in order to determine the literal expressions of the eigenvalues. It was finally decided to use the MATLAB function "eig" to obtain the eigenvalues and their corresponding eigenvectors.
Finally, the expression of the general vector solution U_{SG} in permanent regime can be written as follows, where C_i corresponds to arbitrary constants which can be calculated with the initial and boundary conditions.

$$U_{SG}(x) = \sum_{i=1}^{n} C_i \cdot exp^{r_i \cdot x} \cdot U_i \tag{3.54}$$

As a second step, the particular solution $U_{SP}(x)$ can be determined assuming the following form of the solution.

$$U_{SP}(x) = V \cdot x + W = \begin{pmatrix} v_1 \\ v_2 \\ v_3 \\ v_4 \\ v_5 \\ v_6 \end{pmatrix} \cdot x + \begin{pmatrix} w_1 \\ w_2 \\ w_3 \\ w_4 \\ w_5 \\ w_6 \end{pmatrix} \tag{3.55}$$

The derivative of $U_{SP}(x)$ is therefore equal to:

$$U'_{SP}(x) = \begin{pmatrix} v_1 \\ v_2 \\ v_3 \\ v_4 \\ v_5 \\ v_6 \end{pmatrix} \tag{3.56}$$

$U_{SP}(x)$ has to verify Equation (3.49), hence:

$$\begin{pmatrix} v_1 \\ v_2 \\ v_3 \\ v_4 \\ v_5 \\ v_6 \end{pmatrix} = M \cdot \begin{pmatrix} v_1 \\ v_2 \\ v_3 \\ v_4 \\ v_5 \\ v_6 \end{pmatrix} \cdot x + M \cdot \begin{pmatrix} w_1 \\ w_2 \\ w_3 \\ w_4 \\ w_5 \\ w_6 \end{pmatrix} + \begin{pmatrix} 0 \\ 0 \\ 0 \\ 0 \\ 0 \\ -\frac{Q_{CELL}}{A_{CELL}} \end{pmatrix} \tag{3.57}$$

Thus, the solutions of the system are:

$$\begin{pmatrix} v_1 \\ v_2 \\ v_3 \\ v_4 \\ v_5 \\ v_6 \end{pmatrix} = \begin{pmatrix} v_4 \\ v_4 \\ v_4 \\ v_4 \\ 0 \\ 0 \end{pmatrix}; \begin{pmatrix} w_1 \\ w_2 \\ w_3 \\ w_4 \\ w_5 \\ w_6 \end{pmatrix}$$

$$= \begin{pmatrix} w_3 + \frac{1}{B_{CELL} + G_{CELL}} \cdot \left(Q_{CELL} + G_{CELL} \cdot \left(\frac{u_{CATH}}{E_{CATH}} - \frac{u_{ANODE}}{E_{ANODE}} \right) \cdot \frac{v_4}{2} \right) \\ w_3 + \frac{G_{INTER}}{B_{INTER} + G_{INTER}} \cdot \left(\frac{u_{CATH}}{E_{CATH}} - \frac{u_{ANODE}}{E_{ANODE}} \right) \cdot \frac{v_4}{2} \\ w_3 \\ w_3 + \left(\frac{u_{CATH}}{E_{CATH}} - \frac{u_{ANODE}}{E_{ANODE}} \right) \cdot \frac{v_4}{2} \\ v_4 \\ v_4 \end{pmatrix} \tag{3.58}$$

With

$$v_4 = \frac{\frac{E_{CATH} \cdot Q_{CELL}}{u_{CATH} \cdot (B_{CELL} + G_{CELL})}}{\left(1 - \frac{1}{2} \cdot \left(1 - \frac{u_{ANODE} \cdot E_{CATH}}{u_{CATH} \cdot E_{ANODE}} \right) \cdot \left(\frac{G_{CELL}}{B_{CELL} + G_{CELL}} + \frac{G_{INTER}}{B_{INTER} + G_{INTER}} \right) \right)} \tag{3.59}$$

The expression of the particular solution can be verified by injecting $U_{SP}(x)$ back in Equation (3.49). By superposition, the final solution in permanent regime $U(x)$ can be written as follows.

$$U(x) = \sum_{i=1}^{n} C_i \cdot exp^{r_i \cdot x} \cdot U_i + \begin{pmatrix} v_4 \\ v_4 \\ v_4 \\ v_4 \\ 0 \\ 0 \end{pmatrix} \cdot x$$

$$+ \begin{pmatrix} \frac{1}{B_{CELL} + G_{CELL}} \cdot \left(Q_{CELL} + G_{CELL} \cdot \left(\frac{u_{CATH}}{E_{CATH}} - \frac{u_{ANODE}}{E_{ANODE}} \right) \cdot \frac{v_4}{2} \right) \\ \frac{G_{INTER}}{B_{INTER} + G_{INTER}} \cdot \left(\frac{u_{CATH}}{E_{CATH}} - \frac{u_{ANODE}}{E_{ANODE}} \right) \cdot \frac{v_4}{2} \\ w_3 \\ \left(\frac{u_{CATH}}{E_{CATH}} - \frac{u_{ANODE}}{E_{ANODE}} \right) \cdot \frac{v_4}{2} \\ v_4 \\ v_4 \end{pmatrix} \tag{3.60}$$

The values of the constants C_i can be calculated by solving the system based on the initial and boundary conditions defined in Chapter 3.3.5.

3.4. Transient behavior

The results of the transient operation of SRUs with integrated ESCs and CSCs are presented and discussed in this Chapter. In a first part, the transients applied to the SRUs will be shortly described. In a second part, the results of the transients applied to the simplified model will be detailed, where the ASR is assumed to be constant. In a third part, the results of the extended model are presented, where the ASR is a function of the temperature at each node. The results will be discussed in a third part.

3.4.1. Definition of the transients

The transients considered correspond to the transition from hot standby to either exothermic or endothermic operation. The electrical power injected in the cell required for the thermoneutral operation was calculated iteratively until the outlet and inlet gas temperatures were identical. The electrical power injected in the cell in exothermic mode was then assumed arbitrary to be 20% higher than the electrical load in thermoneutral mode and to be 20% lower in endothermic mode. The steam and the air flow rates at the cathode and at the anode were assumed to be constant during the transients and their initial values were supposed to be instantly adapted to the electrical load in order to obtain the targeted steam conversion rate of 70%.

3.4.2. SRU with integrated ESC (simplified model)

The results of the transients applied on SRUs with integrated ESC are presented hereafter. In addition, two verifications of the model are proposed. First, the temperature profiles of the dynamic model after transient were compared to those of the exact solution in permanent regime determined in Chapter 3.3.7. The corresponding results are presented for ESCs only, even though the same methodology was successfully applied for CSCs. Second, the cathode gases temperature profiles of the model in permanent regime will be compared with those reported by Cai et al. in [142].

3.4.2.1. Transient behavior – exothermic mode

The evolution of the cell temperature in exothermic mode is represented at each node in Figure 3-4. Similar temperature profiles were observed for the interconnect, the cathode, and the anode gases temperatures. The simulation was run for a total of 15 nodes for a better readability of results. For all temperature graphs, the bottom curve corresponds to the temperature profile at the node which is the closest to the SRU inlet, whereas the top curve corresponds to the temperature profile at the node which is the closest to the SRU outlet. The electrical power injected in the ESC depicted in Table 3-1 is about 83.2 W in thermoneutral mode, which means that the electrical power in exothermic mode with an overload of 20% is about 99.8 W. The permanent regime was reached after approx. 800 s (13 min) at the node closest to the SRU outlet.

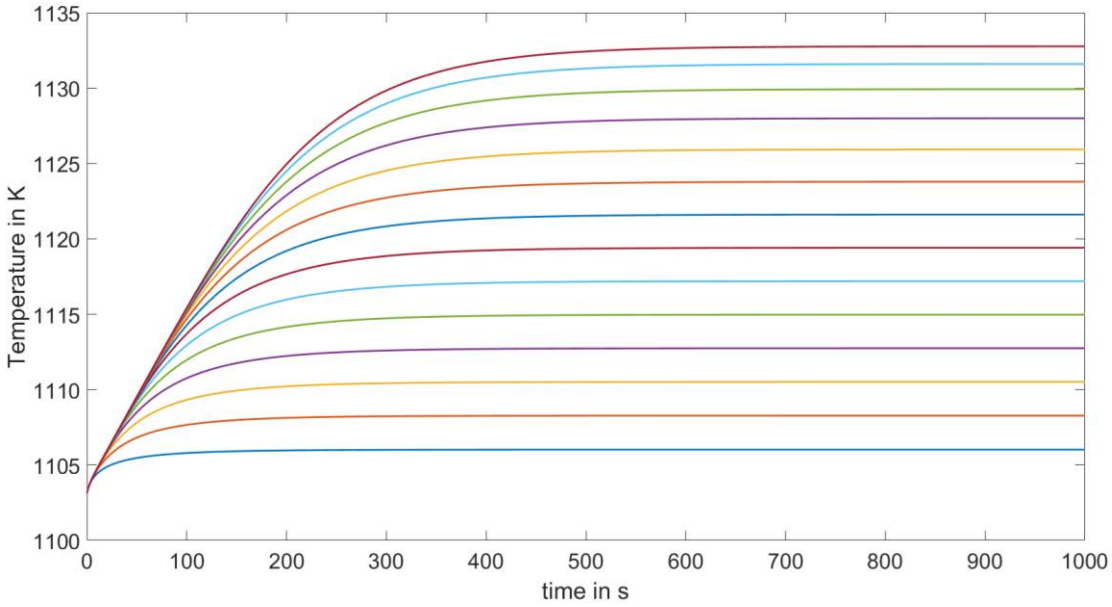


Figure 3-4: Evolution of the cell temperature at the different nodes in endothermic mode (ESC, simplified model)

The different values of thermal gradient calculated after 800 s for a simulation with 100 nodes are summarized in Table 3-2.

Table 3-2: Maximal thermal gradient values along the cell, the interconnect, and the cathode and anode channels for the SRU with integrated ESC in exothermic mode

	Cell	**Interconnect**	**Cathode gases**	**Anode gases**
Inlet temperature (K)	1103 K			
Maximal thermal gradient along the SRU (K)	31.4	30.5	30.9	30.8

Since no overshoot was observed during the transients, the next graphs of transients will only represent the transients at the node closest to the SRU outlet. This will enable to visualize the maximal thermal gradient for each temperature.
Furthermore, the thermal gradients observed for each temperature are very close, as can be seen in Table 3-2. Hence, only the cell temperature transient will be represented in the next graphs, as it is the most critical temperature to be controlled in the SRU.

3.4.2.2. Transient behavior – endothermic mode

The evolution of the cell temperature in endothermic mode is represented in Figure 3-5 at the node closest to the SRU outlet. As a reminder, the electrical power in endothermic mode with a power load of 80% is about 66.5 W. Similarly to the exothermic mode, the permanent regime was reached after 800 s (~13 min) at the node closest to the SRU outlet.

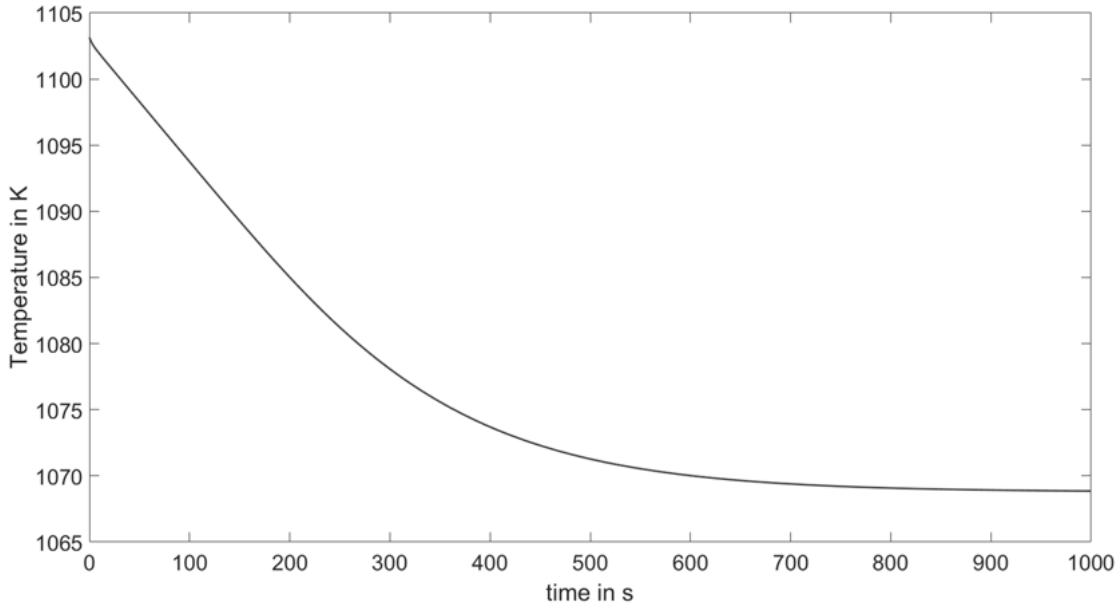


Figure 3-5: Evolution of the cell temperature at the node closest to the SRU outlet in endothermic mode (ESC, simplified model)

The different values of thermal gradient calculated after 800 s for a simulation with 100 nodes are summarized in Table 3-3.

Table 3-3: Maximal thermal gradient values along the cell, the interconnect, and the cathode and anode channels for the SRU with integrated ESC in exothermic mode

	Cell	**Interconnect**	**Cathode gases**	**Anode gases**
Inlet temperature (K)	1103 K			
Maximal thermal gradient along the SRU (K)	34.1	33.3	33.7	33.6

3.4.2.3. Verification with exact solution in permanent regime

The temperature profiles in permanent regime are represented in exothermic and in endothermic mode in Figure 3-6 and in Figure 3-7 respectively.

In both cases, the temperature profiles of the model are very close to the temperature profiles of the exact solution in permanent regime. Hence, the final temperature values obtained in the simplified model are verified. The model resolution was intentionally lowered down using a small number of nodes (only 30) in Figure 3-6 and in Figure 3-7 in order to discern the model output and the exact solution in permanent regime, which was difficult for a high number of nodes (above 100).

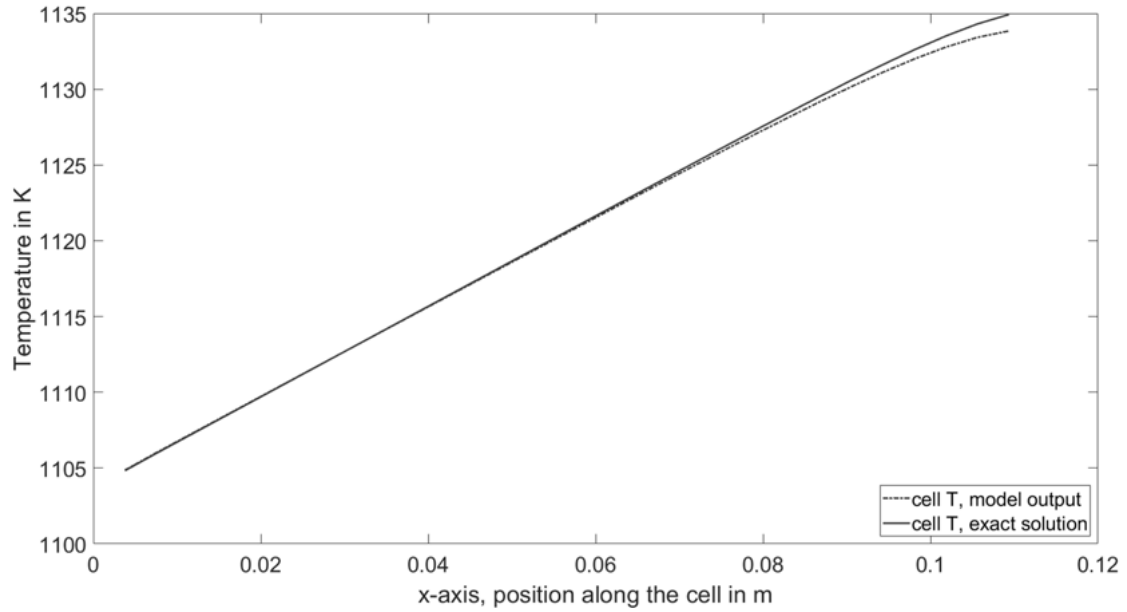


Figure 3-6: Comparison of the cell temperature profiles of the model and in permanent regime in exothermic mode (model output vs. exact solution)

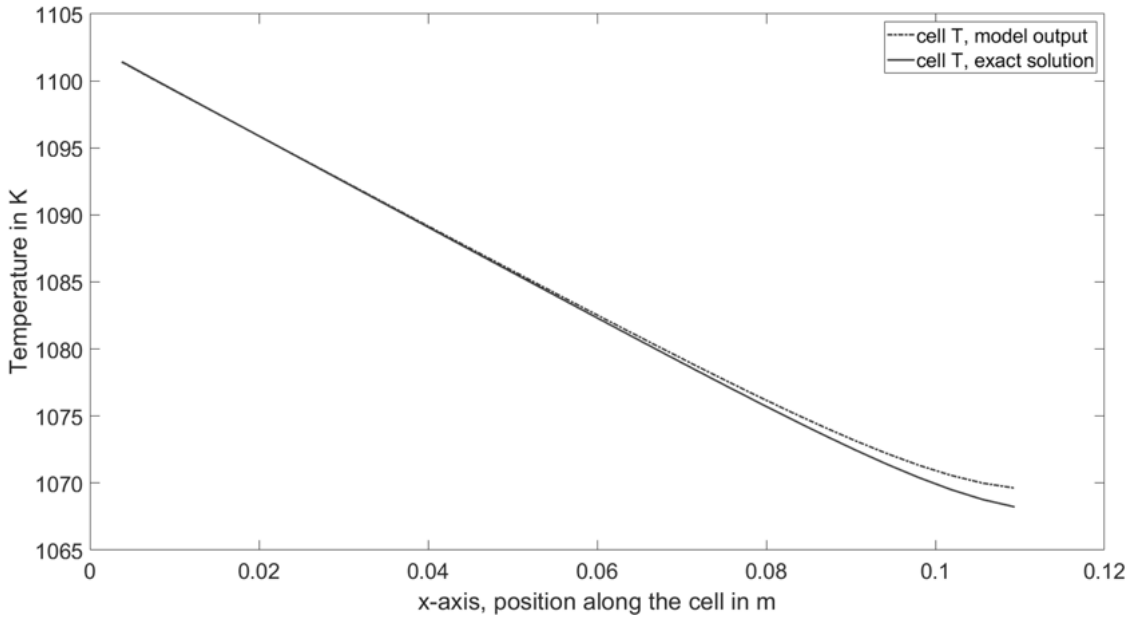


Figure 3-7: Comparison of the cell temperature profiles of the model and in permanent regime in endothermic mode (model output vs. exact solution)

3.4.3. SRU with integrated CSC (simplified model)

3.4.3.1. Transient behavior

The transient behavior of a SRU with integrated CSC was investigated following the same methodology than in Chapter 3.4.2.

The electrical power injected in a CSC depicted in Table 3-1 in thermoneutral mode is about 178.1 W, which means that the electrical power in exothermic mode with an electrical load 20% higher than in

thermoneutral mode is about 213.7 W and that the electrical power injected in endothermic mode at 80% of the electrical load in thermoneutral mode is about 142.4 W.
The evolution of the cell temperature at the node closest to the SRU outlet in exothermic and in endothermic modes are shown in Figure 3-8 and in Figure 3-9 respectively. The simulation was run for a total of 100 nodes.

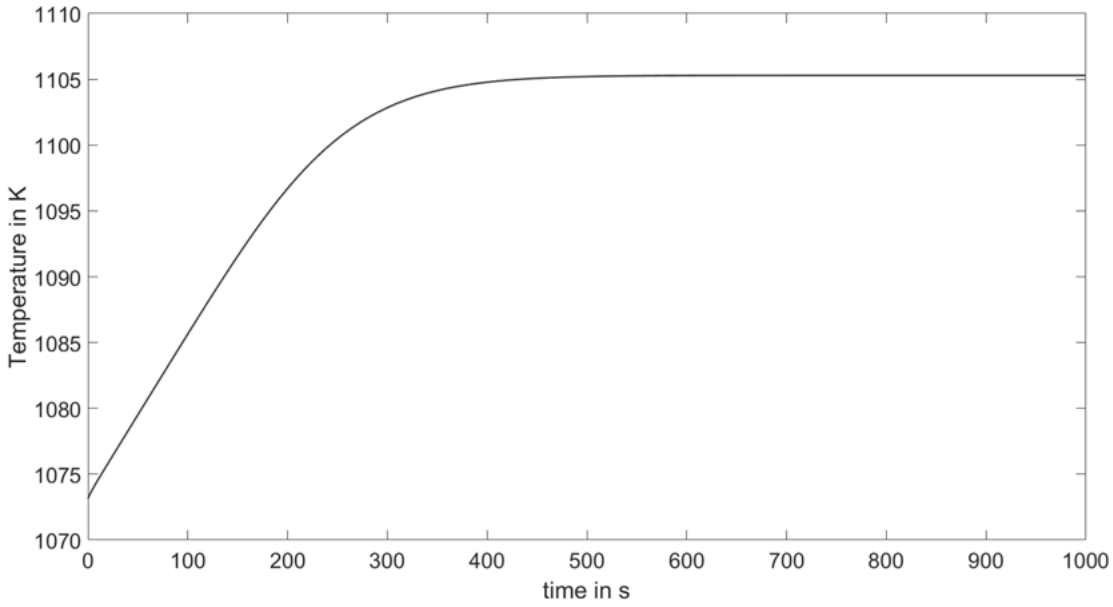


Figure 3-8: Evolution of the cell temperature at the node closest to the SRU outlet in exothermic mode (CSC, simplified model)

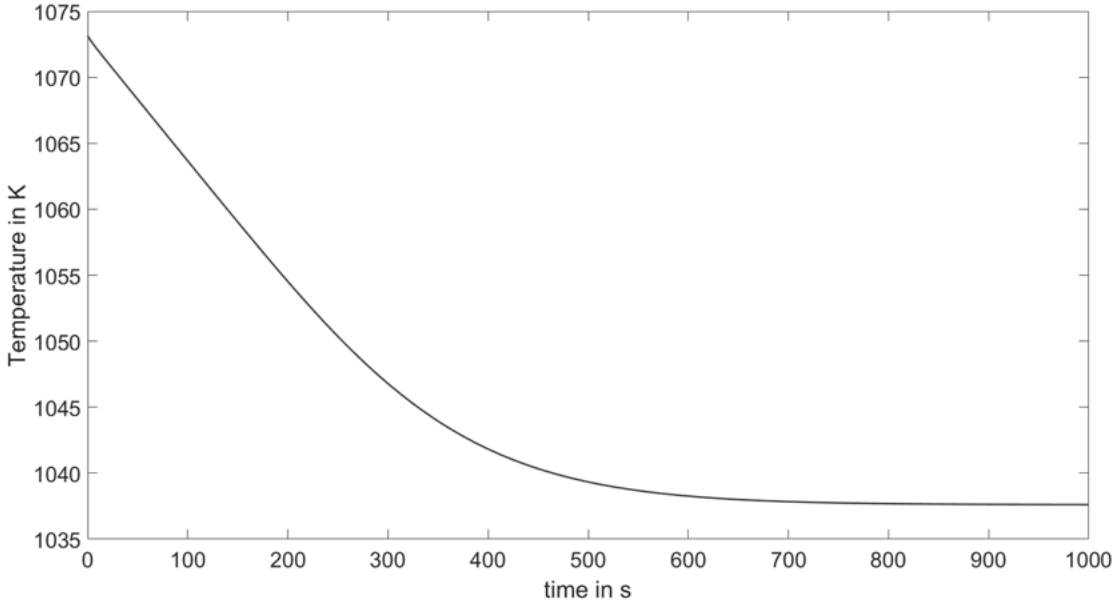


Figure 3-9: Evolution of the cell temperature at the node closest to the SRU outlet in endothermic mode (CSC, simplified model)

The permanent regime was reached after approx. 800 s (~13 min) at the node closest to the SRU outlet. The different values of thermal gradient calculated after 800 s are summarized in Table 3-4.

Table 3-4: Maximal thermal gradient values for the SRU with integrated CSC in exothermic and in endothermic mode (simplified model)

	Cell	Interconnect	Cathode gases	Anode gases
Maximal thermal gradient along the SRU in exothermic mode (K)	32.2	30.6	31.3	30.9
Maximal thermal gradient along the SRU in endothermic mode (K)	35.5	34.1	34.7	34.5

3.4.3.2. Comparison with previous modelling work

In this paragraph, the transient behavior of the simplified model will be compared with a previous 1D dynamic model of a SRU with integrated CSC implemented by Cai et al. in [142]. The objective here will be to compare the temperature profiles and thermal gradients in permanent regime for two operating points with different values of air ratio (0.4 and 14) in endothermic mode, assuming the same input parameters, which are listed in Appendix B. Since no relation between ASR and the temperature was provided in [142], it was assumed that the ASR was constant at 0.35 $\Omega \cdot cm^2$, which corresponds to the ASR value provided in [142] for thermoneutral operation at 1073 K.

Under these conditions, the current density at thermoneutral voltage in the simplified model was 0.96 $A \cdot cm^{-2}$, against 1.04 $A \cdot cm^{-2}$ in [142].

The cathode gases temperature profiles in permanent regime of the simplified model in similar conditions than in the model of Cai et al. (e.g. at a current density corresponding to 70% of that in thermoneutral mode) are presented in Figure 3-10.

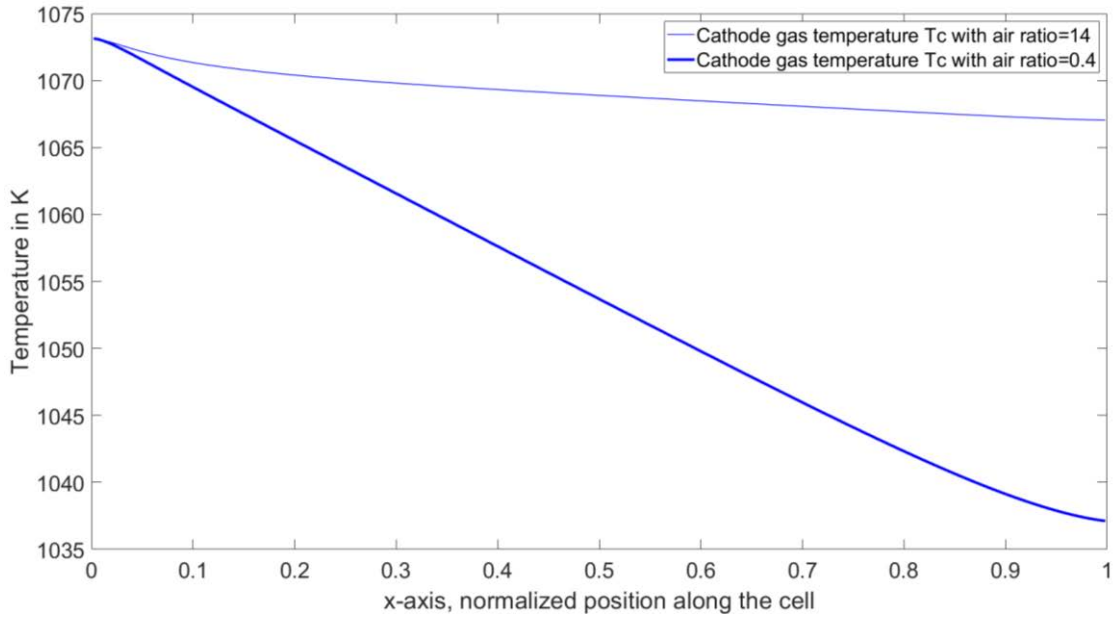


Figure 3-10: Cathode gas temperature distribution along the cell at a current density of 70% of the thermoneutral operation point in the simplified model

The aspect of the temperature profiles are similar in the model of Cai et al. and in the simplified model. The cathode stream outlet temperature for an air ratio of 14 is about 1067 K in this work, compared to 1056 K in [142], which corresponds to an error of 1.0%. Hence, the maximal temperature gradient for an air ratio of 14 is about 6 K in the simplified model, whereas it is about 17 K in [142]. In case of an air ratio of 0.4, the cathode stream outlet temperature is about 1037 K in this work, compared to 1025 K in [142],

which corresponds to an error of 1.2%. As a result, the maximal temperature gradient is about 36 K in the simplified model, whereas it is about 48 K in [142].
In conclusion, the simplified SRU model implemented in this work provides cathode stream outlet temperatures with an acceptable error of max. 1.2% compared to the model implemented by Cai et al. in [142]. Thus, it can be considered verified in endothermic mode (in the range of 70-100% of the current density in thermoneutral operation) and for air ratios in the range of 0.4-14.

3.4.4. SRU with integrated ESC (extended model)

The transient behavior of a SRU with integrated ESC was investigated with the extended model, where the ASR is a function of the cell temperature T_S, using the same methodology applied in Chapter 3.4.2 and 3.4.3.
The electrical power injected in the SRU (see details in Table 3-1) in thermoneutral mode is about 83.9 W, which is slightly higher than the one of the simplified model. The electrical power required in exothermic and endothermic mode are still 20% above and under the electrical power required in thermoneutral mode, which corresponds to 100.7 W and to 67.1 W respectively.
The evolution of the cell temperature in exothermic and in endothermic modes at the node closest to the SRU outlet are shown in Figure 3-11 and in Figure 3-12 respectively. The simulation was run for a total of 100 nodes.

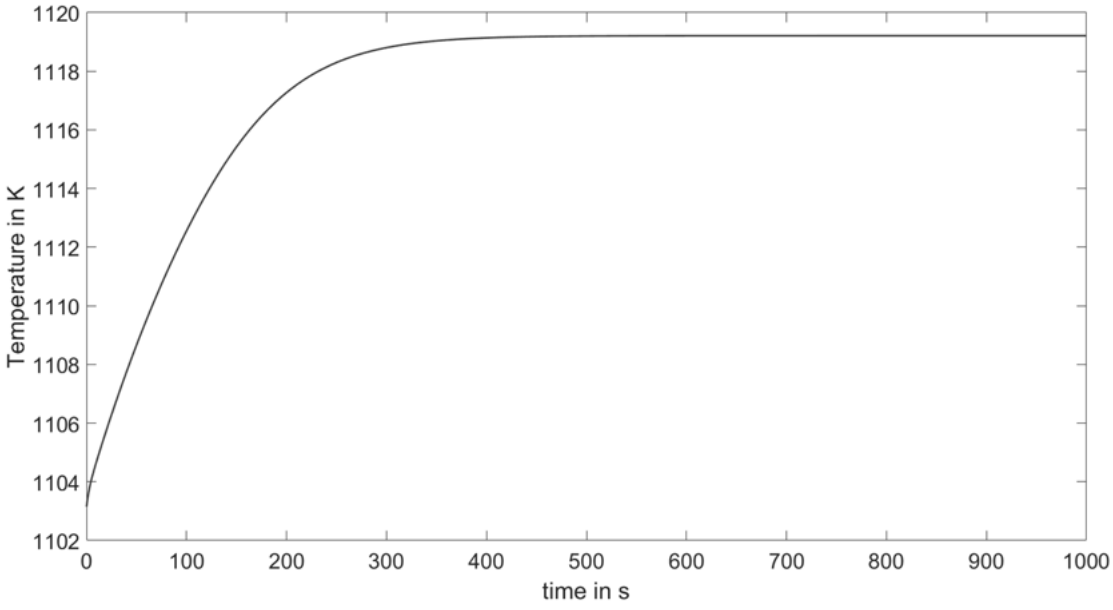


Figure 3-11: Evolution of the cell temperature at the node closest to the SRU outlet in exothermic mode (ESC, extended model)

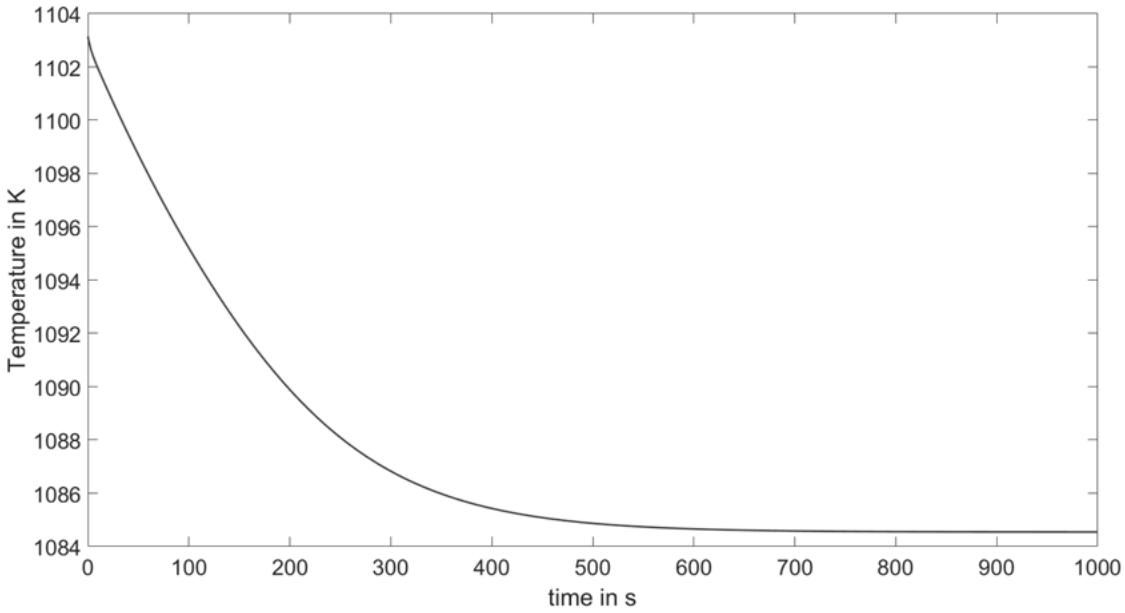


Figure 3-12: Evolution of the cell temperature at the node closest to the SRU outlet in endothermic mode (ESC, extended model)

The permanent regime was reached after approx. 700 s (~12 min) at the node closest to the SRU outlet. The different values of thermal gradient calculated after 700 s are summarized in Table 3-5.

Table 3-5: Maximal thermal gradient values along the SRU in exothermic and in endothermic mode (ESC, extended model)

	Cell	**Interconnect**	**Cathode gases**	**Anode gases**
Maximal thermal gradient along the SRU in exothermic mode (K)	16.1	15.8	15.9	15.9
Maximal thermal gradient along the SRU in endothermic mode (K)	18.6	18.3	18.4	18.4

3.4.5. SRU with integrated CSC (extended model)

The transient behavior of SRU with integrated CSC was also investigated with the extended model.
The electrical power injected in the SRU (see details in Table 3-1) in thermoneutral mode is about 212.5 W, which is slightly higher than the one of the simplified model. The electrical power required in exothermic and endothermic mode are still assumed to be 20% above and under the electrical power required in thermoneutral mode, which corresponds to 212.5 W and to 141.6 W respectively.
The evolution of the different temperatures in exothermic and in endothermic modes are shown in Figure 3-13 and in Figure 3-14 respectively. For each temperature, it was chosen to plot only the profiles of the node closest to the SRU outlet in order to visualize the maximal thermal gradient along the SRU for each temperature. The simulation was run for a total of 100 nodes.

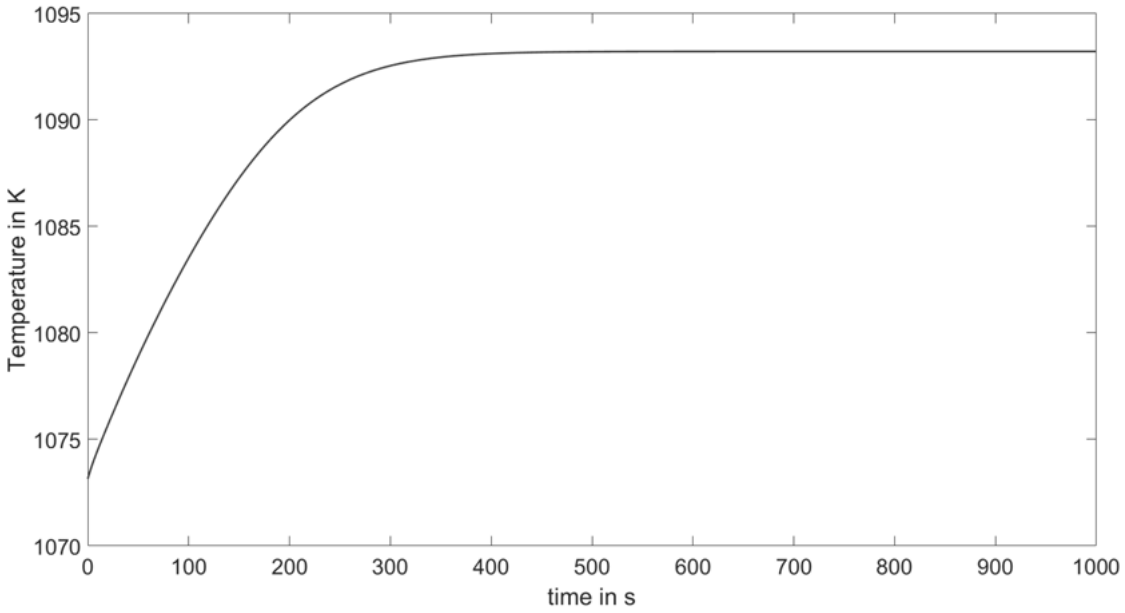


Figure 3-13: Evolution of the cell temperature at the node closest to the SRU outlet in exothermic mode (CSC, extended model)

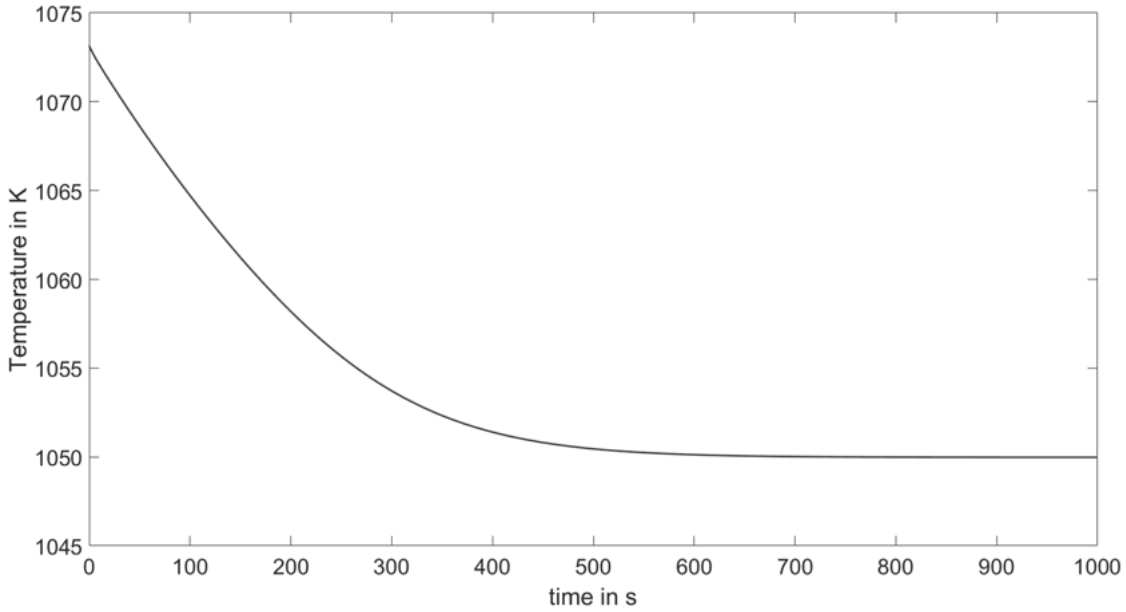


Figure 3-14: Evolution of the cell temperature at the node closest to the SRU outlet in endothermic mode (CSC, extended model)

The permanent regime was reached after approx. 700 s (~12 min) at the node closest to the SRU outlet. The different values of thermal gradient calculated after 700 s are summarized in Table 3-6.

Table 3-6: Maximal thermal gradient values along the SRU in exothermic and in endothermic mode (CSC, extended model)

	Cell	Interconnect	Cathode gases	Anode gases
Maximal thermal gradient along the SRU in exothermic mode (K)	20.1	19.4	19.7	19.6
Maximal thermal gradient along the SRU in endothermic mode (K)	23.1	22.5	22.8	22.7

3.4.6. Results discussion

3.4.6.1. Comparison of CSC and ESC performance

In both simplified and extended models, the electrical power injected in the cell to reach thermoneutral voltage is roughly 70% higher for CSCs than for ESCs (e.g. 142 W for CSCs and 84 W for ESCs in the extended model). Since the electrolyte is much thinner in CSCs, the ASR of CSCs at a given temperature is much lower than that of ESCs (e.g. 0.25 $\Omega \cdot cm^2$ compared to 0.69 $\Omega \cdot cm^2$ at 1073 K). Hence, the ohmic losses in CSCs are significantly lower than in ESCs for the same electrical power input and the electrical power injected in CSCs to reach thermoneutral operation is significantly higher.

3.4.6.2. Thermal gradient

The maximal thermal gradient values along SRUs with integrated ESC and CSC are in the range of 31-36 K for all temperatures (cell, interconnect, anode and cathode gas streams) in the simplified model. As a reminder, the heat generated at each node in both simplified and extended models is function of the difference between operating voltage and thermoneutral voltage (see Equation (3.18)). In the simplified model, the operating voltage in exothermic mode is almost equal for CSCs and ESCs, as is the case in endothermic mode. Hence, the heat generated at each node in both cell types is almost equal and the maximal thermal gradient observed are therefore almost equal. This is not verified in the extended model though, because the ASR varies with the temperature. Indeed, the maximal thermal gradients observed in the extended model are in the range of 19-23 K for SRUs with integrated CSCs and in the range of 16-19 K for SRUs with integrated ESCs. The thermal gradients with CSCs are lower because the ASR of the CSCs considered in this work is less sensible to the temperature than the ASR of ESCs. Based on the ASR value at 1123K, the ASR of CSCs increases by 0.5% when the temperature diminishes by 1 degree, whereas it increases by 1% in the case of ESCs.
The thermal gradient values observed in the extended model are lower than in the simplified model because the ASR varies with the temperature, whereas it is constant in the simplified model. During the transient from hot standby to exothermic mode, the temperature increases, which results in a decrease of the ASR and a reduction of the ohmic losses along the cell. The thermal gradient is therefore lower. Similarly, during the transient from hot standby to endothermic mode, the temperature decreases, which results in an increase of the ASR and an increase of the ohmic losses along the cell. The thermal gradient is also lower. As a consequence, the approximation of a constant ASR made in the simplified model results in a significant loss of accuracy regarding the thermal behavior of the SRU and this simplification hypothesis should be avoided.

The maximal load variations that could theoretically be applicable to the SRUs were also investigated in this work. Based on previous work of Nakajo et al. in [256], it is preferable to limit the local temperature gradients along SOECs to a value of 10 $K \cdot cm^{-1}$ in order to reduce the risks of cell failure. This value was also considered in previous SOEC modelling work [38, 142]. The cell temperature profiles obtained in

this work show that the highest values of local thermal gradient should be observed close to the cell inlet and that the local thermal gradient slowly decreases until the cell outlet (see Figure 3-15).

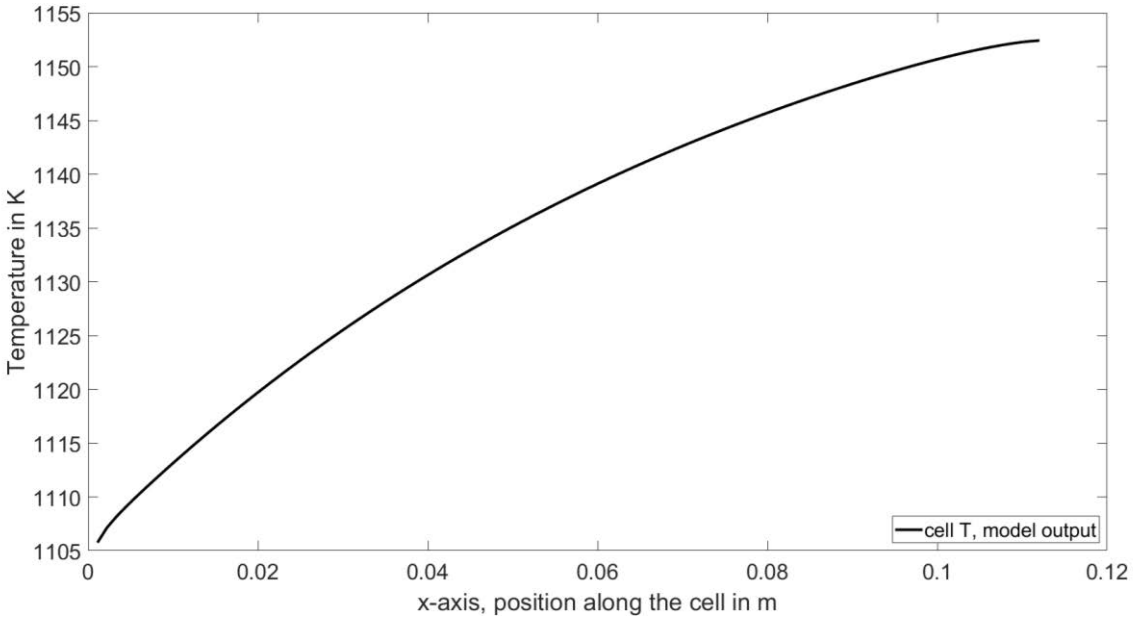


Figure 3-15: Cell temperature profile in exothermic mode corresponding to a maximal local temperature gradient of 10 K·cm^{-1} (SRU with integrated ESC)

Hence, the maximal local thermal gradient is reached along the first centimeter of cell. Therefore, it was sufficient to calculate the thermal gradient along the first centimeter of cell to ensure that the aforementioned condition on the thermal gradient was respected along the entire cell. The maximal and minimal electrical load levels allowed in exothermic and endothermic modes and the corresponding temperature gradients along the cells are reported in the first two rows of Table 3-7 for the different cell types and operating modes, each time with the corresponding average cell operating voltage and current density. In all cases, the air ratio is equal to 2.

These results seem to invalidate the hypothesis of a linear temperature profile along the cell. This approximation would result in a significant overestimation of the temperature gradient allowed along the cell, which would be about 114 K in the linear case (the cell length is 11.4 cm) against 49-68 K in this work (see Table 3-7).

Furthermore, the maximal local cell voltage in exothermic mode is about 1.43 V for ESCs and about 1.4 V in the case of CSCs, which is high. This value should be reduced in order to limit local overvoltages and lower the risk of cell failure. Hence, a maximal local cell voltage of 1.35 V was assumed and the corresponding values of power load and thermal gradient are reported in the two last rows of Table 3-7.

Table 3-7: Maximal and minimal electrical power load injectable in the SRU starting from hot-standby to enable a maximal local cell temperature gradient of 10 K·cm^{-1} and corresponding temperature gradient along the cell (extended model)

	SRU with ESC		**SRU with CSC**	
	Exothermic	**Endothermic**	**Exothermic**	**Endothermic**
Initial temperature (K)	1103		1073	
Percentage of electrical power load in thermoneutral mode (%)	171 (1.33 V, 0.82 A·cm^{-2})	43 (1.19 V, 0.24 A·cm^{-2})	158 (1.36 V, 1.61 A·cm^{-2})	49 (1.19 V, 0.57 A·cm^{-2})

	SRU with ESC		SRU with CSC	
	Exothermic	**Endothermic**	**Exothermic**	**Endothermic**
Maximal thermal gradient along the cell (absolute value, K)	49.3	62.4	52.1	67.6
Percentage of electrical power load in thermoneutral mode with a max local voltage of 1.35 V (%)	128 (1.31 V, 0.64 A·cm^{-2})	Same as above	131 (1.33 V, 1.36 A·cm^{-2})	Same as above
Maximal thermal gradient along the cell for a max. local voltage of 1.35 V (absolute value, K)	21.9	Same as above	30.1	Same as above

Because of the higher ASR, the thermal gradient along SRUs with integrated ESCs are lower than with CSCs when operated within similar electrical power range. Since they present a higher thermal stability, they should be preferred for fluctuating power applications. As a result, the SRUs considered in the following modelling work will only integrate ESCs. However, the higher ASR of ESCs implies current densities (and therefore H_2 production) roughly twice as low (for the same power input), which results in higher footprint of SOE units with ESCs than with CSCs.
Furthermore, the limitation of the electrical power range in exothermic mode to limit the local operation voltage should be refined in future investigations with more accurate calculations of the local voltage with gas compositions profiles calculated at each node rather than with average gas compositions.

3.4.6.3. Time constant

As was observed in [137], the time constant is strongly dependant on the thermal diffusivity a (in m^2.s^{-1}), which corresponds to the ratio of the thermal conductivity of a material divided by the product of its heat capacity with its density (see Equation (3.34)).

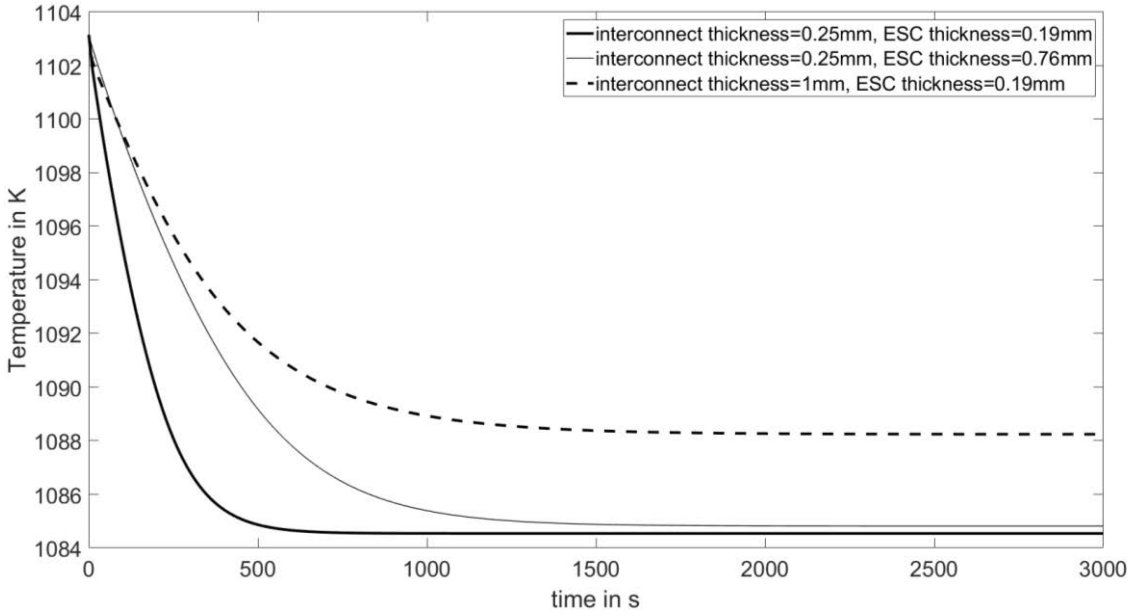


Figure 3-16: Evolution of the ESC outlet temperature in endothermic mode for different values of interconnect and cell thickness (extended model)

The influence of the SRU mass on the time constant is presented in Figure 3-16. The interconnect and the cell thickness were varied for an SRU with integrated ESC. The interconnect thickness was multiplied by a factor four to reach 1 mm and the cell thickness was also multiplied by a factor four to reach 0.76 mm. The increase of cell thickness resulted in a time constant increase from 700 s to approx. 2000 s, but had almost no influence on the cell thermal gradient. The increase of cell thickness lowers the value of the convective heat transfer coefficient in Equation (3.17), hence the heat generated in the cell takes longer to be driven out of the SRU by the anode and cathode gas streams. However, the thermal diffusivity of the cell is significantly lower than that of the interconnect ($7.1 \cdot 10^{-7}$ $m^2 \cdot s^{-1}$ against $6.0 \cdot 10^{-6}$ $m^2 \cdot s^{-1}$ for the interconnect). Hence, the thermal gradient remains almost unchanged compared to the reference case. In case of a thicker interconnect though, the thermal gradient observed along the cell is lower (15 K compared to 18 K in the reference case). Since the interconnect is thicker, a higher amount of heat is transferred to the stream gases in endothermic mode and at a faster pace than from the cell, because the interconnect thermal diffusivity is higher. As a result, the thermal gradient is lower than in the reference case. The increase of interconnect thickness also reduces the convective heat transfer coefficient in Equation (3.16), which slows down the evacuation of the interconnect heat by the stream gases, thus increasing the time constant. Another consequence not taken into account in this work is that the interconnect thickness increase would result in an ASR increase of the SRU, which would also reduce the temperature gradient along the cell.

As it is often delicate to have exhaustive description of the geometric and physicochemicals properties of the equipement modelled in previous work, the time constant obtained in this work could only be qualitatively compared with previous literature values, in order to ensure that the values obtained are realistic. In [137], the time constant was approx. 1020 s (approx. 17 min). A similar value was obtained in [136]. In this work, the time constant is in the range of about 700-800 s. The main reason for these lower values is probably the lower amount of material used for the SRUs, mostly for the interconnect, but also for the cells, whose thickness has been significantly reduced in the past ten years. Another explanation could be the boundary conditions, which might also have a significant influence on the time constant, as

was also reported e.g. in [137]. A transient duration from hot standby to nominal operation of 24 min was reported for the SOE unit implemented during the GrinHy project [257]. However, this value is a conservative estimate because it was obtained in mild load variation conditions to limit cell degradation. Hence, it is likely that significantly lower durations could be achieved.
The time constants reported in this work were lower in the extended model (700 s) than in the simplified model (800 s). When the ASR was assumed to be constant, the heat produced in the cell during the transient was underestimated in endothermic mode (or overestimated in exothermic mode). Hence, a longer time horizon was required to reach the permanent regime in the simplified model.
Furthermore, simulations at different load levels also show that the time constant does not depend on the load variation, which is also coherent with observations made in previous work [137, 138].

3.5. Coupling with power profiles

The SRU response to different electrical power profiles was investigated hereafter with the extended model. In a first step, a simplified power profile composed of different power thresholds was applied to each type of SRU to visualize the transient response, to verify the coherence with the profiles obtained in Chapter 3.4.4 and 3.4.5, and to check the stability of the response in different transient configurations. In a second step, a wind power profile was applied to the SRUs and hydrogen production profiles were obtained. As a result, a first dimensioning of a hydrogen storage unit equipped with a conventional tank was determined. Different options to reduce the size of the hydrogen tank were discussed.

3.5.1. SRU model with simplified power profile

The simplified electrical power profiles were defined based on the electrical power injected in each cell type to reach thermoneutral operation P_{TH} (in W). They are chronologically depicted hereafter.

- At $t = 0$, the SRU is supposed to be in hot standby mode, where the initial temperature in the SRU is everywhere 1073 K (SRU with CSC) or 1103 K (SRU with ESC).
- From $t = 1$ to $t = 600\,s$: a first electrical power threshold to reach exothermic operation corresponding to $1.2 \cdot P_{TH}$ is injected in the cell.
- From $t = 601$ to $t = 1200\,s$: the electrical power is lowered down to P_{TH} back to the thermoneutral operation point.
- From $t = 1201$ to $t = 1800\,s$: the electrical power is lowered down to $0.8 \cdot P_{TH}$ to reach endothermic operation.
- From $t = 1801$ to $t = 2400\,s$: the electrical power in endothermic mode is further reduced down to $0.6 \cdot P_{TH}$.
- From $t = 2401$ to $t = 3000\,s$: the electrical power is increased back to $1.2 \cdot P_{TH}$ to reach exothermic operation.

The electrical power profile and the hydrogen production applied to the different SRUs are represented in Figure 3-17. The evolution of the temperature is represented in Figure 3-18 and is coherent with the transients reported in Chapters 3.4.4 and 3.4.5. The H_2 production profile also presents a transient behavior, because the ASR depends on the cell temperature. When the cell temperature increases, the ASR decreases and the H_2 production increases. When the cell temperature decreases, the ASR increases and the H_2 production decreases.

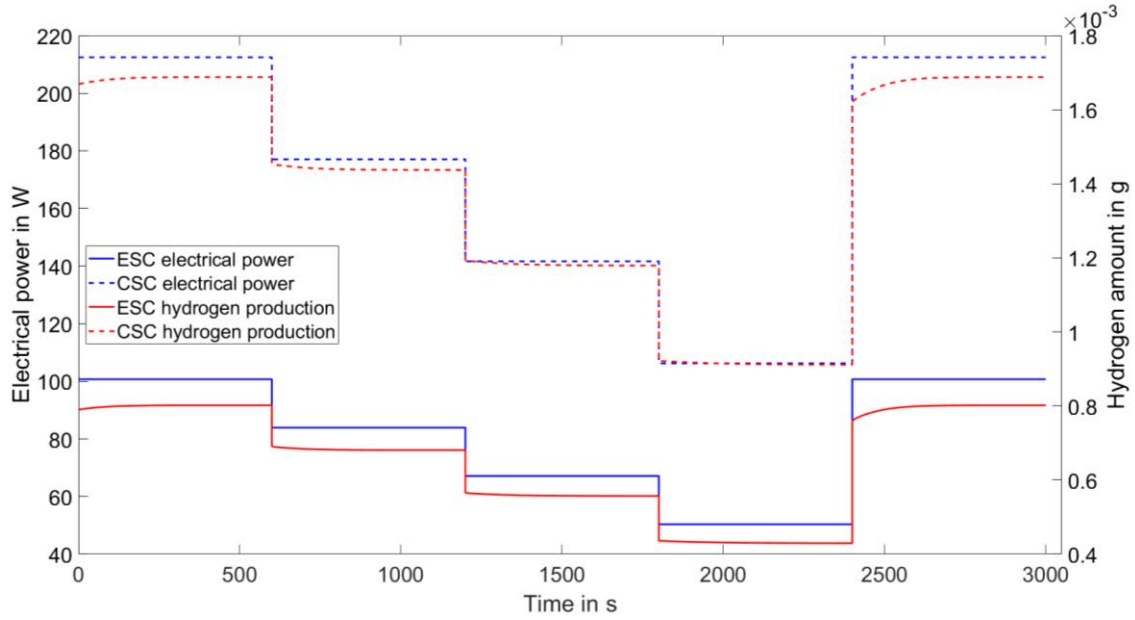


Figure 3-17: Simplified electrical power profiles and hydrogen production of the ESC and CSC

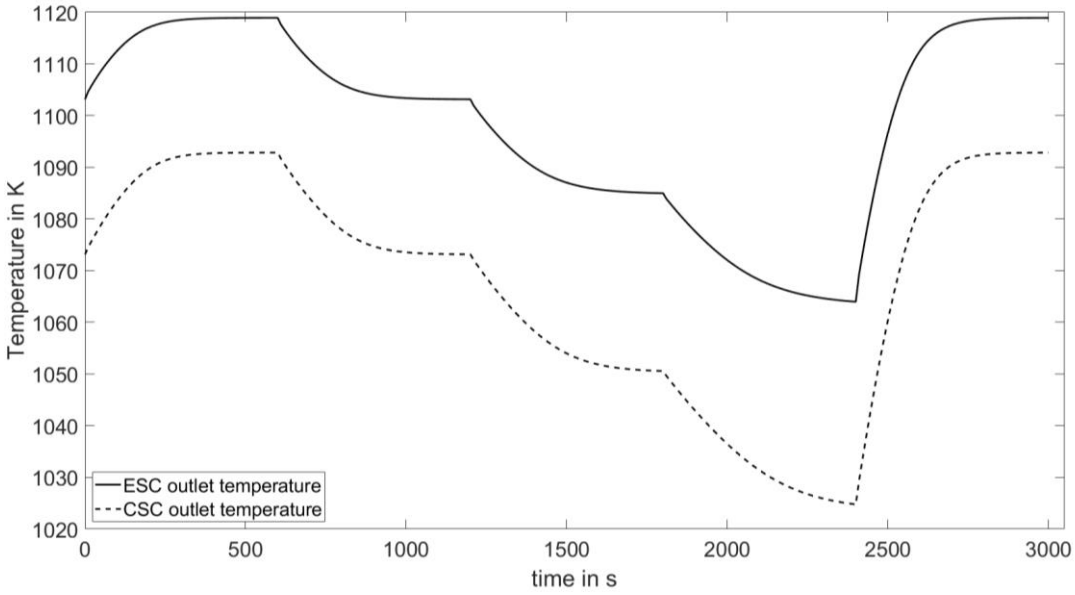


Figure 3-18: Evolution of the ESC and CSC outlet temperatures under simplified power profile

3.5.2. H_2 production and storage unit with simplified power profile

3.5.2.1. Description of the hydrogen production and storage unit

The layout of the hydrogen production and storage unit is schematically represented in Figure 3-19. The hydrogen production unit is composed by two SOE modules and all BoPs required for their operation (heat exchangers, heaters). Its overall architecture corresponds to that of SOE units at present [96]. For each SOE module, the nominal electrical power input of the stacks is 1 MW, so that the nominal power of the SOE unit matches that of the windmill (2 MW after AC/DC conversion). The behavior of all cells in a stack is supposed to be homogeneous, and each cell type (CSC or ESC) is assumed to be operated

either in endothermic or in exothermic mode within the electrical power range defined in Table 3-7. The cell degradation is not taken into account.

H_2 production units also include at least a water pump and an air blower. However, as they only represent a small share of the total electrical unit consumption, they were neglected and therefore not represented in the layout. An admission air temperature of 298 K was assumed and the steam required for the SOE unit was provided at 473 K by the methanation unit. Therefore, the energy consumption required for steam generation was not taken into account in the analysis.

Once produced, the hydrogen rich gas is sent to the drying unit. First, the gas enters a condenser, where most of the steam is condensed by cooling. The dry gas is then compressed up to 10 bar in a two stage mechanical compressor and sent to a pressure swing adsorption unit (PSA), where the remaining steam is then extracted. The high purity H_2 is then compressed from 10 to 40 bar in a single stage mechanical compressor and cooled down before being injected to the H_2 storage tank, where it is stored at 40 bar. It is then fed to the catalytic methanation unit for direct use at 20 bar. The dimensioning of the H_2 storage tank will be discussed in Chapter 3.5.3.2.

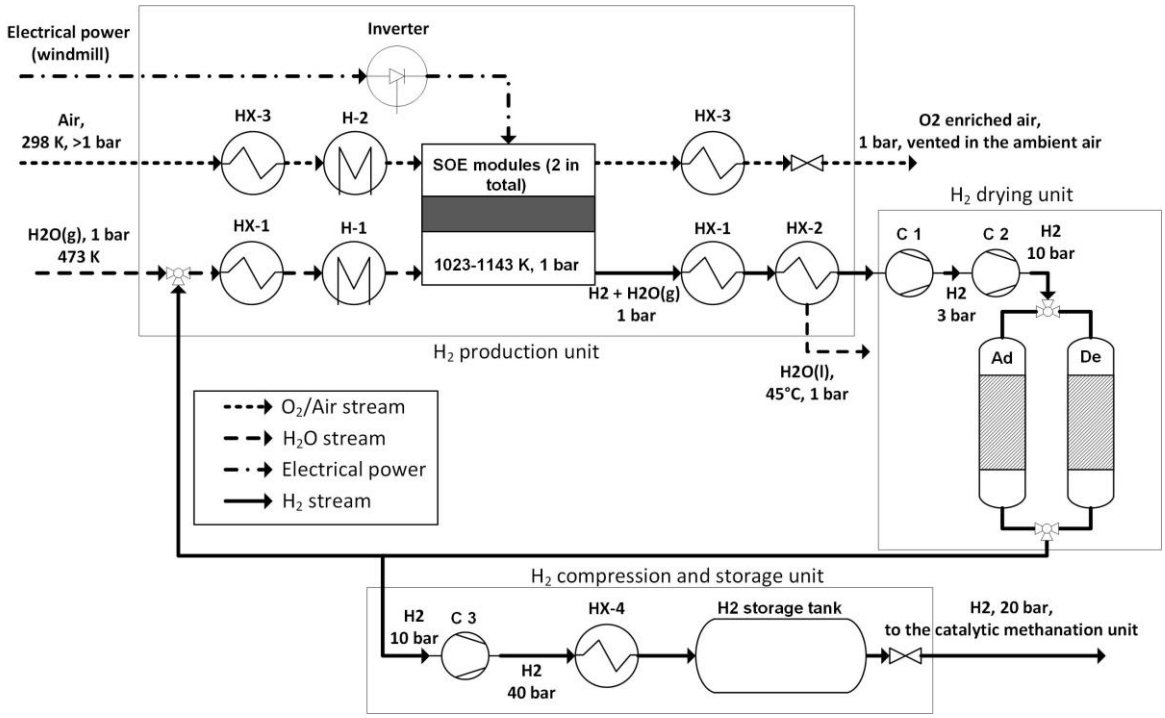


Figure 3-19: Layout of the H_2 production and storage unit

In operation, the BoPs electrical consumption in the H_2 production and storage unit corresponds to the sum of the following electrical consumptions.

- The inverter required to convert the AC power in DC power for injection in the SOE modules with an AC/DC conversion efficiency of 96%;
- The electrical work of the heaters before the cathode and anode inlet of the SOE unit. It corresponds to the electrical work needed to overheat the inlet gases from their outlet temperature out of HX-1 and HX-3 up to the required inlet gas temperature in the SOE stacks. Their power to heat efficiency was assumed to be 100% here;
- The drying unit, where a total electrical consumption of 0.1 $kWh \cdot Nm^{-3}$ H_2 was assumed.

In standby mode, each module is assumed to consume 2% of the nominal power. This value is assumed to cover the heat losses in the stacks and the BoPs work required to circulate the gases in the SOE stacks to maintain their temperature in hot standby mode.

3.5.2.2. Operation strategy of the SOE modules

The electrical power injected in a module is supposed to be equally divided between all stacks. In the case of ESCs, the nominal electrical power injected in a single cell is approx. 107 W in exothermic mode, which corresponds approx. to 58 stacks of 160 cells per module of 1 MW nominal capacity. In the case of CSCs, it is about 232 W per cell in exothermic mode, which corresponds to approx. 27 stacks of 160 cells per module. The operation strategy applied on the two SOE modules is schematically represented in Figure 3-20.

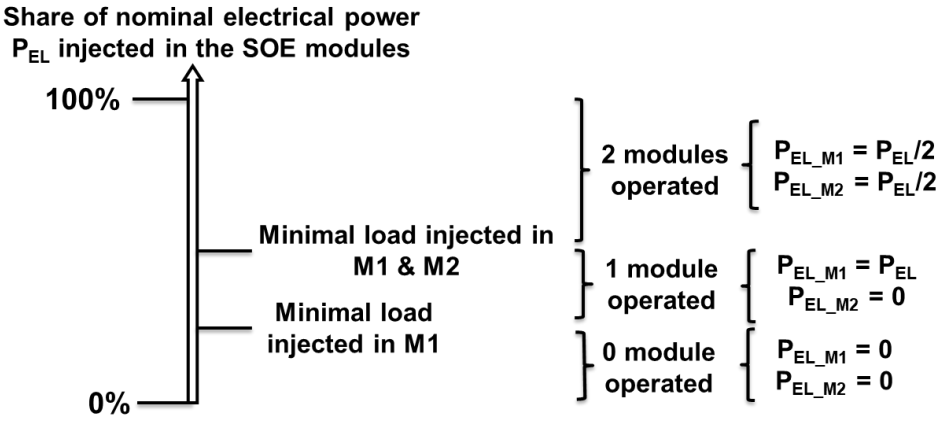


Figure 3-20: Operation strategy of the two SOE modules M1 and M2

When the electrical power available is below the minimal power required to operate a single SOE module in endothermic mode, no module is operated and no electrical power is injected in the stacks. When the electrical power available is above the minimal power load required to operate a single SOE module in endothermic mode, but below the minimal power load required to operate two modules at the minimal power load, a single SOE module is operated. When the electrical power available becomes larger than the minimal power load required to operate two modules, two modules are operated and the electrical power is equally divided between them. The maximal load corresponds to both SOE modules operated at the maximal allowed electrical power in exothermic mode. The maximal and minimal electrical loads allowed in exothermic and endothermic modes are defined for each SRU type in Table 3-7, for the values with a maximal cell operating voltage of 1.35 V. The electrical power injected in a module is also equally divided between all stacks.

3.5.2.3. Results and discussion

A simplified power profile was defined and applied to the H_2 production unit in order to observe and verify the unit response to the different modules operating configurations presented in Chapter 3.5.2.2. The successive electrical load levels applied on the H_2 production unit are chronologically depicted hereafter.

- At $t = 0$, both SOE modules are in standby mode, assuming an homogeneous initial temperature in all SRUs of 1073 K for CSCs or 1103 K for ESCs;
- From $t = 1$ to $t = 600\ s$: the electrical power is set at its nominal value (exothermic SOEC operation);

- From $t = 601$ to $t = 1200\ s$: the electrical power is lowered down to 80% of the nominal power (approx thermoneutral operation);
- From $t = 1201$ to $t = 1800\ s$: the electrical power is lowered down to 30% of the nominal power (endothermic SOEC operation);
- From $t = 1801$ to $t = 2400\ s$: the electrical power is increased up to nominal power again (exothermic SOEC operation);
- From $t = 2401$ to $t = 3000\ s$: the unit is brought back to standby mode.

The electrical power and the hydrogen production profiles in each module are represented for SOE stacks with integrated ESCs in Figure 3-22 and in Figure 3-23. The evolution of the outlet temperature of the hydrogen and steam mixture in each module is represented in Figure 3-21 and is coherent with the transients reported in Chapters 3.4.4 and 3.4.5.
From 1 to 1200 s, the electrical power injected in the two modules (M1 and M2) is the same, hence the evolution of the temperature in the two modules is identical. From 1201 s to 1800 s, the electrical power available is not sufficient to keep both modules switched on. M2 is set to hot standby mode and its temperature slowly decreases down to 1103 K, whereas M1 keeps operating in endothermic mode and its temperature decreases down to 1074 K. The electrical work of the BoPs decreases down to the standby value for M2. From 1801 s to 2400 s, the electrical power is set back up to its nominal value, so that the temperature increases again in the modules. From 2401 s on, the modules are switched to standby mode because no electrical power is available, hence both temperatures decrease down to the standby temperature at 1103 K. The electrical work of the BoPs decreases down to the standby value in both modules.

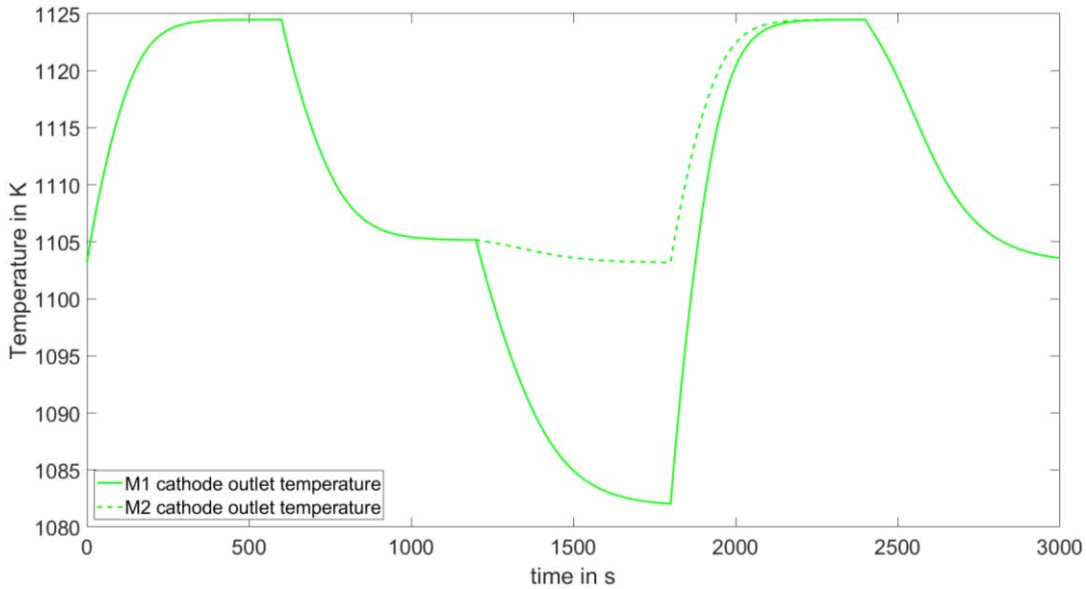


Figure 3-21: Outlet temperatures of the hydrogen and steam mixture for each SOE module

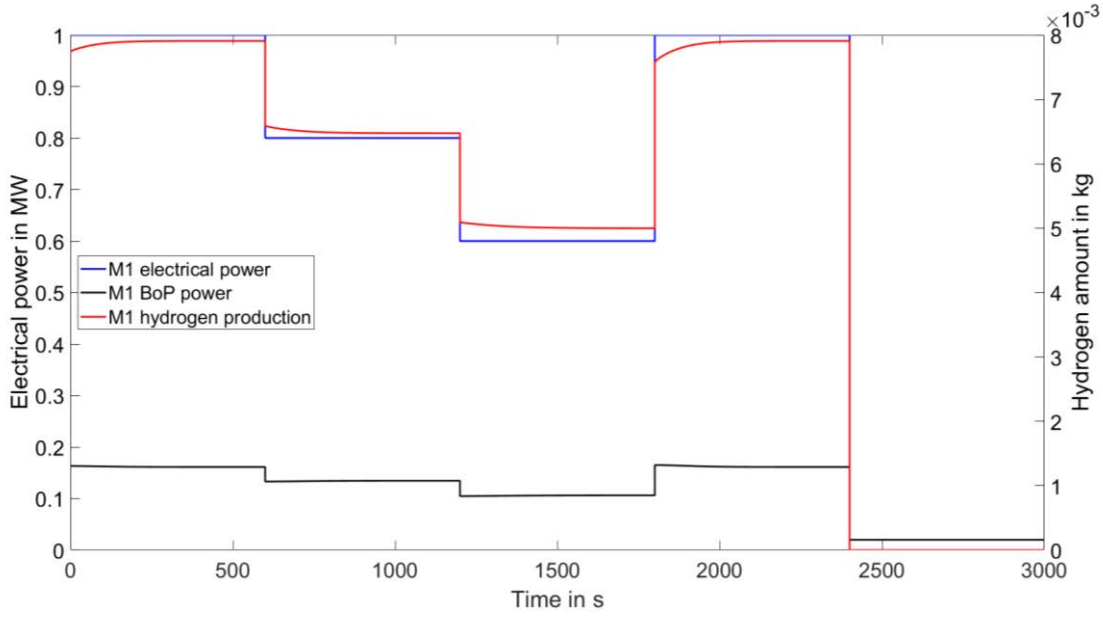


Figure 3-22: Evolution of the H_2 production and of the electrical power injected in the SOE stacks (ESCs) and in the BoPs of M1

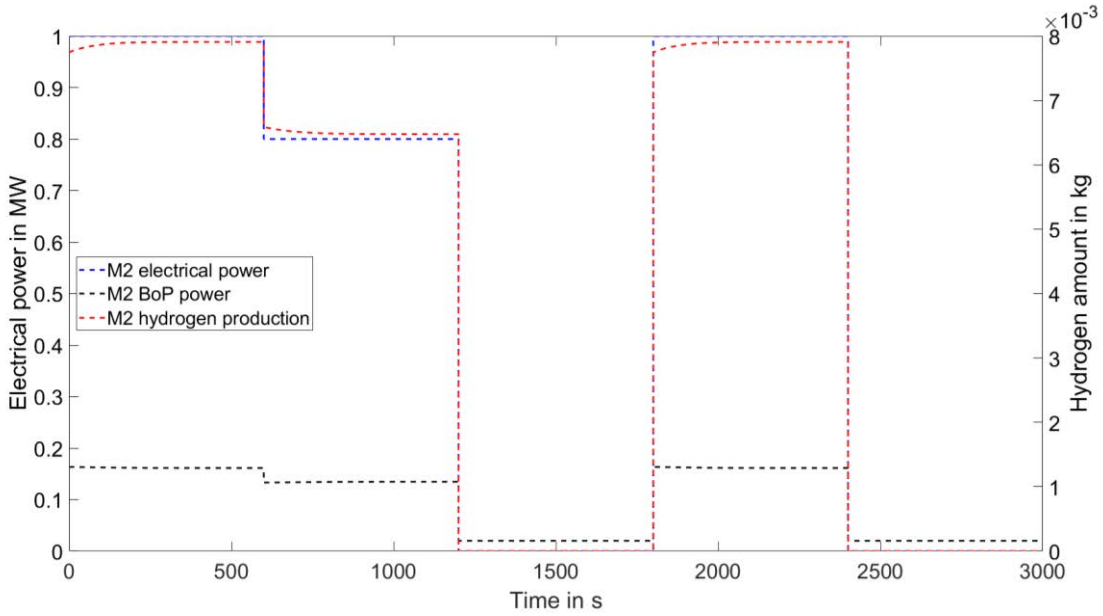


Figure 3-23: Evolution of the H_2 production and of the electrical power injected in the SOE stacks (ESCs) and in the BoPs of M2

The evolution of the energy consumption and of the electrical efficiency in the two modules are presented in Figure 3-24. The energy consumption decreases when switching from standby to exothermic mode until the permanent regime is reached, because the H_2 production increases at the same time. Similarly, the energy consumption initially increases when switching to endothermic operation until the permanent regime is reached, because the H_2 production decreases at the same time. The energy consumption is the same in M1 and M2 except when M2 is put in hot standby mode (from 1201 to 1800 s) and fluctuates in the range of 3.4-3.8 $kWh \cdot Nm^{-3}$ H_2.

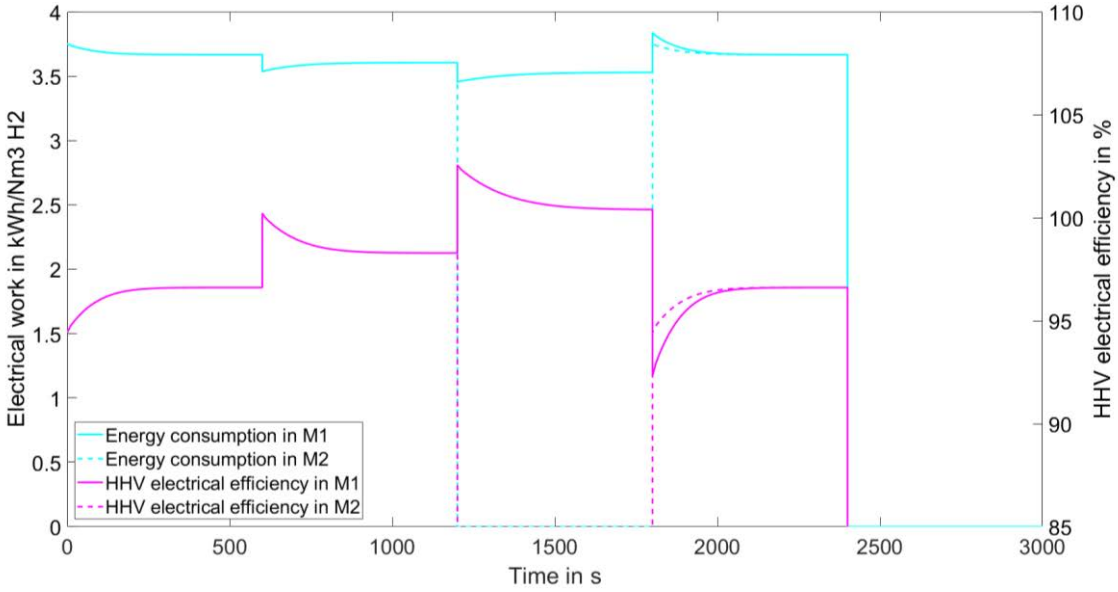


Figure 3-24: Evolution of the energy consumption and of the AC electrical efficiency (HHV) in M1 and M2

The energy consumption between 601 s and 1200 s corresponds to an operation slightly above the thermoneutral operation point with a value of 3.6 kWh·Nm^{-3} H_2. This value is slightly lower than that of onfield SOE units implemented at present (3.7 kWh·Nm^{-3} H_2 in [97]).

The power-to-H_2 AC efficiencies are in the range of 93 to 103% HHV (or 79% to 87% LHV), and about 98% HHV or 83% LHV in thermoneutral operation. Values above 100% HHV (from 601 to 1800 s) were reached because the energy required for steam generation is not included in the calculation of the power-to-H_2 efficiency, since it is provided as cooling steam from the catalytic methanation unit. Higher efficiency values were reached in endothermic mode, because cells show a higher Faraday efficiency than in exothermic mode. The AC efficiency in thermoneutral operation is 11% higher than that of 72% LHV reported for the 160 kW SOE unit implemented during the GrinHy project [257]. This can be explained by the lower efficiency of the AC/DC converter of 88% in [257] compared to the value of 96% assumed in this work. The remaining 3% difference are most likely related to the less efficient heat recovery of the high temperature gases of [257] compared to the one assumed in this work, and to the thermal losses of the stacks in [257], which were not accounted for in this work. The efficiency decreases when the load is above thermoneutral operation, which is coherent with [257]. However, the efficiency increases below thermoneutral operation, whereas it remains stable in [257] and starts decreasing only below 50% load because of thermal losses. When the load increases, the efficiency drops for a short time and increases again as the SOEC temperature stabilizes at a higher value. When the load decreases, the efficiency jumps for a short time and decreases again as the SOEC temperature stabilizes at a lower value. This behavior is coherent with the one reported in [257] during load variations.

3.5.3. H_2 production and storage unit with windpower profiles

3.5.3.1. Windpower profiles and SRU model reduction

The windpower profiles were determined based on the windspeed data recorded during the years 2005, 2006, 2009, and 2010 at the FINO6 platform in the North Sea, with timesteps of 10 minutes [258]. A

[6] Research platforms in the North Sea and the Baltic Sea.

characteristic curve (generated power as function of the wind speed) from a windmill 5M commercialized by the German company REpower Systems SE (now Senvion SE) was used as input to determine the windpower profile used in the model. The general characteristics of the windmill are provided in Appendix B. In this work, the nominal power of the windmill was assumed to be 2 MW after AC/DC conversion.
The computation time of the extended model for a single year of windprofile was estimated to be at least one day. Hence, it was decided to reduce the model to lower the computation time. The H_2 amount produced every 10 min (which corresponds to the timesteps of the power profile) at different load levels was interpolated as function of the energy injected in the SRU during that timeframe. This was done for each type of SRU (with ESC and CSC). The interpolation was limited to the H_2 production only in a first approach, but could be extended to all other model outputs such as temperatures or gas compositions if required. The model was then adapted to integrate the interpolation function in each SOE module. As a result, the H_2 production profile was generated in less than one minute.

3.5.3.2. Dimensioning of the H_2 storage tank and of the methanation unit

The dimensioning of the H_2 storage tank and of the catalytic methanation unit was implemented with the following constraints, under the assumption that all the H_2 produced is injected in the methanation unit.

- The H_2 level stored in the tank cannot be below 0 kg;
- The H_2 level at the beginning and at the end of the year has to be identical;
- The catalytic methanation unit is operated at nominal capacity during the whole year.

The evolution of the H_2 level in the tank is represented for several years in Figure 3-25.
The volume of the H_2 tank V_{TANK} (in m^3) required for the storage of H_2 can be determined with Equation (3.61) derived from the Boyle-Mariotte law, with m_{H2} the maximal H_2 level in the tank in kg, T_{AMB} the ambient temperature set at 298 K, M_{H2} the molar mass of H_2 in kg, p_{H2} the H_2 storage pressure of 4 MPa in the tank, and p_{METH} the H_2 destorage pressure of 2 MPa, the latter assumed here to match the operating pressure of the catalytic methanation unit.

$$V_{TANK} = \frac{m_{H2} \cdot R \cdot T_{AMB}}{M_{H2} \cdot (P_{H2} - P_{METH})} \tag{3.61}$$

The size of the H_2 tank and the nominal capacity of the catalytic methanation unit are summarized for each year in Table 3-8. Hence, the power-to-SNG unit would require a catalytic methanation unit of at least 1.6 MW capacity (based on the HHV of CH_4) and a H_2 storage tank with a volume of at least $19.5 \cdot 10^3$ m^3.

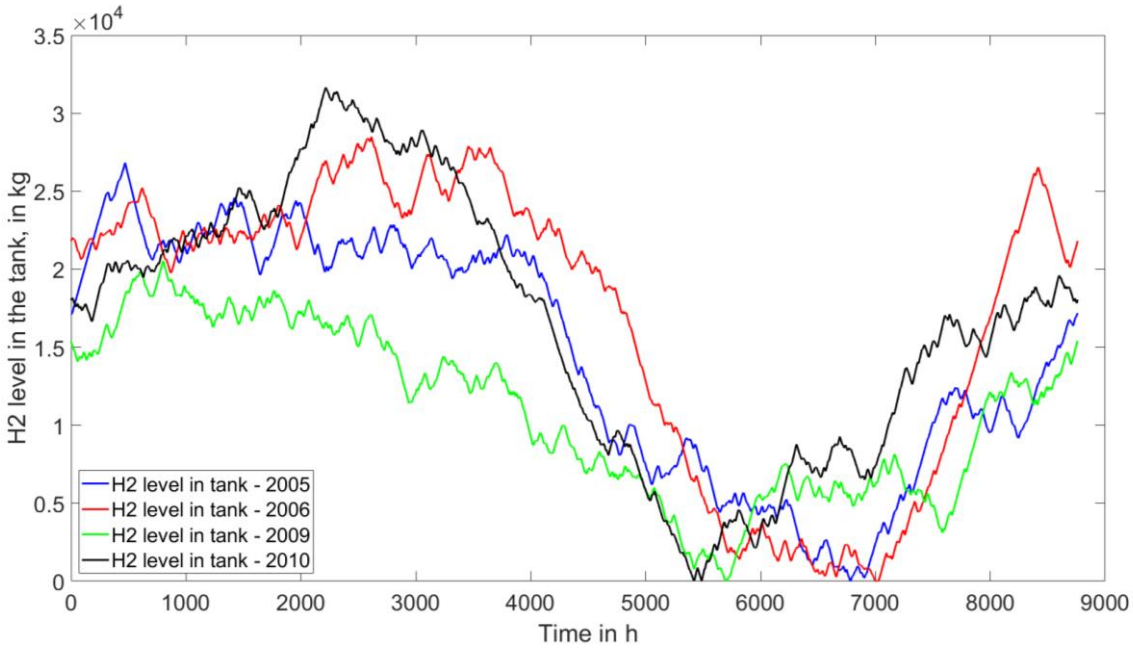


Figure 3-25: Evolution of the H_2 level in the storage tank during the years 2005, 2006, 2009, and 2010 (SOE stacks with ESCs)

Table 3-8: H_2 tank size and nominal capacity of the catalytic methanation unit for different years

Year	Size of H_2 storage tank (m^3)	Nominal capacity of the catalytic methanation unit (kW CH_4 HHV)
2005	$16.5 \cdot 10^3$ m^3	1640
2006	$17.5 \cdot 10^3$ m^3	1590
2009	$12.6 \cdot 10^3$ m^3	1600
2010	$19.5 \cdot 10^3$ m^3	1340

The implementation of such a large tank would generate additional costs, which would negatively impact the economics of power-to-SNG plants. Hence options to reduce its size or remove it are necessary. They will be discussed in Chapter 3.5.3.3.

3.5.3.3. Operation strategies and plant configurations to reduce H_2 storage size

Several options could be applied to reduce the size of the H_2 storage unit and ensuring plant flexibility to absorb the intermittence of the windmill power plant at the same time. They will be presented hereafter and their feasibility will be discussed.

A first option could be to adapt the load of the catalytic methanation unit using the seasonality of the windpower production. As can be seen in Figure 3-25, the H_2 level in the tank increases for all years from 0 to 2500 h, decreases from 2500 h to 6000 h and increases again until the end of the year. However, given the unpredictable behavior of the windpower production from one year to the next, it seems rather difficult to anticipate the load levels at which the methanation unit should be operated, even using predictive and/or learning algorithms. Furthermore, it is probable that this approach alone would not be sufficient to reduce the size of the storage tank to an acceptable value, e.g. below 1000 m^3.

A second option is to increase the H_2 pressure in the tank to reduce its size. In order to reduce the tank size down to 500 m^3 and assuming the maximal H_2 amount in the tank corresponds to the maximal observed in 2010 (approx. 32 tons), a maximal pressure of 800 bar would be required. This option is rather unlikely though, because of the additional costs it implies, which would be consequent in regard of the plant capacity (2 MW). This also raises the issue of safety and authorisations related to the onsite storage of such a large H_2 amount for the plant operator.

A third option would be to use the power grid to secure the minimal H_2 amount required to operate the methanation unit and the SOE unit at minimal load. As a first approach, the minimal and maximal H_2 production of the SOE unit were assumed to match the minimal and maximal H_2 requirements of the catalytic methanation unit. Hence, the maximal capacity of the catalytic methanation unit would be about 3.1 MW based on the HHV of CH_4 and the minimal load about 1.1 MW, which corresponds to 37% of the maximal capacity. Such a load reduction would be difficult to implement for fixed bed or honeycomb reactor technologies. However, it should be feasible for the three-phase reactor technology. In that case, plant concepts 2 and 3 presented in Chapter 2.2 should be adapted to use only three-phase reactors in series.

The operating strategy of the H_2 storage tank is depicted hereafter.

- While the tank is filling, the methanation unit is operated at a load corresponding to the average of the minimal and maximal load;
- If the tank is full, then the load of the catalytic methanation unit is increased to its maximal value until the H_2 level in the tank reaches its minimal value;
- If the tank is empty, then the load of the catalytic methanation unit is lowered down to its minimal capacity to increase the H_2 level in the tank.

The evolution of the H_2 production profile and the H_2 level in the tank in 2010 are represented in Figure 3-26. The capacity of the H_2 tank was set at 500 m^3, which corresponds to a maximal storage amount of 810 kg with maximal and minimal storage pressures of 40 and 20 bar.

The evolution of the electrical power injected in the SOE modules, taken from the grid, and produced in the windmill are represented in Figure 3-27 for the first 500 h of 2010. It can be verified that the electrical power injected in the SOE modules corresponds to the sum of the electrical power provided by the windmill and the one taken from the grid.

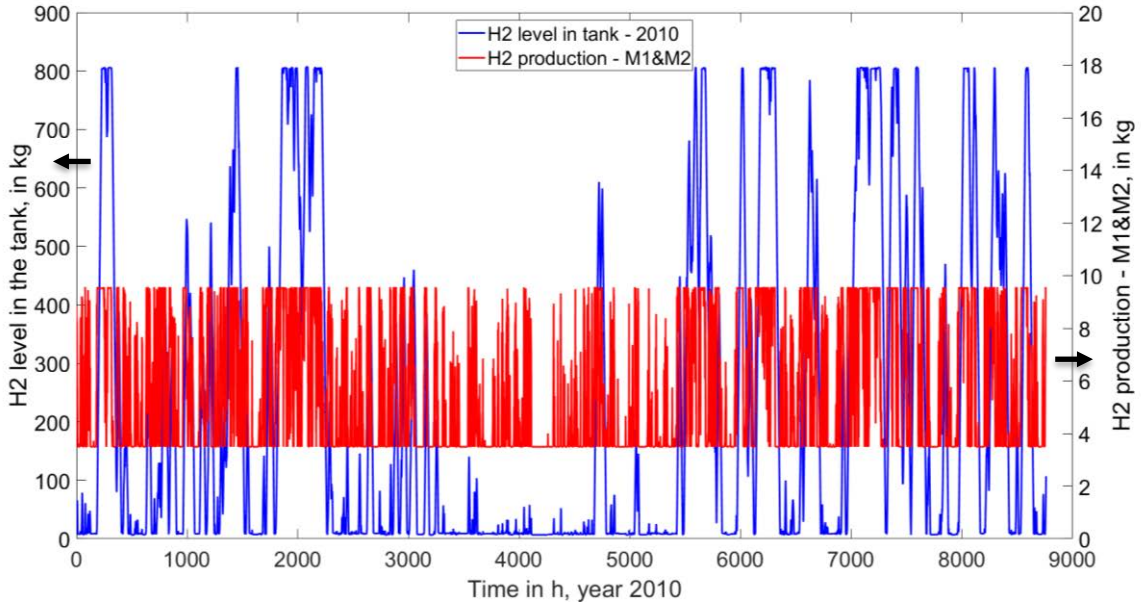


Figure 3-26: Evolution of the cumulated H_2 production in M1 and M2 and of the H_2 level in the tank in 2010

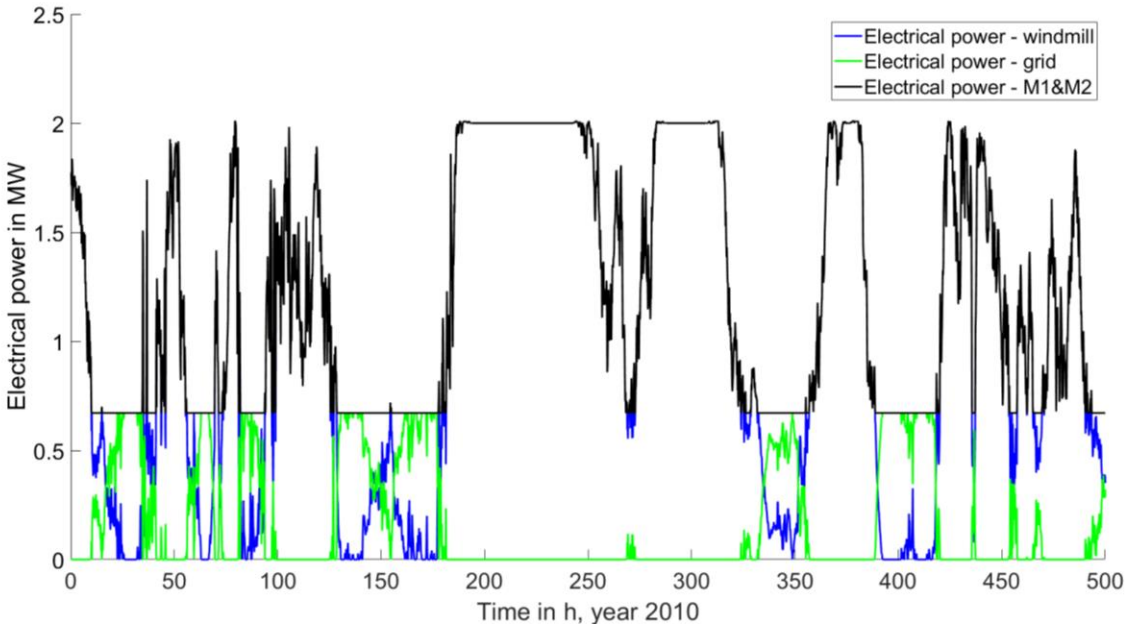


Figure 3-27: Evolution of the electrical power provided by the windmill, taken from the power grid and injected the SOE modules during the first 500 h of 2010.

Hence, it is possible to considerably lower the H_2 tank size with an adapted operating strategy of the H_2 storage unit. However, this is only feasible with the support of the power grid. This option would only be relevant if the average carbon footprint of the power grid enables to achieve significant reduction of the SNG carbon footprint compared to that of natural gas. Furthermore, the operation strategy applied to reduce tank size lowers the thermal coupling efficiency of the SOE unit and the catalytic methanation unit. Indeed, when the H_2 level in the tank is increasing or decreasing, the cooling steam of the methanation is not sufficient to cover the requirements of the SOE unit and an additional steam source is required, which reduces the power-to-SNG plant efficiency.

A fourth option would be to overdimension the windmill power plant and the SOE unit in order to couple only a part of the SOE modules with the catalytic methanation unit. The electrical power output of the previous windmill plant and the electrical power input of the SOE unit could be increased up to 20 MW, whereas the capacity of the methanation unit would remain unchanged (3.1 MW based on the HHV of CH_4). The two SOE modules required for the catalytic methanation unit would only represent a fraction of the total electrical power injected in the H_2 production unit (10% or 2 modules). A key advantage of this option is that these two SOE modules could be operated at full load all year long, with a significantly lower utilization of the power grid and an easier and more efficient operation of the power-to-SNG plant thanks to a constant and sufficient steam recovery from the catalytic methanation unit for the two SOE modules. A second advantage would be to remove the H_2 storage tank between the two SOE modules and the catalytic methanation unit.

The issue of fluctuating windpower production will have to be addressed in the remaining SOE modules, whose transient behavior could be investigated using the models developed in this work. The interest of flexible SOE module operation might become arguable for large scale units (e.g. >50 MW), where switching on and off modules would probably be easier to handle from an industrial standpoint. Nonetheless, the ability of operating modules on a large electrical power range including exothermic and endothermic operation would enable to maintain a higher number of modules switched on in case of partial power load availability, which could improve the plant efficiency. For instance, a 100 MW SOE unit composed of 100 modules with integrated ESCs operating in endothermic mode could operate from approx. 43 to 100% load (see Table 3-7), instead of 100% only for thermoneutral operation. Assuming an available electrical load of 43%, all modules could remain switched on, instead of only 43 modules in case of an on/off module operation. The operating power range could be even larger if SOECs were operated in exothermic mode.

The additional H_2 produced and not converted in SNG could be compressed to high pressures to facilitate transportation before final use, e.g. for mobility applications, or provided at low or intermediate pressure to other industrial customers on site or injected in the natural gas grid. However, the latter cannot be considered as stand-alone solution, as the injection of large H_2 volumes in the gasgrid is sometimes not feasible, e.g. in summertime when the natural gas consumption is low.

As a result, the plant would produce both SNG (as LNG or CNG) and H_2. This multifuel plant concept is schematically represented in Figure 3-28. The plant concept could be extended to other products such as methanol or Fischer-Tropsch products with their derivatives, but also to other biomass or industrial carbon sources (e.g. biogas upgrading units or CO_2 from the steel or the cement industries). Similar polygeneration plant concepts were already proposed in past work, e.g. in [56, 127].

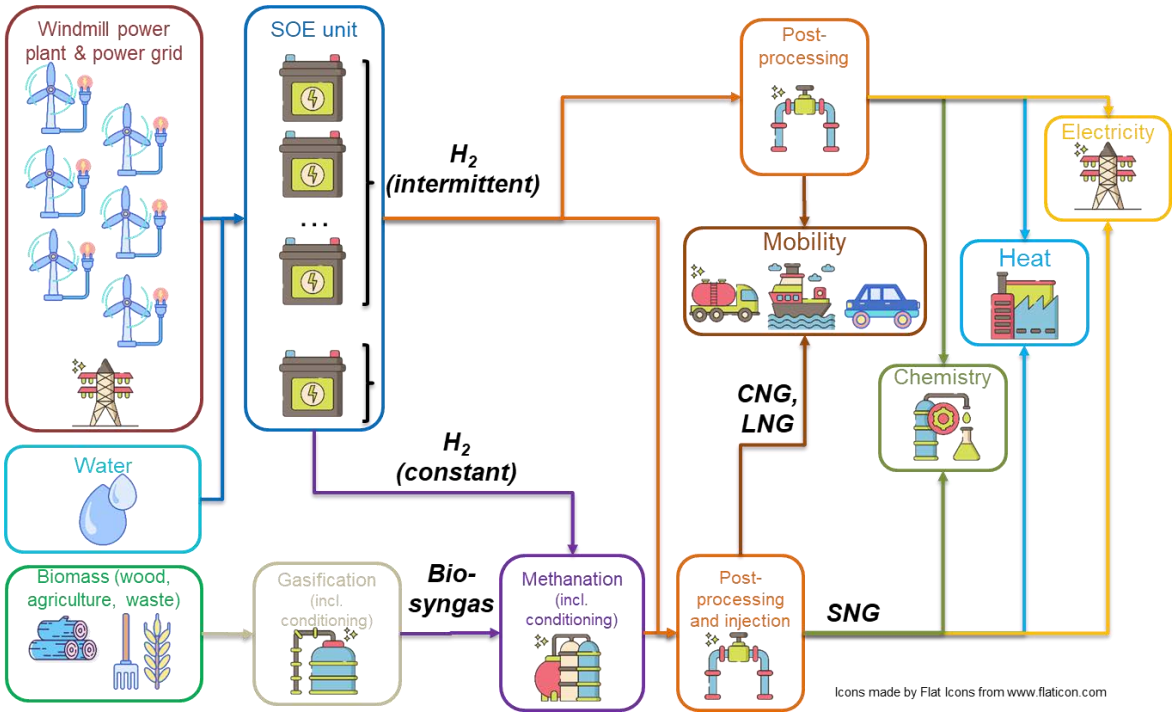


Figure 3-28: Schematic representation of a multifuel plant concept

3.6. Conclusions of Chapter 3

In this Chapter, the development and the first results of a 1D dynamic model to investigate the thermal behavior of SOE units were presented. The model was adapted from Cai et al. in [142] to propose a simplified modelling approach assuming the ASR is linear. The transient behavior of single repeat units (SRU) with two different cells architectures (CSCs and ESCs) was investigated.

First, a simplified model was implemented, where the ASR was assumed to be constant with the cell temperature. The transition from standby mode to exothermic or endothermic mode (20% higher or lower than the electrical power required for thermoneutral operation) was investigated, resulting in comparable transient duration (800 s) and cell temperature gradients (31-35 K) for both SRU types. The model output at the end of the transient was verified by comparison with the exact solution in permanent regime. The model showed good agreement with the model implemented by Cai et al. in [142], with a deviation of cathode stream outlet temperatures of max. 1.2% in endothermic mode (in the range of 70-100% of the current density in thermoneutral operation) and for air ratios in the range of 0.4-14.
Second, an extended model was implemented, in which the ASR depends on the cell temperature, based on different empiric laws for CSCs and ESCs derived from cell experimental data. The transient behavior was also investigated for similar conditions than the simplified model. For both SRU types, the transient duration was 700 s. The temperature gradient along the cell were slightly lower for ESCs, in the range of 16-19 K against 19-23 K for CSCs. The operating electrical power ranges corresponding to a maximal local thermal gradient permitted along the cell of 10 $K \cdot cm^{-1}$ and to a maximal local operation voltage of 1.35 V were calculated when switching from hot standby mode to either exothermic or endothermic mode. They were comparable for both cell architectures, respectively 28% above and 57% below the electrical power required in thermoneutral mode for ESCs, against 31% above and 51% below for CSCs. However, the thermal gradients are lower for ESCs than for CSCs in exothermic mode (22 K against 30 K) and in endothermic mode (62 K against 68 K) because of their higher ASR. Hence, ESCs present a higher thermal stability and should be preferred for intermittent power applications.

The SRU model was then coupled with a simplified power profile and extended to a complete H_2 production and storage unit composed of a SOE unit with two modules including BoPs. The SOE stacks were operated on an extended power range whose limits were based on the aforementioned conditions on local temperature gradient and local operating voltage. The energy consumption of the H_2 production unit fluctuated in the range of 3.4-3.8 $kWh \cdot Nm^{-3}$ H_2. Slightly above thermoneutral operation, a value of 3.6 $kWh \cdot Nm^{-3}$ H_2 was obtained, which is comparable to the performance of onfield SOE units at present. Thanks to the cooling steam recovered from the catalytic methanation unit, high power-to-H_2 AC efficiencies were reached (93-103% HHV). After a first dimensioning of the H_2 storage tank and the catalytic methanation unit, strategies and plant configurations were proposed to reduce the H_2 storage size. The following conclusions could be drawn.
The electrical coupling of SOE units with fluctuating power profiles reduces the performance of the thermal coupling between SOE and catalytic methanation units, which lowers the efficiency of the power-to-SNG plants. Additional plant equipment is required for H_2 storage and steam production, which increases plant costs and results in more complex plant operation.
Multifuel plants producing both H_2 and SNG could simplify the design and operation of power-to-SNG processes. A fraction of the SOE modules operated at nominal capacity would cover the H_2 requirements of the catalytic methanation unit, which would enable to maximize power-to-SNG plant efficiency. The remaining modules would then absorb the power intermittency and produce H_2 at different pressure levels depending on targeted applications. The flexible operation of these modules with SOECs operated in

exothermic and endothermic mode could improve the power-to-H_2 conversion efficiency compared to on/off module operation.

In case of constant electrical power loads, SOECs should preferably be operated in thermoneutral or exothermic mode in case of SOE units coupled with catalytic methanation units, even if a high temperature heat source above 1073 K such as a gasification unit is available (see Chapter 2). In case of fluctuating power load though, the operation power range of SOECs should be enlarged as much as possible to improve the ability to modulate the load and absorb the fluctuations of intermittent power sources. Hence, both exothermic and endothermic operation should be favored, independently of the downstream processes. Past years have shown that the efficiency of SOE systems remains stable down to 50% of the nominal power but significantly drops for lower load levels [257]. Hence, future works at reduced load should focus on the improvement of the BoPs and the efficiency of the thermal integration, as well as on the reduction of heat losses. The ability to operate SOE systems above nominal load still requires significant improvements of cell and system lifetime (currently up to 23 kh and below 10 kh respectively). Additional field testing is required to assess the ultimate potential for load variations of SOE units, for which the best startup time from hot standby to nominal operation reported so far is 24 min.

4. Economic evaluation of power-to-SNG plants

An economic evaluation of the three power to synthetic natural gas (power-to-SNG) plants investigated in Chapter 2 will be implemented in this Chapter. In a first part, the methodology applied for the calculation of investment costs as well as operation and maintenance (O&M) costs of the plants will be presented. In a second part, operating parameters of each plant process and costs assumptions of all plant equipment will be detailed, with a strong focus on the SOE unit. The main results of the techno-economic analysis will be presented, which include the results of the bottom-up cost evaluation of SOE units, as well as the production costs and levelized production costs of SNG for each plant concept. The results on the bottom-up cost evaluation of SOE units were based on the work reported in [8], whereas the results of the evaluation of SNG production costs were adapted from previous work of the IER reported in [11].

4.1. Methodology

The methodology applied for the calculation of investment and O&M costs will be presented hereafter. The pathway towards the actualization of investment and O&M costs will be first depicted. In a second step, the principles used for the determination of investment costs will be detailed, e.g. for scaling-up investment costs to desired equipment size and for taking into account the effect of inflation on investment costs. Here, a strong focus will be made on the bottom-up approach followed for the evaluation of the investment costs of SOE units. In a last step, the calculation of operation and maintenance costs of all plant equipment will be presented.

4.1.1. Annualized costs calculation

In order to enable the comparison of present and future financial flows during the lifetime of a plant, all costs and revenues were annualized. In this work, annualized SNG production costs C_P (in €·MWh^{-1}) were evaluated using Equation (4.1), where K corresponds to the initial investment at year 0 (in €), r to the discount rate, n to the plant lifetime (in years), C_t to all costs during year t (in €, corresponding to O&M costs, but also investment costs required for equipment replacement), and E_t to the energy output of SNG produced during year t (in MWh). Alternatively, initial investment costs at year 0 can be annualized using Equation (4.3) widely used in the literature, e.g. in [12, 152], where A corresponds to the annuity (in €) of the investment K. This allows to write a second formulation of the annualized production costs in Equation (4.1). The levelized production costs of SNG LC_P (in €·MWh^{-1}) can be determined with Equation (4.2), where R_t corresponds to the revenues (in €) during year t from plant by-products such as heat or oxygen for instance [259]. The discount rate was assumed to be 8%, which also includes the inflation in order to reduce the number of parameters used in the analysis.

$$C_P = \frac{K + \sum_{t=1}^{n} \frac{C_t}{(1+d_r)^t}}{\sum_{t=1}^{n} \frac{E_t}{(1+d_r)^t}} = \frac{\sum_{t=0}^{n} \frac{C_t}{(1+d_r)^t}}{\sum_{t=0}^{n} \frac{E_t}{(1+d_r)^t}} \quad (4.1)$$

$$LC_P = \frac{K + \sum_{t=1}^{n} \frac{C_t - R_t}{(1+d_r)^t}}{\sum_{t=1}^{n} \frac{E_t}{(1+d_r)^t}} = \frac{\sum_{t=0}^{n} \frac{C_t - R_t}{(1+d_r)^t}}{\sum_{t=0}^{n} \frac{E_t}{(1+d_r)^t}} \quad (4.2)$$

$$A = \frac{K \cdot d_r \cdot (1 + d_r)^n}{(1 + d_r)^n - 1} \tag{4.3}$$

In this work, all costs values were expressed in € 2017.

4.1.2. Investment costs

4.1.2.1. Investment costs of plant components

The investment costs of plant components were evaluated based on their technical characteristics such as their thermal or electrical power, as well as on process parameters (mostly temperature and pressure), which were extracted from the process layouts detailed in Chapter 2.6.1.
Free on board component costs were converted in installed costs using installation factors, taking into account all costs required for shipping and on-site installation of the equipment (e.g. piping, insulation, painting, electrical connections, building and foundations). Total investment costs of the power-to-SNG plant were calculated as the sum of free on board costs, installation costs and mark-up costs. The latter were estimated to represent 30% of total investment costs and included planning, commissioning, and unforeseen expenses. Higher values of markup costs of more than 60% were already reported, e.g. in [14]. However this assumption was made for a considerably smaller power-to-SNG unit with a SOE unit capacity of approx. 900 kW, whereas SOE units of approx. 14 MW are considered in this work. Hence, it was assumed in this work that these costs should represent a lower share by larger units. The pathway from free on board costs to total investment costs is schematically presented in Figure 4-1.

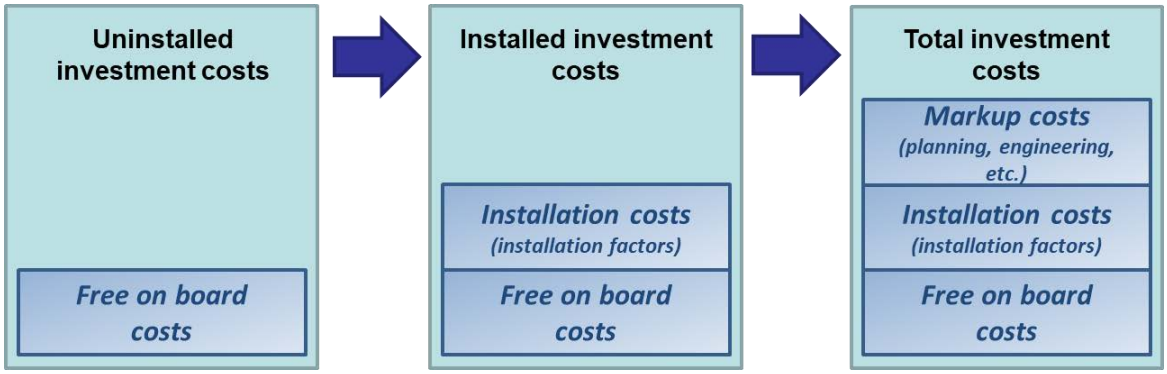


Figure 4-1: Decomposition of total investment costs, based on [11]

All investment costs were annualized using Equation (4.1). Furthermore, investment costs values of plant components before 2017 were converted in € 2017 with Equation (4.4) using the Chemical Engineering Plant Cost Index (CEPCI), in order to take into account the inflation of industrial equipment costs and services. The CEPCI annual values from 1995 to 2017 are summarized in Table C-1 in Appendix C.

$$Value_{2017} = Value_t \cdot \frac{CEPCI_{2017}}{CEPCI_t} \tag{4.4}$$

Furthermore, Equation (4.5) was used for adapting investment costs of equipment to desired component capacity S_{TAR}, where C_{TAR} corresponds to the targeted cost, C_{REF} to the reference cost, S_{REF} to the reference capacity of the equipment, and f to the equipment scaling factor.

$$C_{TAR} = C_{REF} \cdot \left(\frac{S_{TAR}}{S_{REF}}\right)^{f} \quad (4.5)$$

4.1.2.2. Investment costs of SOE units

In the particular case of SOE units, investments costs were determined following a bottom-up approach from raw cell materials up to installed system costs.
A modelling tool was developed to dimension SOE cell and stack manufacturing lines. This allowed in turn to estimate cell and stack production costs and finally installed investment costs of SOE systems. The main steps of the methodology applied are chronologically listed hereafter.

- Calculation of the material costs based on the cells and stacks technical characteristics;
- Calculation of the number of cells and stacks to be produced on an annual and daily basis according to the operation of the cell and stack manufacturing lines;
- Determination of the process flow diagrams for cells and stacks manufacturing;
- Determination of the number of machines required for each process step based on state of the art process speed values;
- Calculation of the manufacturing equipment costs by adding up all investment costs of equipment;
- Determination of the personnel costs assuming a number of operators for each machine. According to the automation level of each manufacturing process, machines can be replaced by robots which were then included in the manufacturing equipment costs;
- Calculation of building costs as the sum of space requirements for machines, storage and offices.

The investment costs of machine and building were converted in annual equivalents using the annuity equation (Equation (4.3) presented in Chapter 4.1.1). For the buildings, a lifetime of thirty years and a discount rate of 2% was assumed. For the machines, a lifetime of seven years was assumed as was done in [152], along with a discount rate of 8%.
The cells and stack production costs C (in €·kW^{-1}) were calculated as the sum of the material costs C_{MAT}, the personnel costs C_{PER}, the operation and maintenance costs C_{OP}, the equipment costs C_{EQ} and the building costs C_B, as written in Equation (4.6). The methodology applied for the calculation of each cost category is detailed in Appendix C for cell and stack manufacturing, whereas cell and stack cost breakdowns are presented in Chapter 4.3.1.4 and 4.3.1.5.

$$C = C_{MAT} + C_{PER} + C_{OP} + C_{EQ} + C_B \quad (4.6)$$

Based on a process layout of the SOE system of Figure 4-3, uninstalled costs of all balance of plant components were determined, e.g. AC/DC converter, pumps, electronics and control, sensors, and heat exchangers.

- The costs of electronics and system control include both hardware and software costs. Hardware costs correspond to the costs for central and individual processing unit, alimentation system, and memory card. The amount of each piece of equipment was obtained based on the number of control and monitored parameters in each SOE module. The cost of each piece of equipment was then determined based on available manufacturer data. Software costs correspond to the manpower costs for the development of control algorithms.
- The sensor costs include the costs of temperature, pressure, voltage, and current sensors, as well as that of mass flow meters.
- For each heat exchanger, a heat transfer coefficient value corresponding to the type of heat transfer considered was chosen in the literature. Based on the heat duty required in the heat

exchanger, the heat exchange area was calculated. The heat exchanger material was chosen based on the nature of the gases considered and on the operating parameters.

An installation factor was then applied to each uninstalled cost to obtain a value of installed investment costs, as was previously explained in Chapter 4.1.2.1.

Installed SOE system costs were finally calculated as the sum of all installed system components costs and are summarized in Table 4-6 in Chapter 4.3.1.6.

Two cases were defined for the calculation of SOE investment costs assuming different capacities of cells and stacks manufacturing lines, corresponding to different SOE unit capacities.

- ***Case 1***: the SOE unit has an electrical power of 15 MW. The SOEC manufacturer shows yearly production volumes of 75 MW and operates manual production lines.
- ***Case 2:*** the SOE unit has an electrical power of 75 MW. The SOEC manufacturer shows yearly production volumes of 375 MW and operates automated production lines.

The capacity of the SOE unit in case 1 matches the one of the SOE unit integrated in the power-to-SNG plants investigated in Chapter 2 (20 MW CH_4 capacity on a HHV basis). Case 2 corresponds to a SOE unit which could be integrated in a 100 MW power-to-SNG plant (based on the HHV of CH_4), which would enable to assess the impact of further upscaling of the SOE technology on SOE costs and SNG production costs.

Also, the capacities of manufacturing lines in the two cases enable to assess the impact of automation on manufacturing costs. Indeed, according to Versa Power, SOFC production lines should be operated manually up to a capacity of 25 MW [109, 260]. The SOCs produced by this company show a current density of 0.36 $A \cdot cm^{-2}$ and an operating voltage of 0.8 V in fuel cell mode, which corresponds to a power density of 0.29 $W \cdot cm^{-2}$. If those cells were operated in electrolysis mode with a current density of -0.9 $A \cdot cm^{-2}$ and an operating voltage of 1.3 V, they would reach a power density of 1.17 $W \cdot cm^{-2}$, which is approx. four times more than in fuel cell mode. Operated in electrolysis mode, those cells would therefore consume 100 MW. Hence, the capacity above which manufacturing lines should be fully automated rather than operated manually can be estimated at about 100 $MW \cdot year^{-1}$, which is between the manufacturing capacities considered in each case (75 $MW \cdot year^{-1}$ and 375 $MW \cdot year^{-1}$). This assumption has to be taken cautiously though, since no SOEC manufacturing line with an annual production capacity of 10-100 MW of cells or stacks is known at present.

4.1.3. Operation and maintenance costs

These costs are composed of operation and maintenance (O&M) costs of the equipment, but also include the costs of plant utilities and feedstocks (e.g. biomass and electrical power), consumables (such as catalysts or active carbon), and personnel costs. The O&M costs of equipment were estimated to represent a share of uninstalled equipment costs (e.g. a few percent). Plant utilities and feedstock costs were evaluated based on a cost value in € per volume, mass or energy unit. The personnel costs were calculated as the sum of the wages of all plant employees. Different wages were assumed for each type of employee, along with a number of employees per shifts and a number of shifts per day for plant operation.

4.2. Scenarios description and main plant hypotheses

4.2.1. Scenarios description

The scenarios aim at evaluating production costs and levelized production costs of SNG for different plant configurations, as well as for different time horizons and possibilities of plant revenues. They are based

on the three plant concepts investigated in Chapter 2, assuming the same plant layouts than those presented in Chapter 2.6.1.

For each plant concept, two different scenarios will be considered, one current and one prospective. They will be based on either current or future investment costs of electrolysis technologies (considering initial investments, but also replacement investments with hypotheses on stack lifetime). This will enable to evaluate in which measure the reduction of electrolysis investment costs could contribute to the reduction of SNG production costs, but also if the SOE technology would be a more profitable option compared to other electrolysis technologies. The corresponding hypotheses are detailed in Chapter 4.3.2.

For each scenario, two options will be considered regarding plant revenues. In case there are no plant revenues, the value of SNG production costs will be calculated. In case of plant revenues, levelized production costs of SNG will be determined based on both oxygen and heat sales. Even though these revenues are possible only in specific site configurations, their leverage for reducing SNG production costs will be evaluated.

The six scenarios considered for the economic analysis are summarized in Table 4-1. For each scenario, the technical features of the corresponding plant concept are recalled from Chapter 2.2 and the considered time horizon and plant revenues specified. Each scenario is referred to with a number corresponding to the plant concept number and with a letter “C” for current or “P” for prospective.

Table 4-1: Description of the economic scenarios associated to the three plant concepts

	Technical plant features							Timeline	Plant revenues	Scenario name
	Biomass feedstock	**Gasifier pressure**	**Syngas conditioning**	**Electrolysis technology**	**Catalytic methanation technology**	**SNG conditioning**	**End product**			
Plant concept 1	Wood	1 bar	-Hot gas and fine cleaning -2 stage compression	PEM 20 bar	Fixed bed, 4 adiabatic reactors (TREMP™ process)	2 stage compression	CNG 250 bar	Current	Heat and O_2 No revenues	S1C
								Prospective	Heat and O_2 No revenues	S1P
Plant concept 2	Wood	20 bar	-Hot gas and fine cleaning	SOE 20 bar	-Three-Phase, 1 reactor -Honeycomb, 1 reactor	2 stage compression	CNG 250 bar	Current	Heat and O_2 No revenues	S2C
								Prospective	Heat and O_2 No revenues	S2P
Plant concept 3	Mix of wood, straw, and sewage sludge	20 bar	-Hot gas and fine cleaning	SOE 20 bar	-Three-Phase, 1 reactor -Honeycomb, 1 reactor	CH_4 liquefaction unit	LNG	Current	Heat and O_2 No revenues	S3C
								Prospective	Heat and O_2 No revenues	S3P

4.2.2. Main techno-economic plant hypotheses

The main techno-economic plant hypotheses made in this work are summarized in Table 4-2. Similar hypotheses as in [11] were made, at the exception of the discount rate, for which a value of 8% was chosen in the reference case (against 5% in [11]). In order to limit the number of parameters considered in this work, the discount rate also included the inflation rate, whereas it was considered as an independent parameter from the discount rate in [11]. In all scenarios, the plants were assumed to operate at nominal capacity with a high number of full load hours (8000 $h \cdot year^{-1}$), corresponding to a plant availability above 90%. Hence, additional plant costs related to the coupling with an intermittent renewable power profile such as the costs of H_2 or CO_2 storage tanks were not considered. This analysis remains relevant in a context where low carbon electrical power from hydraulic or nuclear sources is available all year long. The plant capacity was set at 20 MW based on the HHV of CH_4. Larger units up to 100 MW capacity were not considered in this work, as they would require large amounts of biomass feedstock, thereby raising the issue of biomass availability and logistics.

Table 4-2: Main techno-economic plant hypotheses of the economic evaluation

Parameter	Value	Comments/Sources
Technical hypotheses		
Plant capacity	20 MW CH_4 output	Based on the HHV of CH_4
Full load hours	8,000 $h \cdot year^{-1}$	[11]
Economic hypotheses		
Calculation year	2017	[11]
Plant lifetime	20 years	[11]
Discount rate	8%	Authors hypothesis

4.3. Investment costs of power-to-SNG plant components

The first part of Chapter 4.3 will focus on the SOE unit and will determine the investment costs of installed SOE systems based on a bottom-up evaluation starting from raw SOEC materials reported in [8]. The results of this evaluation will be used in the second part of Chapter 4.3, which will present the hypotheses chosen for the investment cost calculation of the main power-to-SNG plant components.

4.3.1. Investment costs of the SOE unit

The techno economic hypotheses of the bottom-up cost analysis will be detailed hereafter. The SOE cells and stacks architectures will be thoroughly depicted, along with their main operating parameters, components, and the manufacturing lines used for their production. The SOE system layout will also be presented and used as basis for the investment cost calculation of its main components. In each case, associated costs will be calculated. As a result, installed SOE system costs will be determined. A sensitivity analysis will be made in order to identify the most influential cost parameters and the installed investment costs of SOE units will be compared with previous literature values.

4.3.1.1. SOE cells characteristics and manufacturing

Electrolyte supported cells (ESC) tested at EIFER were chosen for the evaluation, as they present the lowest degradation rate ever reported so far with more than 23,000 h operation in industrially relevant conditions with a current density of -0.9 $A \cdot cm^{-2}$ and close to thermoneutral voltage [66, 99]. The corresponding cell characteristics and operating parameters are summarized in Table 4-3. The same

layer configuration and materials as in [66, 99] were assumed. In both cases defined in Chapter 4.1.2.2, the cell stacking was assumed to be ideal, without additional resistance nor degradation and the operating conditions of cells and stacks were supposed to be identical.

Table 4-3: Main features of the electrolyte supported cells (ESCs) used for the cost evaluation

Parameter/property	Source	Unit	Value/hypothesis
Steam conversion rate	Authors hypothesis	(%)	80
Cell active area	Authors hypothesis	(cm^2)	130
Total cell area	Authors hypothesis	(cm^2)	167
Operation voltage	[66, 99]	(V)	1.3
Current density	[66, 99]	($A \cdot cm^{-2}$)	-0.9
Cell geometry	[66, 99]	-	Flat square cell
Electrolyte	[66, 99]	(µm) 6Sc1CeSZ, named SSZ afterwards	130
Ion diffusion layer or adhesion layer (two layers in total)	[66, 99]	(µm) GDC	10
Oxygen electrode (anode)	[66, 99]	(µm) LSCF	25
Hydrogen electrode (cathode)	[66, 99]	(µm) NiO/GDC	25

Under such operating conditions and with an active cell area of 130 cm^2, a cell would absorb an electrical power of 152 W. This would correspond to a yearly production of approx. 493,000 cells in case 1 (75 $MW \cdot year^{-1}$) and of approx. 2,465,000 cells in case 2 (375 $MW \cdot year^{-1}$). A process chain based on state of the art tape casting, screen printing and sintering processes was applied for the manufacturing of SOE cells, adapted from previous work [152]. The costs of powder sizing were neglected in the cost analysis. A detailed description of the cell manufacturing line and a process flow diagram (see Figure C-1) are provided in Appendix C. The main characteristics of the cell production line are summarized in Table 4-4.

Table 4-4: Main characteristics of the cell manufacturing line

Main hypothesis	**Case 1**	**Case 2**
Capacity of the SOEC production line ($MW \cdot year^{-1}$)	75	375
Electrical power of a SOEC (kW)	0.152	0.152
Cell manufacturing line	**Case 1**	**Case 2**
Annual production capacity ($cells \cdot year^{-1}$)	493,097	2,465,483
Investment cost for equipment (k€)	1,334.7	3,365.7
Annualized investment cost for equipment ($k€ \cdot year^{-1}$)	256.4	646.5
Annualized investment cost for equipment ($€ \cdot cell^{-1}$)	0.52	0.26
Annualized investment cost for equipment ($€ \cdot kW^{-1}$ cell)	3.4	1.7

4.3.1.2. SOE stacks characteristics and manufacturing

It was assumed that each stack would integrate 160 cells. This corresponds to approx. 3,082 stacks in case 1 (75 $MW \cdot year^{-1}$) and to approx. 15,409 stacks in case 2 (375 $MW \cdot year^{-1}$). Each cell was sealed

with a stainless steel interconnect made out of Crofer® 22 APU to build a so-called single repeat unit (SRU). Each stack was divided in eight clusters of twenty SRUs, where two clusters were separated by a current collector (in total seven current collectors per stack). Two endplates were disposed on the stack, one on top and one at the bottom. The load frames were then added and used for loading the stack. The stack architecture is schematically represented in Figure 4-2.



Figure 4-2: Schematic representation of the stack architecture chosen in this work

The process chain implemented for stack manufacturing corresponds to state of the art processes and components and was adapted from previous work [152]. A detailed description of the stack manufacturing lines and a process flow diagram (see Figure C-2) are provided in Appendix C. The main characteristics of the cell production line are summarized in Table 4-5.

Table 4-5: Main characteristics of the stack manufacturing line

Main hypothesis	**Case 1**	**Case 2**
Capacity of the SOEC production line (MW·year^{-1})	75	375
Electrical power of a SOE stack (kW)	24.3	24.3
Stack manufacturing line	**Case 1**	**Case 2**
Investment cost for equipment (k€)	4,498.2	8,381.8
Annualized investment cost for equipment (k€·year^{-1})	864.0	1,609.9
Annual production capacity (stacks·year^{-1})	3,082	15,409
Annualized investment cost for equipment (€·stack^{-1})	280.3	104.5
Annualized investment cost for equipment (€·kW^{-1} stack)	11.5	4.3

4.3.1.3. SOE system description

The SOE system layout assumed for the cost evaluation is represented in Figure 4-3. It was determined based on manufacturer inputs and previous process layouts documented in the literature [261]. The main hypothesis regarding system design and operating parameters are detailed hereafter.

- SOE stacks are integrated in SOE modules of 20 stacks each in case 1 for an installed electrical power of 487 kW and in SOE modules of 40 stacks each in case 2 for an installed electrical power of 973 kW.
- The SOE stacks are operated in thermoneutral mode at 1073 K.
- The SOE system is operated at 20 bar. In each SOE module, stacks are integrated in a pressurized vessel, as was reported in [40, 96]. The pressure difference between cathode and anode compartment of a stack is measured with two pressure sensors, as was reported in [96]. The first one is disposed in the anode compartment and the second one in the cathode. Even

though SOE systems using that design were operated at pressures up to several atmospheres, it was not proven so far that pressures as high as 20 bar could be reached.

- The steam required in the SOE unit is entirely generated in the cooling system of a catalytic methanation unit. Enough steam can be produced because of the high steam conversion rate of the SOE cells, taken as 80%. According to previous modelling work, such high steam conversion rates are beneficial for the system efficiency [38, 45, 108, 132] and are also preferred by SOEC manufacturers [96].
- Lab scale experiments are often performed using a mixture of 90% vol. H_2O and 10% vol. H_2 at the inlet of SOECs [66, 99, 161] in order to prevent risks of Ni reduction at the cathode. Even though steam dilution was also applied in industrial size units in previous works [96, 163, 244], it was assumed in this work that the system would be fed with 100% steam at the inlet.
- It was assumed that pure O_2 is produced at the anode of SOECs. Hence, no air sweep system is implemented and the corresponding BoP components (air compressor, air heater and heat exchangers) are not required. The heat content of the oxygen excess is recovered for preheating the SOE inlet gases. The O_2 is then fed to a biomass gasification unit.
- In this configuration, interconnects and heat exchangers resilient to O_2 corrosion at both high pressure and temperature (at 1073 K and 20 bar) would be required. The corrosion behavior of stainless steel interconnects for SOFC applications at atmospheric pressure has been widely investigated, e.g. in [262-265]. The coating of interconnects with perovskite or spinel materials has proved to considerably slow down the corrosion process [262, 263, 265] and to remain efficient even after long term operation up to 18,000 h [264]. Even though the behavior of such interconnects at both high temperature and high O_2 pressure was not reported so far, it was assumed that their corrosion behavior would be satisfying in these operating conditions. As for heat exchangers, the most resilient ones operate with pure O_2 at 800°C and 10 bar and are made out of Inconel alloys, mostly based on Ni and Cr metals [266]. It was also assumed that these heat exchangers could operate in the aforementioned conditions.
- Pressure drops were neglected in all equipment.

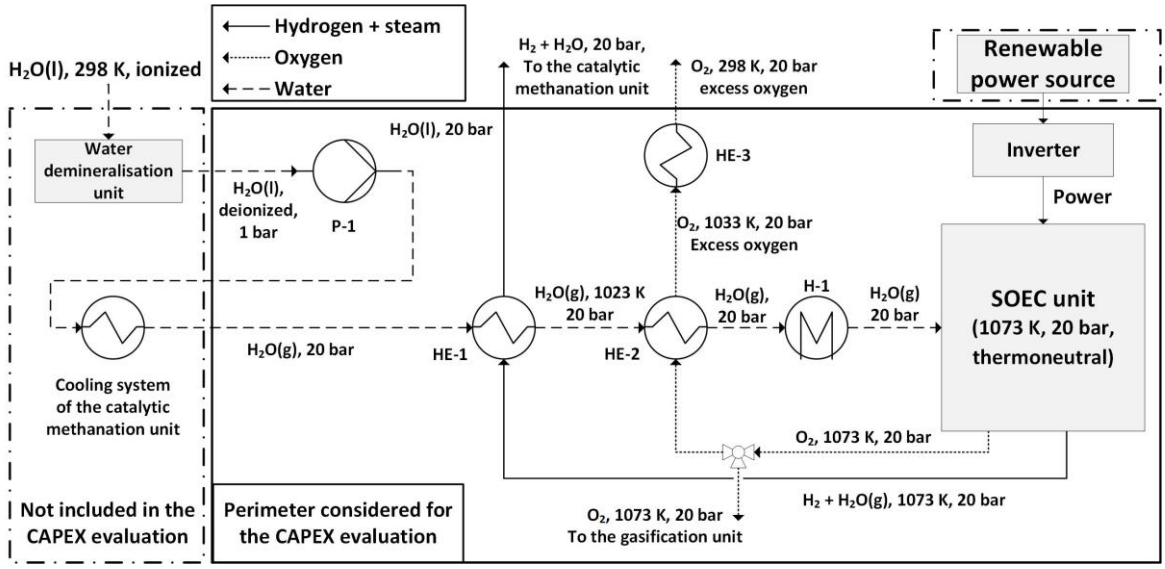


Figure 4-3: SOE system layout assumed for the cost evaluation

The perimeter chosen for the costs evaluation is represented in Figure 4-3. Following costs were excluded.

- The costs of the cooling system for the isothermal catalytic methanation unit, even though it generates the steam injected in the SOE modules. It was considered that it would be required for the thermal management of the methanation unit anyway. Therefore, only the equipment costs for steam overheating were accounted for.
- The costs of hydrogen storage and of water demineralization unit.

A heater (H-1) is required for adjusting the steam temperature from 1043 K up to 1073 K before the electrolysis system. An inverter is applied to adapt the grid tension to the stack tension and convert the AC current in DC current. A heat exchanger (HE-1) is implemented to overheat the steam fed to the SOE system from 673 K up to 1023 K by recovering the heat content of the SOEC outlet gases at the H_2 electrode. A second heat exchanger (HE-2) is used for steam overheating from 1033 K up to 1053 K by cooling down the oxygen produced in the SOEC unit from 1073 K down to 1033 K. A third heat exchanger (HE-3) is used for cooling down the O_2 excess from 1033 K down to 298 K. A pump (P-1) is used for liquid water compression from 1 bar up to 20 bar.

4.3.1.4. Investment costs of SOECs

The cell manufacturing cost breakdowns are represented in Figure 4-4. The materials represent the highest cost share of cells because of the high costs of scandium stabilized zirconia (SSZ). The cost decrease from case 1 to case 2 is related to lower personnel costs (10.4 €·kW^{-1} in case 1 down to 0.67 kW^{-1} in case 2) and lower machine costs (3.5 €·kW^{-1} in case 1 down to 1.8 kW^{-1} in case 2). This can be explained by the higher usage rate of machines in case 2 and by the automation of the cell manufacturing line. While personnel and machine costs decrease, material costs remain constant at 41.4 €·kW^{-1}, which is why their share increases from 72% in case 1 up to 92% in case 2.

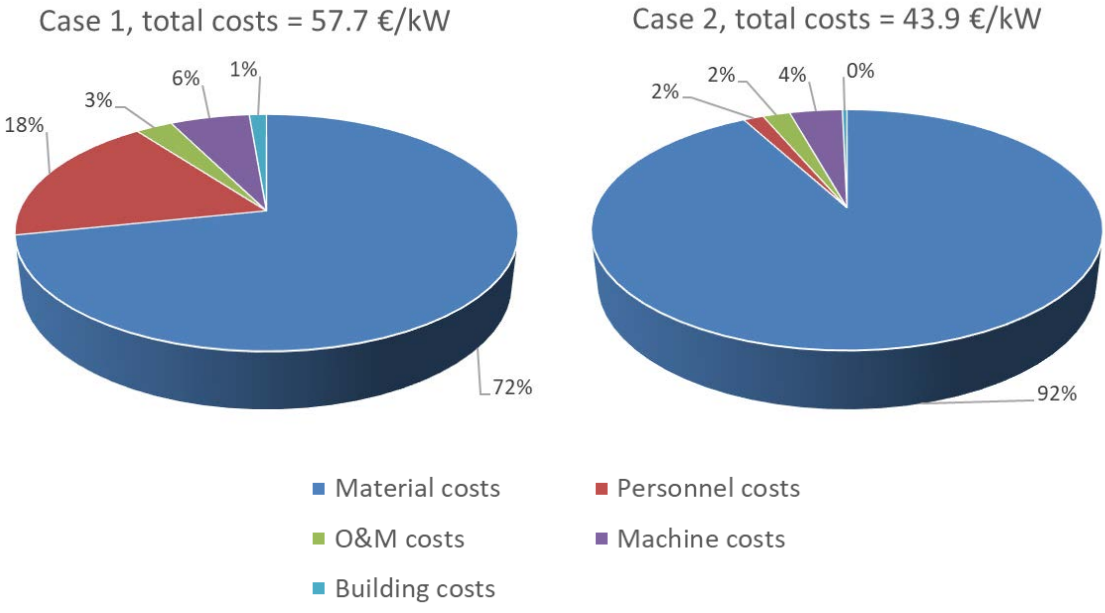


Figure 4-4: Manufacturing cost breakdowns of SOEC cells in case 1 and case 2

4.3.1.5. Investment costs of SOE stacks

The stack manufacturing cost breakdowns are presented in Figure 4-5 on a cost type basis (Figure 4-5a and Figure 4-5b) and on a component basis (Figure 4-5c and Figure 4-5d). According to Figure 4-5a and Figure 4-5b, material costs represent the highest cost share, which increases from 81% in case 1 up to

93% in case 2. All costs for cell manufacturing (material, personnel, O&M, machine and building costs) were included in material costs for stack manufacturing. Stack production costs are lower in case 2 because of lower personnel costs (11.7 €·kW^{-1} in case 1 down to 1.3 €·kW^{-1} in case 2) and lower machine costs (11.7 €·kW^{-1} in case 1 down to 4.3 €·kW^{-1} in case 2), for the same reasons mentioned earlier for the cell manufacturing line. A consequent reduction of machine costs was also reported in numerous SOFC cost assessments when increasing production volumes, e.g. in [152, 156]. It is related to the higher utilization rate of machines, which is also one of the main differences between case 1 and case 2. Important reductions of personnel costs were also observed when increasing the level of automation in [152, 157].

As can be seen in Figure 4-5c and Figure 4-5d, substantial cost reduction can be observed in case 2 because of lower interconnect costs (46.5 €·kW^{-1} in case 1 down to 31.0 €·kW^{-1} in case 2). This costs reduction results from the higher production volumes of interconnects in case 2.

Stack cost breakdowns elaborated in this work could not be quantitatively compared with previous SOFC or SOEC cost breakdowns of the literature, because cell architectures, cell materials, stack operating conditions and SOE unit capacities were significantly different.

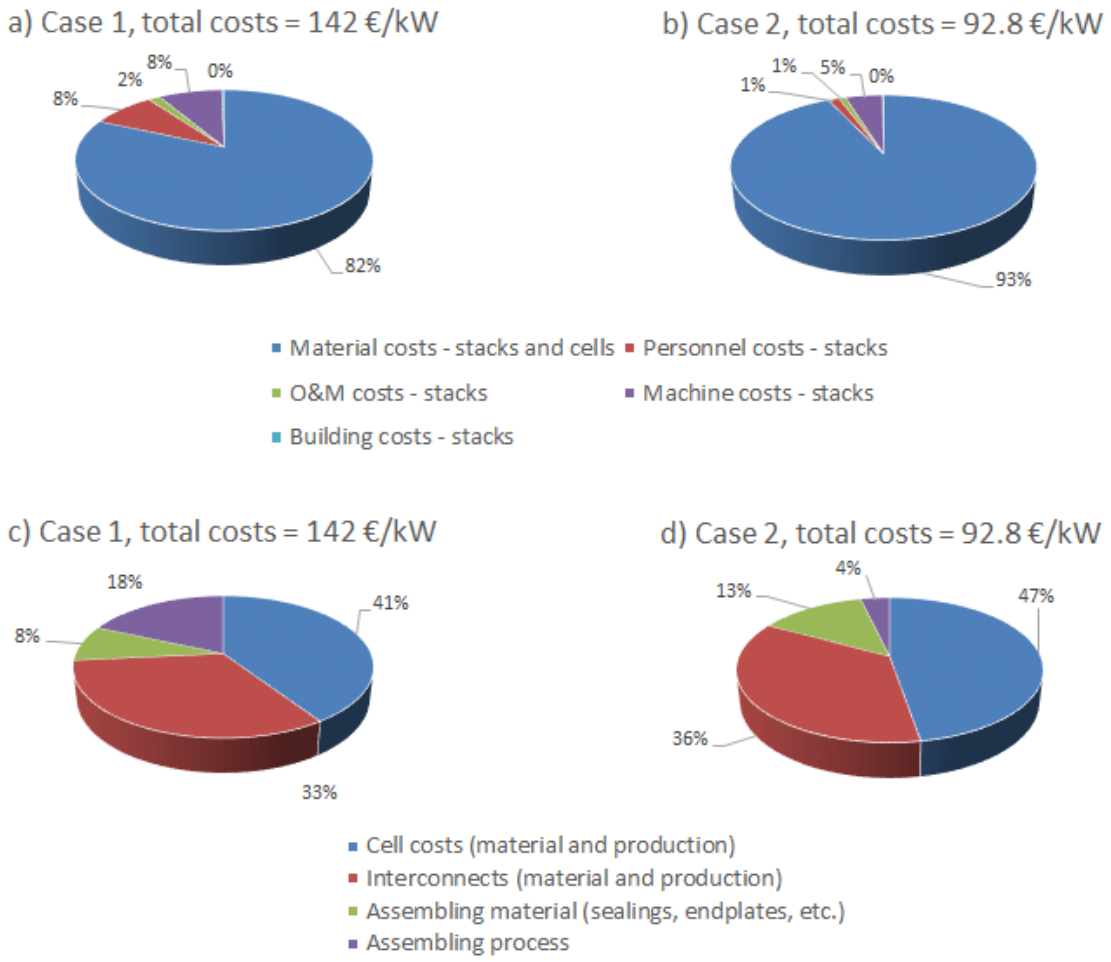


Figure 4-5: Manufacturing cost breakdowns of SOE stacks in case 1 and 2 – a) and b) on a cost type basis, c) and d) on a component basis

4.3.1.6. Investment costs of installed SOE systems

Capital cost breakdowns of installed SOE systems are represented in Table 4-6. Both installed and uninstalled equipment costs are provided in € 2017. They show that the balance of plant (BoP) –defined here as all components but the stacks– represent 64% of the system costs in case 1 (i.e. 278 €·kW^{-1}) and 67% (208 €·kW^{-1}) in case 2, whereas stack costs represent 36% (156 €·kW^{-1}) in case 1 and 33% (102 €·kW^{-1}) in case 2. The AC/DC converter costs represent 53% of the BoP costs (146 €·kW^{-1}) in case 1 and 70% (146 €·kW^{-1}) in case 2. A detailed comparison of system costs breakdowns with literature values can be found in Chapter 4.3.1.8.

Table 4-6: Cost breakdowns of installed SOE systems in cases 1 and 2

		Case 1			Case 2		
	Installation factor	**Free on board cost (k€ 2017)**	**Installed equipment cost (€ 2017·kW^{-1} SOE system)**	**Cost share (%)**	**Free on board cost (k€ 2017)**	**Installed equipment cost (€ 2017·kW^{-1} SOE system)**	**Cost share (%)**
SOE stacks	1.1 [164], [165]	2,127.8 Chapter 4.3.1.5	156.0	36.0	6,958.9 Chapter 4.3.1.5	102.1	32.9
Pressurized vessel[7]	1.1 [164], [165]	531.9	39.0	9.0	1,739.7	25.5	8.2
Electronic, system control and sensors	1.2 [150]	52.8 [150]	4.2	1.0	19.7 [150]	1.6	0.5
AC/DC converter	1 [267]	2,194.0 [267]	146.3	33.7	10,970.1 [267]	146.3	47.2
Heat exchangers	4.11 [163], [231]	305.4 [230, 231]	83.7	19.3	569.2 [230, 231]	31.2	10.1
Heater	4.11 [163],[231]	5.8 [231]	1.6	0.4	20.1 [231]	1.1	0.4
Pump	4.11 [163], [231]	11.7 [268]	3.2	0.7	39.0 [268]	2.1	0.7
Total	**-**	**5,229.5**	**434.0**	100	**20,316.7**	**309.9**	100

As a result, the costs of installed SOE units based on the process layout depicted in Figure 4-3 would be 434 €·kW^{-1} in case 1 and 310 €·kW^{-1} in case 2. These two values will be used as reference for the sensitivity analysis presented in Chapter 4.3.1.7. However, they cannot be used as such for the techno-economic evaluation of SNG production costs in this Chapter, because the process layouts of the SOE units in the power-to-SNG plants detailed in Chapter 2.6.1 are different. How the installed costs determined in Chapter 4.3.1 will be used in the evaluation of SNG production costs is presented in Chapter 4.3.2.

[7] The installed costs of the pressurized vessel are assumed to represent 25% of the installed costs of SOE stacks.

4.3.1.7. Sensitivity analysis

The highest cost shares at the cell, stack and system level were selected and used for the sensitivity analysis. They included raw material costs and current density at cell level, interconnect costs at stack level and AC/DC converter, heat exchangers, and pressurized vessel at the system level. First, the variation interval of each parameter was determined based on literature considerations. Then, the impact of each parameter on the SOE system costs was evaluated and reported in Figure 4-6 based on its minimal and maximal values.

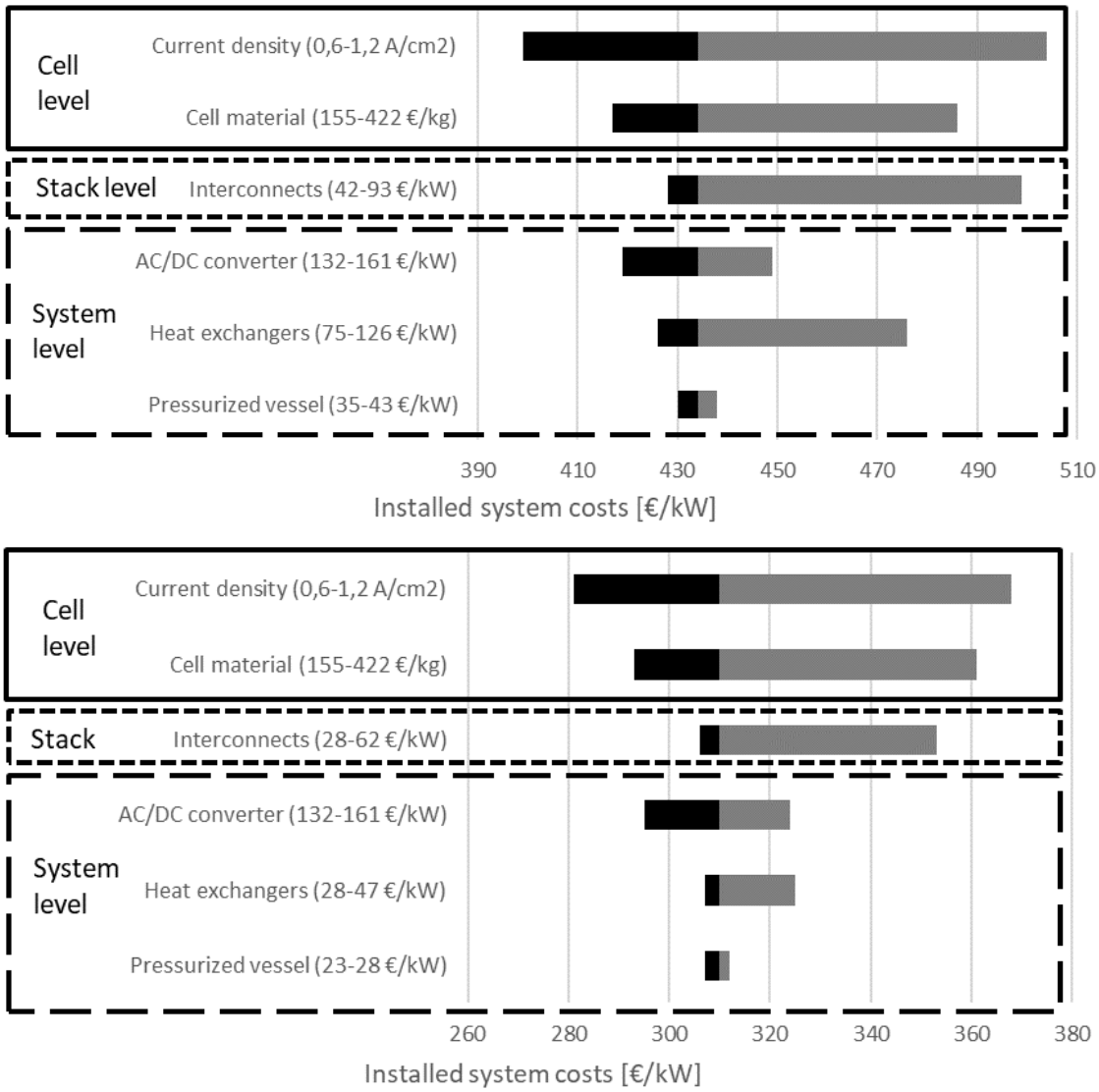


Figure 4-6: Sensitivity analysis on installed investment costs of SOE systems in case 1 (up, reference value 434 €·kW^{-1}) and in case 2 (down, reference value 310 €·kW^{-1})

The current density was varied between -0.6 and -1.2 A·cm^{-2}. The first value corresponds to current density of available SOE units [96], whereas the second corresponds to a value for future SOE units, mentioned e.g. in [27] and allows the comparison with PEM electrolysis units. The cost of scandium stabilized zirconia (SSZ) has by far the highest impact on cell material costs. The price of its most expensive component, scandium oxide, has varied from -30% to +90% around a value of 2,000 $·kg^{-1} between 2011 and 2015 [269]. The same variation interval was assumed here for all cell materials. As

was done in [152], inverter costs and pressurized vessel costs were assumed to vary in the range of ±10%. Similarly, interconnect costs and heat exchangers costs were assumed to decrease by 10% in the best case. However, to account for potential additional costs related to the use of O_2 at both high pressure and high temperature, potential cost increases of 50% and 100% were assumed for heat exchangers and interconnects respectively.

Current density and cell material costs have the highest impact on installed system costs. The reference value for current density was taken as -0.9 $A \cdot cm^{-2}$, even though lower values of -0.6 $A \cdot cm^{-2}$ are used for SOE units at present [96]. This would increase the capital costs of SOE systems from 434 up to 504 $€ \cdot kW^{-1}$ in case 1 and from 310 up to 368 $€ \cdot kW^{-1}$ in case 2. Furthermore, rather low raw material costs from [150] were assumed in the reference case. If those costs would increase by 90%, capital costs of SOE systems would increase from 434 up to 486 $€ \cdot kW^{-1}$ in case 1 and from 310 up to 361 $€ \cdot kW^{-1}$ in case 2.

At the stack level, installed system costs are mostly sensible to interconnect costs (cost variation from 428 up to 499 $€ \cdot kW^{-1}$ in case 1 and from 306 up to 353 $€ \cdot kW^{-1}$ in case 2). They have a lower influence on total installed costs in case 2 because they represent a lower cost share in stack costs than in case 1. Furthermore, conventional sealing techniques were used in our cost evaluation and resulted in negligible sealing costs. Nonetheless, it is not sure that these sealing techniques would still be applied for pressurized SOE stacks, which could result in additional costs.

At the system level, AC/DC converter and heat exchangers costs have a higher impact on the installed system costs than pressurized vessel costs. Installed SOE system costs are much less sensitive to BoP costs than to stack costs.

A worst case estimate resulted in a capital cost increase up to 744 $€ \cdot kW^{-1}$ in case 1 and up to 546 $€ \cdot kW^{-1}$ in case 2. In case the SOE unit would not be thermally coupled with a steam source, steam would have to be produced by an evaporation unit. It was estimated that subsequent equipment costs would increase installed SOE system costs in the reference case by 29% in case 1 (562 $€ \cdot kW^{-1}$) and by 33% (411 $€ \cdot kW^{-1}$) in case 2. This is similar to the cost share reported in [163], where fired heaters represented approx. 25% of total installed SOE costs. In a worst case situation for a stand-alone SOE unit, this would correspond to capital cost of 936 $€ \cdot kW^{-1}$ in case 1 and up to 698 $€ \cdot kW^{-1}$ in case 2.

In conclusion, the current density and the cell material costs have the highest impact on system costs. Hence, it is critical for SOEC manufacturers to decrease the ASR in order to increase the current density injectable in cells for the same operating voltage. The materials costs could be reduced by industrial production of cells, which would drive material costs down. In addition, manufacturers should favor low costs materials or try to substitute expensive materials by cheaper alternatives. The latter is rather complex though, because of the many different mechanical, electrical, and thermal constraints that cell materials have to comply to at the same time. The worst case analysis shows that there is a significant uncertainty related to future costs of the SOE technology, which can double based on the impact of the considered parameters.

4.3.1.8. Comparison with previous investment costs

Capital costs of industrial size SOE units have been scarcely documented so far. The technology readiness level (TRL) of the SOEC technology is still low (6-7) and there are therefore considerable uncertainties on the cost reduction potential of this technology through mass production and upscaling units to industrial size.

The system costs obtained in this paper were summarized in Figure 4-7 along with previous SOE system costs from manufacturers or research institutions [29, 45, 102, 161-165]. The recent work of Smolinka et al. in [27] was not reported on the graph because the capital cost values provided were associated with

very large range of unit capacities from 1 to 100 MW. The literature values were mostly given in €·Nm^{-3}·h. When a value in €·kW^{-1} was provided, it was converted in €·Nm^{-3}·h assuming an energetic system consumption of 3.6 kWh·Nm^{-3} H_2, as was done in [45]. System cost values obtained in both scenarios were plotted in Figure 4-7. Values corresponding to stand-alone SOE units are referred to as "SA", whereas SOE units integrated in power-to-SNG plants with steam recovery are referred to as "PtSNG". The SA values will be preferred for comparison with literature values.

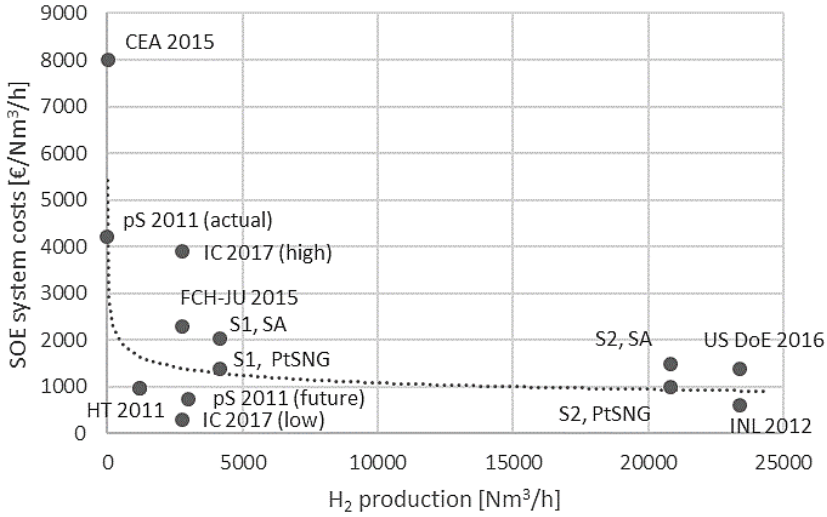


Figure 4-7: Actualized SOE system costs overview, source [29, 45, 102, 161-165], with C1: case 1, C2: case 2, HT: Haldor Topsoe, pS: planSOEC, IC: Imperial College, SA: stand-alone SOE unit, PtSNG: SOE unit integrated in a power-to-SNG plant

In case 1, the H_2 production would be 4,200 Nm^3·h^{-1} for system costs of 2,020 €·Nm^{-3}·h (SA), whereas it would be of approx. 20,800 Nm^3·h^{-1} for system costs of 1,480 €·Nm^{-3}·h in case 2 (SA). If the steam required in the SOEC unit is produced in the catalytic methanation unit, capital costs would decrease down to 1,390 €·Nm^{-3}·h in case 1 (PtSNG) and down to 990 €·Nm^{-3}·h in case 2 (PtSNG), assuming a system consumption of 3.2 kWh·Nm^{-3} H_2 as was done in [45]. System costs in case 2 can be compared with the system costs calculated by INL [163] and the US DoE [164, 165], since H_2 production capacities are similar. In [163], the total investment cost of the SOE unit was 18.7 M$ for an estimated 23,400 Nm^3·h^{-1} capacity, which corresponds to SOE system costs of 610 €·Nm^{-3}·h. This value is considerably lower than the costs of case 2 (1,480 €·Nm^{-3}·h) because of higher stack costs (370 €·Nm^{-3}·h against 210 €·Nm^{-3}·h in [163]) and higher BoP costs (1,110 €·Nm^{-3}·h against 400 €·Nm^{-3}·h in [163]). The values of case 2 are close to the 1,390 €·Nm^{-3}·h reported in [164, 165] and the cost repartition between stacks and BoP is almost the same (25% stacks and 75% BoP in case 2 against 30% stacks and 70% BoP in [164, 165]). System cost estimates in [45] (740 €·Nm^{-3}·h) and in [29] (970 €·Nm^{-3}·h) are much lower than case 1 (2,020 €·Nm^{-3}·h). The costs breakdown of SOE systems was not provided in [29]. However, the repartition between stack and BoP costs is similar in [45] and in case 1, where BoP costs were estimated to be 2.5 to 3 times more expensive than stack costs. Other literature values such as [75, 102] could not be reported in Figure 4-7, since they do not specify unit capacities with their capital cost estimates. Capital costs determined in this work (1,480-2,020 €·Nm^{-3}·h) are in the lower range of estimates (1,100-24,500 €·Nm^{-3}·h in [102] and 1,080-7,100 €·Nm^{-3}·h in [75]). In [102], such low values are associated with a consequent R&D effort as well as a production scale-up, which is coherent with our hypotheses on cell and stack production capacities, on material costs and on operating conditions (voltage and current density).

In a second step, SOE system costs were compared with capital costs of PEM and alkaline electrolysis systems. System costs for future PEM electrolysis units with similar H_2 production capacity as in case 2

were reported in [270]. Capital costs for installed PEM systems were 1,540 €·Nm^{-3}·h (341 €·kW^{-1} with a PEM system consumption of 4.5 kWh·Nm^{-3} H_2), with 490 €·Nm^{-3}·h for the stack costs and 950 €·Nm^{-3}·h for the BoP costs. The value calculated in case 2 is lower (1,480 €·Nm^{-3}·h) and stacks represent a lower cost share (25% against 38% in [270]). This can be explained because PEM systems require low temperature heat exchangers (when SOE systems require high temperature heat exchangers with higher investment costs) and because PEM stacks use expensive platinum as catalytic support in their electrodes. The FCH-JU anticipated similar capital costs for electrolysis technologies by 2030, with 637 €·kW^{-1} for SOE, 255-1,294 €·kW^{-1} for PEM and 377-815 €·kW^{-1} for AEL, assuming unit capacities of 10 MW for each technology [162]. SOE system costs estimated in this work are lower (in the range of 411-562 €·kW^{-1}), however larger electrolysis units (from 15 to 75 MW) were considered. Also, values should rather be compared on a €·Nm^{-3}·h basis than on a €·kW^{-1} basis, since values in €·kW^{-1} fail to take into account the power-to-H_2 conversion efficiency. With a SOE consumption of 3.7 kWh·Nm^{-3} H_2 (conservative value, without heat recovery) and a PEM or alkaline consumption of 4.5 kWh·Nm^{-3} H_2, values reported in [162] would be 2,360 €·Nm^{-3}·h for SOE, 1,150-5,830 €·Nm^{-3}·h for PEM and 1,700-3,670 €·Nm^{-3}·h for alkaline electrolysis. In addition, lower operational expenditures (mainly electricity costs) of SOE units should result in lower H_2 production costs.

4.3.2. Investment costs of main plant components

The main costs assumptions chosen for the calculation of installed investment costs of main plant equipment are gathered in Table 4-7. The majority of these assumptions were supposed to be identical than those of the techno economic analysis implemented by the IFK in [11], except for the electrolysis unit. Indeed, in [11], investment costs of electrolysis units were evaluated using system cost values available in the literature [8, 45], where balance of plant (including AC/DC converter) and H_2 upgrading investment costs were already comprised. These system costs were added to the investment costs of power-to-SNG plant components reported on the detailed process layouts (see Chapter 2.6.1) to determine total plant investment costs. As a result, several balance of plant (BoP) costs of the SOE unit were counted twice, whereas other equipment parts not required in the plant concepts (such as H_2 drying[8]) were also included in the evaluation. Hence, it is rather likely that total investment costs were overestimated. To avoid this, the following approach was followed in this work.
Current and prospective PEM stack investment costs were determined based on recent values reported in the literature [27] and added to other BoP investment costs (including AC/DC converter) corresponding to the process layouts presented in Chapter 2.6.1.

- According to manufacturers, investment costs of 10 MW PEM units are already lower than 4000 €·Nm^{-3}·h. This value, even though conservative, was nonetheless assumed for current costs in this work. Furthermore, PEM stack costs cover 50% of the system costs and the energetic consumption of PEM units is currently about 4.8 kWh·Nm^{-3} (including AC/DC converter) at the beginning of lifetime [27]. In this work, a lower value of 4.5 kWh·Nm^{-3} (including AC/DC converter) at the beginning of lifetime was chosen though, amongst others because of the lower H_2 purity required (no H_2 drying unit is required, see discussion in Chapter 2.3.2.2). As a result, installed costs of PEM stacks are 444 €·kW^{-1}, which corresponds to uninstalled investment costs of 404 €·kW^{-1} with an installation factor of 1.1.

[8] The H_2 purity level for commercial systems is usually very high (5.0) to satisfy the requirements of fuel cells, e.g. for mobility applications. Here though, the humidity level of the H_2 rich gas is low enough after H_2 synthesis for the direct injection in the catalytic methanation unit, so that no H_2 drying step should be required.

- As for prospective values, system costs of 3000 €·Nm^{-3}·h were assumed and the cost share of stacks was supposed to decrease down to 40% [27]. Hence, prospective costs of installed PEM stacks are about 270 €·kW^{-1} (242 €·kW^{-1} for the uninstalled costs, assuming an installation factor of 1.1).

Investment costs of SOE units were evaluated with the following approach.

- Current SOE investment costs were obtained following the same methodology than PEM costs using installed SOE cost values also provided in [27]. SOE systems did not reach the MW scale so far and current values for installed SOE units are about 2,300 €·kW^{-1}. Nonetheless, estimates for larger units are as low as 1,350 €·kW^{-1} in [27]. In this work, an intermediate value of 1,500 €·kW^{-1} was assumed for current installed costs of 15-20 MW SOE units. According to [27], the cost share of stacks represent 30% of the total investment. The stack costs were increased by 25% to account for the additional costs of pressurized operation (the stacks are installed in a pressurized vessel). As a result, installed SOE stack costs were 563 €·kW^{-1}, which corresponds to uninstalled costs of 507 €·kW^{-1} with an installation factor of 1.1.
- Prospective SOE investment costs are based on the values calculated in Chapter 4.3.1.6. Uninstalled stack costs were 182 €·kW^{-1}, which also includes the costs of pressure vessel, electronics and control, and sensors. However, the costs of AC/DC converter, heaters, heat exchangers, and pumps are excluded from this value, because they are calculated independently in this economic evaluation (based on the process layouts of plant concepts 2 and 3 in Chapter 2.6.1). A new evaluation was required because the layout of the stand-alone SOE unit in Chapter 4.3.1.3 is different from the one of the SOE unit integrated in plant concepts 2 and 3. Based on these two power-to-SNG plants layouts, installed SOE costs are about 382 €·kW^{-1}. This value is lower than the 434 €·kW^{-1} calculated for the stand alone SOE unit in Chapter 4.3.1.6, mostly because the costs of steam generation are not included. Moreover, this value is coherent with previous literature estimates for similar SOE units capacities, e.g. from the US DoE [164, 165], the INL [163] and with average manufacturer values recently reported by the Fraunhofer ISE [27] (460 €·kW^{-1} by 2030 and 280 €·kW^{-1} by 2050).

Furthermore, the following differences with [11] also need to be mentioned.

- An installation factor of 4.11 was assumed in this work for most equipment parts based on [163, 231] instead of a value of 3.6 in [11], in order to be coherent with the installation factor value previously used for similar equipment in Chapter 4.3.1.6;
- A same installation factor value of 1.1 was assumed for PEM and SOE stacks in this work (whereas a factor 1.1 was applied for PEM and a factor 1.5 for SOE stacks in [11]). No explanation could be found to justify why the installation factor of pressurized SOE stacks would be significantly higher than the one of PEM stacks.

Table 4-7: Hypotheses selected for the calculation of installed investment costs of main plant components, adapted from [11]

Component	Value	Unit	Year	Reference capacity	Upscaling factor	Comment /source	Installation factor
Biomass conditioning							
Biomass storage	1,200	k€	2002	33.5 t·h^{-1}	0.65	[271]	4.11 [163], [231]
Biomass conveyor	400	k€	2002	33.5 t·h^{-1}	0.8	[271]	
Belt dryer	700	k€	2007	1 MW	0.6	[272]	
Biomass injection	500	k€	2002	33.5 t·h^{-1}	1	[271]	

Component	Value	Unit	Year	Reference capacity	Upscaling factor	Comment /source	Installation factor
Air blower	73.2	k$	2002	1 $m^3 \cdot s^{-1}$	[9]	[11]	
Gasification unit							
Biomass gasifier (Steam-O2, atm)	30,600	k€	2002	68.8 $t \cdot h^{-1}$	0.85	[11, 271]	4.11 [163], [231]
Biomass gasifier (Steam-O2, 20 bar)	42,840	k€	2002	68.8 $t \cdot h^{-1}$	0.85	[11]	
Syngas cleaning							
DBT absorber	61.2	k$	2002	1 m^3	0.3947	[11]	4.11 [163], [231]
Sedimentation tank	57.0	k$	2002	1 $kg \cdot s^{-1}$	[10]	[11]	
Electrolysis							
AC/DC converter	130	€·kW^{-1}	2007	15-20 MW	1	[267]	1
PEM-stacks (current)	404	€·kW^{-1}	2017	15-20 MW	1	[27]	1.1 [164], [165]
PEM-stacks (prospective)	242	€·kW^{-1}	2017	15-20 MW	1		
SOE-stacks (current)	507	€·kW^{-1}	2017	15 MW	1		
SOE-stacks (prospective)	182	€·kW^{-1}	2017	15 MW	1	Chapter 4.3.1.5	
Catalytic methanation							
Fixed bed reactor	5.6	k$	2002	m^3	[11]	[11]	4.11 [163], [231]
Three-Phase reactor	25.1	k$	2002	m^3	[12]	[11]	
Honeycomb reactor	10.9	k$	2002	m^2	[13]	[11]	
SNG post treatment							
CNG injection station	250	k€	2017	-	-	[11]	4.11 [163], [231]
Liquefaction unit	1,564	k€	2015	10 $kt \cdot year^{-1}$	0.7 [273]	[11]	
LNG-tank (stationary)	145	k€	2016	19 t LNG	0.7 [11]	[274]	
Water treatment unit							
Water conditioning[14]	500	k€	2004	30 MW	0.8	[271]	4.11 [163], [231]

[9] Costs in $ 2002 evaluated with following formula: 103,820 + 73,246·Capacity (in $m^3 \cdot s^{-1}$) – 3,431.2·(Capacity (in $m^3 \cdot year^{-1}$))^2

[10] Costs in $ 2002 evaluated with following formula: 9,617 + 56,968·Capacity (in $kg \cdot s^{-1}$) – 1,296·(Capacity (in $kg \cdot year^{-1}$))^2

[11] Costs in $ 2002 evaluated with following formula: 19,788 + 5,627·Capacity (in m^3) – 86.8·(Capacity (in m^3))^2

[12] Costs in $ 2002 evaluated with following formula:21,141 + 25,064·Capacity (in m^3) – 1,296·(Capacity (in m^3))^2

[13] Costs in $ 2002 evaluated with following formula: 10,920 + 166·Capacity (in m^2)

[14] Reference cost value for a conditioning unit feeding a unit with a thermal power of 30 MW (HHV).

The hypotheses for main plant equipment replacement are summarized in Table 4-8.
At the beginning of stack lifetime, the operation tension of SOECs is 1.3 V. It is assumed to be of 1.5 V at the end of stack lifetime before stack replacement. Indeed at this voltage level, it is admitted that the SOE technology is not advantageous anymore compared to low temperature electrolysis technologies. With the hypotheses of Table 4-8, these values correspond to a yearly degradation rate of 3.1%. To maintain the same level of H_2 production assuming a constant current density, the electrical power provided to the SOE unit has to increase by 3.1% each year. This increase was taken into account for the calculation of the annual electrical power consumption of the SOE unit.
As for PEM stacks, the operation tension was assumed to be 1.8 V at the beginning of lifetime and 2.1 V at the end of lifetime. With the hypotheses of Table 4-8, these values correspond to a yearly degradation rate of approx. 1.7%. This value is coherent with the multi annual work plan 2014-2020 of the FCH JU, where a degradation rate of 0.25%·kh^{-1} was reported for state of the art units in 2017 (i.e. 2% per year for a PEM unit operated 8000 h·$year^{-1}$) [104]. To maintain the same level of H_2 production assuming a constant current density, the electrical power provided to the PEM unit was supposed to increase by this value each year. This increase was taken into account for the calculation of the annual electrical power consumption of the SOE unit.
Hence, the average power consumption of the SOE electrolysis unit (stacks and inverter only) including cell degradation is 3.8 kWh.Nm^{-3} in the current scenarios and 3.6 kWh.Nm^{-3} in the prospective scenarios, whereas it is about 4.9 kWh.Nm^{-3} for the PEM unit (stacks and inverter only) in both current and prospective scenarios.

Table 4-8: Hypotheses for the replacement of main plant equipment, adapted from [11]

Main component	Hypothesis	
Fixed-bed methanation reactor	Entire replacement of the catalyst every 5 years	
Three-Phase methanation reactor	Continuous replacement	
Honeycomb methanation reactor	Entire replacement of the catalyst every 5 years	
PEM electrolysis unit	Stack lifetime of 80 kh, 10 years lifetime with 8,000 full load hours per year (1 replacement of all stacks over the plant lifetime)	
SOE electrolysis unit	**Current case**	**Prospective case**
	Stack lifetime of 40 kh, 5 years lifetime with 8,000 full load hours per year (3 replacements of all stacks over the plant lifetime)	Stack lifetime of 80 kh, 10 years lifetime with 8,000 full load hours per year (1 replacement of all stacks over the plant lifetime)
SNG drying unit	Complete replacement of the zeolite every 5 years	

4.4. Operation and maintenance costs

The operation and maintenance costs were assumed to represent a share of the initial installed investment costs of equipment. The corresponding values are gathered in Table 4-9.

Table 4-9: Share of investment costs assumed for the calculation of operation and maintenance costs [11]

Plant unit	Value	Comment
Biomass conditioning, gasification, syngas post treatment, SNG post-	3%	-

Plant unit	Value	Comment
treatment, CNG or LNG synthesis, and water treatment		
PEM electrolysis	3%	Stacks replacement not included, author hypothesis
SOE electrolysis	4%	Stacks replacement not included, author hypothesis
Catalytic methanation	3%	Catalyst replacement not included

The prices of plant feedstocks and by-products are presented in Table 4-10. As a reminder, plant concepts 1 and 2 are both using wood as feedstock. However, a mixture of wood, straw and sewage sludge with a mass proportion of one third each is used in plant concept 3 (see Chapter 2.2). Hence the feedstock cost in plant concept 3 is taken as the arithmetic average between all feedstock costs. As was defined in Chapter 4.2.1, additional plant revenues were considered in all six scenarios. They include both O_2 and residual heat sales.

These additional revenues were not included in the analysis of [90]. They were nonetheless considered in this work in order to evaluate in which measure they could contribute to reduce SNG production costs, assuming a best case configuration.

O_2 sales come from the excess O_2 produced at high purity in the electrolysis unit (no air-sweep system at the anode of the electrolysis cells). It is supposed to be sold as such to another industrial customer on-site. Hence, no further costs for post-processing treatments of this by-product (e.g. compression and bottling) were considered and the revenues correspond therefore to a best case value.

Heat sales come from the heat recovered from the most valuable residual heat sources available in the different plant concepts. The heat is assumed to be injected in a district heating network with the same characteristics than the one of Karlsruhe (see Chapter 2.6.3.2). In plant concept 1, the heat amount injected in the network is about 3.4 MW, whereas it is about 1.3 MW in plant concept 2 and 2.0 MW in plant concept 3. The costs for connecting the heat sources to the district heating network were not included in the analysis, hence the heat revenues have also to be considered as best case values.

Table 4-10: Prices of feedstocks and by-products considered in this work, extended from [11]

Plant feedstock or product	Value	Unit	Source/ comment
Wood (35% humidity)	80	€·MT^{-1}	[11]
Straw (15% humidity)	81	€·MT^{-1}	[11]
Sewage sludge (70% humidity)	-50	€·MT^{-1}	[11]
Electrical power price (all plant uses)	50	€·MWh^{-1}	[11]
Oxygen (by-product)	0.035	€·Nm^{-3}	[16]
Waste heat (by-product for power production or district heating supply)	30	€·MWh^{-1}	[16]

Other costs include plant consumables and personnel costs. They will be shortly detailed here, as they only represent a small contribution to the SNG production costs. Costs related to plant consumables include limestone, ZnO, dibenzyltoluene (DBT), feed water, iron oxide pellets, zeolite, Ni based catalyst, and active carbon. The corresponding cost hypotheses are provided in Table C-3 in Appendix C. As for personnel costs, they amount up to 642 k€·year^{-1}. The detail of the costs is provided in Table C-4 in Appendix C.

4.5. SNG production costs

The production costs and levelized production costs of SNG determined in this work will be presented hereafter. For each plant concept, cost breakdowns will be provided for O&M and total investment costs (including markup costs, see Figure 4-1 in Chapter 4.1.2.1), along with a detailed decomposition of SNG production costs and levelized production costs in the current scenarios. The same will be done for the prospective scenarios, for which only the main changes in cost breakdowns and SNG production costs will be commented. The repartition of the plant components for each plant concept in the different plant units (electrolysis, methanation, syngas post-treatment, SNG post-treatment, etc.) is provided in Figure C-3, Figure C-4, and Figure C-5 in Appendix C.

4.5.1. Plant concept 1

4.5.1.1. Current scenario (S1C)

The costs breakdowns of total investment (i.e. including markup costs) and O&M costs are shown in Figure 4-8. The total investment costs are 63.2 M€. The electrolysis unit and the syngas post-treatment unit represent the largest shares of investment costs, with 22% and approx. 15% respectively. The electrical power costs and the biomass costs cover 62% and 14% of the costs respectively. The total investment costs cover 20% of the SNG production costs and the O&M costs 80%.

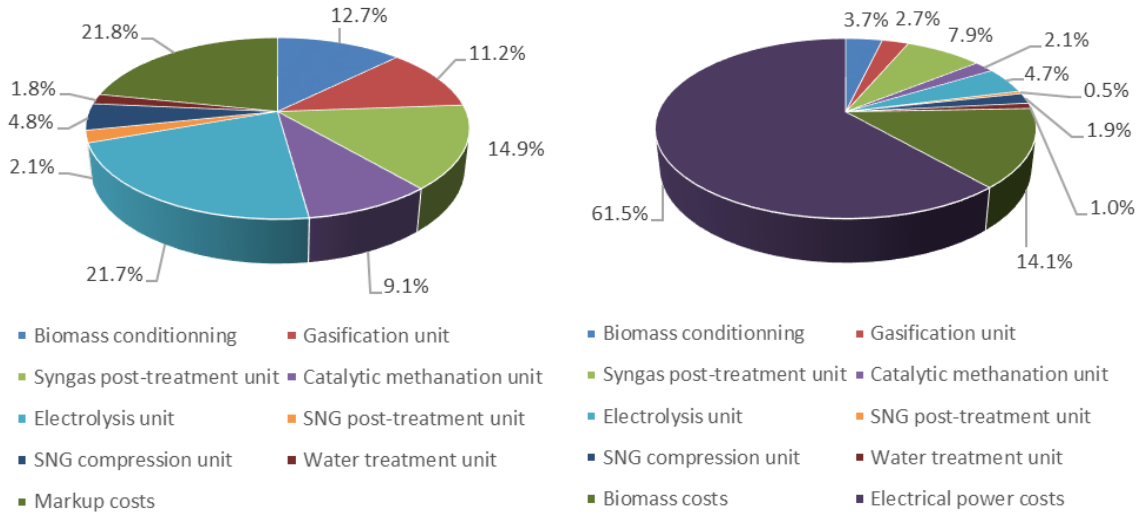


Figure 4-8: Total investment costs breakdown (left, total 21.0 €·MWh^{-1}) and O&M costs breakdown (right, total 85.2 €·MWh^{-1}, total plant revenues excluded) in S1C

The decomposition of SNG production costs is provided in Figure 4-9. The SNG production costs are about 106 €·MWh^{-1} HHV, whereas the levelized production costs of SNG are 95 €·MWh^{-1} HHV (including heat and oxygen sales of 5.1 €·MWh^{-1} and 6.1 €·MWh^{-1} respectively, which corresponds in total to 10.6% of the SNG production costs).

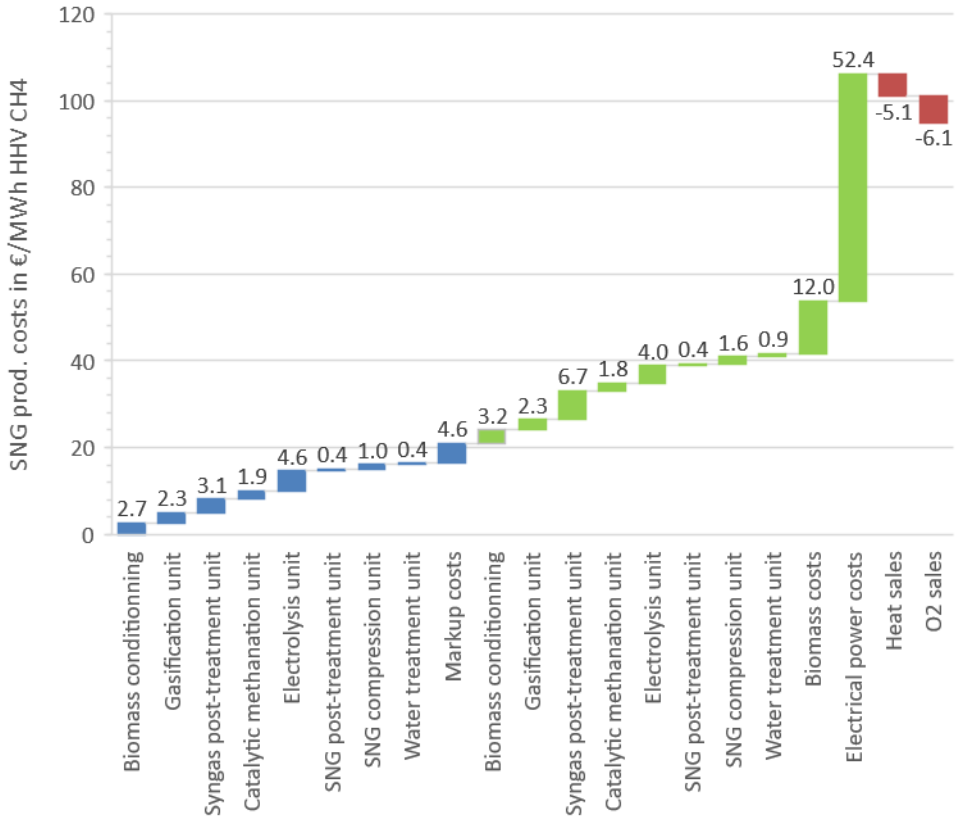


Figure 4-9: Decomposition of SNG production costs in plant concept 1 (S1C, total investment costs in blue, O&M costs in green, plant revenues in red), total production costs without plant revenues 106.2 €·MWh^{-1} HHV

4.5.1.2. Prospective scenario (S1P)

In S1P, the costs breakdowns of O&M and total investment remain rather unchanged compared to S1C, hence they were not provided here. The total investment costs are 59.0 M€. The main difference in the total investment costs repartition is the lower share covered by the PEM electrolysis unit (16% against 22% in the current scenario) because of the lower PEM investment costs in S1P. The electrical power costs and the biomass costs still cover the majority of O&M, with 62% and 14% of the costs respectively. The SNG production costs are reduced down to 104 €·MWh^{-1} HHV and the levelized production costs of SNG down to 92 €·MWh^{-1} HHV (heat and O_2 sales correspond to 10.9% of the SNG production costs). This is explained by the lower contribution of the PEM electrolysis unit of 6.0 €·MWh^{-1} (investment costs and O&M costs), whereas it was about 8.6 €·MWh^{-1} in the current scenario. The total investment costs cover 19% of the SNG production costs and the O&M costs 81%.

4.5.2. Plant concept 2

4.5.2.1. Current scenario (S2C)

The costs breakdowns of total investment and O&M costs are shown in Figure 4-10. The total investment costs are 59.2 M€. The electrolysis unit and the gasification unit represent the largest shares of total investment costs, with 28% and approx. 16% respectively. The electrical power costs and the biomass costs cover the largest share of O&M with 55% and 18% respectively. The total investment costs cover 25% of the SNG production costs and the O&M costs 75%.

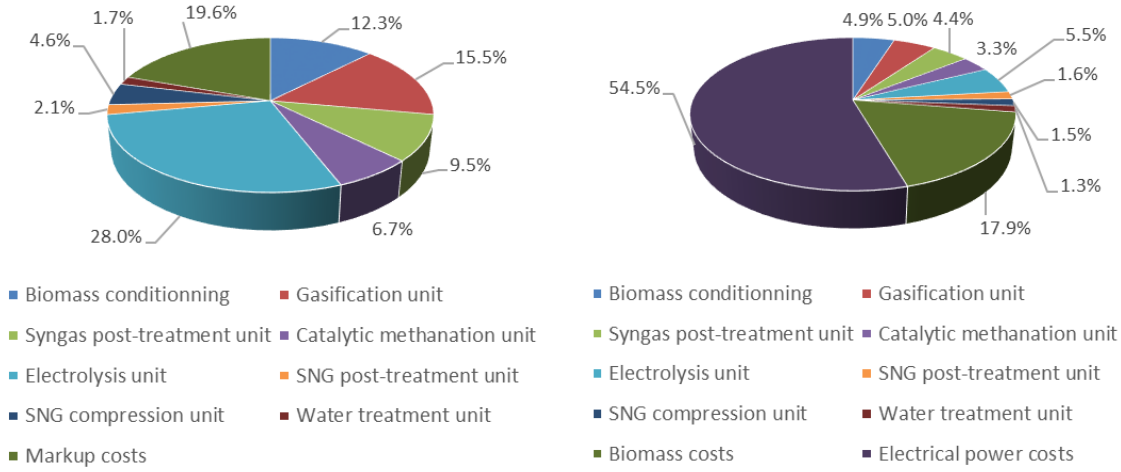


Figure 4-10: Total investment costs breakdown (left, total 21.9 €·MWh^{-1}) and O&M costs breakdown (right, total 66.9 €·MWh^{-1}, total plant revenues excluded) in S2C

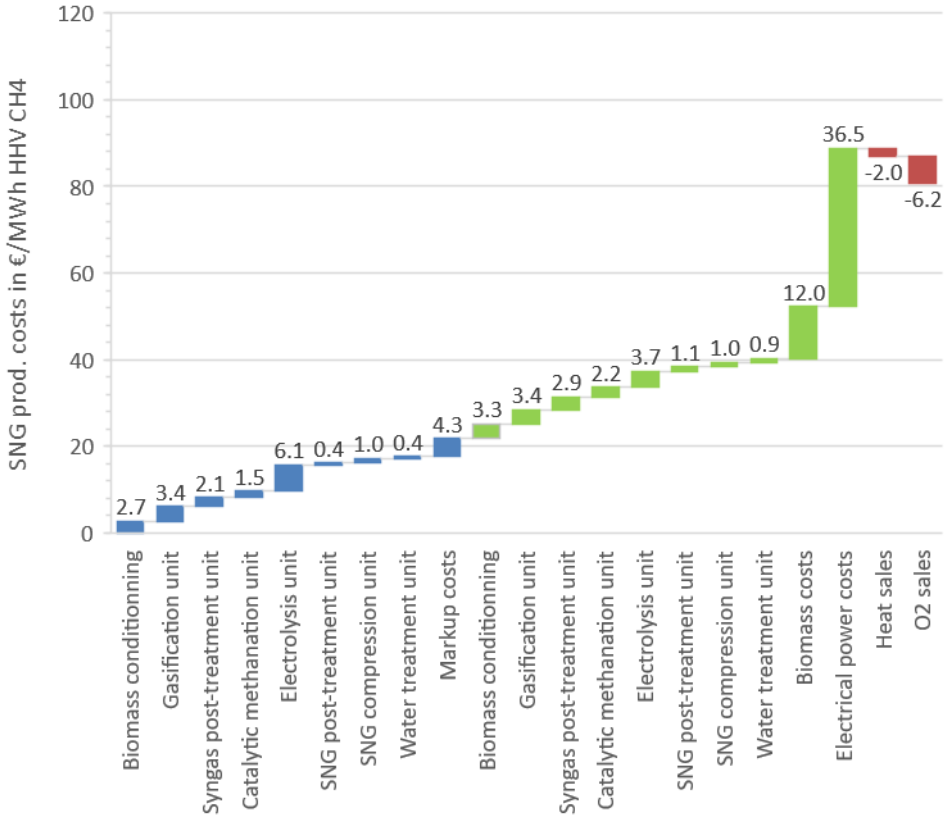


Figure 4-11: Decomposition of SNG production costs in plant concept 2 (S2C, total investment costs in blue, O&M costs in green, plant revenues in red), total production costs without plant revenues 88.8 €·MWh^{-1} HHV

The decomposition of SNG production costs is provided in Figure 4-11. The SNG production costs are about 89 €·MWh^{-1} HHV, whereas the levelized production costs of SNG are 81 €·MWh^{-1} HHV (including heat and oxygen sales of 2.0 €·MWh^{-1} and 6.2 €·MWh^{-1} respectively, which corresponds in total to 9.1% of the SNG production costs).

4.5.2.2. Prospective scenario (S2P)

In S2P, the costs breakdowns of O&M and total investment remain rather unchanged compared to S2C, hence they were not provided here. The total investment costs are 53.1 M€. The main difference in the total investment costs repartition is the lower share covered by the SOE unit (11%, against 28% in S2C) because of the cumulated effect of lower stack investment costs and longer stack lifetime in S1P. The electrical power costs and the biomass costs still cover the majority of O&M, with 56% and 18% of the costs respectively. The SNG production costs are reduced down to 83 €·MWh^{-1} HHV and the levelized production costs of SNG down to 75 €·MWh^{-1} HHV (heat and O_2 sales correspond to 9.8% of the SNG production costs). This can be mainly explained by the lower contribution of the SOE unit of 3.9 €·MWh^{-1}, whereas it was about 9.8 €·MWh^{-1} in S2C. The total investment costs cover 21% of the SNG production costs and the O&M costs 79%.

4.5.3. Plant concept 3

4.5.3.1. Current scenario (S3C)

The costs breakdowns of total investment and O&M costs are shown in Figure 4-12. The total investment costs are 66.6 M€. The SOE unit and the gasification unit represent the largest shares of total investment costs, with 26% and approx. 14% respectively. The electrical power costs and the biomass costs cover the largest share of O&M with 58% and 10% respectively.

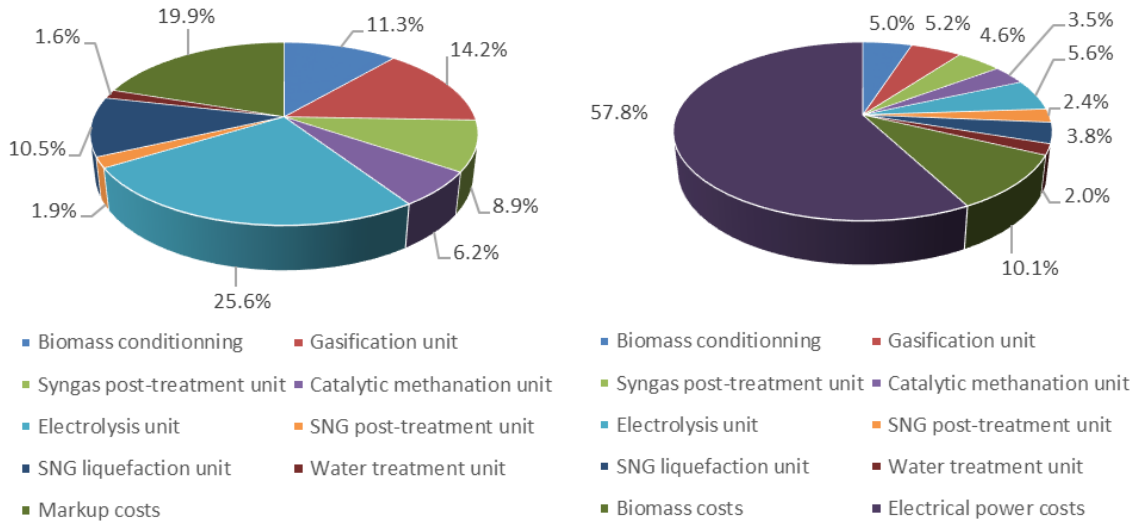


Figure 4-12: Total investment costs breakdown (left, total 24.2 €·MWh^{-1}) and O&M costs breakdown (right, total 63.8 €·MWh^{-1}, total plant revenues excluded) in S3C

The decomposition of SNG production costs is provided in Figure 4-13. The SNG production costs are about 88 €·MWh^{-1} HHV, whereas the levelized production costs of SNG are 79 €·MWh^{-1} HHV (including heat and oxygen sales of 3.0 €·MWh^{-1} and 5.9 €·MWh^{-1} respectively, which corresponds in total to 10.1% of the SNG production costs). The total investment costs cover 27% of the SNG production costs and the O&M costs the remaining 73%.

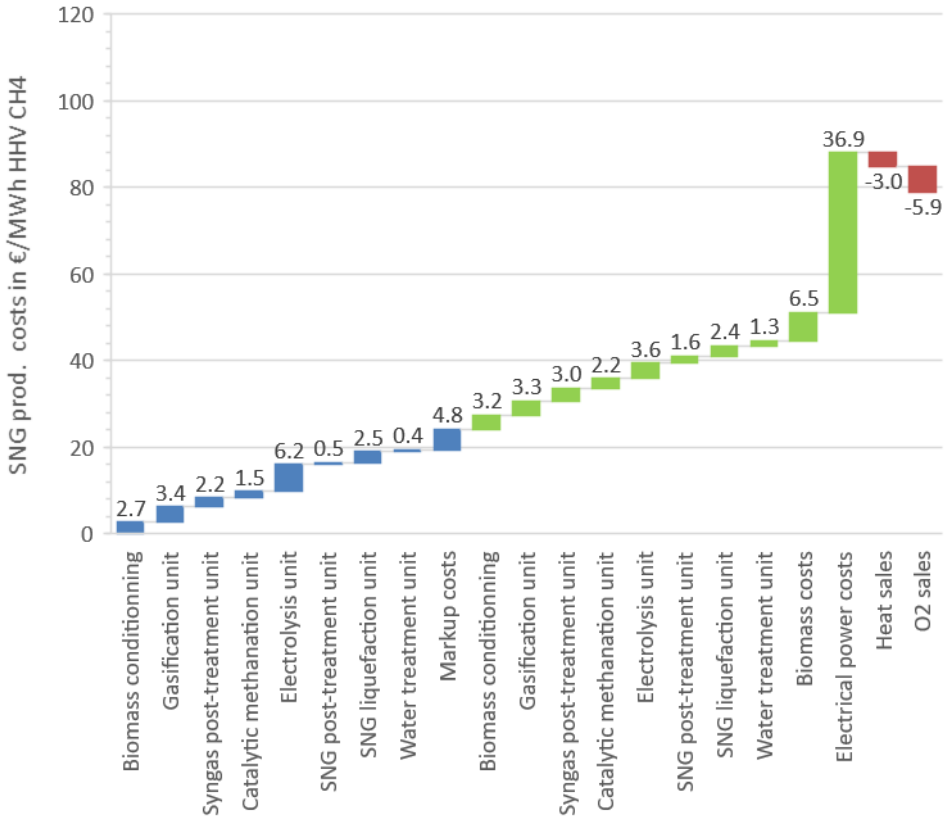


Figure 4-13: Decomposition of SNG production costs in plant concept 3 (S3C, total investment costs in blue, O&M costs in green, plant revenues in red), total production costs without plant revenues 88.0 €·MWh^{-1} HHV

4.5.3.2. Prospective scenario (S3P)

In the prospective scenario, the costs breakdowns of O&M and total investment costs remain rather unchanged ompared to S3C, hence they were not provided here. The total investment costs are 60.4 M€. The main difference in the total investment costs repartition is the lower share covered by the SOE unit (10%, against 26% in S3C) because of the cumulated effect of lower investment costs of SOE stacks and longer stack lifetime in S3P. The electrical power costs and the biomass costs still cover the majority of O&M, with 59% and 10% of the costs respectively. The SNG production costs are reduced down to 82 €·MWh^{-1} HHV and the levelized production costs of SNG down to 73 €·MWh^{-1} HHV (heat and O_2 sales correspond to 10.9% of the SNG production costs). This can be mainly explained by the lower contribution of the SOE unit of 3.8 €·MWh^{-1}, whereas it was about 9.8 €·MWh^{-1} in S3C. The total investment costs cover 24% of the SNG production costs and the O&M costs 76%.

4.5.3.3. Discussion of results

In the current scenarios, the CNG production costs in S1 are significantly higher than in S2 (106 €·MWh^{-1} against 89 €·MWh^{-1} in S2) mostly because of the higher costs of electricity (52.4 €·MWh^{-1} against 36.5 €·MWh^{-1} in S2), which can be explained by the significantly higher electrical consumption of the PEM unit in comparison to the SOE unit. The sum of total investment and O&M costs (without electricity costs) is almost similar in both scenario (53.8 €·MWh^{-1} in S1 and 52.3 €·MWh^{-1} in S2). This can be explained by the fact that the lower costs of the atmospheric gasification unit and of the electrolysis unit in S1 are compensated by the higher costs of the syngas purification unit.

The SNG production costs are slightly lower in S3 than in S2 (88 €·MWh^{-1} against 89 €·MWh^{-1}), most of all because of the lower biomass feedstock costs in S3 (6.5 €·MWh^{-1} against 12.0 €·MWh^{-1}). At the same time, higher investment and O&M costs of the SNG liquefaction unit in S3 compared to those of the SNG compression unit in S2 enable to partially offset the difference of SNG production costs in both scenarios. Indeed, in S3, the biomass feedstock is a mixture of wood, straw and sewage sludge in equal mass proportions with an overall price of 37 €·MT^{-1}, whereas the biomass feedstock used in S2 is wood with a price of 80 €·MT^{-1} more than twice as high (see Table 4-10). However, biomass costs in S3 are more than half the costs in S2 because of the high ash content in the sewage sludge, which results in higher feedstock amounts in S3 to get the same CH_4 output in both plant concepts.

In the prospective scenarios, the CNG production costs in S1 are also significantly higher than in S2 (104 €·MWh^{-1} against 83 €·MWh^{-1} in S2) because the electrical consumption of PEM units is higher than that of SOE units. The difference of SNG production cost between S1 and S2 increases in the prospective scenarios compared to the current scenarios because larger investment costs reduction can be achieved for SOE units than for PEM units.
The differences of SNG production costs in S2P and S3P can be justified in the same way than for S2C and S3C.

4.5.4. Sensitivity analysis

4.5.4.1. Choice and justification of the key sensitivity parameters

As a reminder, one of the main objectives of this work is to assess in which measure electrolysis related costs (mostly the costs of the SOE technology) can contribute to the reduction of SNG production costs. Hence, only the impact of the most influential electrolysis parameters on the SNG production costs will be considered in this sensitivity analysis and the impact of other plant unit parameters will not be discussed. Based on the sensitivity analysis in Chapter 4.3.1.7, the investment costs of SOE units are mostly sensitive to stack components costs (cell material, interconnects) and to the current density, which indicates the amount of electrical power that can be injected in a stack. All other parameters such as heat exchangers or AC/DC converter have a lower influence on the investment costs of SOE units and will therefore not be included. Hence, the following parameters will be considered.

- The influence of stack component costs will be assessed by varying the installed investment costs of stacks. The variation of stack lifetime is considered to be included in the stack investment cost, since it determines how often stacks need to be replaced.
- The electrical power costs, as they represent a large share of SNG production costs in all scenarios (in the range of 55-62%).

Both parameters were commonly used in previous sensitivity analyses, e.g. in [14, 164, 165].
In the current scenarios, both parameters will be considered, as they also correspond to the highest cost shares. In the prospective scenarios however, the share of investment costs for electrolysis stacks is not preponderant (because of the supposed costs reductions through mass production and improved lifetime). Hence this parameter will not be included in the prospective sensitivity analysis. Electrical power costs still have a strong influence on SNG production costs though, and will therefore be the key parameter investigated in the sensitivity analysis of the prospective scenarios.
As for the variation intervals considered, the electrical power costs are assumed to vary in the range of 0-100 €·MWh^{-1}, with a reference value of 50 €·MWh^{-1}, as was done in [11]. The variation intervals of the stack costs for the current scenarios were defined as follows for PEM and SOE technologies.

- Based on manufacturer assertions, installed investment costs of PEM units can already be lower than 4,000 €·Nm^{-3}·h. Hence, a minimal value of 3,000 €·Nm^{-3}·h was assumed for the sensitivity analysis in the current scenarios. A conservative, maximal value of approx. 6,600 €·Nm^{-3}·h (1,470 €·kW^{-1} with an energetic consumption of 4.5 kWh·Nm^{-3}) was assumed, in accordance with the central value of present costs for PEM units reported in [27]. With a stack costs share covering 50% of system costs at present and an energy consumption of 4.5 kWh·Nm^{-3}, installed PEM stack costs fluctuate between 333 and 735 €·kW^{-1} (-25% and +65% compared to the reference value of 444 €·kW^{-1} determined in Chapter 4.3.2).
- Installed investment costs of SOE units were assumed to vary in the range of 1,350-2,300 €·kW^{-1} at present, which correspond to the central and progressive values reported for SOE units in [27]. These values were assumed to be adapted to large units of more than 10 MW considered in this work. With a stack cost share of 30% and a cost increase of 25% for pressurized operation, installed investment costs of SOE stacks are in the range of 506-863 €·kW^{-1} (-10% and +50% compared to the reference value of 563 €·kW^{-1} determined in Chapter 4.3.2).

4.5.4.2. Results

The evolution of the SNG production costs as function of the electrical power costs is represented in Figure 4-14. In order to improve the readability of the Figure, the following curves are not shown.

- The curves corresponding to the scenarios S3C and S3P, since SNG production costs are almost equal for the plant concepts 2 and 3, and that the comparison between plant concept 1 and 2 is more relevant, because both plants produce CNG ;
- The curves of levelized production costs, because the values of levelized production costs are close to those of production costs and their evolution as a function of the electrical power is identical. Also, the curves of SNG production costs were preferred, because heat and oxygen can be sold only in particular industrial site configurations.

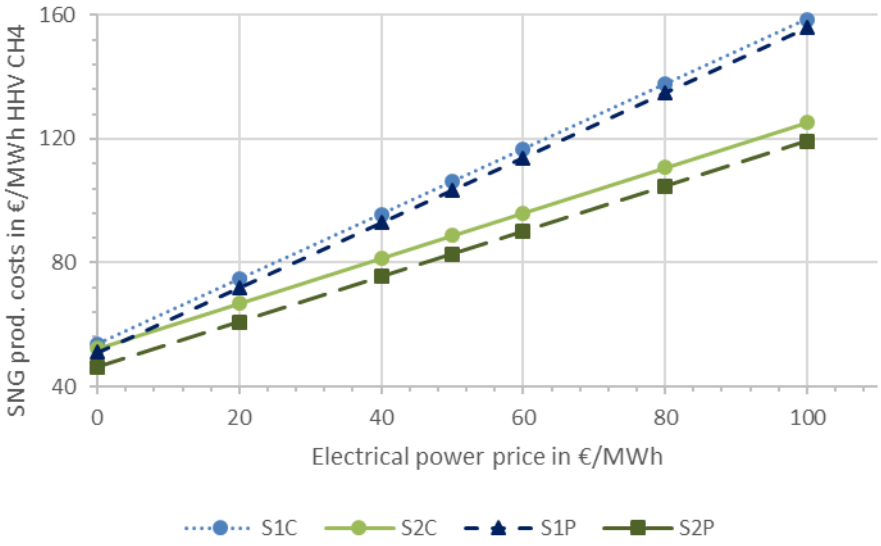


Figure 4-14: SNG production costs as function of the electrical power prices in S1C, S1P, S2C, and S2P, reference value of electrical power prices 50 €·MWh^{-1}, 8,000 full load hours per year

The electrical power prices have a higher influence on the SNG production costs in S1C and S1P than in S2C and S2P. This can be explained by the much higher electrical consumption of PEM units compared to SOE units. The difference of SNG production costs between all scenarios is about maximum 8 €·MWh^{-}

[1] when the electrical power prices are 0 €·MWh^{-1} and this value keeps on increasing with the electrical power prices to reach approx. 39 €·MWh^{-1} for electrical power prices of 100 €·MWh^{-1}. Assuming an electrical power price equal to zero, the SNG production costs could be as low as 46 €·MWh^{-1}, which would almost be competitive with conventional natural gas prices for all sectors in France (average value 40.6 €·MWh^{-1} between 2011 and 2017, HHV based value without VAT) [23].

Assuming the same stack lifetime of 40 kh in S2C and S2P, the SNG production costs would drop from 89 €·MWh^{-1} in S2C down to 84 €·MWh^{-1} in S2P because of the lower stack investment costs (value not represented in Figure 4-14). This value is only slightly higher than that of 83 €·MWh^{-1} obtained in S2P for a 80 kh stack lifetime. In other words, the reduction of stack investment costs would have a higher impact on SNG production costs than the improvement of stack lifetime.

The evolution of SNG production costs as function of installed investment costs of stacks is represented in Figure 4-15. For the same reasons mentioned earlier, the curves of levelized production costs and production costs in S3C were not represented.

When installed investment costs of PEM stacks increase from 333 up to 735 €·MWh^{-1} (from -25% up to 65% compared to the reference value of 444 €·MWh^{-1}), SNG production costs increase from 105 up to 111 €·MWh^{-1}. When installed investment costs of SOE stacks increase from 507 up to 863 €·MWh^{-1} (from -10% up to 50% compared to the reference value of 563 €·MWh^{-1}), SNG production costs increase from 88 up to 93 €·MWh^{-1}. The slope of the curve is identical in both scenarios because all other costs contribution to the SNG production costs than the stacks remain the same.

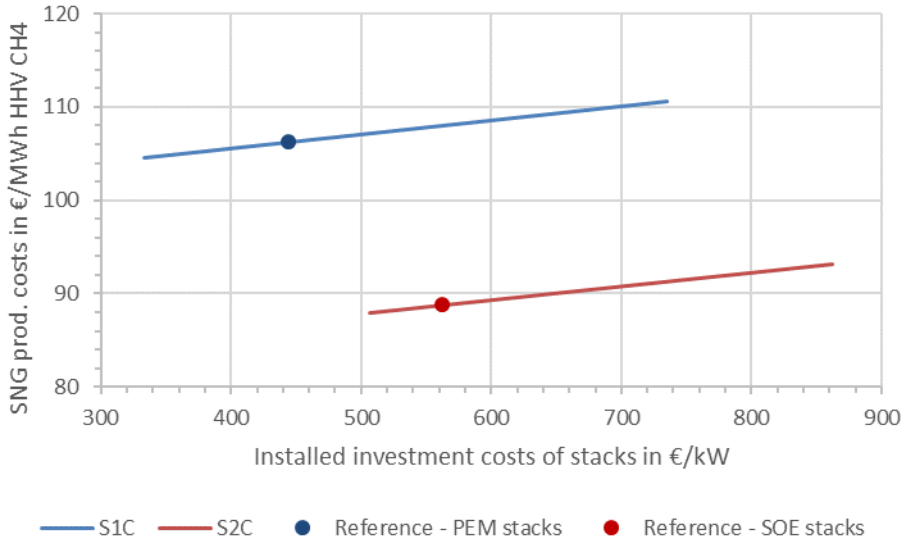


Figure 4-15: SNG production costs as function of stack installed investment costs in S1C and S2C, with electrical power prices of 50 €·MWh^{-1} and 8,000 full load hours per year

4.6. Comparison with SNG, biomethane, and natural gas costs

SNG production costs determined in this work will be compared to the costs or the price of the products listed hereafter. Here again, only the scenarios S1 and S2 will be used for the analysis, as the SNG production costs in scenarios S2 and S3 are very close.

- SNG from power-to-SNG plants. The comparison will be limited to plant concepts for bio-syngas upgrading using electrolytic H_2 from a SOE unit or a PEM unit. Previous power-to-SNG production costs with integrated SOE units were already reviewed in Chapter 1.1.4.2 [14-17, 19]. Here, only the sources with plant capacities comparable to the one considered in this work

(20 MW capacity, based on the HHV of CH_4) and with production costs excluding plant revenues, such as [16], [17], [56], and [241] will be discussed;

- Bio-methane (bio-CH_4) from gasification. Here, the most relevant comparison is the 20 MW bio-methane plant (based on the LHV of CH_4) of the GoBiGas project in Gothenburg, Sweden [198, 275]. Bio-CH_4 was produced from different feedstock, e.g. wood, through gasification and syngas upgrading through catalytic methanation, without electrolytic H_2;
- Bio-methane from anaerobic digestion, considering two different typical unit capacities (100 $Nm^3 \cdot h^{-1}$ and 260 $Nm^3 \cdot h^{-1}$ CH_4). The production costs related to the first unit capacity were investigated in the French context in [276] for direct injection of bio-methane in the gas grid, for on-site compression and transportation before injection to the grid, and for on-site liquefaction and transportation before injection to the grid. The second unit capacity corresponds to a German plant injecting bio-methane in the local gas grid [277].
- The average price of natural gas for all sectors in France between 2011 and 2017 [23].

All production costs are summarized in Figure 4-16.

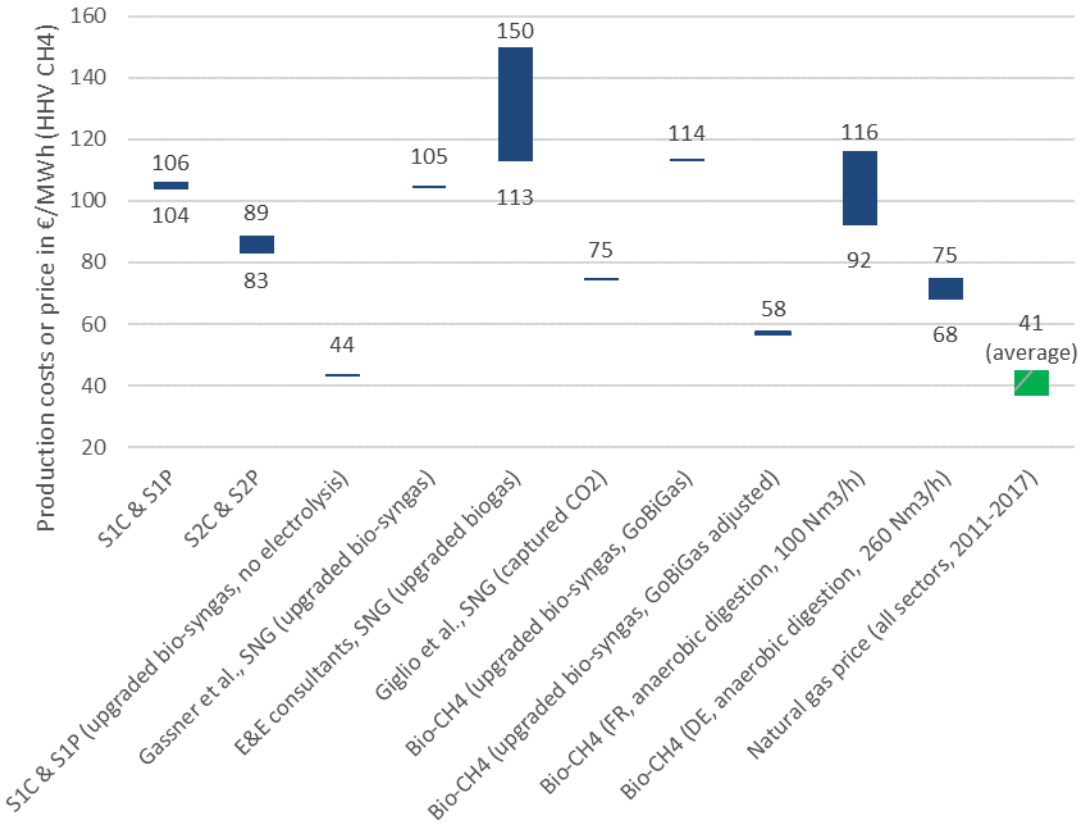


Figure 4-16: Comparison of the SNG production cost in S1 and S2 with several values for CH_4 based products and with the average price of natural gas in France, sources [16, 17, 23, 241, 275-277]

Economic evaluations of power-to-SNG plant concepts similar to the ones investigated in this work were scarcely reported so far. Gassner et al. reported the economic analysis of a concept similar to plant concept 1 in [241], with a low temperature electrolysis unit whose technology was not specified and with a wood input of 20 MW LHV, which is approx. twice as large as the capacity considered in plant concept 1. SNG production costs were provided in MW electrolysis per MW wood for ratios up to 1.5. Extrapolating the curves to higher ratios up to 1.8 similar to those of plant concept 1, SNG production costs would be approx. 105 €·MWh^{-1}, which matches well the 104-106 €·MWh^{-1} obtained in S1. The hypotheses are

nonetheless considerably different in these works. The lower CAPEX, the higher efficiency of the electrolysis unit (300 €·kW^{-1} and 85% LHV efficiency compared to 416-594 €·kW^{-1} and 67% LHV efficiency in S1), and the lower price of wood assumed in [241] (16.7 €·MWh^{-1} compared to 80 €·MWh^{-1} in S1) compensate the higher electricity price (88.9 €·MWh^{-1} compared to 50 €·MWh^{-1} in S1) and result in a similar SNG production cost.

Sigurjonsson and Clausen reported the economic evaluation of a polygeneration system able to operate as a power-to-SNG plant with a SNG output of 168 MW in [56], with features similar to plant concept 2. The SNG selling price required to start generating revenues after 20 years[15] (with an interest rate of 7%) was estimated to be 55 €·MWh^{-1}. This means that the SNG production cost has to be lower than this value in order to be able to reimburse the total investment costs and the O&M costs of the plant over the years. This low value compared to the SNG production costs in S2 can be explained by the low biomass feedstock price at 25.6 €·MWh^{-1} and the low electricity price at 25 €·MWh^{-1}, as well as the low investment costs of the SOE unit below 120 €·kW^{-1}. With similar hypotheses than S2 for these parameters, the electrical power costs in [56] would be multiplied by two and increase by 20 €·MWh^{-1}, whereas the biomass costs would be multiplied by three and increase by 30 €·MWh^{-1}. Since the SOE unit represents one third of the investment costs in [56] and as the investment costs are approx. three times lower than that of S2P, the investment costs would double and increase by 15 €·MWh^{-1}. As a result, SNG production costs should be lower than 120 €·MWh^{-1} for the plant to be profitable after twenty years, which is more coherent with the SNG production costs in S2P (83 €·MWh^{-1}).

In 2014, E&E consultants estimated that production costs of SNG upgraded from biogas with electrolytic H_2 synthesized in a 10 MW SOE unit would be 150 €·MWh^{-1} by 2030 and could drop down to 113 €·MWh^{-1} by 2050 [16]. The 2030 value is considerably higher than the values in S2 (83-89 €·MWh^{-1}). Even though the price of electricity assumed is low (25 €·MWh^{-1} against 50 €·MWh^{-1} in S2), the number of full load hours is also much lower (e.g. 2,000 h·year^{-1} for 2030 against 8,000 h·year^{-1} in S2) and explains the higher costs observed in [16]. The reduction of the SNG production cost from 2030 to 2050 reported in [16] is mostly related to the increase of full load hours up to 3,000 h·year^{-1}.

Giglio et al. estimated SNG production costs to be approx. 75 €·MWh^{-1} in [17], where SNG was produced from captured CO_2 in a 8 MW plant (based on the LHV of SNG) with an integrated 10 MW SOE unit, assuming 8,000 h·year^{-1} operation and an electricity price of 50 €·MWh^{-1}. This value is lower than those of S2 (83-89 €·MWh^{-1}), which can be explained amongst others by the fact that the costs of CO_2 capture were not included in the analysis.

SNG production costs in S1 and S2 (83-106 €·MWh^{-1}) can be compared to those of the 20 MW SNG plant of the GoBiGas project (114 €·MWh^{-1}). The GoBiGas plant only valorizes about 30% of the carbon content of biomass, whereas it is more than 97% in S1 and S2 because of the additional H_2 input from the SOE unit. As a result, much larger biomass conditioning, gasification, and syngas treatment units and consequently much larger auxiliaries are required than in S1 and S2 to reach the same plant output. Moreover, additional equipment not required in the plant concepts of S1 and S2, such as a CO_2 separation unit are also required. If all the biomass carbon content of the GoBiGas plant was valorized with electrolytic H_2, a much smaller syngas production unit would be required, with a capacity 3.7 times smaller in first approximation[16]. The same scaling factors of investment and O&M costs (for personal, maintenance, and other costs) in the techno economic evaluation of SNG production costs provided by Thunman et al. in [275] for the GoBiGas plant were applied to downscale plant costs to a 3.7 times smaller

[15] NB : as this value does not correspond to a production cost, it was not reported on the Figure with other production costs of the literature discussed in this paragraph.

[16] The factor 3.7 is calculated as 100%/30%·1.11=3.7, where 1.11 corresponds to the ratio of HHV and LHV of CH_4.

unit. As for consumables and feedstock costs, they were divided by 3.7. As a result, SNG production costs of a smaller GoBiGas unit with full valorization of the biomass carbon content would be 58 €·MWh^{-1}. This value is significantly higher compared to the costs of syngas production and catalytic methanation in S1 and S2 (44 €·MWh^{-1}) for the following reasons. First, the GoBiGas plant used an air assisted gasification unit and required a CO_2 separation unit, whereas a more compact O_2 assisted gasification unit was preferred in this work. Second, no CO_2 separation unit was required because of the electrolytic hydrogen supply.

SNG production costs in S2 could become competitive with the bio-CH_4 production costs from small biogas upgrading units of 100 and 260 Nm^3·h^{-1} (92 €·MWh^{-1} in [276] and 68-75 €·MWh^{-1} in [277] respectively, injection and biogas production costs included). In the case of a 100 Nm^3·h^{-1} unit with no direct access to the gas grid, additional costs for compression in bottle racks or even liquefaction before transport are required and production costs may increase up to 116 €·MWh^{-1}. In that case, the SNG produced in both S1 and S2 would become competitive with biogas upgrading units. Hence, the SNG produced by power-to-SNG plants could be competitive with bio-CH_4 from biogas upgrading plants, which would nonetheless require large power-to-SNG plant capacities.

Still, even in the most favorable case, SNG production costs in S2 and S3 are two times more expensive than the average price of natural gas for all sectors in France.

4.7. Conclusions of Chapter 4

An economic evaluation of the three power-to-SNG plant concepts presented earlier in this work was implemented in this Chapter.

First, SOE investment costs for large scale units were evaluated in the context of power-to-SNG plants. As discussed in Chapter 1, electrolysis covers the major part of power-to-SNG plant costs, hence accurate electrolysis cost estimates are required for the evaluation of SNG production costs. Moreover, investment costs of large SOE units were scarcely documented so far and even less so in the context of power-to-SNG plants. Hence, a bottom-up cost analysis of SOE units in the range of 10-100 MW starting from raw cell materials was implemented. As a result, the costs of an installed SOE unit integrated in a power-to-SNG plant would be 434 €·kW^{-1} for a 15 MW unit and 310 €·kW^{-1} for a 75 MW unit. In case of a stand-alone SOE unit, these costs would increase up to 562 €·kW^{-1} and 411 €·kW^{-1} respectively. The most influential parameters on the installed investment costs of SOE units are the current density at the thermoneutral operation point (1.3 V at 1073 K) and the cell materials, which represent 23% of uninstalled system costs for a 15 MW unit and 34% in the case of a 75 MW unit.
These SOE system cost values could not be used directly for the economic evaluation of the power-to-SNG plants of Chapter 2, because the plant layouts of the SOE units are different in the two cases. However, uninstalled costs of pressurized stacks (including pressure vessel, electronics, controls, and sensors) estimated at 182 €·kW^{-1} for a 15 MW SOE unit were used as reference value of stack costs in the economic evaluation of production costs and levelized production costs of SNG in the prospective scenarios for plant concepts 2 and 3.

Second, production costs and levelized production costs of SNG were determined for all three plant concepts and compared, including an analysis and a comparison of the cost structure obtained for each plant concept. The calculated values of SNG production costs are summarized in Figure 4-17.

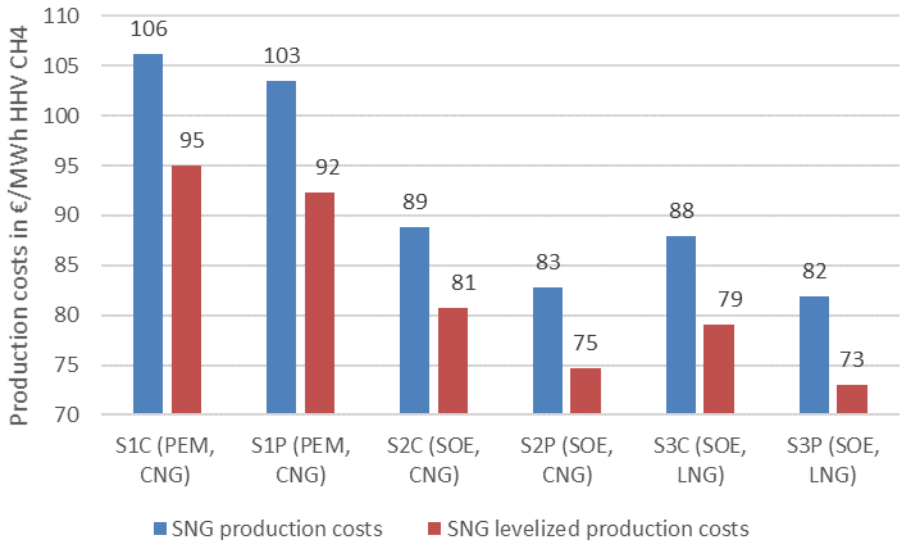


Figure 4-17: Overview of the production costs and the levelized production costs of SNG in all scenarios investigated in this work

The total investment costs cover 19 to 27% and the O&M costs 73 to 81% of the SNG production costs. The electrolysis unit represent the largest share of investment costs in all current scenarios (in the range of 22-28%), but this share significantly decreases in all prospective scenarios (down to 10-16%) and

becomes lower than the share of other plant units (such as the gasification unit, the biomass conditioning unit or the syngas treatment unit). As a more general observation, the investment costs breakdowns are highly dependent on the boundaries chosen for each plant unit, as well as on plant configuration and thermal integration.
As for the O&M costs, the highest cost shares are covered in all scenarios by the electrical power costs (55-62%) and by the biomass feedstock costs (10-18%).
Plant revenues from both heat and O_2 enable to reduce the SNG production costs by 11% in the best case. However, the number of industrial sites where both these by-products could be sold to customers is limited. Hence, they cannot be seen as business model facilitators for power-to-SNG pathways.
The most influent parameters on the SNG production costs are the investment costs of stacks (initial and replacement investment) and the electricity price in the current scenarios. However, because of the mass production and the improved lifetime of stacks, only the electricity price remains a key driver of SNG production costs in the prospective scenarios.

Third, SNG production costs determined in this work were compared to other production costs of methane based products, such as SNG from power-to-CH_4 plants, bio-CH_4 from gasification or from anaerobic digestion, but also with the price of natural gas. The differences with previous production cost values for SNG produced in power-to-SNG plants or in biomass-to-SNG plants with comparable capacities could be justified. In the best case, SNG production costs calculated in this work would still be two times higher than the average price of natural gas for all sectors in France.

Conclusions

In this work, the energy analysis of three innovative power-to-SNG plant concepts with integrated electrolysis, gasification, and catalytic methanation units was implemented, which also included plant characterization in terms of carbon utilization, cooling water and net water requirements. The plant concepts combined different electrolysis technologies (PEM, SOE), catalytic methanation technologies (fixed bed, three phase, honeycomb), and biomass gasification feedstock (sewage sludge, straw, wood), for the synthesis of different products (CNG or LNG).
For each plant, a theoretical maximal plant efficiency was calculated based on a simplified process flow diagram and a pinch diagram. A full explicit thermal integration was then implemented. The efficiency of the integrated plant was very close to the maximal theoretical efficiency, which tends to validate the relevance of the thermal integrations from an energy standpoint. The plant concepts with integrated SOE units show high efficiency values up to 81.8% for SNG, up to 81.0% for CNG and up to 78.5% for LNG (based on the HHV of end-products), which are significantly higher than the values with integrated PEM electrolysis unit (64.9% or 64.4% with SNG resp. with CNG as end-product). The efficiency is significantly higher, mostly because the cooling steam of the catalytic methanation unit can be directly injected in the SOE unit. These efficiency values highlight the potential for efficiency improvement and operating cost reduction of the SOEC technology compared to conventional electrolysis technologies (PEM and alkaline by extension) when coupled to steam sources.
Options for the valorization of residual heat were also discussed. For plants with a low temperature electrolysis unit, the valorization of the excess steam in a steam turbine could only increase plant efficiency by a few percent. In the case of power-to-SNG plants with a SOE unit, the residual heat should preferably be injected in a district heating network, such as the one of Karlsruhe.

The second main contribution of this work was the implementation of a 1D dynamic model to investigate the thermal behavior of SRUs integrated in a SOE stack. The model was adapted from previous work to propose a simplified modelling approach, where the ASR is assumed to be linear. The transient behavior of two different cells architectures electrolyte supported cells (ESC) and cathode supported cells (CSCs) was investigated and compared.
First, a simplified model was implemented, where the ASR was assumed to be constant with cell temperature. The transition from standby mode to exothermic or endothermic mode was investigated, resulting in comparable transient duration and cell temperature gradients for both SRU types. The model output at the end of the transient was verified by comparison with the exact solution in permanent regime. The model also showed good agreement with the model reported by Cai et al. in [142], with a deviation of cathode stream outlet temperatures of max. 1.2% in endothermic mode.
Second, an extended model was implemented, in which the ASR depends on the cell temperature, based on different empiric laws for CSCs and ESCs derived from cell experimental data. The transient behavior was investigated for similar conditions than the simplified model. The electrical power ranges corresponding to a maximal local thermal gradient permitted along the cell of 10 $K \cdot cm^{-1}$ and to a maximal local operation voltage of 1.35 V were calculated when switching from hot standby mode to either exothermic or endothermic mode. They were comparable for both cell architectures. However, the thermal gradients were lower for ESCs than for CSCs in exothermic mode (22 K against 30 K) and in endothermic mode (62 K against 68 K) because of their higher ASR. Hence, ESCs should be preferred for intermittent power applications because of their higher thermal stability.

Third, the SRU model was then coupled with a simplified power profile and extended to a complete H_2 production and storage unit composed of a SOE unit with two modules including BoPs. The SOE stacks were operated in an extended power range whose limits were based on the aforementioned conditions on local temperature gradient and local operating voltage. The energy consumption of the H_2 production unit fluctuated in the range of 3.4-3.8 $kWh \cdot Nm^{-3}$ H_2. Thanks to the cooling steam recovered from the catalytic methanation unit, high power-to-H_2 AC efficiencies were reached (93-103% HHV). After a first dimensioning of the H_2 storage tank and the catalytic methanation unit, strategies and plant configurations were proposed to reduce the H_2 storage size. The following conclusions could be drawn.
The electrical coupling of SOE units with fluctuating power profiles reduces the performance of the thermal coupling between SOE and catalytic methanation units, which lowers the efficiency of the power-to-SNG plants, but also increases plant costs and complexifies plant operation. Multifuel plants producing both H_2 and SNG could simplify the design and operation of power-to-SNG processes. A fraction of the SOE modules operated at nominal capacity would cover the H_2 requirements of the catalytic methanation unit, whereas the remaining modules would absorb the power intermittency. The flexible operation of these modules with SOECs operated in exothermic and endothermic mode could improve the power-to-H_2 conversion efficiency compared to on/off module operation.
In case of constant electrical power load and assuming SOE units coupled with catalytic methanation units, SOECs should preferably be operated in thermoneutral or exothermic mode, even if a high temperature heat source above 1073 K such as a gasification unit is available. In case of fluctuating power load though, the operation power range of SOECs should be enlarged as much as possible to improve the ability to modulate the load and absorb the fluctuations of intermittent power sources. Hence both exothermic and endothermic operation should be favored, independently of the downstream processes.

An economic evaluation of the three power-to-SNG plant concepts was also implemented, assuming a CH_4 capacity of 20 MW HHV.
First, a bottom-up cost analysis of SOE units in the range of 10-100 MW starting from raw cell materials was implemented in the context of power-to-SNG plants, which was scarcely reported in the literature so far. As a result, the costs of an installed SOE unit integrated in a power-to-SNG plant would be 434 €·kW^{-1} for a 15 MW unit and 310 €·kW^{-1} for a 75 MW unit. The most influential parameters on the installed investment costs of SOE units are the current density at the thermoneutral operation point (1.3 V at 1073 K) and the cell materials.
Second, production costs and levelized production costs of SNG were determined for all three plant concepts based on current and prospective scenarios. The SNG production costs are in the range of 104-106 €·MWh^{-1} CH_4 (HHV) for plants with PEM units and could be lowered down to 82-89 €·MWh^{-1} CH_4 (HHV) for plants with SOE units. Plant revenues from both heat and O_2 could further reduce the SNG production costs by 11% in the best case. The total investment costs cover 19 to 27% and the O&M costs 73 to 81% of the SNG production costs. The electrolysis unit represent the largest share of investment costs in all current scenarios (in the range of 22-28%), but this share significantly decreases in all prospective scenarios (down to 10-16%) and becomes lower than the share of other plant units (such as the gasification unit, the biomass conditioning unit or the syngas treatment unit). As for the O&M costs, the largest cost shares are covered in all scenarios by the electrical power costs (from 55 to 62%) and by the biomass feedstock costs (10-18%). The most influent parameters on the SNG production costs are the investment costs of stacks (initial and replacement investment) and the electricity price in the current scenarios. However, because of the mass production and the improved lifetime of stacks, only the electricity price remains a key driver of SNG production costs in the prospective scenarios. In the most

favorable configuration, SNG production costs calculated in this work would still be two times higher than the average price of natural gas for all sectors in France.

In future work, the effect of long-term operation of power-to-methane units, such as the degradation of SOECs and of the methanation catalyst, affect plant operation and should be investigated. Further paths for model improvement include the consideration of pressure drops, which were neglected in all investigated plant concepts. Moreover, thermal losses were not accounted for besides in the SOE unit and taking them into account should result in lower overall plant efficiencies. Another relevant improvement of this work could be the implementation of optimization algorithms in order to identify optimized operating conditions of power-to-SNG plants (e.g. temperature and pressure) corresponding to single or multi-objectives, such as maximized energy efficiency, SNG output, and residual heat recovery. A further step could be to integrate a cost function in these algorithms to take into account the tradeoff between technical and economic performance.

As for the 1D model implemented in this work, there are several aspects that could be improved in the future. The modelling of BoP components should be consolidated with experimental data in order to take into account their transient behavior in the model response. Furthermore, the validity of the SRU model itself should be checked with experimental data at system level in order to limit thermal interferences of furnaces usually occurring during cell or stack testing in laboratory environment. However, it is rather unsure if this would be feasible in a near future, since this data is difficult to obtain. This model should also be considered in future work for the development of real time control strategies, because of its limited computation time, but also because of its industry oriented implementation pathway, where an estimate of the ASR or of its dependence to the temperature is sufficient to obtain a first evaluation of the SRUs thermal response to fluctuating power loads. Future experimental work should focus on achieving stable system efficiency at power loads below 50%, mostly by improving the BoPs, the thermal integration, and reducing heat losses. The ability to operate SOE systems above nominal load still requires significant improvements of cell and system lifetime (currently up to 23 kh and below 10 kh respectively). Additional field testing is required to assess the ultimate potential of SOE units to absorb load fluctuations, as the best startup time from hot standby to nominal operation reported so far is 24 min.

Several aspects would enable to refine the economic evaluation implemented in this work. For the SOEC technology, additional work in the following research areas would be helpful for future analyses i) the development of stack designs for pressurized operation and ii) the development of stack or BoP components suitable for the processing of high temperature pressurized oxygen. Moreover, the results of the bottom-up cost analysis of SOE units in the range of 10-100 MW could be consolidated by adding several features, such as enlarging the capacity range from 1 MW to 1 GW or extending the analysis to SOE stacks with CSCs. The capacity range of other plant processes, such as gasification, catalytic methanation or gas purification should also be extended. Furthermore, the economic assessment should be extended to power-to-SNG plants operated in fluctuating mode, in order to evaluate the additional costs related to the H_2 storage, to the overdimensioned plant units (e.g. the electrolysis and the catalytic methanation units), and to the lower plant availability. For large power-to-SNG units above 50 MW, the biomass availability could become challenging, hence the model should also be extended to industrial carbon sources with larger carbon streams, e.g. from the cement or the steel industry. In that case, the CO_2 price and the impact of CO_2 taxes should also be included as a parameter in the sensitivity analysis.

References

[1] BP Statistical review of World Energy. BP; 2019.

[2] Hall CAS, Lambert JG, Balogh SB. EROI of different fuels and the implications for society. Energy Policy. 2014;64:141-52.

[3] Dams and development - A new framework for decision making. https://www.internationalrivers.org/sites/default/files/attached-files/world_commission_on_dams_final_report.pdf, accessed 08.10.2019: World Commission on Dams; 2000.

[4] Floquart H, Pervès JP. Intermittence et foisonnement de l'électricité éolienne en Europe de l'Ouest - Quelles compensations espérer entre pays? - Qu'attendre du stockage de l'électricité intermittente sous forme d'hydrogène? https://www.sauvonsleclimat.org/images/articles/pdf_files/etudes/A%20Eolien%20en%20Europe,%20foisonnement%20et%20production%20de%20H2.pdf, accessed 10.08.2019: Sauvons le Climat; 2012.

[5] Synthèse du rapport Secten 2019. https://www.citepa.org/images/III-1_Rapports_Inventaires/SECTEN/rapport/Citepa_Secten-2019_01_Synthese.pdf, accessed 08.10.2019: Centre Interprofessionnel Technique d'Etudes de la Pollution Atmosphérique (Citepa); 2019.

[6] Graf F. Klimaschutzplan und Dekarbonisierung: Welche Rolle spielt Gas? In: fokus.energie, editor. Brennpunkt; 2019 [Karlsruhe, Germany].

[7] Havard H, Duthilleul A, Follenfant P, Govillot N. Stockage souterrain de gaz. https://www.economie.gouv.fr/files/files/directions_services/cge/Rapports/2017_04_21_Rapport_Stockage_gaz.pdf, accessed 08.12.2019: Inspection Générale des Finances, Conseil Général de l'Economie, Conseil Général de l'Environnement et du Développement Durable; 2017.

[8] Anghilante R, Colomar D, Brisse A, Marrony M. Bottom-up cost evaluation of SOEC systems in the range of 10–100 MW. International Journal of Hydrogen Energy. 2018;43:20309-22.

[9] Anghilante R, Müller C, Schmid M, Colomar D, Ortloff F, Spörl R, et al. Innovative power-to-gas plant concepts for upgrading of gasification bio-syngas through steam electrolysis and catalytic methanation. Energy Conversion and Management. 2019;183:462-73.

[10] Müller C, Anghilante R, Schmid M, Härdtlein M, Spörl R, Colomar D, et al. CNG und LNG aus biogenen Reststoffen – ein Konzept zur ressourcenschonenden Kraftstoffproduktion. Chemie Ingenieur Technik. 2020;92:144-55.

[11] Final report of the Baden-Wurttemberg project Res2CNG - Innovative production of SNG and CNG from biogenic waste and residues. DVGW Research Center at Engler-Bunte Institute of Karlsruhe Institute of Technology (KIT), Insititute of Combustion and Power Plant Technology Stuttgart, Institute of Energy Economics and Rational Energy Use Stuttgart, European Institute for Energy Research; 2018.

[12] Fu Q, Mabilat C, Zahid M, Brisse A, Gautier L. Syngas production via high-temperature steam/CO2 co-electrolysis: an economic assessment. Energ Environ Sci. 2010;3:1382-97.

[13] Ebbesen SD, Graves C, Mogensen M. Production of Synthetic Fuels by Co-Electrolysis of Steam and Carbon Dioxide. International Journal of Green Energy. 2009;6:646-60.

[14] De Saint Jean M. Etude énergétique et évaluation économique d'une boucle de stockage - déstockage d'énergie électrique d'origine renouvelable sur méthane de synthèse à l'aide d'un convertisseur électrochimique réversible SOEC - SOFC. France Ecole nationale supérieure des mines de Paris; 2014.

[15] De Saint Jean M, Baurens P, Bouallou C, Couturier K. Economic assessment of a power-to-substitute-natural-gas process including high-temperature steam electrolysis. International Journal of Hydrogen Energy. 2015;40:6487-500.

[16] Etude portant sur l'hydrogène et la méthanation comme procédé de valorisation de l'électricité excédentaire. http://www.grtgaz.com/fileadmin/engagements/documents/fr/Power-to-Gas-etude-ADEME-GRTgaz-GrDF-complete.pdf, accessed 08.12.2019: ADEME, GRTgaz, GrDF; 2014.

[17] Giglio E, Lanzini A, Santarelli M, Leone P. Synthetic natural gas via integrated high-temperature electrolysis and methanation: Part II—Economic analysis. Journal of Energy Storage. 2015;2:64-79.

[18] de Bucy J. The potential of power-to-gas. http://www.enea-consulting.com/wp-content/uploads/2016/01/ENEA-Consulting-The-potential-of-power-to-gas.pdf, accessed 08.12.2019: enea consulting; 2016.

[19] Wang L, Chen M, Küngas R, Lin T-E, Diethelm S, Maréchal F, et al. Power-to-fuels via solid-oxide electrolyzer: Operating window and techno-economics. Renewable and Sustainable Energy Reviews. 2019;110:174-87.

[20] Graf F, Götz M, Henel M, Schaaf T, Tichler R. Abschlussbericht - Technoökonomische Studie von Power-to-Gas-Konzepten. https://www.dvgw.de/medien/dvgw/forschung/berichte/g3_01_12_tp_b_d.pdf, accessed 08.12.2019: DVGW-Forschungsstelle am Engler-Bunte-Institut des Karlsruher Instituts für Technologie (KIT), DBI Gas- und Umwelttechnik GmbH, Outotec GmbH, Energieinstitut an der Johannes Kepler Universität; 2014.

[21] G. Müller-Syring MH, W. Köppel, H. Mlaker, M. Sterner, T. Höcher. Entwicklung von modularen Konzepten zur Erzeugung, Speicherung und Einspeisung von Wasserstoff und Methan ins Erdgasnetz. DVGW Forschung. 2013.

[22] Götz M, Lefebvre J, Mörs F, McDaniel Koch A, Graf F, Bajohr S, et al. Renewable Power-to-Gas: A technological and economic review. Renewable Energy. 2016;85:1371-90.

[23] Bilan énergétique de la France pour 2017. https://www.statistiques.developpement-durable.gouv.fr/sites/default/files/2019-02/datalab-bilan-energetique-de-la-france-pour-%202017-fevrier%202019.pdf, accessed 08.10.2020: Commissariat général au développement durable; 2019.

[24] Götze T. Die AUDI-e-gas-Anlagein Werlteein P2G-Projekt am Standort einer Biogasanlage. Niedersächsische Energietage; 2017 [Hannover, Germany].

[25] Prix de l'électricité en France et dans l'Union européenne en 2018. https://www.statistiques.developpement-durable.gouv.fr/sites/default/files/2019-06/datalab-essentiel-180-prix-electricite-france-ue-2018-juin2019.pdf, accessed 08.10.2019: Commissariat général au développement durable; 2018.

[26] A. Petersson AW. Biogas upgrading technologies - developments and innovations. IEA Bioenergy. 2009.

[27] Smolinka T, Wiebe N, Sterchele P, Palzer A, Lehner F, Jansen M, et al. Studie IndWEDe - Industrialisierung der Wasserelektrolyse in Deutschland: Chancen und Herausforderungen für nachhaltigen Wasserstoff für Verkehr, Strom und Wärme. https://www.now-gmbh.de/content/service/3-publikationen/1-nip-wasserstoff-und-brennstoffzellentechnologie/indwede-studie_v04.1.pdf, accessed 08.10.2019: Fraunhofer-Institut für Solare Energiesysteme ISE, E4tech Sàrl, Fraunhofer-Institut für Produktionstechnologie und Automatisierung IPA; 2018.

[28] Advisors GoCS. Novel carbon capture and utilisation technologies. https://ec.europa.eu/research/sam/pdf/sam_ccu_report.pdf, accessed 09.11.2019: European Commission, Directorate-General for Research and Innovation; 2018.

[29] Biogas-SOEC Electrochemical upgrading of biogas to pipeline quality by means of SOEC electrolysis. Haldor Topsoe A/S, Ea Energieanalyse, Topsoe Fuel Cell A/S, RISØ DTU; 2011.

[30] Fasihi M, Efimova O, Breyer C. Techno-economic assessment of CO2 direct air capture plants. Journal of Cleaner Production. 2019;224:957-80.

[31] Danish project BioCat. 2018. http://biocat-project.com/.

[32] Lardon L. Biocat - Power to Gas technology by Biological methanation Integration to a resource treatment plant. Power-to-X Conference; 2016 [Grenoble, FR].

[33] European project STORE&GO. 2018. https://www.storeandgo.info/.

[34] Schirrmeister S. Carbon capture technologies for PtX-Fuels. CO2 reuse summit; 2019 [Berlin, Germany].

[35] European project JUPITER 1000. 2018. https://www.jupiter1000.eu/.

[36] Audi e-gas project. 2018. http://www.powertogas.info/power-to-gas/pilotprojekte-im-ueberblick/audi-e-gas-projekt/.

[37] Sveinbjörnsson D, Münster E. Deliverable 1.1.1 of the FutureGas project - Upgrading of Biogas to Biomethane with the Addition of Hydrogen from Electrolysis. PlanEnergi; 2017.

[38] Petipas F. Conception et conduite de systèmes d'électrolyse à haute température alimentés par des énergies renouvelables [Ph.D. thesis]. France: Ecole nationale supérieure des mines de Paris; 2013.

[39] Danish project El upgraded biogas. 2018. https://energiforskning.dk/en/node/7155.

[40] HELMETH Deliverable 2.5: Report on the stand-alone Electrolyser testing. Sunfire GmbH; 2017.

[41] European project HELMETH (Integrated High-Temperature Electrolysis and Methanation for Effective Power to Gas Conversion). 2018. http://www.helmeth.eu/.

[42] European project GrInHy (Green Industrial Hydrogen). 2015. http://www.green-industrial-hydrogen.com/home/.

[43] Breaktrough for Power-to-X: Sunfire puts first co-electrolysis into operation and starts scaling. 15.01.2019. https://www.sunfire.de/en/company/news/detail/breakthrough-for-power-to-x-sunfire-puts-first-co-electrolysis-into-operation-and-starts-scaling, accessed 08.05.2019.

[44] Jeanmonod G, Diethelm S, Van Herle J. The effect of SO2 on the Ni-YSZ electrode of a solid oxide electrolyzer cell operated in co-electrolysis. Journal of Physics: Energy. 2020;2:034002.

[45] planSOEC - R&D and commercialization roadmap for SOEC electrolysis - R&D of SOEC stacks with improved durability. Topsoe Fuel Cell A/S, H2 Logic A/S, RISØ DTU; 2011.

[46] De Saint Jean M, Baurens P, Bouallou C. Parametric study of an efficient renewable power-to-substitute-natural-gas process including high-temperature steam electrolysis. Int J Hydrogen Energy. 2014;39:17024-39.

[47] Stempien JP, Ni M, Sun Q, Chan SH. Production of sustainable methane from renewable energy and captured carbon dioxide with the use of Solid Oxide Electrolyzer: A thermodynamic assessment. Energy. 2015;82:714-21.

[48] De Saint Jean M, Lacroix V, Baurens P, Bouallou C. Procédé power-to-gaz par couplage evht / méthanation. XIV Congrès SFGP; 2013 [Paris, FR].

[49] Giglio E, Lanzini A, Santarelli M, Leone P. Synthetic natural gas via integrated high-temperature electrolysis and methanation: Part I—Energy performance. Journal of Energy Storage. 2015;1 22–37.

[50] Giglio E, Deorsola FA, Gruber M, Harth SR, Morosanu EA, Trimis D, et al. Power-to-Gas through High Temperature Electrolysis and Carbon Dioxide Methanation: Reactor Design and Process Modeling. Industrial & Engineering Chemistry Research. 2018;57:4007-18.

[51] Wang L, Pérez-Fortes M, Madi H, Diethelm S, herle JV, Maréchal F. Optimal design of solid-oxide electrolyzer based power-to-methane systems: A comprehensive comparison between steam electrolysis and co-electrolysis. Applied Energy. 2018;211:1060-79.

[52] Anghilante R, Müller C, Schmid M, Colomar C, Ortloff F, Spörl R, et al. Innovative CNG and LNG plant concepts for bio-syngas upgrading though steam electrolysis (SOEC) and catalytic methanation. In: Ivers-Tiffée E, editor. Proceeding of the 13th European SOFC& SOE Forum; 2018 [Lucerne, SW].

[53] Luo Y, Wu X-y, Shi Y, Ghoniem AF, Cai N. Exergy analysis of an integrated solid oxide electrolysis cell-methanation reactor for renewable energy storage. Applied Energy. 2018;215:371-83.

[54] Clausen LR. Energy efficient thermochemical conversion of very wet biomass to biofuels by integration of steam drying, steam electrolysis and gasification. Energy. 2017;125:327-36.

[55] Gruber M, Weinbrecht P, Biffar L, Harth S, Trimis D, Brabandt J, et al. Power-to-Gas through thermal integration of high-temperature steam electrolysis and carbon dioxide methanation - Experimental results. Fuel Processing Technology. 2018;181:61-74.

[56] Sigurjonsson HÆ, Clausen LR. Solution for the future smart energy system: A polygeneration plant based on reversible solid oxide cells and biomass gasification producing either electrofuel or power. Applied Energy. 2018;216:323-37.

[57] Lorenzi G, Lanzini A, Santarelli M, Martin A. Exergo-economic analysis of a direct biogas upgrading process to synthetic natural gas via integrated high-temperature electrolysis and methanation. Energy. 2017;141:1524-37.

[58] Hansen JB. Process for converting biogas to a gas rich in methane In: USTPO, editor. Denmark: Haldor Topsoe A/S; 2013.

[59] Sarić M, Dijkstra JW, Haije WG. Economic perspectives of Power-to-Gas technologies in bio-methane production. Journal of CO2 Utilization. 2017;20:81-90.

[60] Monaco F, Lanzini A, Santarelli M. Making synthetic fuels for the road transportation sector via solid oxide electrolysis and catalytic upgrade using recovered carbon dioxide and residual biomass. Journal of Cleaner Production. 2018;170:160-73.

[61] Köppel W, Bajohr S, Sauer J. Vergleichende Bewertung von PtX-Prozessen zur Bereitstellung von Kraftstoffen aus erneuerbaren Quellen. DVGW-Forschungsstelle am Engler-Bunte-Institut des Karlsruher Instituts für Technologie (KIT), Karlsruher Institut für Technologie –Engler-Bunte-Institut, Karlsruher Institut für Technologie –Institut für Katalyseforschung und -Technologie; 2019.

[62] Udagawa J, Aguiar P, Brandon NP. Hydrogen production through steam electrolysis: Model-based dynamic behaviour of a cathode-supported intermediate temperature solid oxide electrolysis cell. Journal of Power Sources. 2008;180:46-55.

[63] Grondin D, Deseure J, Ozil P, Chabriat JP, Grondin-Perez B, Brisse A. Computing approach of cathodic process within solid oxide electrolysis cell: Experiments and continuum model validation. Journal of Power Sources. 2011;196:9561-7.

[64] Bertei A, Mertens J, Nicolella C. Electrochemical Simulation of Planar Solid Oxide Fuel Cells with Detailed Microstructural Modeling. Electrochimica Acta. 2014;146:151-63.

[65] García-Camprubí M, Izquierdo S, Fueyo N. Challenges in the electrochemical modelling of solid oxide fuel and electrolyser cells. Renewable and Sustainable Energy Reviews. 2014;33:701-18.

[66] Schefold J, Brisse A, Poepke H. Long-term Steam Electrolysis with Electrolyte-Supported Solid Oxide Cells. Electrochimica Acta. 2015;179:161-8.

[67] Becker WL, Braun RJ, Penev M, Melaina M. Production of Fischer–Tropsch liquid fuels from high temperature solid oxide co-electrolysis units. Energy. 2012;47:99-115.

[68] Bermejo JS, Munoz-Anton J, Gonzalez-Aguilar J, Romero M. Part load operation of a solid oxide electrolysis system for integration with renewable energy sources. Int J Hydrogen Energy. 2015;40:8291-303.

[69] F. Petipas AB, Chakib Bouallou. Model-based behaviour of a high temperature electrolyser system operated at various loads. Journal of Power Sources. 2013;239:584-95.

[70] Henke M, Willich C, Kallo J, Friedrich KA. Theoretical study on pressurized operation of solid oxide electrolysis cells. International Journal of Hydrogen Energy. 2014;39:12434-9.

[71] Vogt UF, Schlupp M, Burnat D, Züttel A. Novel Developments in Alkaline Water Electrolysis. 8th International Symposium Hydrogen & Energy; 2014 [Zhaoquing, China].

[72] Santos DMF, Sequeira CAC, Figueiredo JL. Hydrogen production by alkaline water electrolysis. Química Nova. 2013;36:1176-93.

[73] Carmo M, Fritz DL, Mergel J, Stolten D. A comprehensive review on PEM water electrolysis. International Journal of Hydrogen Energy. 2013;38:4901-34.

[74] Thomas D. PEM water electrolysis: ready for large-scale CO2 utilization projects. CO2 reuse summit; 2019 [Berlin, Germany].

[75] Bertuccioli L, Chan A, Hart D, Lehner F, Madden B, Standen E. Development of water electrolysis in the European Union. Cambridge (UK), Lausanne (CH): Element Energy, E4tech Sarl; 2014.

[76] Lehner M, Tichler R, Steinmüller H, Koppe M. Power-to-Gas: Technology and Business Models. SpringerBriefs in Energy. Springer, Cham; 2014.

[77] European project REFHYNE. 2019. https://refhyne.eu/.

[78] Air Liquide invests in the world's largest membrane-based electrolyzer to develop its carbon-free hydrogen production. 25.02.2019. https://industry.airliquide.ca/air-liquide-invests-worlds-largest-membrane-based-electrolyzer-develop-its-carbon-free-hydrogen, accessed 07.07.2019.

[79] Spacil HS, Tedmon CS. Electrochemical Dissociation of Water Vapor in Solid Oxide Electrolyte Cells: I . Thermodynamics and Cell Characteristics. Journal of The Electrochemical Society. 1969;116:1618-26.

[80] Weissbart J, Smart WH, Inami SH, McCullough CM, Ring SA. Development of a carbon dioxide-water solid oxide electrolyte electrolysis system: first annual report. NASA 1969.

[81] Doenitz W, Schmidberger R, Steinheil E, Streicher R. Hydrogen production by high temperature electrolysis of water vapour. International Journal of Hydrogen Energy. 1980;5:55-63.

[82] Doenitz W, Schmidberger R. Concepts and design for scaling up high temperature water vapour electrolysis. International Journal of Hydrogen Energy. 1982;7:321-30.

[83] Kazempoor P, Braun RJ. Model validation and performance analysis of regenerative solid oxide cells for energy storage applications: Reversible operation. International Journal of Hydrogen Energy. 2014;39:5955-71.

[84] Ebbesen SD, Knibbe R, Mogensen M. Co-Electrolysis of Steam and Carbon Dioxide in Solid Oxide Cells. Journal of the Electrochemical Society. 2012;159:F482-F9.

[85] Sebdani MM, Baniassadi M, Jamali J, Ahadiparast M, Abrinia K, Safdari M. Designing an optimal 3D microstructure for three-phase solid oxide fuel cell anodes with maximal active triple phase boundary length (TPBL). International Journal of Hydrogen Energy. 2015;40:15585-96.

[86] Subbarao EC, Maiti HS. Solid Electrolytes with Oxygen Ion Conduction. Solid State Ionics. 1984;11:317-38.

[87] Ormerod RM. Solid oxide fuel cells. Chemical Society Reviews. 2003;32:17-28.

[88] Corre GPG, Irvine JTS. High Temperature Fuel Cell Technology. Hydrogen and Fuel Cells - Fundamentals, Technologies and Applications: WILEY-VCH; 2010.

[89] Yildiz B, Kazimi MS. Efficiency of hydrogen production systems using alternative nuclear energy technologies. International Journal of Hydrogen Energy. 2006;31:77-92.

[90] Sunfire GmbH. PowerCore – The efficient energy converter. https://www.sunfire.de/en/products-and-technology, accessed 01.03.2020.

[91] Laguna-Bercero MA. Recent advances in high temperature electrolysis using solid oxide fuel cells: A review. Journal of Power Sources. 2012;203:4-16.

[92] Brisse A, Schefold J, Zahid M. High temperature water electrolysis in solid oxide cells. International Journal of Hydrogen Energy. 2008;33:5375-82.

[93] Jensen SH, Sun X, Ebbesen SD, Knibbe R, Mogensen M. Hydrogen and synthetic fuel production using pressurized solid oxide electrolysis cells. International Journal of Hydrogen Energy. 2010;35:9544-9.

[94] O'Brien JE, Zhang X, Housley GK, DeWall K, Moore-McAteer L, Tao G. High Temperature Electrolysis Pressurized Experiment Design, Operation, and Results. US Department of Energy; 2012.

[95] Bernadet L, Laurencin J, Roux G, Montinaro D, Mauvy F, Reytier M. Effects of Pressure on High Temperature Steam and Carbon Dioxide Co-electrolysis. Electrochimica Acta. 2017;253:114-27.

[96] Posdziech O. Development of High-Temperature Electrolysers for Renewable Electricity Storage. Hydrogen Days; 2015 [Prag, Czech Republic].

[97] Sunfire GmbH. Factsheet of Sunfire HyLink. https://www.sunfire.de/files/sunfire/images/content/Produkte_Technologie/factsheets/Sunfire-HyLink_FactSheet.pdf, accessed 08.05.2019.

[98] Hydrogenics. Brochure on Renewable Hydrogen Solutions. http://www.hydrogenics.com/wp-content/uploads/Renewable-Hydrogen-Brochure.pdf, accessed 08.05.2019.

[99] Schefold J, Brisse A, Poepke H. 23,000 h steam electrolysis with an electrolyte supported solid oxide cell. International Journal of Hydrogen Energy. 2017;42:13415-26.

[100] Frey CE, Fang Q, Sebold D, Blum L, Menzler NH. A Detailed Post Mortem Analysis of Solid Oxide Electrolyzer Cells after Long-Term Stack Operation. Journal of The Electrochemical Society. 2018;165:F357-F64.

[101] Geipel C, Herbrig K, Mittmann F, Pötschke M, Reichel L, Strohbach T, et al. Stack Development and Industrial Scale-Up. 13th European SOEFC & SOE Forum; 2018 [Lucerne, Switzerland].

[102] Schmidt O, Gambhir A, Staffell I, Hawkes A, Nelson J, Few S. Future cost and performance of water electrolysis: An expert elicitation study. International Journal of Hydrogen Energy. 2017;42:30470-92.

[103] Posdziech O. GrInHy - Green Industrial Hydrogen via reversible high-temperature electrolysis. https://www.fch.europa.eu/sites/default/files/documents/ga2011/4_Session%206_GrInHy%20%28ID%204811832%29.pdf, accessed 08.10.2019: Sunfire GmbH; 2018.

[104] Multi- Annual Work Plan 2014 - 2020. https://ec.europa.eu/research/participants/data/ref/h2020/other/legal/jtis/fch-multi-workplan_en.pdf, accessed 08.05.2019: FCH-JU; 2014.

[105] Fang Q, Blum L, Menzler NH. Performance and Degradation of Solid Oxide Electrolysis Cells in Stack. ECS Transactions. 2015;68:3491-503.

[106] Final report of the EU project ADEL "Advanced Electrolyser for Hydrogen Production with Renewable Energy Sources". https://www.fch.europa.eu/sites/default/files/project_publisheable_reports/Publishable%20Summary%20-%20FCH_JU_ADEL%28256755%29_Final_Report.pdf, accessed 08.10.2019: HTceramix SA; 2013.

[107] Chen M, Høgh JVT, Nielsen JU, Bentzen JJ, Ebbesen SD, Hendriksen PV. High Temperature Co-Electrolysis of Steam and CO2 in an SOC Stack: Performance and Durability. Fuel Cells. 2013;13:638-45.

[108] O'Brien JE, McKellar MG, Harvego EA, Stoots CM. High-temperature electrolysis for large-scale hydrogen and syngas production from nuclear energy - summary of system simulation and economic analyses. International Journal of Hydrogen Energy. 2010;35:4808-19.

[109] Petri R. Reversible Solid Oxide Electrolysis. Electrolytic Hydrogen Production Workshop; 2014 [Golden, CO].

[110] Fu Q, Schefold J, Brisse A, Nielsen JU. Durability Testing of a High-Temperature Steam Electrolyzer Stack at 700 °C. Fuel Cells. 2014;14:395-402.

[111] Schefold J, Brisse A, Surrey A, Walter C. 80,000 current on/off cycles in a one year long steam electrolysis test with a solid oxide cell. International Journal of Hydrogen Energy. 2019.

[112] Deliverable 3.5 of the EU project GrInHy - Green Industrial Hydrogen via Reversible High-Temperature Electrolysis - Report on results on cell and stack tests. https://cordis.europa.eu/project/rcn/204283/results/en, accessed 08.09.2019: EIFER; 2018.

[113] Brisse A, Zeller M, Ludwig B, Brabandt J. Solid Oxide Electrolyser System operational at the H2 refueling station of Karlsruhe. In: Ivers-Tiffée E, editor. Proceeding of the 13th European SOFC& SOE Forum; 2018 [Lucerne, SW].

[114] Kanoglu M, Ayanoglu A, Abusoglu A. Exergoeconomic assessment of a geothermal assisted high temperature steam electrolysis system. Energy. 2011;36:4422-33.

[115] Petrakopoulou F, Sanz-Bermejo J, Dufour J, Romero M. Exergetic analysis of hybrid power plants with biomass and photovoltaics coupled with a solid-oxide electrolysis system. Energy. 2016;94:304-15.

[116] Houaijia A, Breuer S, Thomey D, Brosig C, Säck JP, Roeb M, et al. Solar Hydrogen by High-temperature Electrolysis: Flowsheeting and Experimental Analysis of a Tube-type Receiver Concept for Superheated Steam Production. Energy Procedia. 2014;49:1960-9.

[117] Sanz-Bermejo J, Muñoz-Antón J, Gonzalez-Aguilar J, Romero M. Optimal integration of a solid-oxide electrolyser cell into a direct steam generation solar tower plant for zero-emission hydrogen production. Applied Energy. 2014;131:238-47.

[118] Stempien JP, Ni M, Sun Q, Chan SH. Thermodynamic analysis of combined Solid Oxide Electrolyzer and Fischer–Tropsch processes. Energy. 2015;81:682-90.

[119] Cinti G, Baldinelli A, Di Michele A, Desideri U. Integration of Solid Oxide Electrolyzer and Fischer-Tropsch: A sustainable pathway for synthetic fuel. Applied Energy. 2016;162:308-20.

[120] Chen B, Xu H, Ni M. Modelling of SOEC-FT reactor: Pressure effects on methanation process. Applied Energy. 2017;185:814-24.

[121] Bernical Q, Joulia X, Noirot-Le Borgne I, Floquet P, Baurens P, Boissonnet G. Sustainability Assessment of an Integrated High Temperature Steam Electrolysis-Enhanced Biomass to Liquid Fuel Process. Industrial & Engineering Chemistry Research. 2013;52:7189-95.

[122] Samavati M, Martin A, Nemanova V, Santarelli M. Integration of solid oxide electrolyser, entrained gasification, and Fischer-Tropsch process for synthetic diesel production: Thermodynamic analysis. International Journal of Hydrogen Energy. 2018;43:4785-803.

[123] Hillestad M, Ostadi M, Alamo Serrano Gd, Rytter E, Austbø B, Pharoah JG, et al. Improving carbon efficiency and profitability of the biomass to liquid process with hydrogen from renewable power. Fuel. 2018;234:1431-51.

[124] Clausen LR. Maximizing biofuel production in a thermochemical biorefinery by adding electrolytic hydrogen and by integrating torrefaction with entrained flow gasification. Energy. 2015;85:94-104.

[125] Clausen LR, Houbak N, Elmegaard B. Technoeconomic analysis of a methanol plant based on gasification of biomass and electrolysis of water. Energy. 2010;35:2338-47.

[126] Andika R, Nandiyanto ABD, Putra ZA, Bilad MR, Kim Y, Yun CM, et al. Co-electrolysis for power-to-methanol applications. Renewable and Sustainable Energy Reviews. 2018;95:227-41.

[127] Lythcke-Jørgensen C, Clausen LR, Algren L, Hansen AB, Münster M, Gadsbøll RØ, et al. Optimization of a flexible multi-generation system based on wood chip gasification and methanol production. Applied Energy. 2017;192:337-59.

[128] Pozzo M, Lanzini A, Santarelli M. Enhanced biomass-to-liquid (BTL) conversion process through high temperature co-electrolysis in a solid oxide electrolysis cell (SOEC). Fuel. 2015;145:39-49.

[129] Stempien JP, Liu Q, Ni M, Sun Q, Chan SH. Physical principles for the calculation of equilibrium potential for co-electrolysis of steam and carbon dioxide in a Solid Oxide Electrolyzer Cell (SOEC). Electrochimica Acta. 2014;147:490-7.

[130] Stoots CM, O'Brien JE, Herring JS, Hartvigsen JJ. SYNGAS PRODUCTION VIA HIGH-TEMPERATURE COELECTROLYSIS OF STEAM AND CARBON DIOXIDE. Journal of Fuel Cell Science and Technology. 2009:Medium: X; Size: 011014 (12 pages).

[131] Sun XF, Chen M, Jensen SH, Ebbesen SD, Graves C, Mogensen M. Thermodynamic analysis of synthetic hydrocarbon fuel production in pressurized solid oxide electrolysis cells. International Journal of Hydrogen Energy. 2012;37:17101-10.

[132] Anghilante R, Lefebvre J. Coupling a High Temperature Electrolyzer and a Three-Phase Methanation Reactor using Matlab Simulink. In: Christiansen N, Hansen JB, editors. Proceeding of the 11th European SOFC& SOE Forum; 2014 [Lucerne, SW].

[133] Wendel C, Braun R. Modeling and design of a novel solid oxide flow battery system for grid-energy storage. 10th European SOFC Forum; 2012 [Lucerne, Switzerland].

[134] Penchini D, Cinti G, Discepoli G, Desideri U. Theoretical study and performance evaluation of hydrogen production by 200 W solid oxide electrolyzer stack. International Journal of Hydrogen Energy. 2014;39:9457-66.

[135] Serincan MF, Pasaogullari U, Sammes NM. Effects of operating conditions on the performance of a micro-tubular solid oxide fuel cell (SOFC). Journal of Power Sources. 2009;192:414-22.

[136] Ivers-Tiffée E, Weber A, Schmid K, Krebs V. Macroscale modeling of cathode formation in SOFC. Solid State Ionics. 2004;174:223-32.

[137] Menon V, Janardhanan VM, Tischer S, Deutschmann O. A novel approach to model the transient behavior of solid-oxide fuel cell stacks. Journal of Power Sources. 2012;214:227-38.

[138] Achenbach E. Response of a solid oxide fuel cell to load change. Journal of Power Sources. 1995;57:105-9.

[139] Cao H, Deng Z, Li X, Yang J, Qin Y. Dynamic modeling of electrical characteristics of solid oxide fuel cells using fractional derivatives. International Journal of Hydrogen Energy. 2010;35:1749-58.

[140] Lawlor V, Griesser S, Buchinger G, Olabi AG, Cordiner S, Meissner D. Review of the micro-tubular solid oxide fuel cell: Part I. Stack design issues and research activities. Journal of Power Sources. 2009;193:387-99.

[141] Kazempoor P, Ommi F, Dorer V. Response of a planar solid oxide fuel cell to step load and inlet flow temperature changes. Journal of Power Sources. 2011;196:8948-54.

[142] Cai Q, Adjiman CS, Brandon NP. Optimal control strategies for hydrogen production when coupling solid oxide electrolysers with intermittent renewable energies. Journal of Power Sources. 2014;268:212-24.

[143] Botta G, Romeo M, Fernandes A, Trabucchi S, Aravind PV. Dynamic modeling of reversible solid oxide cell stack and control strategy development. Energy Conversion and Management. 2019;185:636-53.

[144] Yang C, Shu C, Miao H, Wang Z, Wu Y, Wang J, et al. Dynamic modelling and performance analysis of reversible solid oxide fuel cell with syngas. International Journal of Hydrogen Energy. 2019;44:6192-211.

[145] Wang Y, Banerjee A, Deutschmann O. Dynamic behavior and control strategy study of CO2/H2O co-electrolysis in solid oxide electrolysis cells. Journal of Power Sources. 2019;412:255-64.

[146] Luo Y, Shi YX, Li WY, Cai NS. Dynamic electro-thermal modeling of co-electrolysis of steam and carbon dioxide in a tubular solid oxide electrolysis cell. Energy. 2015;89:637-47.

[147] Fogel S, Kryk H, Hampel U. Simulation of the transient behavior of tubular solid oxide electrolyzer cells under fast load variations. International Journal of Hydrogen Energy. 2019;44:9188-202.

[148] Isenberg AO. Energy conversion via solid oxide electrolyte electrochemical cells at high temperatures. Solid State Ionics. 1981;3:431-7.

[149] Carlson E. Assessment of Planar Solid Oxide Fuel Cell Technology. US Department of Energy; 1999.

[150] Battelle. Manufacturing cost analysis of 1kW and 5kW solid oxide fuel cell (SOFC) for auxilliary power applications. US Department of Energy; 2014.

[151] Thijssen J. The Impact of Scale-Up and Production Volume on SOFC Manufacturing cost. US Department of Energy; 2007.

[152] Weimar MR, Chick LA, Gotthold DW, Whyatt GA. Cost Study for Manufacturing of Solid Oxide Fuel Cell Power Systems. US Department of Energy; 2013.

[153] Otomo J, Oishi J, Miyazaki K, Okamura S, Yamada K. Coupled analysis of performance and costs of segmented-in-series tubular solid oxide fuel cell for combined cycle system. International Journal of Hydrogen Energy. 2017;42:19190-203.

[154] Scataglini R, Wei M, Mayyas A, Chan SH, Lipman T, Santarelli M. A Direct Manufacturing Cost Model for Solid‐Oxide Fuel Cell Stacks. Fuel Cells. 2017;17:825-42.

[155] Carlson EJ, Yang Y, Fulton C. Solid Oxide Fuel cell Manufacturing Cost Model: Simulating Relationships between Performance, Manufacturing and Cost of Production. US Department of Energy; 2004.

[156] Battelle. Manufacturing Cost Analysis of 100 and 250 kW Fuel Cell Systems for Primary Power and Combined Heat and Power Applications. US Department of Energy; 2016.

[157] Scataglini R, Mayyas A, Wei M, Chan SH, Lipman T, Gosselin D, et al. A Total Cost of Ownership Model for Solid Oxide Fuel Cells in Combined Heat and Power and Power-Only Applications. University of California; 2015.

[158] James BD, DeSantis DA. Manufacturing Cost and Installed Price Analysis of Stationary Fuel Cell Systems. Strategic Analysis Inc.; 2015.

[159] Thijssen J. Conceptual design of POX/SOFC 5 kW net system Cambridge, MA, USA, : Arthur D. Little for US Department of Energy; 2001.

[160] Otomo J, Oishi J, Mitsumori T, Iwasaki H, Yamada K. Evaluation of cost reduction potential for 1 kW class SOFC stack production: Implications for SOFC technology scenario. International Journal of Hydrogen Energy. 2013;38:14337-47.

[161] Reytier M, Di Iorio S, Chatroux A, Petitjean M, Cren J, De Saint Jean M, et al. Stack performances in high temperature steam electrolysis and co-electrolysis. International Journal of Hydrogen Energy. 2015;40:11370-7.

[162] Lyperopoulos N. Commercialisation of Energy Storage in Europe. 2015.

[163] Harvego EA, O'Brien JE, McKellar MG. System Evaluation and Life-Cycle Cost Analysis of a Commercial-Scale High Temperature Electrolysis Hydrogen Production Plant. In: ASME, editor. International Mechanical Engineering Congress and Exposition; 2012 [Houston, TX]. p. 875-84.

[164] James BD, DeSantis DA, Saur G. Final Report: Hydrogen Production Pathways Cost Analysis (2013 – 2016). US Department of Energy; 2016.

[165] Peterson D, Miller E. DOE Hydrogen and Fuel Cells Program Record 16014: Hydrogen Production Cost from Solid Oxide Electrolysis. US Department of Energy; 2016.

[166] Reytier M, Cren J, Petitjean M, Chatroux A, Gousseau G, Di Iorio S, et al. Development of a Cost-Efficient and Performing High Temperature Steam Electrolysis Stack. ECS Transactions. 2013;57:3151-60.

[167] Sabatier P, Senderens JB. Nouvelles synthèses du méthane. Compte Rendu de l'Académie des Sciences Paris. 1902;134:514-6.

[168] Vannice MA. The Catalytic Synthesis of Hydrocarbons from Carbon Monoxide and Hydrogen. Catalysis Reviews. 1976;14:153-91.

[169] Gao J, Wang Y, Ping Y, Hu D, Xu G, Gu F, et al. A thermodynamic analysis of methanation reactions of carbon oxides for the production of synthetic natural gas. RSC Advances. 2012;2:2358-68.

[170] Koschany F, Schlereth D, Hinrichsen O. On the kinetics of the methanation of carbon dioxide on coprecipitated NiAl(O)x. Applied Catalysis B: Environmental. 2016;181:504-16.

[171] Kopyscinski J, Schildhauer TJ, Vogel F, Biollaz SMA, Wokaun A. Applying spatially resolved concentration and temperature measurements in a catalytic plate reactor for the kinetic study of CO methanation. Journal of Catalysis. 2010;271:262-79.

[172] Baumhakl C. Substitute Natural Gas Production with direct Conversion of Higher Hydrocarbons: Friedrich-Alexander-University of Erlangen-Nürnberg; 2014.

[173] Schlereth D. Kinetic and Reactor Modeling for the Methanation of Carbon Dioxide: Technical University of Munich; 2015.

[174] Jensen JH, Poulsen JM, Andersen NU. From coal to clean energy. Nitrogen+Syngas. 2011;310.

[175] Maitlis PM, de Klerk A. Greener Fischer-Tropsch Processes for Fuels and Feedstocks: Wiley-VCH Verlag GmbH & Co. KGaA; 2013.

[176] Seemann MC, Schildhauer TJ, Biollaz SMA. Fluidized Bed Methanation of Wood-Derived Producer Gas for the Production of Synthetic Natural Gas. Industrial & Engineering Chemistry Research. 2010;49:7034-8.

[177] Kopyscinski J, Schildhauer TJ, Biollaz SMA. Production of synthetic natural gas (SNG) from coal and dry biomass – A technology review from 1950 to 2009. Fuel. 2010;89:1763-83.

[178] Lefebvre J, Gotz M, Bajohr S, Reimert R, Kolb T. Improvement of three-phase methanation reactor performance for steady-state and transient operation. Fuel Processing Technology. 2015;132:83-90.

[179] Lefebvre J, Trudel N, Bajohr S, Kolb T. A study on three-phase CO2 methanation reaction kinetics in a continuous stirred-tank slurry reactor. Fuel. 2018;217:151-9.

[180] Energy Lab 2.0 Dreiphasen-Methanisierung geht in Betrieb. https://www.elab2.kit.edu/144.php, accessed 10.09.2019.

[181] Partner description of the Engler Bunte Institut at the Karlruhe Institute of Technology in the MethQuest project. https://www.methquest.de/partner/portraits/detail/artikel/das-kit-ebi-ceb-stellt-sich-vor/, accessed 10.09.2019.

[182] Schollenberger D, Bajohr S, Gruber M, Reimert R, Kolb T. Scale‐Up of Innovative Honeycomb Reactors for Power‐to‐Gas Applications – The Project Store&Go. Chemie Ingenieur Technik. 2018;90:696-702.

[183] Graf F. The future of energy supply. https://www.dvgw-ebi.de/download/081_083_StoreandGo_IMPACTPUBLICATION.PDF, accessed 06.09.2019.

[184] Robota H. Fischer-Tropsch synthesis in a microchannel reactor: the influence of Co/SiO2 catalyst structure on FTS performance. 7th International Petroleum Technology Conference; [Doha, Qatar].

[185] Bouquet N. Industrial compact HEX reactors for P2G / P2L systems. Power-to-X Conference; 2016 [Grenoble, FR].

[186] Liu Z, Chu B, Zhai X, Jin Y, Cheng Y. Total methanation of syngas to synthetic natural gas over Ni catalyst in a micro-channel reactor. Fuel. 2012;95:599-605.

[187] Müller K, Städter M, Rachow F, Hoffmannbeck D, Schmeißer D. Sabatier-based CO2-methanation by catalytic conversion. Environmental Earth Sciences. 2013;70:3771-8.

[188] Bank R. Power-to-Gas Utilisation of Wind and Solar Energy. Presentation of the Deggendorf site of MAN Diesel & Turbo SE; 2017.

[189] Li H, Chen Q, Zhang X, Finney KN, Sharifi VN, Swithenbank J. Evaluation of a biomass drying process using waste heat from process industries: A case study. Applied Thermal Engineering. 2012;35:71-80.

[190] Kemp IC. Fundamentals of Energy Analysis of Dryers. In: Tsotsas E, Mujumdar AS, editors. Modern Drying Technology Volume 4: Energy Savings: Wiley‐VCH Verlag GmbH & Co. KGaA; 2012.

[191] Kumar A, Jones DD, Hanna AM. Thermochemical Biomass Gasification: A Review of the Current Status of the Technology. Energies. 2009;2.

[192] Review of Technologies for Gasification of Biomass and Wastes - Final report. E4Tech; 2009.

[193] Koido K, Iwasaki T. Biomass Gasification: A Review of Its Technology, Gas Cleaning Applications, and Total System Life Cycle Analysis. In: Poletto M, editor. Lignin - Trends and Applications. https://www.intechopen.com/books/lignin-trends-and-applications/biomass-gasification-a-review-of-its-technology-gas-cleaning-applications-and-total-system-life-cycl, accessed 08.08.2019: IntechOpen; 2017.

[194] Hofbauer H, Rauch R, Ripfel-Nitsche K. Report on Gas Cleaning for Synthesis Applications. University of Technology of Vienna; 2007.

[195] Abdoulmoumine N, Adhikari S, Kulkarni A, Chattanathan S. A review on biomass gasification syngas cleanup. Applied Energy. 2015;155:294-307.

[196] Zwart RWR, Van der Drift A, Bos A, Visser HJM, Cieplik MK, Könemann HWJ. Oil-based gas washing—Flexible tar removal for high-efficient production of clean heat and power as well as sustainable fuels and chemicals. Environmental Progress & Sustainable Energy. 2009;28:324-35.

[197] Held J. Gasification - Status and technology. Swedish Gas Center; 2012.

[198] Larsson A, Gunnasrsson I, Tengberg T. The GoBiGas Project - Demonstration of the Production of Biomethane from Biomass via Gasification. Göteborg Energi AB; 2018.

[199] Leibold H, Hornung A, Seifert H. HTHP syngas cleaning concept of two stage biomass gasification for FT synthesis. Powder Technology. 2008;180:265-70.

[200] Heyne S, Liliedahl T, Marklund M. Biomass gasification - a synthesis of technical barriers and current research issues for deployment at large scale. The Swedish Knowledge Center for Renewable Transportation Fuels; 2013.

[201] Bain RL, Dayton DC, Carpenter DL, Czernik SR, Feik CJ, French RJ, et al. Evaluation of Catalyst Deactivation during Catalytic Steam Reforming of Biomass-Derived Syngas. Industrial & Engineering Chemistry Research. 2005;44:7945-56.

[202] Netušil M, Ditl P. Natural Gas Dehydration. In: Gupta SB, editor. Natural Gas - Extraction to End Use. https://www.intechopen.com/books/natural-gas-extraction-to-end-use/natural-gas-dehydration, accessed 08.08.2019: IntechOpen; 2012.

[203] DVGW G 260 (A): Gasbeschaffenheit. Technische Regel- Arbeitsblatt: DVGW Deutscher Verein des Gas- und Wasserfaches e. V.; 2013.

[204] DVGW G 262 (A): Nutzung von Gasen aus regenerativen Quellen in der öffentlichen Gasversorgung. Technische Regel- Arbeitsblatt: DVGW Deutscher Verein des Gas- und Wasserfaches e. V.; 2011.

[205] Kraftstoffe für Kraftfahrzeuge – Erdgas – Anforderungen und Prüfverfahren. Berlin ICS 7516030: DIN Deutsches Institut für Normung e. V.; 2008.

[206] Prescriptions techniques du distributeur GRDF. GRDF; 2017.

[207] DVGW G 280 (A): Gasodorierung. Technische Regel – Arbeitsblatt: DVGW Deutscher Verein des Gas- und Wasserfaches e. V.; 2018.

[208] Véhicules fonctionnant au gaz naturel - Intervenir en toute sécurité. www.inrs.fr/dms/inrs/CataloguePapier/ED/TI-ED-6003/ed6003.pdf, accessed 08.09.2019: Institut National de Recherche et de Sécurité; 2010.

[209] Daten und Fakten Erdgas - Gas-mobilität PKW LKW Bus - Umweltauswirkungen, Technologie und Wirtschaftlichkeit gasbasierter Mobilität. https://www.dvgw.de/medien/dvgw/leistungen/publikationen/daten-fakten-gasmobilitaet.pdf, accessed 08.09.2019: Deutscher Verein des Gas- und Wasserfaches e.V.; 2018.

[210] Wärtsilä. LNG plants - mini and small scale liquefaction technology. https://cdn.wartsila.com/docs/default-source/product-files/ogi/lng-solutions/brochure-o-ogi-lng-liquefaction.pdf, accessed 08.09.2019.

[211] LNG Limited. OSMR - Liquefaction Process for LNG Projects. https://www.lnglimited.com.au/site/PDF/2358_0/OSMRTechnology, accessed 09.08.2019.

[212] Gasconsult LNG. ZR-LNG – Dual Methane Expander LNG Liquefaction Process. http://www.gasconsult.com/wp-content/uploads/2018/02/ZR-LNG-Technical-Summary-2018-.pdf, accessed 09.08.2019.

[213] Giesler S. Efficient production of fuel from biogenic residues. 17.07.2017. https://www.biooekonomie-bw.de/en/articles/news/efficient-production-of-fuel-from-biogenic-residues/, accessed 08.07.2019.

[214] Danish project SYNFUEL. 2018. http://www.synfuel.dk/.

[215] NIST Chemistry WebBook. https://webbook.nist.gov/chemistry/, accessed 13.09.2019: U.S. Department of Commerce.

[216] Otto SR, Denier JP. An introduction to programming and numerical methods in MATLAB: Springer; 2005.

[217] Jensen SH, Sun X, Ebbesen SD, Chen M. Pressurized Operation of a Planar Solid Oxide Cell Stack. Fuel Cells. 2016;16:205-18.

[218] Søren Højgaard Jensen XS, Sune Dalgaard Ebbesen, Ruth Knibbe, Mogens Mogensen. Hydrogen and synthetic fuel production using pressurized solid oxide electrolysis cells. international journal of hydrogen energy 2010;35.

[219] Riedel M, Heddrich MP, Friedrich KA. Analysis of pressurized operation of 10 layer solid oxide electrolysis stacks. International Journal of Hydrogen Energy. 2019;44:4570-81.

[220] Riedel M, Heddrich MP, Ansar A, Fang Q, Blum L, Friedrich KA. Pressurized operation of solid oxide electrolysis stacks: An experimental comparison of the performance of 10-layer stacks with fuel electrode and electrolyte supported cell concepts. Journal of Power Sources. 2020;475:228682.

[221] Apfel H, Rzepka M, Tu H, Stimming U. Thermal start-up behaviour and thermal management of SOFC's. Journal of Power Sources. 2006;154:370-8.

[222] Anghilante R, Lefebvre J, Colomar C, Kolb T. Improving the conversion efficiency of a Power-to-Gas plant by coupling a dynamic SOEC system with a three-phase methanation reactor. Energy Science and Technology; 2015 [Karlsruhe, Germany].

[223] Tietz F, Sebold D, Brisse A, Schefold J. Degradation phenomena in a solid oxide electrolysis cell after 9000 h of operation. Journal of Power Sources. 2013;223:129-35.

[224] Schefold J, Brisse A, Tietz F. Nine Thousand Hours of Operation of a Solid Oxide Cell in Steam Electrolysis Mode. Journal of The Electrochemical Society. 2011;159:A137-A44.

[225] HyLYZER electrolyser. http://www.hydrogenics.com/2018.

[226] Schmid M, Beirow M, Schweitzer D, Waizmann G, Spörl R, Scheffknecht G. Product gas composition for steam-oxygen fluidized bed gasification of dried sewage sludge, straw pellets and wood pellets and the influence of limestone as bed material. Biomass and Bioenergy. 2018;117:71-7.

[227] Schweitzer D, Gredinger A, Schmid M, Waizmann G, Beirow M, Spörl R, et al. Steam gasification of wood pellets, sewage sludge and manure: Gasification performance and concentration of impurities. Biomass and Bioenergy. 2018;111:308-19.

[228] Schweitzer D, Beirow M, Gredinger A, Armbrust N, Waizmann G, Dieter H, et al. Pilot-Scale Demonstration of Oxy-SER steam Gasification: Production of Syngas with Pre-Combustion CO2 Capture. Energy Procedia. 2016;86:56-68.

[229] Introduction to Pinch Technology. Linnhoff March; 1998.

[230] Sinnott R. Coulson & Richardson's Chemical Engineering. 4th Edition: Elsevier; 2005.

[231] Seider WD, Seader JD, Lewin DR. Product and Process Design - Principles Synthesis, Analysis, and Evaluation. 3rd Edition: Wiley-VCH Verlag GmbH & Co. KGaA; 2009.

[232] Linnhoff B, Ahmad S. Cost optimum heat exchanger networks—1. Minimum energy and capital using simple models for capital cost. Computers & Chemical Engineering. 1990;14:729-50.

[233] Ahmad S, Linnhoff B, Smith R. Cost optimum heat exchanger networks—2. targets and design for detailed capital cost models. Computers & Chemical Engineering. 1990;14:751-67.

[234] Canada NR. Pinch Analysis: For the Efficient Use of Energy, Water & Hydrogen. 2003.

[235] Mit der Pinch-Technologie Prozesse und Anlagen optimieren - Eine Methode des betrieblichen Energie- und Stoffstrommanagements. Landesanstalt für Umweltschutz Baden-Württemberg; 2003.

[236] Klemeš JJ, Varbanov PS, Walmsley TG, Jia X. New directions in the implementation of Pinch Methodology (PM). Renewable and Sustainable Energy Reviews. 2018;98:439-68.

[237] Clausen LR, Butera G, Jensen SH. High efficiency SNG production from biomass and electricity by integrating gasification with pressurized solid oxide electrolysis cells. Energy. 2019;172:1117-31.

[238] Technology Roadmap: High-Efficiency, Low-Emissions Coal-Fired Power Generation. International Energy Agency; 2012.

[239] Hüvel B, Eisenhauer G. Fernwärmeverbund in Karlsruhe Technik und Kosten. Fernwärme international. 1993.

[240] Martínez I, Romano MC. Flexible sorption enhanced gasification (SEG) of biomass for the production of synthetic natural gas (SNG) and liquid biofuels: Process assessment of stand-alone and power-to-gas plant schemes for SNG production. Energy. 2016;113:615-30.

[241] Gassner M, Maréchal F. Thermo-economic optimisation of the integration of electrolysis in synthetic natural gas production from wood. Energy. 2008;33:189-98.

[242] Morosanu EA, Saldivia A, Antonini M, Bensaid S. Process Modeling of an Innovative Power to LNG Demonstration Plant. Energy & Fuels. 2018;32:8868-79.

[243] Koytsoumpa EI, Karellas S, Kakaras E. Modelling of Substitute Natural Gas production via combined gasification and power to fuel. Renewable Energy. 2018.

[244] Peters R, Deja R, Blum L, Nguyen VN, Fang QP, Stolten D. Influence of operating parameters on overall system efficiencies using solid oxide electrolysis technology. International Journal of Hydrogen Energy. 2015;40:7103-13.

[245] Elcogen. Technical data of our standard Solid Oxide cells. https://elcogen.com/products/solid-oxide-fuel-cells/, accessed 01.03.2020.

[246] VDM Metals. Crofer 22 APU. Material Data Sheet No. 4046. https://www.vdm-metals.com/fileadmin/user_upload/Downloads/Data_Sheets/Data_Sheet_VDM_Crofer_22_APU.pdf, accessed 01.03.2020.

[247] Navasa M, Yuan JL, Sunden B. Computational fluid dynamics approach for performance evaluation of a solid oxide electrolysis cell for hydrogen production. Applied Energy. 2015;137:867-76.

[248] Udagawa J, Aguiar P, Brandon NP. Hydrogen production through steam electrolysis: Model-based steady state performance of a cathode-supported intermediate temperature solid oxide electrolysis cell. Journal of Power Sources. 2007;166:127-36.

[249] Iora P, Aguiar P, Adjiman CS, Brandon NP. Comparison of two IT DIR-SOFC models: Impact of variable thermodynamic, physical, and flow properties. Steady-state and dynamic analysis. Chemical Engineering Science. 2005;60:2963-75.

[250] Incropera FP, Dewitt DP, Bergman TL, Lavine AS. Fundamentals of heat and mass transfer: John Wiley & Sons; 2007.

[251] White FM. Viscous Fluid Flow. Second Edition: McGraw-Hill, Inc.; 1991.

[252] Shakeri F, Dehghan M. The method of lines for solution of the one-dimensional wave equation subject to an integral conservation condition. Computers & Mathematics with Applications. 2008;56:2175-88.

[253] Marucho MD, Campo A. Suitability of the Method Of Lines for rendering analytic/numeric solutions of the unsteady heat conduction equation in a large plane wall with asymmetric convective boundary conditions. International Journal of Heat and Mass Transfer. 2016;99:201-8.

[254] Ferreira SR. Freezing time of a slab using the method of lines. International Journal of Refrigeration. 2017;75:77-94.

[255] Campo A, Garza J. Transversal Method of Lines for Unsteady Heat Conduction With Uniform Surface Heat Flux. Journal of Heat Transfer. 2014;136:111302--7.

[256] Nakajo A, Wuillemin Z, Van Herle J, Favrat D. Simulation of thermal stresses in anode-supported solid oxide fuel cell stacks. Part I: Probability of failure of the cells. Journal of Power Sources. 2009;193:203-15.

[257] Deliverable 5.2 of the EU project GrInHy - Green Industrial Hydrogen via Reversible High-Temperature Electrolysis - Final report on 7,000 h operational results. https://cordis.europa.eu/project/id/700300/results, accessed 06.06.2020: Sunfire GmbH; 2019.

[258] Research platforms in the North Sea and Baltic Sea. 2020. https://www.fino-offshore.de/en/, accessed 04.11.2020.

[259] Hannula I. Co-production of synthetic fuels and district heat from biomass residues, carbon dioxide and electricity: Performance and cost analysis. Biomass and Bioenergy. 2015;74:26-46.

[260] Richards M, Tang E, Petri R. Solid Oxide Fuel Cell Manufacturing Overview. Hydrogen and Fuel Cell Technologies Manufacturing R&D Workshop; 2012 [Washington, DC].

[261] Hansen JB. Fuel processing for fuel cells and power to fuels as seen from an industrial perspective. Journal of Catalysis. 2015;328:280-96.

[262] Fu Q, Tietz F, Sebold D, Wessel E, Buchkremer H-P. Magnetron-sputtered cobalt-based protective coatings on ferritic steels for solid oxide fuel cell interconnect applications. Corrosion Science. 2012;54:68-76.

[263] Grolig JG, Froitzheim J, Svensson J-E. Coated stainless steel 441 as interconnect material for solid oxide fuel cells: Evolution of electrical properties. Journal of Power Sources. 2015;284:321-7.

[264] Bianco M, Ouweltjes JP, Van herle J. Degradation analysis of commercial interconnect materials for solid oxide fuel cells in stacks operated up to 18000 hours. International Journal of Hydrogen Energy. 2019;44:31406-22.

[265] Froitzheim J, Canovic S, Nikumaa M, Sachitanand R, Johansson LG, Svensson JE. Long term study of Cr evaporation and high temperature corrosion behaviour of Co coated ferritic steel for solid oxide fuel cell interconnects. Journal of Power Sources. 2012;220:217-27.

[266] Douxchamps O, Baudelet E, Leroux B, Constantin G, Tsiava R, Symoens B. Oxygen heat exchanger. Google Patents; 2013.

[267] Greiner CJ, Korpas M, Holen AT. A Norwegian case study on the production of hydrogen from wind power. International Journal of Hydrogen Energy. 2007;32:1500-7.

[268] Heat Exchanger Cost Estimate. 2014. http://www.matche.com/equipcost/Exchanger.html.

[269] Ricketts N, Basile D, Rangott M. Amended Technical Report and Preliminary Economic Assessment on the Nyngan Scandium Project, NSW, Australia. 2015.

[270] Colella WG, James BD, Moton JM, Saur G, Ramsden T. Techno-economic Analysis of PEM Electrolysis for Hydrogen Production. Electrolytic Hydrogen Production Workshop; 2014 [Golden, CO].

[271] Müller-Langer F. DBFZ Report Nr. 9 - Analyse und Bewertung ausgewählter zukünftiger Biokraftstoffoptionen auf der Basis fester Biomasse. Technische Universität Hamburg-Harburg; 2011.

[272] Schulz W, Heitmann S, Hartmann D, Manske S, Peters Erjawetz S, Risse S, et al. Verwertung von Wärmeüberschüssen bei landwirtschaftlichen Biogasanlagen. Bremer Energie Institut; 2007.

[273] Lischke A, Windmüller D, Wurster R, Weindorf W, Heidt C, Naumann K. Identifizierung von Hemmnissen der Nutzung von LNG und CNG im schweren Lkw-Verkehr sowie Möglichkeiten zu deren Überwindung. DLR, ifeu, LBST, DBFZ; 2015.

[274] Bünger U, Landinger H, Weindorf W, R. Wurster R, Zerhusen J, Zittel W. Vergleich von CNG und LNG zum Einsatz in LKW im Fernverkehr. Eine Expertise für die Open Grid Europe GmbH: Abschlussbericht. Ludwig-Bölkow-Systemtechnik GmbH; 2016.

[275] Thunman H, Gustavsson C, Larsson A, Gunnarsson I, Tengberg F. Economic assessment of advanced biofuel production via gasification using cost data from the GoBiGas plant. Energy Science & Engineering. 2019;7:217-29.

[276] Laurent P, Benchimol S, Guianvarc D. Etude technique, économique et environnementale sur l'injection portée de biométhane dans le réseau gaz. ADEME; 2016.

[277] Patterson T, Esteves S, Wolf A, Kastenholz H, Lotz A, Miltner M, et al. Best practice case study for a biomethane production facility, Emmertsbühl biogas plant, Germany - Deliverable 2.2 of the IEE project Bio-Methane Regions. University of Glamorgan, Wirtschaftsförderungsgesellschaft des Landkreises Schwäbisch Hall mbH, Technical University of Vienna; 2012.

[278] Papakonstantinou JM, Tapia RA. Origin and Evolution of the Secant Method in One Dimension. The American Mathematical Monthly. 2013;120:500-17.

[279] BESCO GmbH. Datasheet of the windmill REpower 5M. http://www.besco.de/5m_de.pdf, accessed 04.04.2020.

[280] Goesswein J. Operational Results of Worlds Largest Wind Energy Converter REpower 5M and Project Status of the First Offshore Wind Industrializing Offshore Wind Farm using 5 MW Turbines. Offshore Wind and Other Marine Renewable Energies in Mediterranean and European Seas: Resources, Technology and Applications: 2006 [Rome, Italy].

[281] Turton R, Shaeiwitz JA, Bhattacharyya D, Whiting WB. Analysis, Synthesis, and Design of Chemical Processes. 4th Edition: Pearson Education; 2018.

[282] Mascle C, Wygowski W. Fabrication avancée et méthodes industrielles – Tome 2: Presses internationales Polytechniques; 2013.

Appendix A – Additional results of Chapter 2

Fluid property package – validity domains of entropy and enthalpy functions

The validity domains on which the enthalpy and entropy functions of fluids were determined are summarized hereafter. For several fluids, the validity domain was extended to higher temperature values by closing energy balances of high temperature processes with a high precision, such as the high temperature electrolysis (up to 1123 K) and the gasification (at 1123 K).

Table A-1: Validity domain of entropy functions and maximal error at interpolated points

Fluid name	Validity domain (temperature and pressure range)	Maximal error for the interpolated points (%)
H_2	273.15 – 998.15 K 0.1 – 22 bar	0.297
O_2	273.15 – 998.15K 0.2 – 22bar	0.163
$H_2O(g)$	493.15 – 1273.15 K 0.1 – 22 bar	0.257

Table A-2: Validity domain of enthalpy functions and maximal error at interpolated points

Fluid name	Validity domain (temperature and pressure range)	Maximal error for the interpolated points (%)
CO_2	273.15 – 1098.15 K 0.4 – 22.5 bar	0.226
H_2	273.15 – 998.15 K 0.1 – 82.5 bar	0.0790
CH_4	273.15 – 623.15 K 0.4 – 82.5 bar	0.139
C_2H_4	273.15 – 448.15 K 0.1 – 20 bar	0.024
O_2	273.15 – 998.15 K 0.1 – 22 bar	0.127
N_2	273.15 – 1273.15 K 0.7 – 22 bar	0.144
$H_2O(g)$	278.15 – 1273.15 K 0.05 – 22 bar	0.118
$H_2O(l)$	278.15 – 1273.15 K 0.05 – 22 bar	0.089

Description of the secant method

The first step of the secant method is schematically represented in Figure A-1. It uses two starting points, namely x_0 and x_1. A secant is drawn between the points $(x_0, f(x_0))$ and $(x_1, f(x_1))$, which enables to write Equation (A.1).

$$\frac{y - f(x_0)}{f(x_1) - f(x_0)} = \frac{x - x_0}{x_1 - x_0} \tag{A.1}$$

The intersection of the secant (pink dotted line in Figure A-1) with the x axis is named x_2. With $y = 0$, the value of x_2 can be determined with Equation (A.2).

$$x_2 = x_0 - (x_1 - x_0)\frac{f(x_0)}{f(x_1) - f(x_0)} \tag{A.2}$$

The next iteration starts setting $x_0 = x_1$ and $x_1 = x_2$. The aim is to determine the first value of x_2 for which the function f is close enough to the root (yellow dot in Figure A-1).

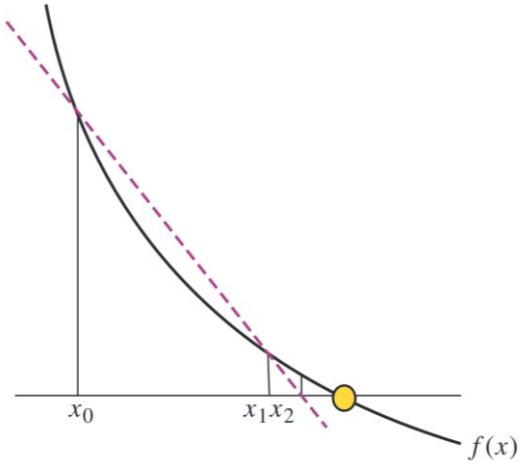


Figure A-1: First step of the secant method [278]

The solver runs until the absolute value of y is smaller than the tolerance required. In this work, the tolerance was set at 10^{-8}. When the desired root precision is reached, the temperature value is returned.

Overall heat transfer coefficients

The overall heat transfer coefficient used in this work are summarized below. They correspond to the average overall heat transfer coefficient values provided for shell and tube heat exchangers in [230].

Table A-3: Overall heat transfer coefficients used for the calculation of the heat transfer area [230]

Heat transfer configuration (hot fluid-cold fluid)	Overall heat transfer coefficient ($W \cdot m^{-2} \cdot k^{-1}$)
Gas-Gas	30
Gas-Vapour	65
Gas-Liquid	160
Liquid-Liquid	1150
Vapour-Liquid	1250

Extended SOE stack model

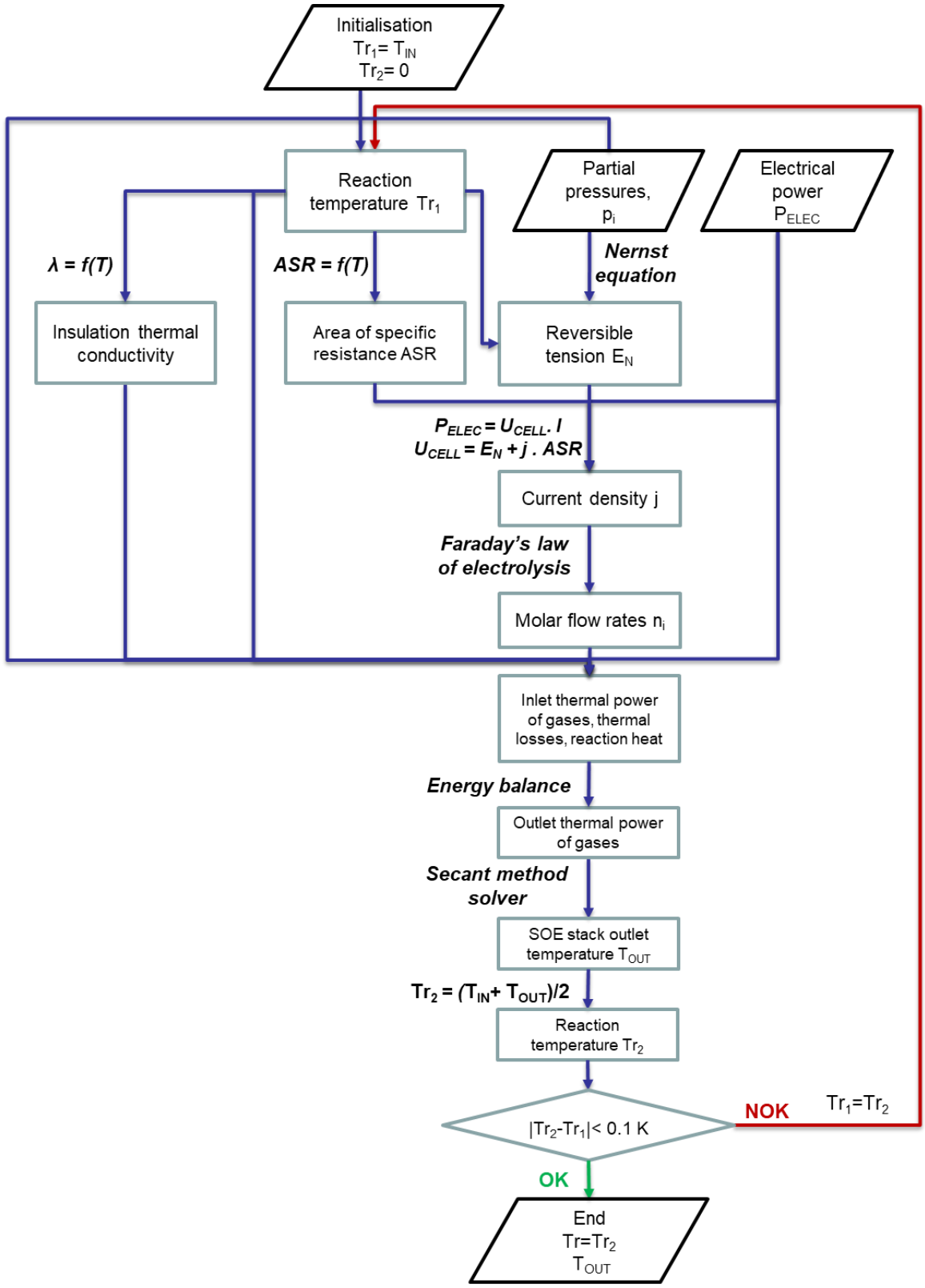


Figure A-2: Flowchart of the extended SOE stack model for the determination of the reaction and outlet temperatures in endothermic, thermoneutral, and exothermic mode

Detailed description of pinch diagrams

Each pinch diagram will be divided in segments corresponding to a temperature interval or a temperature value. For each segment, the contributions of all streams involved will be detailed in a table for the hot steams and the cold streams composite curves.

As a reminder, the ramp of the hot streams curve (red curve) on a temperature interval can be determined by adding up the thermal power contributions of all streams on that temperature interval.

The thresholds correspond either to a steam vaporization or condensation threshold or to a constant heat requirement or heat production of a plant process, e.g. to the reaction heat produced in an isotherm methanation reactor.

The reaction heat of the catalytic methanation reactor operated in isothermal mode in plant concepts 2 and 3 is released at constant temperature. Hence, a vaporization threshold can be observed at 593 K (Reactor 1 or R1) on the red curves in Figure A-4 and Figure A-5. In plant concept 1 however, adiabatic methanation reactors are used. For this reason, ramps but no thresholds can be observed in Figure A-5.

Plant concept 1

Table A-4: Detailed description of the Pinch diagram of plant concept 1

Interval	Temperature (K) Interval/Value	Hot streams (available)[17]	Temperature (K) Interval/Value	Cold streams (required)[18]
1	923-1123	SG	973-1073	$G(O_2)$
2	793-923	SG+R1	485-973	$G(O_2)$+$G(H_2O)$
3	673-793	SG+R1+R2	485	VT from $G(H_2O)$
4	653-673	SG+R1+R2+R3	423-485	$G(O_2)$+$G(H_2O)$
5	618-653	R1+R2+R3	343-423	$G(O_2)$+$G(H_2O)$+BD
6	613-618	R1+R2+R3+R4	323-343	$G(H_2O)$+BD
7	573-613	R1+R2+R3+R4+DBT	298-323	$G(H_2O)$+BD+PEM
8	512-573	R3+R4+DBT		
9	485-512	R3+R4+DBT+C(SG)		
10	459-485	R3+R4+C(SG)+WC+DBT		
11	438-459	R3+R4+C(SG)+WC+C(SNG,S1, S2)+DBT		
12	413-438	R4+VD(SG)+WK+VD(SNG,S1, S2)+DBT		
13	348-413	R4+C(SG)+WC+C(SNG,S1, S2)=***SUM***		
14	343-348	***SUM***+RME		
15	338-343	***SUM***+RME+PEM		
16	333-338	***SUM***+RME+PEM+BD+SG		
17	323-333	***SUM***+PEM+BD+SG		
18	318-323	***SUM***+BD+SG		

[17] Mit BD: biomass drying, DBT: dibenzyltoluene, PEM: process heat released by the PEM-electrolyzer, RME: rapsmethylester, Ri: methanation reactor number i, SG: syngas, C: compressor, Si: stage number i, SNG: synthetic natural gas, VT: vaporization threshold, WC: water condensate.

[18] See footnote above, with G : gasifier

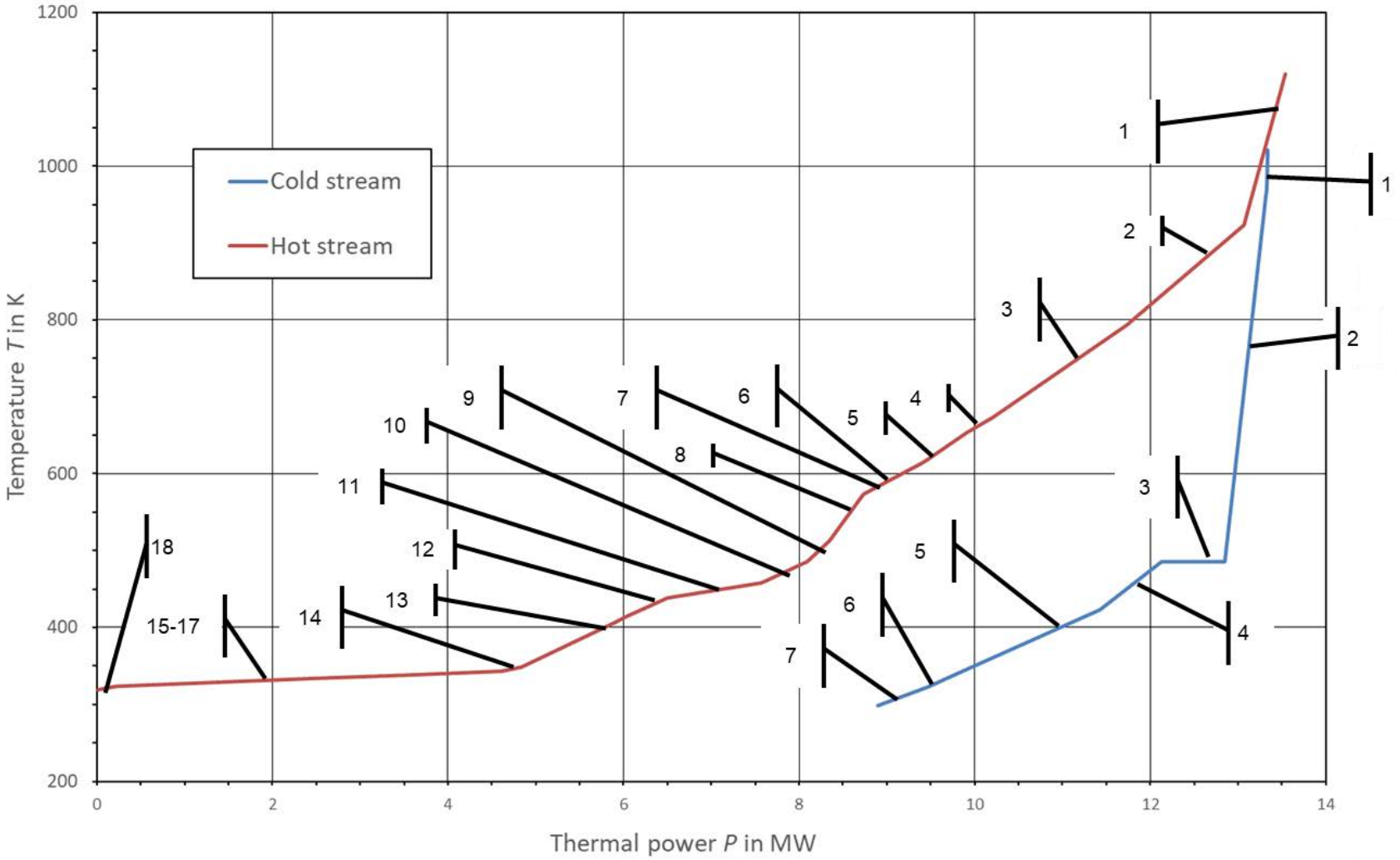


Figure A-3: Pinch diagram of plant concept 1 – segment decomposition

Plant concept 2

Table A-5: Detailed description of the Pinch diagram of plant concept 2

Interval	Temperature (K) Interval/Value	Hot streams (available)[19]	Temperature (K) Interval/Value	Cold streams (required)[20]
1	1073-1123	SG	973-1073	SOE(H_2O)+G(O_2)
2	653-1073	SG+SOE(H_2, H_2O,O_2)	593-973	SOE(H_2O)+G(O_2,H_2O)
3	613-653	SOE(H_2,H_2O,O_2)	538-593	SOE(H_2O)+G(O_2,H_2O)+R1(IG)
4	593-613	SOE(H_2,H_2O,O_2) +DBT	485-538	SOE(H_2O)+VG(O_2,H_2O)+R1 +R2(IG)
5	593	R1(RH)	485	VT(CS of R1 and R2)
6	563-593	SOE(H_2,H_2O,O_2) +DBT	423-485	SOE(H_2O)+G(O_2,H_2O)+R1 +R2(IG+CW)
7	538-563	SOE(H_2,H_2O,O_2) +DBT +R2(RH+OG)	413-423	SOE(H_2O)+G(O_2,H_2O)+R1 +R2(IG+CW)+BD
8	485-538	SOE(H_2,H_2O,O_2) +DBT+R2(OG)	318-413	SOE(H_2O)+G(O_2,H_2O) +R1(EG+CW)+R2(CW)+BD
9	459-485	SOE(H_2,H_2O,O_2) +DBT+R2(OG) +WC=***SUM***	298-318	SOE(H_2O)+VG(O_2)+G(H_2O) +R1+R2(CW)+BD
10	453-459	***SUM***+C(SNG, S1, S2)		
11	413-453	***SUM***+C(SNG, S1, S2)+SG		
12	338-413	SOE(H_2,H_2O,O_2) +R2(OG)+WC +C(SNG, S1, S2)+SG+BD		
13	318-338	SOE(H_2,H_2O,O_2) +R2(OG)+WC +C(SNG, S1, S2)+SG		

[19] Mit BD: biomass drying, DBT: dibenzyltoluene, PEM: process heat released by the PEM-electrolyzer, RME: rapsmethylester, Ri: methanation reactor number i, SG: syngas, C: compressor, Si: stage number i, SNG: synthetic natural gas, VT: vaporization threshold, WC: water condensate, RH: reaction heat, OG: outlet gases, IG: inlet gases, CW: cooling water, CS: cooling steam

[20] See footnote above, with G : gasifier

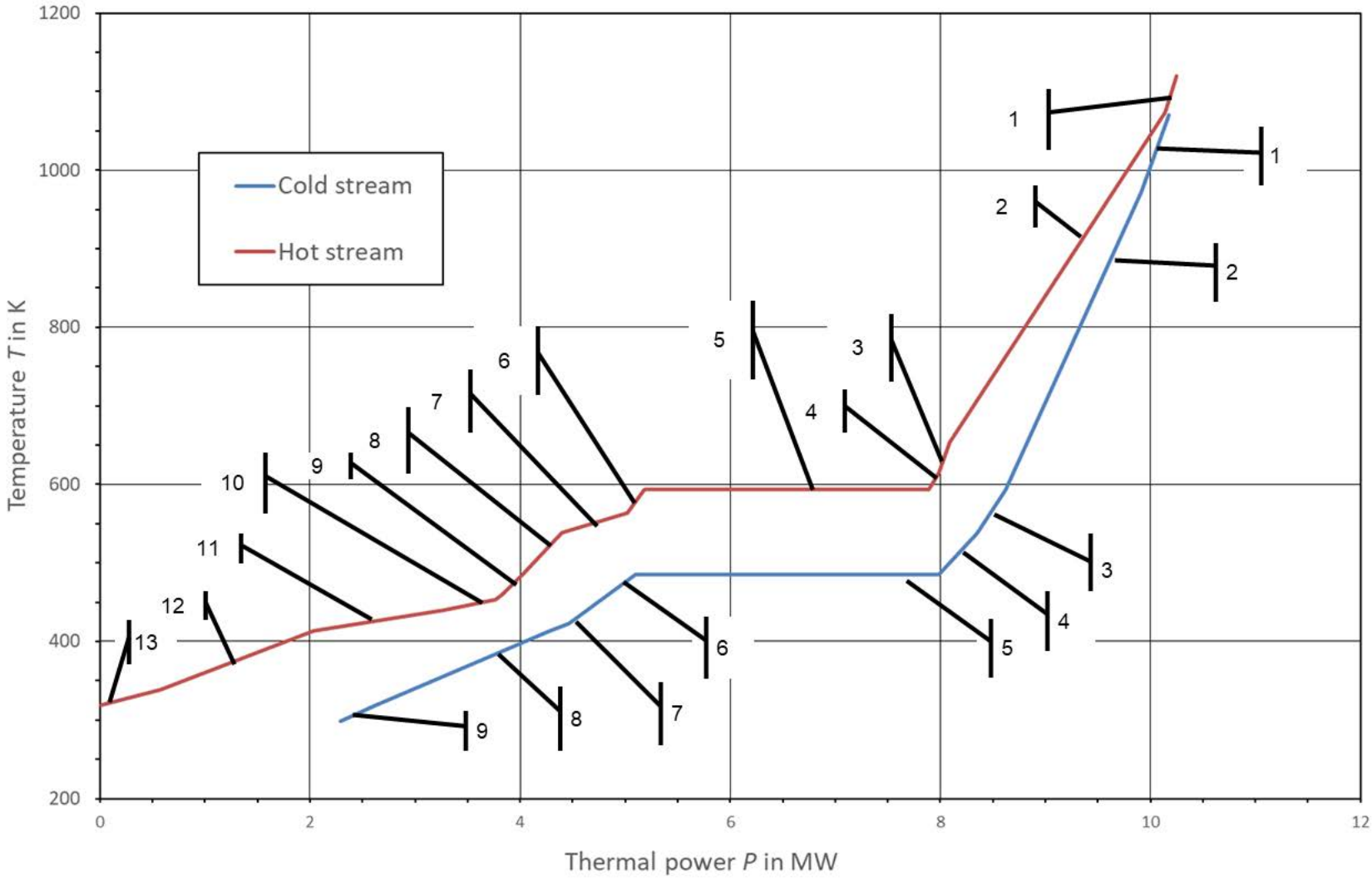


Figure A-4: Pinch diagram of plant concept 2 – segment decomposition

Plant concept 3

Table A-6: Detailed description of the Pinch diagram of plant concept 3

Interval	Temperature (K) Interval/Value	Hot streams (available)[21]	Temperature (K) Interval/Value	Cold streams (required)[22]
1	1073-1123	SG	973-1073	SOE(H_2O)+G(O_2)
2	653-1073	SG+SOE(H_2,H_2O,O_2)	593-973	SOE(H_2O)+G(O_2,H_2O)
3	613-653	SOE(H_2,H_2O,O_2)	538-593	SOE(H_2O)+G(O_2,H_2O) +R1(IG)
4	593-613	SOE(H_2,H_2O,O_2)+DBT	485-538	SOE(H_2O)+G(O_2,H_2O)+R1 +R2(IG)
5	593	R1(RH)	485	VT(CS of R1 and R2)
6	563-593	SOE(H_2,H_2O,O_2)+DBT	423-485	SOE(H_2O)+G(O_2,H_2O)+R1 +R2(IG+CW)
7	538-563	SOE(H_2,H_2O,O_2)+DBT +R2(RH+OG)	413-423	SOE(H_2O)+G(O_2,H_2O)+R1 +R2(IG+CW)+BD
8	485-538	SOE(H_2,H_2O,O_2)+DBT +R2(OG)	318-413	SOE(H_2O)+G(O_2,H_2O) +R1(IG+CW)+R2(CW) +BD
9	459-485	SOE(H_2,H_2O,O_2)+DBT +R2(OG)+WC=***SUM***	298-318	SOE(H_2O)+G(O_2)+G(H_2O) +R1+R2(CW)+BD
10	453-459	***SUM***+C(SNG, S1, S2)		
11	413-453	***SUM***+C(SNG, S1, S2)+SG		
12	373-413	SOE(H_2,H_2O,O_2)+R2(OG)+WC +C(SNG, S1, S2)+SG+BD		
13	373	VT(LNG-plant)		
14	338-373	SOE(H_2,H_2O,O_2) +R2(OG)+WC +C(SNG, S1, S2)+SG+BD		
15	318-338	SOE(H_2,H_2O,O_2) +R2(OG)+WC +C(SNG, S1, S2)+SG		

[21] Mit BD: biomass drying, DBT: dibenzyltoluene, PEM: process heat released by the PEM-electrolyzer, RME: rapsmethylester, Ri: methanation reactor number i, SG: syngas, C: compressor, Si: stage number i, SNG: synthetic natural gas, VT: vaporization threshold, WC: water condensate, RH: reaction heat, OG: outlet gases, IG: inlet gases, CW: cooling water, CS: cooling steam

[22] See footnote above, with G : gasifier

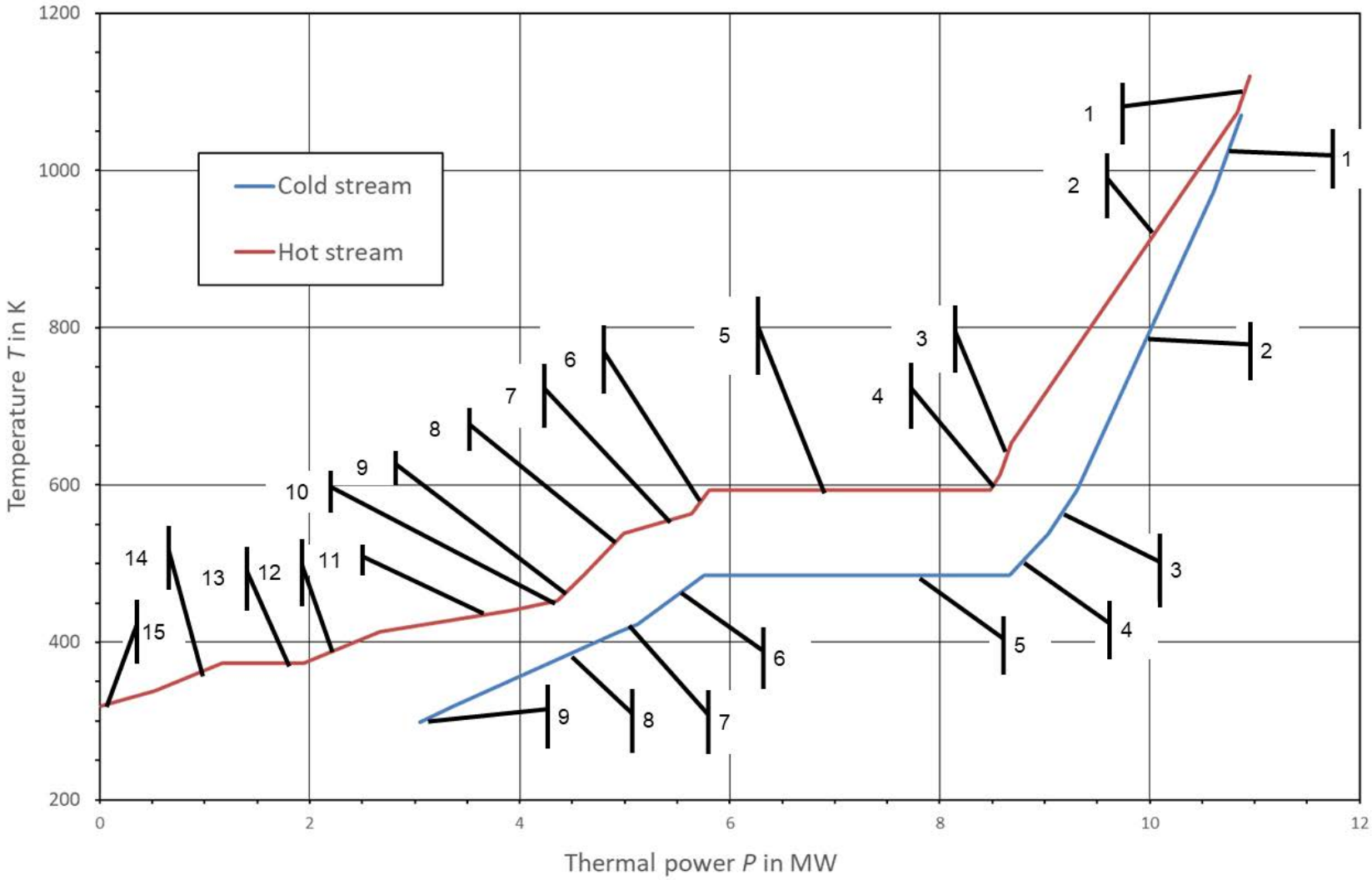


Figure A-5: Pinch diagram of plant concept 3 – segment decomposition

Appendix B – Additional results of Chapter 3

List of parameters used for model comparison

Table B-1: Parameters used fort he comparison of the simplified model with previous work [142, 248]

Parameter	Unit	Value
Cathode channel height	m	0.001
Anode channel height	m	0.001
Interconnect thickness	m	$500 \cdot 10^{-6}$
Cell length	m	0.1
Cell width	m	0.1
Cathode thickness	m	$500 \cdot 10^{-6}$
Electrolyte thickness	m	$20 \cdot 10^{-6}$
Anode thickness	m	$50 \cdot 10^{-6}$
Solid structure heat capacity	$J \cdot kg^{-1} \cdot K^{-1}$	500
Interconnect heat capacity	$J \cdot kg^{-1} \cdot K^{-1}$	500
Solid structure thermal conductivity	$W \cdot m^{-1} \cdot K^{-1}$	2
Interconnect thermal conductivity	$W \cdot m^{-1} \cdot K^{-1}$	25
Solid structure density	$kg \cdot m^{-3}$	5900
Interconnect density	$kg \cdot m^{-3}$	8000
Cathode stream Nusselt number	-	3.09
Anode stream Nusselt number	-	3.09
Cathode stream inlet temperature	K	1073
Cathode stream inlet composition	mol% H_2/ mol% H_2O	10/90
Anode stream inlet temperature	K	1073
Anode stream inlet composition	mol% N_2/ mol% O_2	79/21
Operating pressure	Pa	$0.1 \cdot 10^6$
Steam utilisation factor	%	80

Main characteristics of the Repower 5M windmill

Table B-2: Main technical parameters of the REpower 5M windmill [279]

Parameter	Unit	Value
Rated Power	kWe	5000
Cut-in wind speed	$m \cdot s^{-1}$	3.5
Rated Wind speed	$m \cdot s^{-1}$	13
Cut-out wind speed (offshore)	$m \cdot s^{-1}$	30
Cut-out wind speed (onshore)	$m \cdot s^{-1}$	25

Parameter	Unit	Value
Certification according to	-	TK I, GL Offshore (extended with design for 10.5 m/s annual average wind speed)
Rotor diameter	m	126
Speed range, normal operation	rpm	6.9-12.1
Principle control	-	Blade angle and speed control, electrical pitch
Gearbox design	-	Combined planetary/Spur wheel gears
Transmission ratio	-	Approx. 97
Generator design	-	Double fed asynchronous generator, 6 poles
Generator speed range	rpm	Approx. 670-1170
Rotor mass	tons	Approx. 120
Nacelle mass (without rotor)	tons	Approx. 290

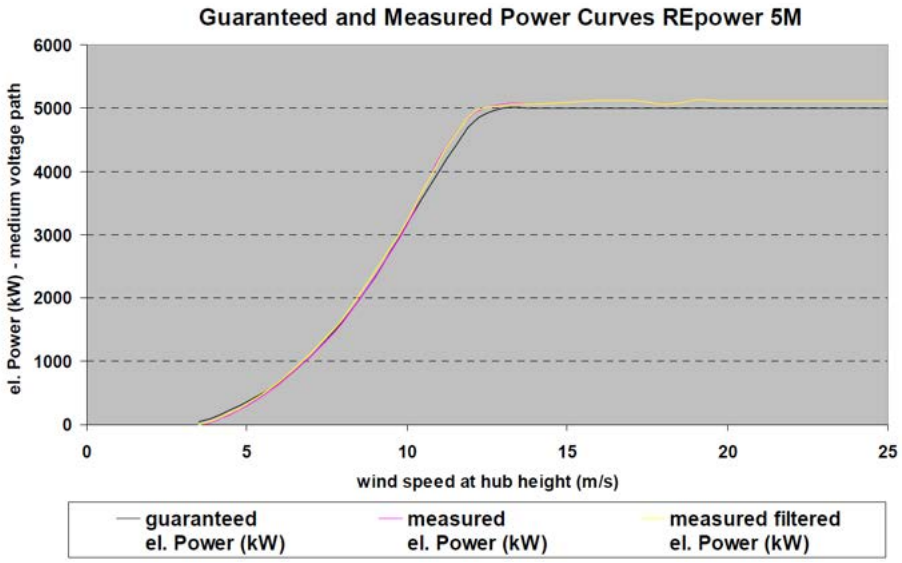


Figure B-1: Power generated by the windmill REpower 5M as function of the wind speed [280]

Appendix C – Additional results of Chapter 4

Chemical Engineering Plant Cost Index (CEPCI) annual values

Table C-1: CEPCI annual values from 1995 to 2017 [281]

Year	CEPCI value	Year	CEPCI value
1995	381.1	2007	525.4
1996	381.7	2008	575.4
1997	386.5	2009	521.9
1998	389.5	2010	550.8
1999	390.6	2011	585.7
2000	394.1	2012	584.6
2001	394.3	2013	567.3
2002	395.6	2014	576.1
2003	402	2015	556.8
2004	444.2	2016	541.7
2005	468.2	2017	567.5
2006	499.6		

SOE cell and stack manufacturing lines

SOE cell manufacturing line

The process flow diagram of the electrolyte supported cell manufacturing line is represented in Figure C-1. Once the oxide powder reaches the proper size, it is mixed with organic blenders and ball milled. The electrolyte layer is tape casted, sintered and laminated to adapt its thickness. The cells are then laser cut and sintered at 1273-1573 K for electrolyte densification. The diffusion layers are then screen printed, dried at 373 K and sintered at 1273-1573 K. The same processes are applied for electrode deposition. After acceptance at the quality control, the cells are sent to the stack manufacturing line. Scrap rates from 15 % and 13 % were assumed in scenario 1 and 2 respectively. They were calculated as the sum of the scrap after laser cutting (14 % in scenario 1 and 12 % in scenario 2) and of cells rejected after quality control (a 1 % value was assumed in both scenarios). The scrap from laser cutting was determined by comparing the cell area with the tape casting area obtained from documentation of tape casting machine manufacturers. These value are higher than the 10 % and 3 % scrap rate assumed for SOFC cells in [152] and [150]. However, the cell area were considerably larger (ca. 400 cm^2 in [152] and 488 to 822 cm^2 in [150] against 167 cm^2 in this work) and according to [151] larger cells (up to 1,000-2,000 cm^2) enable lower scrap rates. The thermal management of such large cells operated with high current densities would be too difficult to implement, this is why the cell area chosen in this work is much smaller.

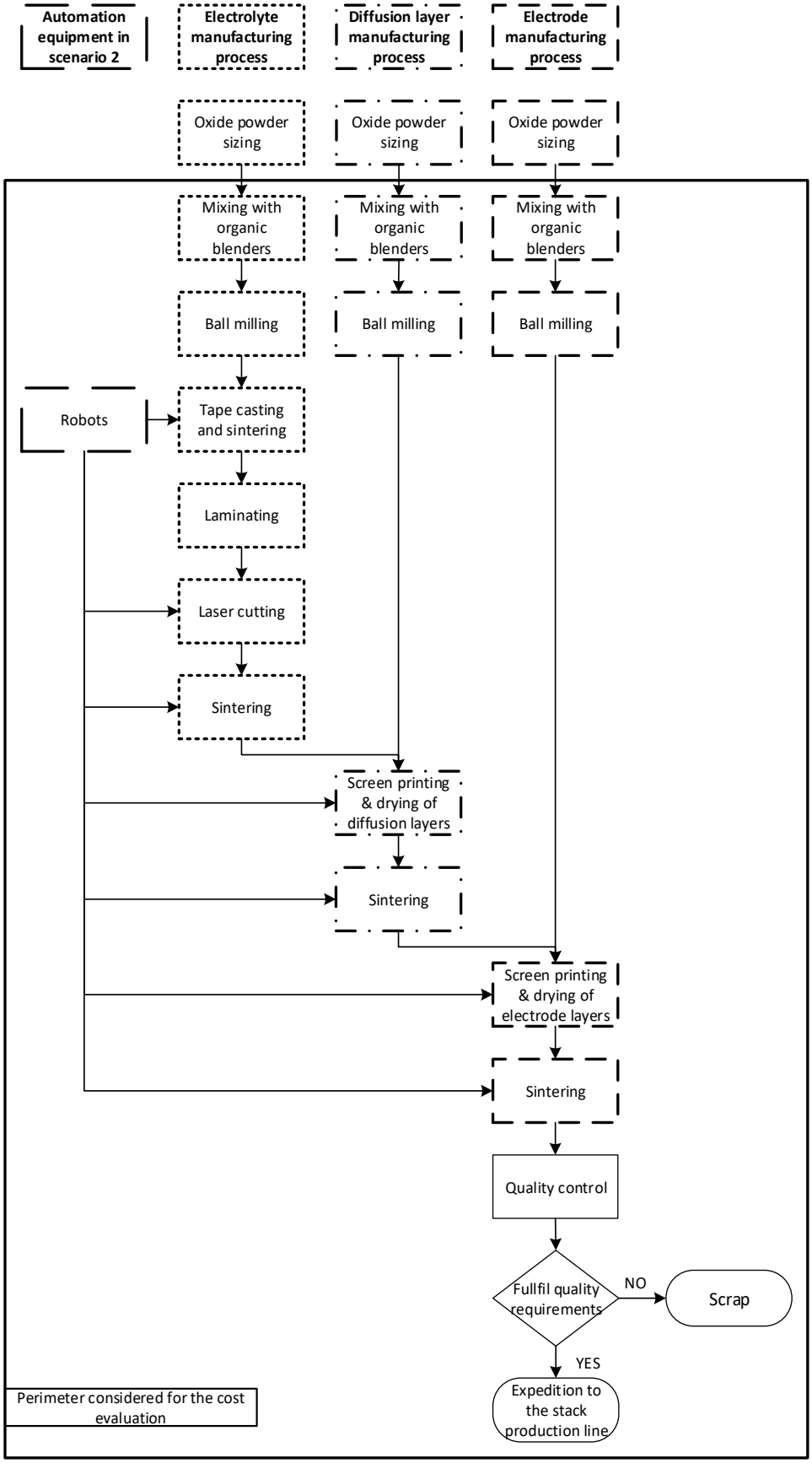


Figure C-1: Process flow diagram of the cell manufacturing line

SOE stack manufacturing line

The process chain implemented in the stack manufacturing line is represented in Figure C-2 and was adapted from previous work [152]. The interconnects are stamped and then laser etched to draw the flow channels on their surface. The interconnects are then coated with a perovskite based material and sintered in a high temperature furnace at 1273 K. The perovskite material is processed in a ball miller before the coating treatment. The stacks are then mounted on assembling stations and welded in a furnace at 873 to 1148 K. They are then checked for quality control on test benches and sent to the storage room. As was done in [45], a stack scrap rate of 1% was assumed for rejection during stack quality control.

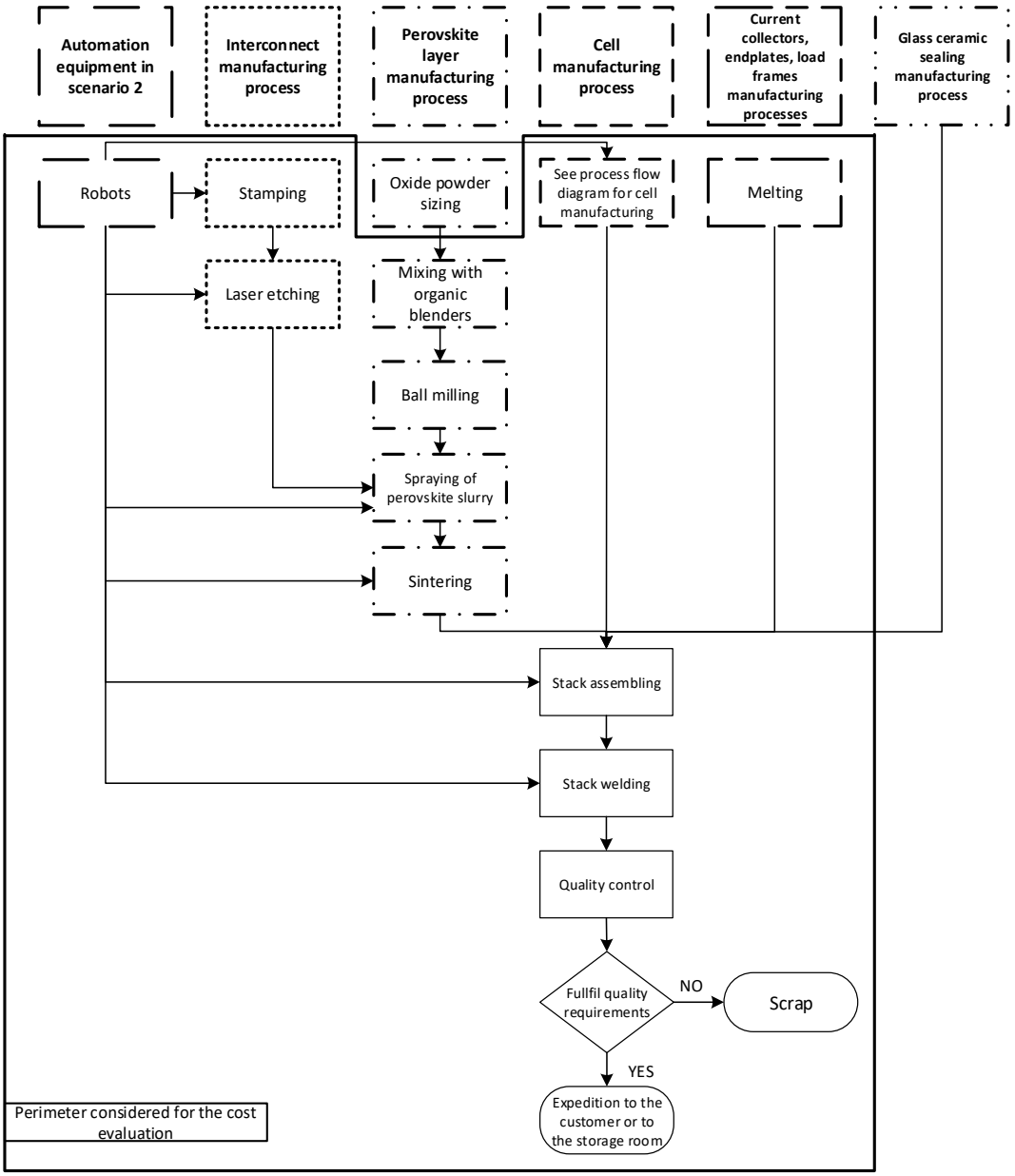


Figure C-2: Process flow diagram of the stack manufacturing line

Determination of the different cost categories for SOE cells and stack production

Material costs

The raw material costs used for cell manufacturing are gathered in Table C-2 and were taken from [150] and from quotations obtained from off-shore suppliers. The free on board costs were estimated to represent 70% of the total raw material costs. The same organic solvent mixture than the one used in [152] for anode tape casting was applied. The required amount of material already takes into account the cell scrap rates.

Table C-2: Raw materials quantity and manufacturing costs of a SOEC cell, source [150] and EIFER calculations

Materials	**Material costs (free on board price for 2,500 kg order, in €·kg^{-1})**	**Required amount (g·cell^{-1}, scenario 1)**	**Required amount (g·cell^{-1}, scenario 2)**	**Scenario 1 (€·cell^{-1})**	**Scenario 2 (€·cell^{-1})**
LSCF	53	2.8	2.8	0.21	0.21
SSZ	256	15.3	14.9	5.58	5.45
CGO	42	2.7	2.6	0.16	0.16
NiO/CGO (50%/50%-vol)	23/42	3.3	3.2	0.15	0.15
Organic solvents	-	24.5	23.9	0.26	0.26
Total cell cost	-	-	-	6.37	6.23

The stacks material costs were calculated as the sum of the material costs required for stack assembling. Interconnects in Crofer 22APU were chosen. Interconnect prices can be found on supplier websites, but the volumes currently sold are considerably lower than the volumes targeted in this work. For this reason, an in-house extrapolation function was developed based on suppliers cost values to evaluate the costs of interconnects for production volumes matching the requirements in both scenarios.
A conventional borosilicate glass and lanthanum oxide material was used for stack sealing. Based on the sealing pattern, the mass of sealing material required for each SRU and consequently for each stack was calculated.
Material costs for the upper load frame, the lower load frame, the endplates and the current collectors were also included. The weight of each part was estimated based on the weight values reported in [152]. Manufacturing costs in €·kg^{-1} available in [282] were then used to determine part costs in a €·kW^{-1} stack basis. A stack scrap rate of 1% was assumed for rejection during quality control.

Equipment costs

Free on board equipment costs for cell and stack manufacturing lines were determined with quotations from suppliers and previous literature values [151, 152]. Installed equipment costs were obtained by multiplying the free on board costs with a factor 1.1. The number of machines required for each process step was estimated based on state of the art process speed values [150] and on considerations to adapt the dimensions of the equipment to the dimensions of the cells or stacks.

Building costs

Building costs were evaluated based on the total area required for establishing the cell and stack manufacturing lines. The building area was calculated based on the space requirements of the machines, administration, and storage and also included the land area. The area values for building and land obtained were then multiplied with official German average construction costs for industrial building and average land costs in the Baden-Wurttemberg region to determine final building investment costs. The costs were then amortized assuming a building lifetime of thirty years as was done in [152] and using an actualization rate of 2% corresponding to the German context.

Personnel costs

It was assumed that the cell and the stack manufacturing lines were operated manually during one eight hours shift in scenario 1. The lines were automated to operate on a three eight hours shifts basis in scenario 2. Personnel requirements (operators, engineers) were assumed for each machine in both manufacturing lines, using similar considerations as in [152]. A yearly cost per employee was assumed and allowed to calculate the personnel costs.
For both cell and stack manufacturing lines, an operator was in charge of the cell quality control. This operation cannot be automated because of its complexity and of the high costs required for its automation. Two operators were considered in each scenario for material and raw material handling. Two operators were also required to oversee the equipment. In scenario 2, a number of robots was assigned to each machine to automate the cell and the stack manufacturing line. In both scenario, operators were required to run test benches for stack quality control, because this task was considered too complex to be automated.

Operation and maintenance costs

The operation and maintenance costs (excluding power costs) were assumed to represent 3% of the total investment costs of building and machines, as was done in [152]. As for power costs, values from 0.7 to 1.3% of the total manufacturing costs were reported in [152]. An average value of 1% was assumed in scenario 1. Other sources report a slight increase of the power costs share from 0.1 to 0.2%, when increasing five times SOFC system capacity [150]. Therefore a higher power costs share of 1.2% was assumed in scenario 2. The increase of power consumption in scenario 2 is related to the automation of the manufacturing lines.

Plant consumables and personnel costs of the power-to-SNG plants

Plant consumables

Table C-3: Overview of cost assumptions made for plant consumables [11]

Name	Value	Unit	Reference year
Limestone	50	€·t^{-1}	2018
Zinc oxide (ZnO)	20	€·kg^{-1}	2012
Dibenzyltoluene (DBT)	3	€·kg^{-1}	2017
Feed water	6	€·m^{-3}	2012
Iron oxide pellets	1850+240 Waste disposal costs	€·t^{-1}	2017
Zeolite	2.14	€·kg^{-1}	2017
Ni catalyst	107	€·kg^{-1}	2015
Active carbon	0.4	€·kg^{-1}	2014

Personnel costs

Table C-4: Personal requirements and associated costs assumed for plant operation [11]

Type of employee	Number per shift	Shifts per day	Total manpower	Costs per employee (in k€·year^{-1})	Total costs (in k€·year^{-1})
Production manager	1	1	1	98.9	98.9
Plant supervision	1	3	3	67.9	203.6
Operator	2	2	4	45.2	181.0
Workshop	1	2	2	67.9	135.7
Administration	0.5	1	0.5	45.2	22.6
Total	**-**	**-**	**10.5**	**-**	**641.8**

Equipment repartition used for the cost evaluation

The equipment repartition used for the cost evaluation of the three plant concepts are represented in Figure C-3, Figure C-4, and Figure C-5 respectively.

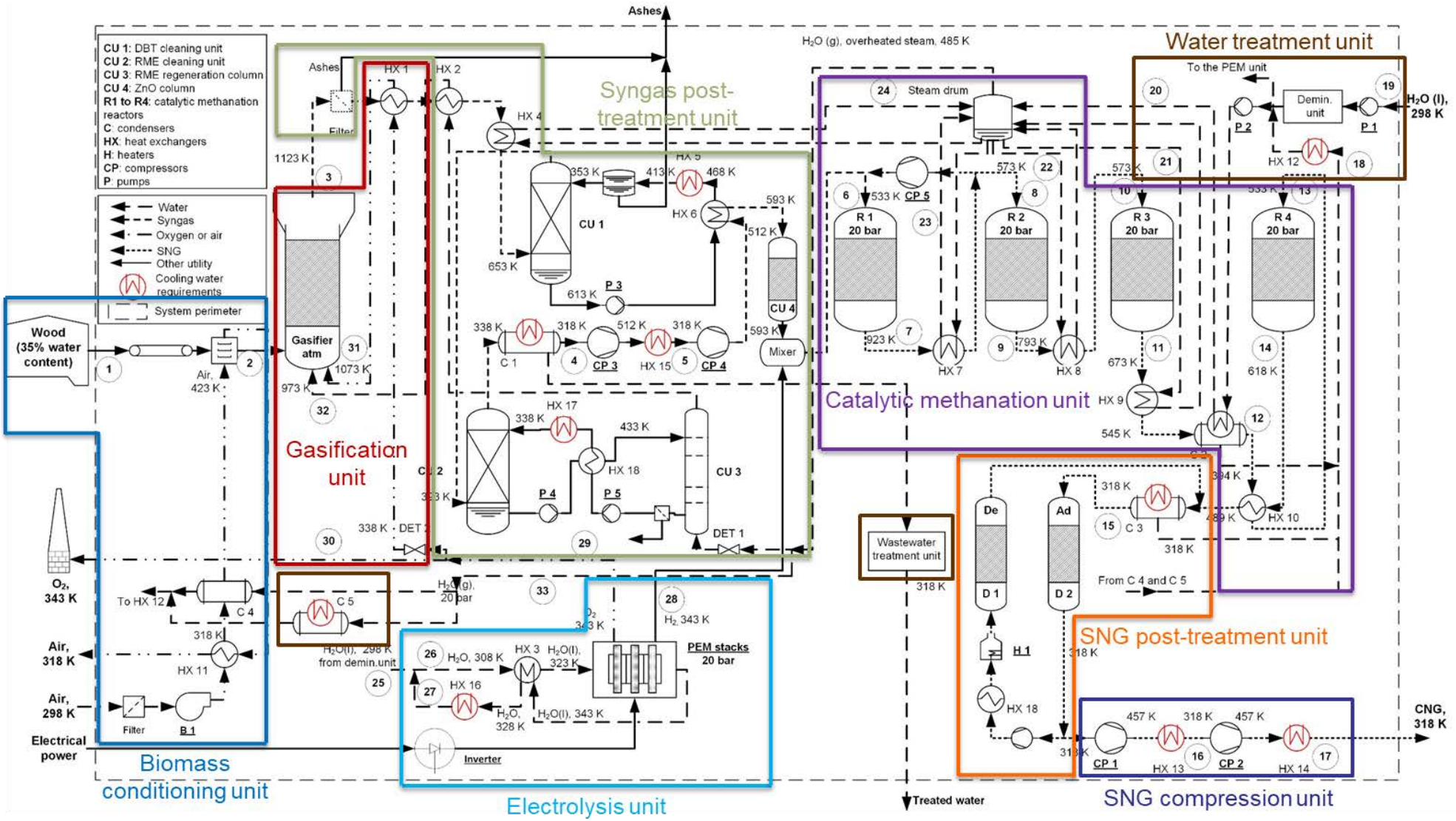


Figure C-3: Equipment repartition used for the cost evaluation of plant concept 1

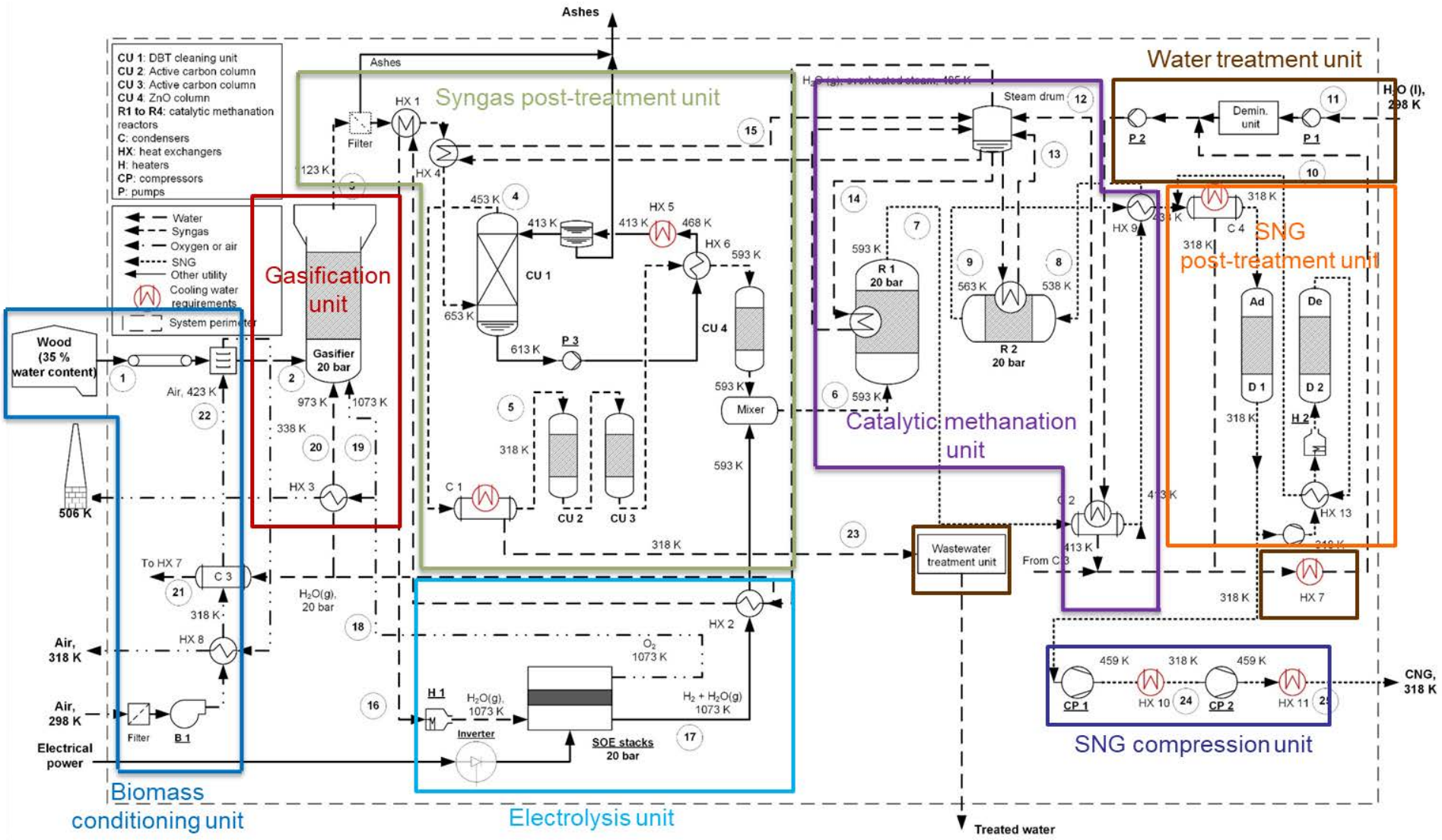


Figure C-4: Equipment repartition used for the cost evaluation of plant concept 2

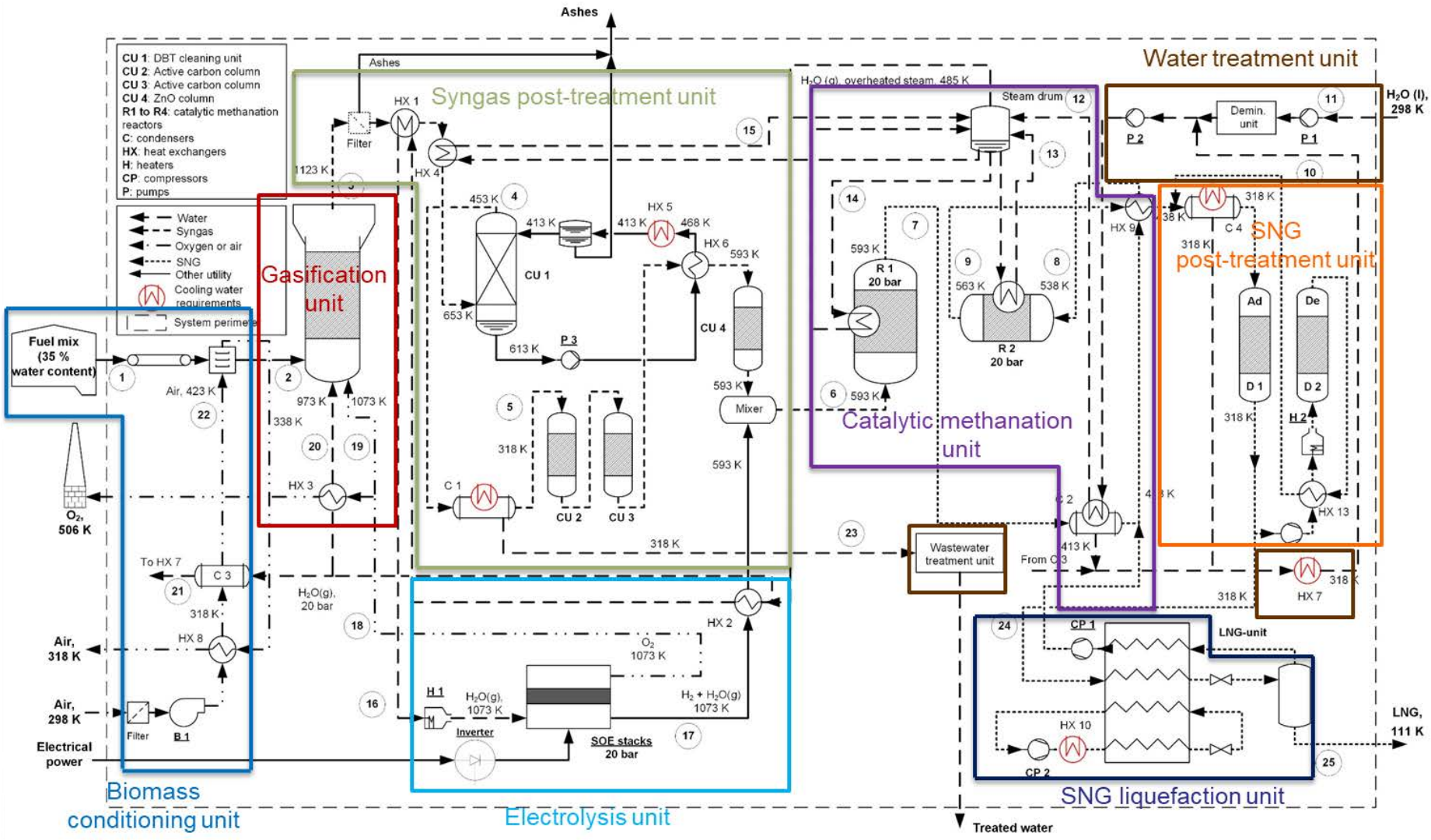


Figure C-5: Equipment repartition used for the cost evaluation of plant concept 3

Résumé du manuscrit

Contexte et enjeux

En 2018, les combustibles fossiles représentaient 85% de la consommation d'énergie dans le monde, le pétrole étant la source d'énergie la plus utilisée [1]. L'épuisement des ressources de pétrole conventionnel facilement accessibles pourrait signicativement réduire la quantité d'énergie nette à disposition dans l'économie mondiale et avoir de sérieuses conséquences sur notre qualité de vie [2]. De plus, l'opinion publique est de plus en plus consciente des problèmes liés au changement climatique. Ces deux constats plaident en faveur d'une forte augmentation de la production d'énergies renouvelables et de leur intégration accélérée dans le système énergétique. En Europe, le législateur a mis au point le paquet climat-énergie 2020, qui prévoit de réduire les émissions de gaz à effet de serre (GES) de 20% d'ici fin 2020 par rapport à leur niveau de 1990, de faire passer la part de la consommation d'énergie renouvelables à 20% et d'augmenter l'efficacité énergétique de 20%. Ces objectifs ont débouché sur une augmentation forte et régulière de la consommation d'énergies renouvelables dans l'Union Européenne.

Néanmoins, les sources d'électricité renouvelables sont intermittentes et leur intégration dans le système énergétique –particulièrement dans le réseau électrique– constitue un défi pour les raisons suivantes :

- Le déséquilibre croissant entre production et consommation électrique lié à l'augmentation de la part d'électricité photovoltaïque (PV) et éolienne qui devrait rendre l'équilibrage du réseau électrique de plus en plus difficile à l'avenir ;
- La congestion du réseau électrique lié à la concentration élevée des capacités de production renouvelables dans certaines zones qui excèdent les capacités de transport locales du réseau électrique ;
- Le manque de capacités de stockage disponibles à proximité des capacités de production renouvelables, qui entraîne souvent leur déconnexion du réseau électrique pour ne pas compromettre son équilibre et aboutit de fait à la perte de la production énergétique correspondante ;
- Le potentiel limité en Europe pour la mise en place de nouveaux barrages et stations de pompage-turbinage (STEP) [3] ;
- L'inexistence de solutions matures et efficaces pour le stockage de l'énergie électrique en tant que tel ou sous forme d'énergie cinétique, potentielle ou chimique ;
- Les possibilités limitées d'équilibrer le réseau électrique à l'échelle Européenne, entre autres pour des raisons climatiques [4].

De plus, la réduction des émissions de gaz à effet de serre (GES) demeure un problème délicat.

- Des solutions alternatives comme les véhicules électriques auront besoin de temps pour remplacer les véhicules à moteur à combustion interne dans le secteur des transports ;
- La substitution des combustibles fossiles avec d'autres sources d'énergie est parfois impossible, par exemple lorsqu'ils sont employés comme combustible dans des procédés à haute temperature spécifiques où le chauffage électrique n'est techniquement pas envisageable ou encore dans leurs usages comme précurseurs chimiques dans l'industrie ;
- Depuis 1990, la majorité des réductions d'émissions de GES en France ont été obtenues dans l'industrie manufacturière, dans un contexte où l'activité économique correspondante était probablement relocalisée ailleurs (voir Figure 0-1). Même si des réductions d'émissions

significatives sont visibles dans le secteur de l'énergie, les émissions dans le secteur des transports par exemple ont significativement augmenté sur la même période.

Une solution potentielle à ces deux problèmes pourrait être le recours aux voies de type power-to-gaz ou power-to-liquids, qui permettent la conversion d'électricité bas carbone (par exemple nucléaire) ou renouvelable en carburants de synthèse gazeux ou liquides. Ceci permettrait de remplacer les combustibles fossiles par leurs équivalents renouvelables ou bas carbone d'une part, mais aussi de stocker et transporter l'électricité renouvelable sous forme de vecteur d'énergie chimique d'autre part.

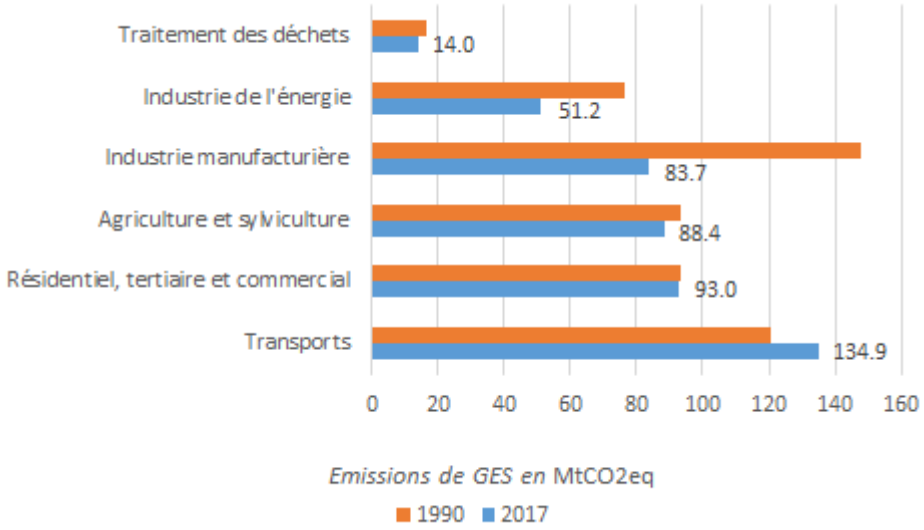


Figure 0-1: Evolution des émissions de GES par secteur en France entre 1990 et 2017 [5]

Dans ce contexte, le gaz naturel de synthèse (GNS) semble être une alternative prometteuse. En effet, par comparaison aux autres vecteurs d'énergie chimique, le GNS présente les avantages suivants :

- Une infrastructure existante et déjà pleinement développée qui permet le transport efficace du gaz naturel sur de longues distances et qui offre de larges capacités de stockage en comparaison à d'autres vecteurs d'énergie (les capacités de stockage du gaz naturel en réservoir souterrain représentent ainsi 265 TWh en Allemagne [6] et 152 TWh en France [7]) ;
- L'usage déjà largement répandu du gaz naturel dans de nombreux secteurs industriels, qui permet une pénétration potentiellement accrue de l'électricité renouvelable dans l'économie.

Les différentes filières de production du GNS sont représentées schématiquement sur la Figure 0-2, avec les intrants à gauche, les applications des produits à droite et les étapes intermédiaires de conversion au centre. Le GNS peut être produit seulement à partir de biogaz (filière biométhane) ou de bio-syngaz, mais une part significative du contenu carbone de la biomasse est alors perdu et émis sous forme de CO_2. L'ajout de H_2 produit par électrolyse permet de maximiser la valorisation de ce contenu carbone.

Plusieurs unités de démonstration semi-industrielles de conversion d'électricité en gaz naturel de synthèse (power-to-SNG) ont été déployées ces dernières années en Europe. Elles intègrent des technologies d'électrolyse de l'eau liquide à basse température (de 323 K à 353 K) de type membrane à échange de protons (PEM) ou alkaline pour la première étape de conversion d'électricité en H_2, présentent des rendements power-to-SNG limités et sont coûteuses principalement à cause des coûts des électrolyseurs. Néanmoins, la technologie d'électrolyse à oxydes solides (SOC) basée sur des matériaux céramiques et fonctionnant à haute température (entre 973 K et 1173 K) avec de la vapeur d'eau pourrait constituer une alternative prometteuse.

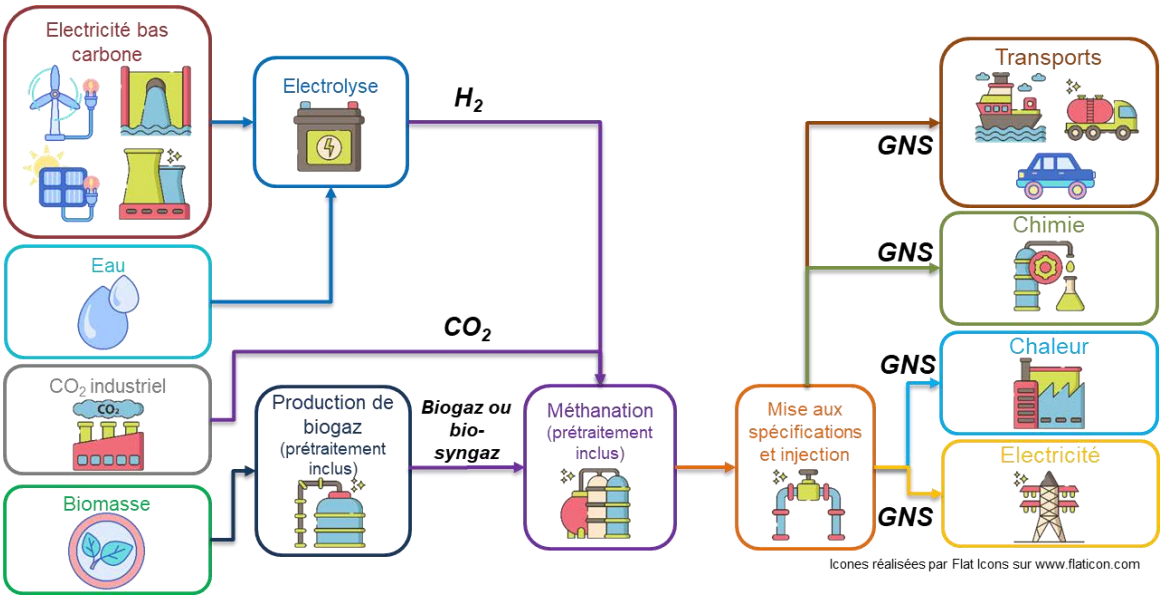


Figure 0-2: Représentation schématique des différentes filières de production du GNS

La vapeur de refroidissement produite lors du procédé exothermique de méthanation catalytique pourrait être injectée dans une unité d'électrolyse à oxydes solides (SOE), ce qui permettrait de réduire la consommation énergétique et d'augmenter le rendement power-to-SNG. Néanmoins, un tel concept d'installation n'a jusqu'ici jamais été démontré à l'échelle industrielle. La technologie SOE reste coûteuse et le potentiel ultime de réduction des coûts par mise à l'échelle des unités et des lignes de production demeure incertain. De plus, la capacité de cette technologie à opérer sous charge électrique variable est bien moins documentée que celle des autres technologies.

Objectifs

De fait, ce manuscrit s'intéressera au potentiel de la technologie SOE dans le contexte des installations power-to-SNG en étudiant dans quelle mesure des unités SOE peuvent améliorer l'efficacité, la flexibilté et la rentabilité de ces installations.

Dans un premier chapitre, le concept général de la production d'électricité à partir de gaz naturel synthétique sera présenté, suivi d'une revue de la littérature des technologies impliquées dans chaque étape de conversion de l'électricité et de la biomasse en gaz naturel de synthèse. A ce niveau, l'accent sera mis sur la technologie SOE, d'abord sur la description de ses caractéristiques techniques, ensuite sur les travaux antérieurs de modélisation technique et économique de la SOE comme procédé autonome ou intégré dans des installations power-to-SNG.

Dans un deuxième chapitre, des évaluations énergétiques de certains concepts d'installations power-to-SNG seront réalisées sur la base de modèles MATLAB® et Simulink®. Ces installations viseront à transformer le bio-syngaz obtenu par gazéification en GNS par ajout d'H_2 électrolytique en utilisant différentes combinaisons de technologies. Dans ce travail, seules l'injection dans le réseau gazier et les applications de type mobilité seront considérées pour le GNS produit. Chaque concept d'installation sera présenté avec ses principales hypothèses de modélisation, suivi de la description de la méthodologie appliquée pour l'évaluation énergétique. Des indicateurs de performance seront définis et utilisés pour comparer les différents concepts.

Le troisième chapitre examinera le fonctionnement des systèmes SOE sous charge électrique variable afin d'évaluer dans quelle mesure il peut améliorer la flexibilité des installations power-to-SNG. Un modèle dynamique sera développé afin d'étudier le comportement thermique des unités SOE sous charge électrique variable. Dans un deuxième temps, le modèle sera couplé à des profils de charge électrique. Des profils de production d'H_2 seront générés et utilisés pour proposer un premier dimensionnement de l'unité de stockage d'H_2 et de l'unité de méthanation catalytique en aval. Des stratégies d'exploitation et des configurations d'installation pour réduire ou supprimer l'unité de stockage seront étudiées, ainsi que les modes d'exploitation les plus appropriés des unités SOE en fonction de l'intermittence de la charge électrique et de la configuration du couplage thermique.

Dans un dernier chapitre, une évaluation technoéconomique des concepts d'installations étudiés sera réalisée afin de déterminer le coût de production du gaz naturel de synthèse, qui incluera aussi une analyse détaillée des coûts d'investissement des unités SOE de taille industrielle. Une analyse de sensibilité des coûts de production du gaz naturel de synthèse sera effectuée afin d'identifier les paramètres les plus influents sur les coûts. Enfin, le coût de production sera comparé à celui du bio-méthane et du gaz naturel conventionnel.

Résultats

Dans ce travail, une analyse énergétique de trois concepts innovants d'installations power-to-SNG avec des unités intégrées d'électrolyse, de gazéification et de méthanisation catalytique est réalisée. Ces installations sont également caractérisées en termes de rendement carbone, de besoins en eau de refroidissement et de besoins nets en eau. Les concepts d'installations associent différentes technologies d'électrolyse (PEM, SOE), de méthanation catalytique (lit fixe, lit bouillonnant, nid d'abeille) et de type de biomasse à gazéifier (boues d'épuration, paille, bois), pour la synthèse de différents produits (gaz naturel comprimé ou liquéfié, encore appelés GNC ou GNL).

Pour chaque installation, un rendement maximal théorique est calculé sur la base d'un schéma procédé simplifié et d'un diagramme de pincement. Une intégration thermique explicite complète est ensuite réalisée. L'efficacité de l'installation intégrée est très proche de l'efficacité théorique maximale, ce qui tend à valider la pertinence des intégrations thermiques choisies d'un point de vue énergétique. Les concepts d'installations avec des unités SOE intégrées montrent des valeurs de rendement élevées jusqu'à 81,8% pour le GNS, jusqu'à 81,0% pour le GNC et jusqu'à 78,5% pour le GNL (en base PCS des produits finaux), qui sont sensiblement plus élevées que les valeurs avec des unités d'électrolyse PEM (64,9% ou 64,4% pour la synthèse de GNS ou de GNC). Le rendement est nettement plus élevé, principalement parce que la vapeur de refroidissement de l'unité de méthanation catalytique peut être valorisée dans l'unité SOE. Ces valeurs de rendement mettent en évidence le potentiel d'amélioration du rendement et de réduction des coûts d'exploitation de la technologie SOEC par rapport aux technologies d'électrolyse classiques (PEM et alcaline par extension) lorsqu'elle est couplée à des sources de vapeur.

Différentes options pour la valorisation de la chaleur résiduelle sont également discutées. Pour les installations équipées d'une unité d'électrolyse à basse température, la valorisation de la vapeur excédentaire dans une turbine à vapeur ne pourrait augmenter le rendement power-to-SNG de l'installation que de quelques %. Dans le cas des installations power-to-SNG avec une unité SOE, la chaleur résiduelle devrait de préférence être injectée dans un réseau de chauffage urbain, tel que celui de Karlsruhe.

La deuxième contribution principale de ce travail a été de développer un modèle dynamique 1D pour étudier le comportement thermique des unités de répétitions (SRU) intégrées dans un stack SOE. Le modèle a été adapté à partir de travaux antérieurs pour proposer une approche de modélisation simplifiée dans laquelle les potentiels d'activation et de surtension des SOEC sont négligés, ce qui est une approximation valable dans le domaine de fonctionnement où la résistance surfacique spécifique (ASR) est linéaire. Les comportements transitoires de deux architectures de cellules, les cellules à électrolyte support (ESC) et les cellules à cathode support (CSC), sont étudiés et comparés.

Tout d'abord, un modèle simplifié est développé, où l'ASR est supposé constant quelque soit la température de la cellule. L'étude du passage du hot standby au mode exothermique ou endothermique montre que les durées transitoires et des gradients de température des cellules sont comparables pour les deux types de SRU. Les profils de températures à la fin du transitoire sont vérifiés par comparaison avec la solution exacte en régime permanent. Le modèle donne également des résultats comparables au modèle développé par Cai et al. dans [140], avec une déviation des températures de sortie du flux cathodique de max. 1,2% en mode endothermique.
Deuxièmement, un modèle étendu est développé, dans lequel l'ASR dépend de la température de la cellule, sur la base de différentes lois empiriques pour les CSC et les ESC, issues de données expérimentales au niveau cellule. Le comportement transitoire est étudié dans des conditions similaires à celles du modèle simplifié. Les plages de puissance électrique correspondant à un gradient thermique local maximal autorisé le long de la cellule de 10 $K \cdot cm^{-1}$ et à une tension de fonctionnement locale maximale de 1,35 V ont été calculées lors du passage du hot standby au mode exothermique ou endothermique. Elles sont comparables pour les deux architectures de cellules. Cependant, les gradients thermiques sont plus faibles pour les ESC que pour les CSC en mode exothermique (22 K contre 30 K) et en mode endothermique (62 K contre 68 K) en raison de leur ASR plus élevé. Par conséquent, les ESC sont à privilégier pour des applications avec charge électrique variable en raison de leur stabilité thermique plus élevée.
Troisièmement, le modèle SRU a ensuite été couplé à un profil de puissance simplifié et étendu à une unité complète de production et de stockage d'H_2 composée d'une unité SOE avec deux modules, auxiliaires inclus. Les stacks SOE sont exploités dans une gamme de puissance étendue dont les limites sont basées sur les conditions précédentes en termes de gradient de température local et de tension de fonctionnement locale. La consommation d'énergie de l'unité de production d'H_2 fluctue entre 3,4 et 3,8 $kWh \cdot Nm^{-3}$ H_2. Grâce à la vapeur de refroidissement produite dans l'unité de méthanation catalytique, des rendements AC élevés de conversion de l'électricité en H_2 peuvent être atteints (93-103% en base PCS). Après un premier dimensionnement du réservoir de stockage d'H_2 et de l'unité de méthanation catalytique, des stratégies et des configurations d'installations sont proposées pour réduire la taille du stockage d'H_2. Les conclusions suivantes ont pu être tirées.
Le couplage électrique des unités SOE avec des profils de puissance fluctuants réduit les performances du couplage thermique entre les unités SOE et les unités de méthanation catalytique, ce qui diminue l'efficacité des installations power-to-SNG, mais en augmente également les coûts et en complexifie le pilotage. Les installations « multifuels » produisant à la fois de l'hydrogène et du gaz naturel de synthèse pourraient simplifier la conception et le fonctionnement des installations power-to-SNG. Une fraction des modules SOE fonctionnant à capacité nominale couvriraient les besoins en H_2 de l'unité de méthanation catalytique, tandis que les modules restants absorberaient l'intermittence de l'électricité renouvelable. Le fonctionnement flexible de ces modules avec des SOEC pouvant être opérées en mode exothermique ou endothermique permettrait d'améliorer le rendement de conversion de l'électricité vers l'H_2 par rapport à un fonctionnement des modules en marche/arrêt.

En cas de charge électrique constante, les SOEC doivent de préférence fonctionner en mode thermoneutre ou exothermique dans le cas d'unités SOE couplées à des unités de méthanation catalytique, même si une source de chaleur à haute température supérieure à 1073 K telle qu'une unité de gazéification est disponible. Toutefois, en cas de fluctuation de la charge électrique, la plage de puissance de fonctionnement des SOEC devrait être élargie autant que possible afin d'améliorer la capacité à moduler la charge et à absorber les fluctuations des sources d'électricité intermittentes. Il convient donc de privilégier le fonctionnement à la fois en exothermique et en endothermique, indépendamment des procédés en aval de la production d'H_2.

Une évaluation économique de trois concepts d'installations power-to-SNG a également été réalisée, en supposant une capacité de production de CH_4 de 20 MW (en base PCS).
Tout d'abord, une analyse ascendante des coûts des unités SOE de 10 à 100 MW est réalisée en partant des matériaux entrant dans la fabrication des cellules jusqu'aux coûts du système installé dans le contexte d'installations power-to-SNG, démarche assez peu fréquente dans la littérature jusqu'à présent. En conséquence, les coûts d'une unité SOE installée intégrée dans une installation power-to-SNG seraient de 434 €·kW^{-1} pour une unité de 15 MW et de 310 €·kW^{-1} pour une unité de 75 MW. Les paramètres les plus influents sur les coûts d'investissement des unités SOE installées sont la densité de courant au point de fonctionnement thermoneutre (1,3 V à 1073 K) et les matériaux des cellules.
Deuxièmement, les coûts de production et les coûts de production nivelés du GNS ont été déterminés pour les trois concepts d'installations sur la base de scénarios actuels et prospectifs. Les coûts de production du SNG sont compris entre 104 et 106 €·MWh^{-1} CH_4 (en base PCS) pour des installations avec unités PEM . Ils pourraient être abaissés à 82-89 €·MWh^{-1} CH_4 (en base PCS) pour les installations avec unités SOE. Les revenus générés par la vente de la chaleur résiduelle et de l'O_2 excédentaire pourraient réduire les coûts de production du GNS de 11% dans le meilleur des cas. Les coûts d'investissement totaux couvrent 19 à 27% des coûts de production du GNS et les coûts d'opération et de maintenance (O&M) 73 à 81%. L'unité d'électrolyse représente la plus grande part des coûts d'investissement dans tous les scénarios actuels (de l'ordre de 22 à 28%), mais cette part diminue sensiblement dans tous les scénarios prospectifs (jusqu'à 10 à 16%) et devient inférieure à la part couverte par les autres unités de l'installation (telles que l'unité de gazéification, l'unité de conditionnement de la biomasse ou l'unité de traitement du gaz de synthèse).
Dans tous les scénarios, les coûts de l'énergie électrique et les coûts des matières premières de la biomasse représentent la plus grande partie des coûts O&M (de 55 à 62% pour les premiers et de 10 à 18% pour les seconds). Les paramètres les plus influents sur les coûts de production du GNS sont les coûts d'investissement des stacks (investissement initial et de remplacement) et le prix de l'électricité dans les scénarios actuels. Toutefois, en raison de la production de masse et de la durée de vie améliorée des stacks, seul le prix de l'électricité reste un facteur clé des coûts de production du GNS dans les scénarios prospectifs. Dans la configuration la plus favorable, les coûts de production du GNS calculés dans ce travail seraient environ deux fois plus élevés que le prix moyen du gaz naturel en France tous secteurs confondus entre 2011 et 2017.

Perspectives

Les effets du fonctionnement à long terme des installations power-to-SNG, tel que la dégradation des SOEC et du catalyseur de méthanation, affectent leur performance et devraient être pris en compte dans de futurs travaux. Les pertes de charge ont été négligées dans tous les concepts étudiés et pourraient également être incluses, tout comme les pertes thermiques dans l'unité SOE.

Une autre amélioration pertinente de ces travaux pourrait être la mise en place d'algorithmes d'optimisation afin d'identifier des conditions d'opération optimales des installations power-to-SNG (par exemple la température et la pression des différents procédés) selon des objectifs simples ou multiples, tels que l'efficacité énergétique maximale, la maximisation de la production de GNS ou encore la maximisation de la récupération de la chaleur résiduelle. Une autre étape pourrait consister à intégrer des fonctions de coûts dans ces algorithmes pour tenir compte du compromis entre les performances techniques et économiques.

Quant au modèle 1D développé dans ces travaux, plusieurs aspects pourraient être améliorés à l'avenir. La modélisation des auxiliaires pourrait être consolidée avec des données expérimentales afin de prendre en compte leur comportement transitoire dans la réponse du modèle. En outre, la validité du modèle SRU lui-même devrait être vérifiée avec des données expérimentales au niveau système afin de limiter les interférences thermiques des fours qui se produisent lors des essais au niveau cellule ou stack en laboratoire. Cependant, il n'est pas certain que cela soit possible dans un avenir proche, car ces données sont difficiles à obtenir. Ce modèle pourrait aussi permettre de développer des stratégies de contrôle en temps réel, en raison de son temps de calcul limité. Il pourrait assez facilement être utilisé dans l'industrie, car une estimation de l'ASR de la cellule ou de sa dépendance à la température est suffisante pour obtenir une première évaluation de la réponse thermique des SRU aux fluctuations de la charge électrique.
Les futurs travaux expérimentaux devraient se concentrer sur le maintien du rendement du système pour des charges électriques inférieures à 50% du nominal, principalement en améliorant les auxiliaires, l'intégration thermique et en réduisant les pertes de chaleur. La capacité à faire fonctionner les systèmes SOE au-dessus de la charge nominale nécessite encore des améliorations significatives de la durée de vie des cellules et des systèmes (actuellement jusqu'à 23 kh et moins de 10 kh respectivement). Des essais terrains supplémentaires sont nécessaires pour évaluer le potentiel ultime des unités SOE à absorber les fluctuations de charge, car le meilleur temps de démarrage entre hot standby et fonctionnement nominal signalé jusqu'à présent est de 24 min.

Plusieurs aspects permettraient d'affiner l'évaluation économique présentée ici. Pour la technologie SOEC, des travaux supplémentaires dans les domaines de recherche suivants seraient utiles pour de futures analyses i) le développement de designs de stacks pour le fonctionnement sous pression et ii) le développement de composants de stacks ou d'auxiliaires adaptés au fonctionnement sous oxygène pressurisé à haute température. En outre, l'analyse ascendante des coûts des unités SOE dans la gamme de 10 à 100 MW pourrait être consolidée en élargissant la gamme de capacité de 1 MW à 1 GW ou en étendant l'analyse aux stacks SOE avec des CSC. La gamme de capacité des autres procédés de l'installation, tels que la gazéification, la méthanation catalytique ou la purification des gaz, devrait également être étendue. Pour les grandes unités power-to-SNG de plus de 50 MW, la disponibilité de la biomasse pourrait devenir un défi, c'est pourquoi le modèle devrait être étendu aux sources de carbone industrielles ayant des flux de carbone plus importants, par exemple dans l'industrie du ciment ou de l'acier. Dans ce cas, le prix du CO_2 devrait également être inclus comme paramètre dans l'analyse de sensibilité.

Flexibilisation et intégration des unités d'électrolyse à oxydes solides dans des installations de conversion d'électricité en gaz naturel de synthèse

Résumé : La technologie d'électrolyse à oxydes solides (SOE) pourrait permettre d'améliorer l'efficacité des installations de conversion d'électricité en gaz naturel de synthèse (SNG) et de réduire leur coût, grâce à une integration thermique performante, à l'industrialisation de la technologie et une flexibilisation des unités pour la pénétration de l'électricité renouvelable. Une analyse énergétique détaillée de trois concepts d'installations power-to-SNG innovants est d'abord réalisée avec une intégration thermique détaillée. Les installations intégrant des unités SOE et produisant du GNC ou du GNL présentent des rendements d'au moins 78,5% sur base PCS, bien plus élevés que pour les installations intégrant des unités d'électrolyse PEM qui produisent du GNC avec un rendement de 64,4%. La réponse thermique des unités SOE soumises à des variations de charge électrique est ensuite étudiée sur la base d'un modèle dynamique 1D à l'échelle d'une cellule (SOEC). Les cellules « électrolyte support » sont thermiquement plus stables que les « électrode support » et donc plus adaptées à des charges électriques variables. Le modèle est ensuite étendu à une unité entière de production et de stockage d'H_2 et couplé à différents profils électriques. L'unité affiche une consommation énergétique de 3,4-3,8 kWh·Nm^{-3} H_2 et un rendement élevé de l'électricité vers l'H_2 (93-103%) par récupération de la vapeur de méthanation. Un dimensionnement du réservoir d'H_2 et de l'unité de méthanation est réalisé avec un profil électrique éolien. Les charges électriques variables réduisent l'efficacité des installations power-to-SNG, en augmentent les coûts et en complexifient l'opération. Les installations multifuels semblent être l'option la plus prometteuse pour gérer l'intermittence de la production d'électricité. Etendre la gamme d'opération des SOECs aux modes exotherme et endotherme améliorerait les rendements de l'électricité vers l'H_2 en comparaison au mode marche/arrêt. Pour une charge électrique constante, les SOECs doivent préférablement être opérées au thermoneutre ou en mode exotherme. Enfin, les coûts de production du SNG sont évalués, en commençant par une estimation ascendante des coûts d'investissement d'unités SOE. Les coûts de production du SNG des concepts étudiés vont de 82 à 89 €·MWh^{-1} CH_4 (PCS) avec des unités SOE, valeurs plus faibles que pour des unités PEM, mais qui restent deux fois supérieures au prix moyen du gaz naturel en France.

Mots clés: power-to-methane, SOEC, analyse énergétique, analyse économique, modélisation dynamique, gaz naturel de synthèse

Flexibilisation and integration of solid oxide electrolysis units in power to synthetic natural gas plants

Abstract : The solid oxide electrolysis technology (SOE) could improve the conversion efficiency of power-to-synthetic natural gas (SNG) plants and reduce their costs, provided that i) a performant thermal integration is implemented ii) the technology is implemented at industrial scale, and iii) plants can absorb the intermittency of renewable power sources. First, the energy analysis of three innovative power-to-SNG plant concepts is implemented. For each concept, a full explicit thermal integration is proposed. Plants with integrated SOE units show efficiencies higher than 78.5% (based on the HHV of the SNG) for the production of CNG and LNG, significantly higher than plants with PEM units with a 64.4% efficiency for CNG production. Second, the thermal response of SOE units to electrical power loads is investigated with a 1D dynamic model at the cell level (SOEC). Electrolyte support cells present a higher thermal stability than electrode support cells and should be preferred for fluctuating power applications. The model was then extended to a full H_2 production and storage unit and coupled with different electrical power profiles. The units shows an energy consumption of 3.4-3.8 kWh·Nm^{-3} H_2 and a high power-to-H_2 conversion efficiency (93-103%) because of the steam recovery from the methanation unit. A first dimensioning of the H_2 storage tank and the methanation unit is proposed, assuming a windmill power profile. Fluctuating power profiles reduce the efficiency of power-to-SNG plants, increase their costs and complexify their operation. Multifuel plants seem to be the most promising option to tackle the issue of intermittent power production. Extending the operation range of SOECs to exothermic and endothermic modes would improve power-to-H_2 conversion efficiencies compared to on/off operation. In case of constant power load though, SOECs should preferably be operated at the thermoneutral point or in exothermic mode. Third, SNG production costs corresponding to the aforementioned plant concepts are evaluated, starting with a bottom-up cost evaluation of SOE units. The SNG production costs are in the range of 82-89 €·MWh^{-1} CH_4 (HHV) with SOE units, which is lower than with PEM units, but remains two times higher than the average price of conventional natural gas for all sectors in France.

Keywords: power-to-methane, SOEC, energy analysis, economic evaluation, dynamic modeling, synthetic natural gas